Université Libre de Bruxelles
Faculté des Sciences Appliquées
BATir Dept.

Année académique
2008-2009

Numerical modeling of the surface and the bulk deformation in a small scale contact. Application to the nanoindentation interpretation and to the micro–manipulation.

Péter Zoltán Berke

Promoteur: Prof. Ph. Bouillard
Co-promoteur: Prof. T.J. Massart

Building, Architecture, and Town Planning (BATir) Dept.
Université Libre de Bruxelles, av. F. D. Roosevelt 50
CP 194/2, 1050 Bruxelles, Belgique

Recherche financée par la Communauté Française de Belgique

Dissertation originale présentée en vue de l'obtention
du grade de Docteur en Sciences de l'Ingénieur

Acknowledgments

I wish to express my appreciation to Professors Philippe Bouillard and Thierry J. Massart for serving as my advisors during my work, as well as for their invaluable guidance of this research. The many enriching exchanges we had along the research work and their ability to look at problems in new and innovative ways have been indispensable to me throughout. I would especially like to thank Professor Thierry J. Massart for his availability, patience and enthusiasm about my work, and for his pertinent advices in technical questions.

Aside from Professors Philippe Bouillard and Thierry Massart, thanks also to Professors Stephane Godet, Issam Doghri, Ron Peerlings, Pierre Lambert, Marie–Paule Delplancke–Ogletree, and Andrey Solov'yov for their willingness to serve on the PhD committee.

Special thanks to Professors Marie–Paule Delplancke–Ogletree and Frank Ogletree for their advices and clear explanations on experimental procedures.

I would like to express the warmest thanks to Professor Andrey Solov'yov and his research group at Frankfurt Institute of Advanced Studies for their help and guidance in the atomic level simulations. I look forward to our continued collaboration.

My work has been made possible by the financial support of the French–speaking Community of Belgium (ARC convention 04/09-310); this support is gratefully acknowledged.

I owe a large debt of gratitude to a number of friends and colleagues who have been generous with their technical expertise and friendship during the past years. Although the list of these people is too long to be given in totality, I would especially like to thank Kfir Menchel and Vincent Decouvreur.

I specially thank Yulia Tyutikova, who by her words and actions gave me support through all the highs and lows, providing invaluable encouragement. Thanks also to her family, especially Waldemar Junker and Janina Junker for their support and encouragement.

I have become the person I am today thanks to the continuous support and love of my family. I hope this work is in some way indicative of all I have learned from them. It is with love and gratitude that I dedicate this dissertation to my father, Dr. Péter Berke.

Résumé

L'adaptation des surfaces pour des fonctions prédéterminées par le choix des matériaux métalliques ou des couches minces ayant des propriétés mécaniques avancées peut potentiellement permettre de réaliser des nouvelles applications à petites échelles. Concevoir de telles applications utilisant des nouveaux matériaux nécessite en premier lieu la connaissance des propriétés mécaniques des matériaux ciblés à l'échelle microscopique et nanoscopique. Une méthode souvent appliquée pour caractériser les matériaux à petites échelles est la nanoindentation, qui peut être vue comme une mesure de dureté à l'échelle nanoscopique.

Ce travail présente une contribution relative à l'interprétation des résultats de la nanoindentation, qui fait intervenir un grand nombre de phénomènes physiques couplés à l'aide de simulations numériques. A cette fin une approche interdisciplinaire, adaptée aux phénomènes apparaissant à petites échelles, et située à l'intersection entre la physique, la mécanique et la science des matériaux a été utilisée. Des modèles numériques de la nanoindentation ont été conçus à l'échelle atomique (modèle discret) et à l'échelle des milieux continus (méthode des éléments finis), pour étudier le comportement du nickel pur. Ce matériau a été choisi pour ses propriétés mécaniques avancées, sa résistance à l'usure et sa bio–compatibilité, qui peuvent permettre des applications futures intéressantes à l'échelle nanoscopique, particulièrement dans le domaine biomédical. Des méthodes avancées de mécanique du solide ont été utilisées pour prendre en compte les grandes déformations locales du matériau (par la formulation corotationelle), et pour décrire les conditions de contact qui évoluent au cours de l'analyse dans le modèle à l'échelle des milieux continus (traitement des conditions de contact unilatérales et tangentielles par une forme de Lagrangien augmenté).

L'application des modèles numériques a permis de contribuer à l'identification des phénomènes qui gouvernent la nanoindentation du nickel pur. Le comportement viscoplastique du nickel pur pendant nanoindentation a été identifié dans une étude expérimentale–numérique couplée, et l'effet cumulatif de la rugosité et du frottement sur la dispersion des résultats de la nanoindentation a été montré par une étude numérique (dont les résultats sont en accord avec des tendances expérimentales). Par ailleurs, l'utilisation de l'outil numérique pour une autre application à petites échelles, la manipulation des objets par contact, a contribué à la compréhension de la variation de l'adhésion électrostatique pendant micromanipulation. La déformation plastique des aspérités de surface sur le bras de manipulateur (en nickel pur) a été identifiée comme une source potentielle d'augmentation importante de l'adhésion pendant la micromanipulation, qui peut potentiellement causer des problèmes de relâche et de précision de positionnement, observés expérimentalement.

Les résultats présentés dans cette thèse montrent que des simulations numériques basées sur

la physique du problème traité peuvent expliquer des tendances expérimentales et contribuer à la compréhension et l'interprétation d'essais couramment utilisé pour la caractérisation aux petites échelles. Le travail réalisé dans cette thèse s'inscrit dans un projet de recherche appelé 'mini–micro–nano' ($m\mu n$), financé par la Communauté Française de Belgique dans le cadre de 'l'Action de Recherche Concertée', convention 04/09-310.

Abstract

The adaptation of surfaces for specific functions by the use of metallic materials and thin films with advanced mechanical properties can potentially lead to novel applications on the small scales. The conception of nanoscale devices taking advantage of new materials requires the characterization of these materials on the micro– and nanoscales in the first place. One of the frequently used methods of material characterization on small scales is the nanoindentation, being conceptually a nanoscale hardness measurement.

This thesis presents a contribution to the interpretation of nanoindentation results, involving a large number of coupled phenomena by using numerical simulations. For this purpose an interdisciplinary approach was chosen, adapted to small scale phenomena combining concepts from physics, mechanics and material science. Numerical models were developed to study the behavior of pure nickel on the atomic scale (discrete description), and on the scale of continuum mechanics (finite element method). This material was chosen for its advanced mechanical and wear properties coupled to bio–compatibility, which can lead to interesting future applications particularly in the biomedical field. Advanced methods of solid mechanics were applied to consider the local finite deformation applied to the material (using a corotational formulation) and to take contact conditions into account in the finite element model (using an augmented Lagrangian treatment of normal and tangential contact).

The application of the numerical models contributed to the identification of the physics governing the nanoindentation. The rate–dependent plastic behavior of pure nickel in nanoindentation was identified in a coupled experimental–numerical study, and the cumulative effect of surface roughness and friction on the dispersion of nanoindentation results was shown through a numerical study (with results in good agreement with experimental trends). The continuum scale numerical tool was used to model a different application on small scales, the manipulation of objects by contact. The plastic flattening of the surface asperities of the microgripper (made of pure nickel) was identified in a numerical study as source of an important increase of contact adhesion during micromanipulation, which can potentially result in release and accuracy issues, also observed experimentally.

The results of this thesis show that physically–based numerical simulations yield results that can potentially explain experimental trends and contribute to the better understanding of the nanoscale world. The research work presented in this thesis and the related results contribute to a research project entitled ‘mini–micro–nano’ ($m\mu n$) with the financial support of ‘Action de Recherche Concertée’ convention 04/09-310 sponsored by the French–speaking Community of Belgium.

Related publications

Berke, P., Tam, E., Delplancke-Ogletree, M.-P. and Massart, T.J. 2009. Study of the rate-dependent behavior of pure nickel in conical nanoindentation through numerical simulation coupled to experiments. Mechanics of Materials, **41**, 154-164

Berke, P., Delplancke-Ogletree, M.-P., Lyalin, A., Semenikhina, V.V. and Solov'yov, A.V. Simulation of the nanoindentation procedure on Nickel on the smallest length scale: a simple atomistic level model. in *Latest Advances in Atomic Cluster Collisions: structure and dynamics from the nuclear to the biological scale* (edited by J.-P. Connerade and A.V. Solov'yov), Imperial College Press, London (2008), 205-224

Berke, P., Houdaigui, F.E., Massart, T.J. Coupled friction and roughness surface effects in shallow spherical nanoindentation. Submitted for publication in 2008

Sausse Lhernould, M., Berke, P., Massart, T.J., Régnier, S. and Lambert, P. Variation of the adhesive electrostatic forces on a rough surface due to the deformation of roughness asperities during micromanipulation of a spherical rigid body. Submitted for publication in 2008

Attended conferences

Berke, P., Tam, E., Massart, T.J. and Delplancke-Ogletree, M.-P. Coupled experimental-numerical rate-dependent analysis of conical nanoindentation on pure nickel. (poster) AVS 54th International Symposium and Exhibition, 14-19 October 2007, Seattle (USA)

Berke, P., Massart, T.J. and Tam E., Coupled experimental-numerical analysis of nanoindentation on pure Nickel. (oral presentation in Modeling and Simulation of Nano Materials and Mechanics section) 9th United States National Congress on Computational Mechanics (US-NCCM), 23-26 July 2007, San Francisco (USA)

Berke, P., Delplancke-Ogletree, M.-P., Lyalin, A., Semenikhina, V.V. and Solov'yov, A.V. Simulation of the nanoindentation procedure on Nickel on the smallest length scale: a simple atomistic level model. (oral presentation and contribution in the proceedings in Clusters on surface section) The Second International Symposium, Atomic cluster collisions: Structure and dynamics from the nuclear to the biological scale, 19-23 July 2007, Darmstadt (Germany)

Berke, P. and Massart, T.J. Numerical simulation of the nanoindentation experiment: influence of the experimental uncertainties. (oral presentation and contribution in the proceedings, Materials for MEMS section) Third International Conference on Multiscale Materials Modeling, 18-22 September 2006, Freiburg (Germany)

Berke, P. and Massart, T.J. Numerical simulation of the nanoindentation experiment: sensitivity analysis of the experimental parameters. (oral presentation and contribution in the proceedings, Industrial Applications section) III European Conference on Computational Mechanics Solids, Structures and Coupled Problems in Engineering, 5-8 June 2006, Lisbon (Portugal)

Contents

Chapter 1

Introduction

1.1 Motivation of the study

This thesis aims at giving a contribution to the understanding of the behavior of surfaces on the micro– and nanoscale via numerical simulations.

The research work presented in this thesis and the related results contribute to a research project entitled 'mini–micro–nano' ($m\mu n$) with the financial support of an 'Action de Recherche Concertée' convention 04/09-310 sponsored by the French–speaking Community of Belgium. This part of the project spanned for 4 years including the prime objective of the present work, leading to both fundamental and applied research tasks (design of a gripper on the microscale). This project involved three departments of the Université Libre de Bruxelles (ULB), responsible for the experimental tasks (Chemicals and Materials Dept.), the numerical modeling related to the understanding of material behavior on the small scales (BATir Dept.) and the design of potential future applications (Beams Dept.) exploiting the accumulated experience. This thesis constitutes a part of the second contribution. For more detailed information on the objectives and organization of the $m\mu n$ project the reader can consult [ARC(04/09-310) 2003].

The physics on small scales is different from the macroscale we are familiar with and involves more complex phenomena. For their understanding, and considering their complexity, numerical models can be very helpful.

As an example, the main issues of the manipulation of objects by contact on small scales in the high–precision industry and in medical applications are related to releasing them (in micro–handling tasks under a microscope, pick, hold and place operations of micro–components or in assembly operations of micro–mechanisms) disturbing their accurate spacing [Carpick *et al.* 2001, 2002]. Release problems stem from the adhesion between the object and the gripper arm and its potential increase during the gripping and manipulating procedure. Identifying the key physical phenomena governing the experiments on small scales via numerical simulations can

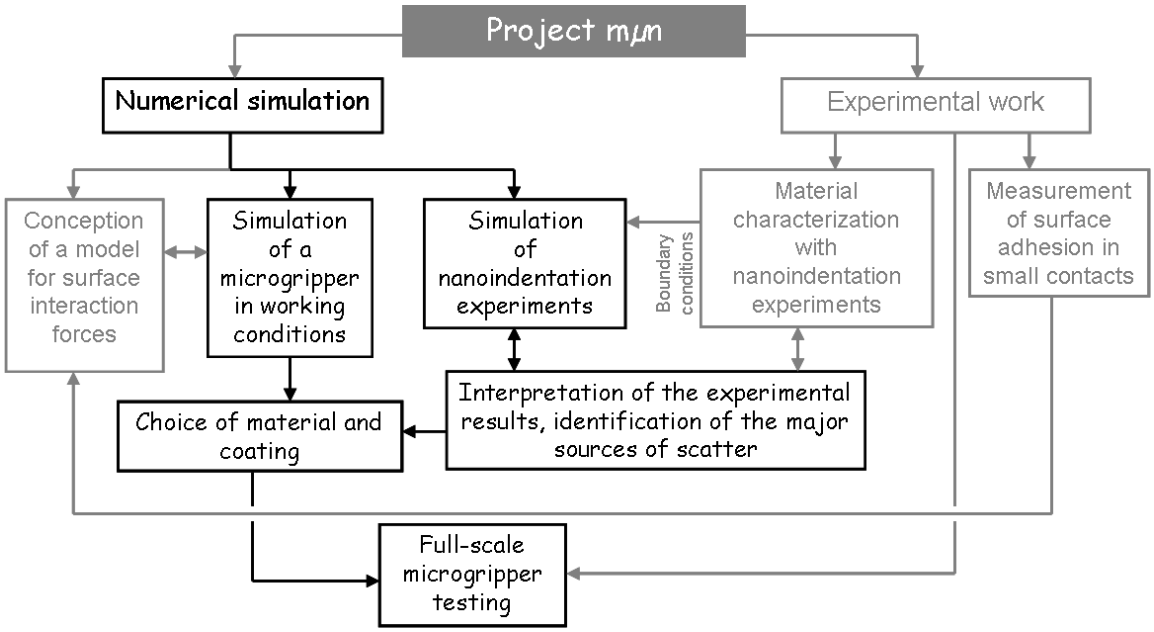

Figure 1.1: Highlighted items of the chart correspond to the contribution of this thesis to the research tasks of the $m\mu n$ project [ARC(04/09-310) 2003].

for example substantially contribute to the identification of the parameters of an applicable material.

In micro–electro–mechanical system (MEMS) applications involving moving parts, improved mechanical properties and wear resistance of the materials used to produce components can result in significant improvements of the performance and reliability of these microscale devices. The frequently used base material, silicon, has many advantages in nano–fabrication (considering the vast experience with this material in this field), but its mechanical properties cannot be fitted for all demands. A recent field of interest is the use of metallic materials in MEMS applications for their advanced mechanical and wear properties compared to silicon. Particularly the use of pure nickel and pure titanium base materials on the nanoscale results in significant additional advantages considering their bio–compatibility, which can potentially lead to a broadening of the domain of application of MEMS to surgical and biomedical applications.

The use of novel materials and advanced single–or multi–layer material systems for adapting the surface properties for a given function first implies characterizing their mechanical properties. This allows to identify their strengths and weaknesses for future applications. One of the frequently used methods for material testing on small scales [André *et al.* 2007; Laconte *et al.* 2004], particularly adapted for the characterization of thin film mechanical properties, is the nanoindentation [Baker 2001]. Nanoindentation can be considered conceptually as a hardness test made on the small scale, i.e. a hard indenter with a predefined geometry is pushed

in the sample material. Contrary to the traditional hardness measurements, the applied load–indenter displacement curves (or shortly 'load–displacement curves') are continuously monitored in nanoindentation. The load–displacement curves are considered to be the response of the material and are the basis of analytical post–treatment methods (using a number of assumptions), which aim at the identification of material properties of the sample, usually the elastic modulus. However, since a large number of spurious and coupled contributions (e.g. sample surface roughness and friction, effect of the substrate, etc.) can intervene in the load–displacement curves and considering the complex physics of the nano–hardness measurement, numerical models can give additional insight into the physics involved. They can help in assessing the correctness of the underlying assumptions of the post–treatment methods and contribute to the identification of the main sources of dispersion in nanoindentation results and to the interpretation of experimentally observed trends.

In summary, the use of specific metallic materials (pure nickel and pure titanium) and surface functionalization on the micro–and nanoscale by the application of thin films, can lead to interesting applications, particularly in the biomedical field. Numerical models can potentially contribute to the understanding of the behavior of these materials on small scales. Since the overall material behavior is the convolution of physics stemming from different scales, and even though it is not purposed to investigate all the scales of interest, different types of numerical models were set up on different scales, to investigate the various contributions to the material behavior. As a result, the approach to solve the related problems uses advanced numerical methods, and somehow involves interdisciplinary aspects between physics, mechanics and material science.

1.2 Outline of the thesis

The plan of the thesis is as follows. First, to set the scene, the experimental material testing procedure considered here, i.e. the nanoindentation and the related issues, are presented in Chapter 2. This chapter explains in more detail how the convolution of the effects of different material behaviors and sources of scattering may result in an unclear relationship between material properties and the load–displacement curve, leading to serious ambiguities in the interpretation of nanoindentation data. This is the reason why the contribution of numerical models to the understanding and interpretation of nanoindentation results may be of importance.
In Chapter 3, the objectives and the related applications of numerical methods of nanoindentation on different scales are presented. An atomic level numerical model of nanoindentation was set up to investigate the physics at the nanoscale. This discrete numerical model, has the prime advantage of identifying trends related to the variation of physical parameters. The atomic scale

numerical model and the issued results are presented in Section 3.1. The main drawback of such small scale discrete numerical models is the lack of possible direct quantitative correlation with experimental results. For a direct qualitative and quantitative comparison with experimental results a continuum scale numerical model, using the finite element method was developed.
In Chapter 4 the necessary numerical developments; adding contact constraints and nonlinear material behavior in a finite deformation description on the continuum scale are presented and discussed.
Chapter 5 illustrates the applications of this continuum scale numerical model to the problem of nanoindentation (Section 5.1 to Section 5.4) and to micromanipulation (Section 5.5). Section 5.1 constitutes a preliminary numerical study investigating the influence of some indentation parameters on nanoindentation results of pure nickel, using a rate–independent material model (i.e. the material behavior is independent from the rate of strain). An interesting feature of the developed continuum scale model is the possibility of a direct comparison with experiments, which is exploited in Section 5.2, considering rate–dependent material effects in conical nanoindentation of pure nickel. The objective of Section 5.3 is the numerical evaluation of the dispersion in nanoindentation results of pure nickel due to the effect of sample surface roughness and friction on the contact interface in realistic indentation conditions. Section 5.4 discusses the performance of two experimental post–treatment methods (implemented in a numerical post–treatment tool) in the varying numerical indentation configurations considered in Chapter 5 (different material properties and behavior, including surface roughness and friction). The attention is then shifted to the problem of micromanipulation in Section 5.5, aiming for a better understanding of the adhesive electrostatic effects and their variation due to the plastic deformation of surface roughness in the gripper–manipulated object contact. Finally, the conclusions are made on the research work discussed in this thesis in Chapter 6, together with the outlook and the further developments it implies.

1.3 Main contributions of the thesis

The contributions of this thesis can be divided in two groups: the development of numerical models, and their application to the considered nanoscale problems, contributing to the understanding of phenomena on small scales.
Nanoindentation modeling is addressed on two scales in this thesis: an atomic scale discrete model (Section 3.1), and a continuum scale model using the finite element method (Chapter 4) were developed using advanced numerical techniques. The special care taken in the choice of the numerical ingredients allowed coupling experimental and numerical studies on the continuum scale.
Applying the developed numerical models lead to the following main results.

It is shown in a coupled experimental–numerical investigation that considering the rate–dependent plastic behavior of pure nickel in conical nanoindentation is a physically–based need (Section 5.2). All of the experimentally observed trends are reproduced in the numerical simulations using a simple rate–dependent plastic material behavior, with a material parameter set in the physically sound domain for metals.

It is shown, using a numerical model, that the effect of friction and of surface roughness on the dispersion of nanoindentation raw and post–treated results are cumulative, i.e. considering friction on a rough surface increases the scattering (Section 5.3). The resulting dispersion is found to be sufficiently high, so that it could be wrongly interpreted as variations in the elastic properties of the material.

It is shown through a two–scale mechanical model set up on the continuum scale, coupled to electrostatic simulations that the flattening of the surface asperities during micromanipulation gives rise to a significant increase of the contact adhesion (Section 5.5). The magnifying factor of the adhesive electrostatic forces due to the plastic deformation of the surface asperities is evaluated and it is found to give a contribution to the difficulty to release objects when the squeezing manipulation force is released.

Chapter 2

Material property measurement by nanoindentation

Among the prime goals of the project, the characterization of bulk materials and coatings by nanoindentation is the focus of this chapter of the thesis. The nanoindentation experimental procedure and two methods used to derive an elastic modulus from the load–displacement data are presented first. Then, some frequent sources of scattering in nanoindentation, and the resulting ambiguities related to the difficulty of the deconvolution of the potential contributions to the indentation response are discussed.

The relative movement on the contact interface of nanoscale devices induces friction and wear in the contacting material pair, which can have disturbing effects. Applying suitable surface coatings on the substrate material can deliver substantial improvements considering performance and reliability, and broaden the field of application to the biomedical field. The use of pure nickel and pure titanium materials and metallic substrate with thin film coatings forming potentially bio–compatible systems is of high interest, considering their interesting mechanical and wear properties compared to the widely used silicon.

Surface engineering requires in first instance measuring the mechanical properties of the substrate material and of the coatings. The success of small scale applications depends among others on the solution of materials issues, such as mechanical properties associated with the design and fabrication. The remarkably small thicknesses of the deposited film layers which can be as thin as a few nanometers severely restricts the choice of applicable mechanical characterization methods. This implies that the measuring equipment itself has to be adapted to the nanoscale, which leads to one of the frequently used nanoscale material testing methods, the nanoindentation measuring procedure.

A great deal of effort has been directed towards the development of techniques for characterizing the mechanical properties of small volumes of material. Testing methods on small scales

concurrent to nanoindentation can be found in André *et al.* [2007]; Laconte *et al.* [2004]. The principle of the nanoindentation experiment is similar to the micro–hardness measurement but in contrast to traditional hardness testers, the nanoindentation system allows the application of a specified force (on the order of micronewtons) or displacement (on the order of nanometers) to obtain a load–displacement curve. This continuously recorded load–displacement curve is considered to be the mechanical fingerprint of the material response to the deformation, and it is used to determine usually the elastic modulus of the sample material via analytical post–treatment methods involving a number of simplifying assumptions. Nanoindentation is mainly used for its advantage to allow a local measurement of material properties of bulk materials, substrates coated with thin films and multi–layer sandwiches directly, in working conditions. As opposed to most alternative testing methods, in nanoindentation the actual complete system (substrate and thin film layers) is the subject of the measurement without changing its integrity for the purpose of the measurement (by removing the substrate in a pre–measure etching step to test the coating, for example). Moreover, since in real–life applications the material working conditions involve contact loading, the number of assumptions made for the prediction of the performance of a material system by nanoindentation (using similar loading conditions) is kept to a possible minimum. Respecting the complex stress and strain state resulting from contact loading may be of importance in thin film delamination and fracture studies for example [Abdul-Baqi 2002; Geng *et al.* 2007; Latella *et al.* 2007; van den Bosch 2007].

2.1 Nanoindentation, equipment and experimental conditions

The nanoindentation experiments of the research project were performed using a Hysitron Triboindenter [Hysitron 2008]. The indentation equipment consists of a frame on which the indenter actuator, the thermally isolated indentation chamber (used because nanoindentation due to its high accuracy is sensible to thermal gradients), and the sample holding plate are attached (Fig.2.1). For a more detailed information on nanoindentation, the reader is referred to [Baker 2001]. The indenter tips are exchangeable, and can have different standard geometries (axisymmetric or sharp–edged), and they are usually made of diamond. The choice of the diamond, being the hardest natural material is necessary to enforce a low tip deformation for the sake of accuracy [Jeong & Lee 2005], and reproducibility of the experiments. It has to be emphasized, that the actual tip geometry is usually not known in detail. Moreover with an increasing number of indentations a cumulative irreversible deformation of the indenter tip is usually observed. It can be evaluated by adequate imaging techniques, as shown in Section 5.2, but it is far form being a common practice, since it is extremely time–consuming.

In coupled experimental–numerical studies a conical indenter can be used for the sake of consistency between the experimental conditions and the numerical model having an axial symmetry,

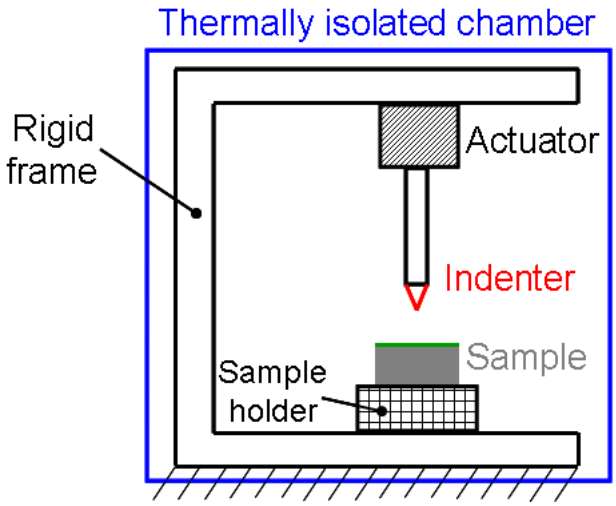

Figure 2.1: Schema of the nanoindentation equipment.

and thus avoiding 3D modeling. However, due to accuracy issues in the fabrication of spherical–capped conical indenter tips, the agreement between the actual and the nominal radius of $2\mu m$ seems to be in some regions approximate (Fig.2.2). The influence of this inaccuracy is studied in Section 5.1. Potential tip misalignment may also be a source of error, however for conical shaped indenters, its influence is rather small, at least as long as the indentation depth does not exceed the height of the spherical cap [Pelletier *et al.* 2007].

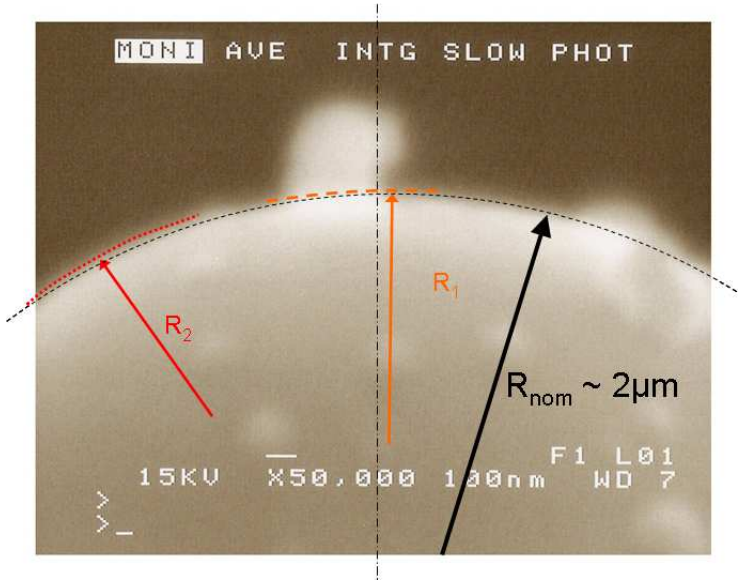

Figure 2.2: The accuracy of the fabrication of the indenter tips cannot guarantee in all cases a constant radius of curvature of the tip $R_1 > R_2$, SEM image presented in Tam [2006].

Important experimental parameters are determined by the sample preparation procedure, having the goal to approach as much as possible the ideal nanoindentation configuration, i.e. to reduce surface roughness, to decrease the effect of oxide layers and impurities, to remove work–hardened layers, to relieve residual stresses and to decrease unwanted anisotropy.

Spurious effects related to the sample surface roughness in nanoindentation can have a high influence in many practical configurations. This problem is addressed in Section 5.3. Surface roughness effects are especially important in the small indentation depth regime [Berke & Massart 2006; Bouzakis *et al.* 2001; Wang *et al.* 2007b; Warren & Guo 2006; Yu *et al.* 2004]. Note that with special care in the sample preparation procedure used on pure nickel and pure titanium bulk materials, the arithmetic roughness value of the sample surfaces could be kept to a few nanometers only. This satisfying consistency between the experiments and idealized numerical conditions allowed performing the coupled experimental–numerical study in Section 5.2. In practice however, the surface roughness of thin films, can reach average values of 30–40nm [Barshilia & Rajam 2002; de Souza *et al.* 2005, 2006; Fang *et al.* 2007; Kumar *et al.* 2006] which become comparable to the imposed indentation depth, limited by the film thickness. In extreme cases the influence of surface roughness may lead to high dispersion, resulting in difficulties in exploiting and interpreting nanoindentation results.

The actual nanoindentation set of the tested material is preceded by a *calibration step*, in which the potentially varying testing procedure–related experimental parameters are evaluated, such as: the approximation of the actual indenter geometry (tip area function), the evaluation of the indenter frame stiffness (frame compliance) and spurious indenter displacement due to thermal gradients in the indentation chamber (thermal drift). For a detailed presentation of these standard notions the reader can consult [Tam 2006; Tripathy 2005]. In this step a reference indentation in a material with known properties, usually fused quartz is performed. The resulting load–displacement curves are used as a reference in the post–treatment methods.
Nanoindentation follows a predefined loading sequence where the applied force is specified as a function of time. Generally three parts of the loading sequence are distinguished (Fig.2.3): the loading period where the applied force is increased until a peak value, the holding period where for a prescribed amount of time this peak load is maintained, and finally the unloading period where the applied force is decreased gradually to zero. The force levels are increased once the indenter–sample contact is established. The first step, or load increment, made to establish contact between the sample surface and the indenter tip causes a non–zero initial penetration, and therefore results in a threshold in both force level and indentation depth with a relative influence being the most pronounced in small indentation depth. The maximum value of the applicable peak load is a characteristic for the nanoindentation equipment, and was fixed to be under $10mN$. The minimum value of the peak load is determined, depending on the indenter tip and the sample material to obtain meaningful results, considering that the scattering in nanoindentation results is the highest in small indentation depth. The indenter speed usually varies between some tens of nm/s to some $\mu m/s$ in the experiment. The duration of the holding period is limited by increasing effects of thermal drift (indenter displacement due to spurious

thermal gradients). Usually a large number of indentations (hundreds) are performed in one set, which is a need to reach a stable average in nanoindentation [Bouzakis & Michailidis 2004].

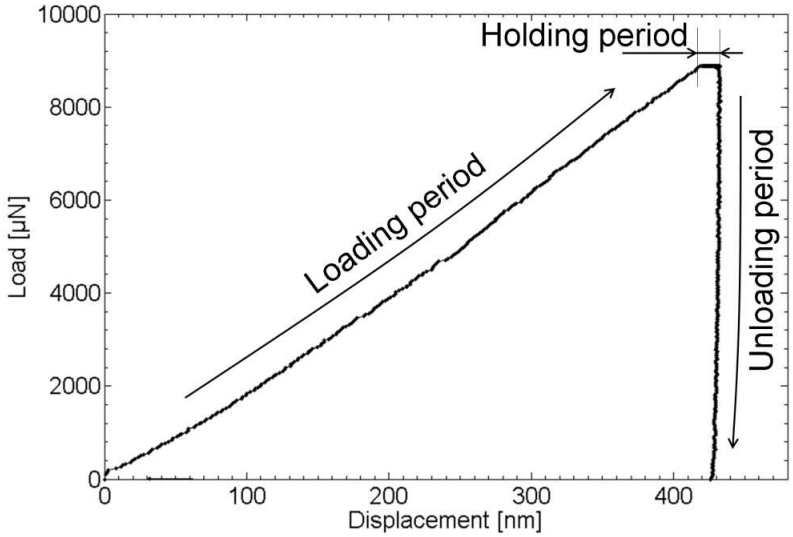

Figure 2.3: Load–displacement curve portions corresponding to the loading, holding and unloading periods. The plotted experimental load–displacement curve is of pure nickel, with a $5s$–$10s$–$5s$ loading, holding and unloading time, respectively at $9000\mu N$ peak load in conical nanoindentation [Tam 2006].

2.2 Post–treatment of nanoindentation data – numerical tool

The Young's modulus of the sample can be extracted from nanoindentation data with various post–treatment procedures. Note that material parameters obtained from nanoindentation are relative values compared to a reference value associated to the indentation of a material with known properties, measured in the calibration step of the experiments [Baker 1997; Fischer-Cripps 2006].

Two frequently used post–treatment methods for nanoindentation data were considered in this work: a method proposed by Oliver and Pharr [Oliver & Pharr 1992] and another proposed in Ni *et al.* [2004], both having the goal to identify the elastic modulus and the nano–hardness of the tested material (more details concerning these methods are given in the corresponding section of the Appendix). The nano–hardness of a material is not an intrinsic material property, since it is usually defined as the ratio of the peak load and the projected contact area $H_{nano} = \dfrac{F_{max}}{A_{proj}^{cont}}$, and thus depends on the elastic and plastic behavior of the material via F_{max} and on the deformed contact geometry via A_{proj}^{cont}. Hence, the focus in this work was rather set on the post–treated elastic modulus, considered as an intrinsic material property.

The above experimentally applied methods are usually built in functions within the measuring

equipment. They were implemented in a numerical tool such as to allow the post–treatment of raw experimental indentation data, as well as data issued from numerical simulations in a similar manner as in the experiments. The post–treatment tool aims for a large flexibility and interactivity so that the user can intervene, and adjust some otherwise unaccessible parameters of the post–treatment methods considered here; and allows following step–by–step the procedure. Applying experimental post–treatment methods to numerical indentation data allowed to study the influence of various parameters of indentation not only on raw nanoindentation data but also on the value of the post–treated elastic modulus, and to focus on the practical implications of the work.

Different post–treatment methods potentially show different performance in predicting the elastic modulus of the tested material, which raises the question of which method should be preferred in which conditions. Section 5.4 aims at providing an answer to this question by a discussion on the performance of the two considered post–treatment methods based on the indentation configurations considered in Sections 5.1 to 5.3 (with varying material properties and behavior, surface roughness and friction).

The common simplifying assumptions of both post–treatment methods are:

- flat and smooth sample contact surface,
- frictionless contact between the indenter tip and the sample,
- the behavior of the indenter–sample contact in the unloading period is elastic and rate–independent. This means that potential viscoelastic effects [Cheng & Cheng 2005; Ovaert *et al.* 2003; Zhang *et al.* 2008] are not taken into account,
- the values of the Poisson's ratio of both the sample ν_{sample} and the indenter material ν_{ind} are known, or approximated.

The first post–treatment method considered here is the most widely spread method, proposed by Oliver and Pharr [Oliver & Pharr 1992], used for its simplicity and its broad range of application. This method is based on the assumption of purely elastic unloading of the indenter–sample frictionless contact. It only uses the unloading segment of the load–displacement curve of nanoindentation to compute the contact stiffness for further processing. Along with this simplicity, it requires the knowledge of a geometrical quantity called contact depth h_c defined on an actual deformed contact configuration, which itself depends on potential pile–up or sink–in phenomena (Fig.2.4). The contact depth is evaluated from the maximum indentation depth h_{max} by making simplifying assumptions. Note that a significant improvement for the approximation of h_c could result from the measurement of the experimental indent profile, which can furthermore give additional information about the deformation procedure during indentation [Bolzon

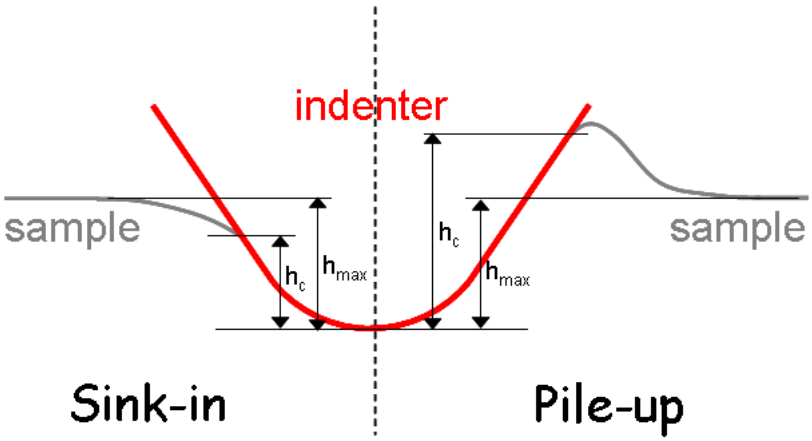

Figure 2.4: Definition of the contact depth h_c used in the Oliver and Pharr post–treatment method. The influence of potential sink–in and pile–up phenomena on h_c can become significant in nanoindentation experiments.

et al. 2004; Nagy *et al.* 2006]. However, it is a complex and time consuming procedure, and thereby it is rarely performed systematically after nanoindentation tests.
Post–treatment methods are also sources of nanoindentation scattering due to their assumptions and approximations which are not always applicable practically. One of the main sources of dispersion recognized in the literature is related to the approximation of the deformed shape of the indenter imprint and thereby the value of h_c [Habbab *et al.* 2006; Taljat & Pharr 2004].

The second post–treatment method, proposed by Ni et al. [Ni *et al.* 2004] has the goal to overcome the main drawback of the Oliver and Pharr method, i.e. the evaluation of the contact depth, and thereby increase the accuracy of the prediction in the case of spherical nanoindentation. This post–treatment method is based on trends determined by numerical simulations of nanoindentation using the finite element method. The assumptions of the numerical work of this post–treatment method in addition to the common assumptions are:

- the indenter tip geometry is spherical,
- the material is elastic–plastic with isotropic power law hardening,
- the behavior of the material is rate–independent.

Based on the numerical results, Ni et al. defined non–dimensional functions of the indentation problem in terms of the contact stiffness, the total work W_t and the elastic work of indentation W_e, corresponding to the area under the loading and the unloading portions of the load–displacement curve respectively. These functions are used for the evaluation of the Young's modulus of the tested material. The corresponding drawback is that this method is more sensitive to changes in any portion of the curve and to the variations in the load levels affecting

directly the integrated work quantities.

Finally, for the sake of a more complete overview, energy–based methods [Beegan *et al.* 2005; Kusano & Hutchings 2003] have to be mentioned, that use this latter type of methodology to evaluate more advanced material properties, such as plastic flow data [Cao & Lu 2004; Giannakopoulos & Suresh 1999; Ma *et al.* 2003; Zhao *et al.* 2006]. The identification of the plastic material parameters from nanoindentation data was not considered in this work. For more detailed information on the performance of frequently applied post–treatment methods of nanoindentation and for a detailed description of the post–treatment methods used here the reader is referred to [Beegan *et al.* 2005; Kusano & Hutchings 2003] and [Ni *et al.* 2004; Oliver & Pharr 1992], respectively.

2.3 Nanoindentation results and sources of dispersion

The result of a nanoindentation experiment is the load–displacement curve, being considered as the sample material response to indentation. Usually a relatively accurate set of nanoindentations presents a scattering of around 10-20% in the load–displacement curves. This dispersion stems from various sources, among which some listed in the following frequently add to the ones already discussed before (related to the machine inaccuracy, the tip geometry, the sample preparation).

Pop–ins are sudden displacement bursts observed during the loading period, as shown in Fig.2.5. They are characteristic in $10nm$ depth for conical indentations in pure nickel with the indenter of $2\mu m$ radius of curvature. Pop–ins are usually explained in the literature by sudden dislocation nucleations [Fujikane *et al.* 2008; Zong & Soboyejo 2004]. Even though pop–ins occur usually in small indentation depths, the load–displacement curves can be strongly altered by this phenomenon, consequently giving questionable nanoindentation results. Note that the post–treatment method of Oliver and Pharr is less sensitive to pop–ins, since since it is based on the unloading period of the load–displacement curve.
The residual imprint on the sample surface after nanoindentation is on the order of a micrometer of diameter when considering high force levels ($9mN$) and a blunt indenter type with a conical geometry (with a nominal radius of curvature of $2\mu m$) leaving a relatively large imprint. In the case of annealed pure nickel for example, the average grain size of the nickel sample was two orders of magnitude larger than the imprint size. As a consequence nanoindentations could be performed in crystalline materials in the middle of the grains to avoid grain boundaries, regions that show a potentially different material behavior than the material inside the grain [Aifantis & Ngan 2007; Lian *et al.* 2007]. Note that the grain material properties are aimed for in the case

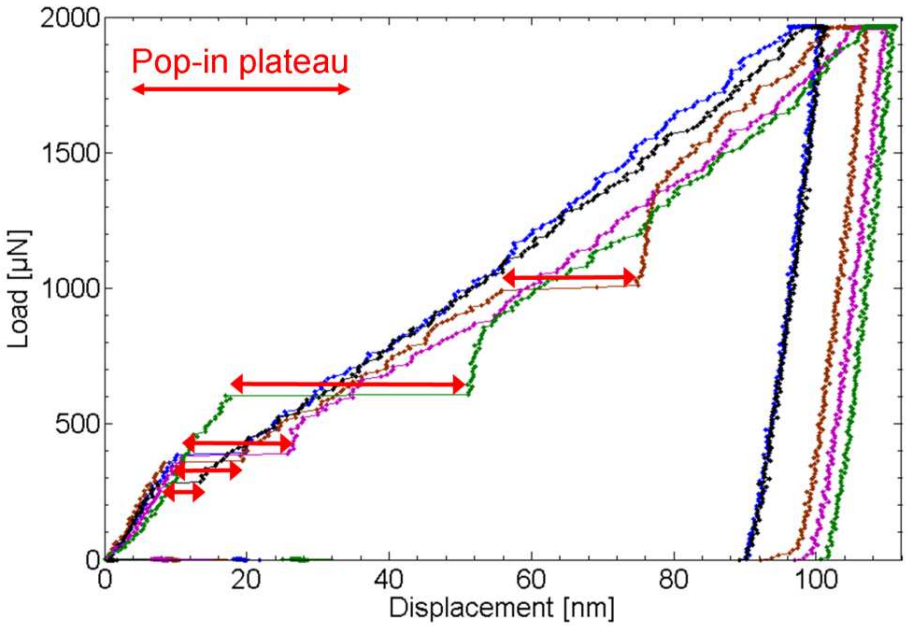

Figure 2.5: Pop–ins for nanoindentations of pure nickel at 2000μN peak load with a conical indenter of 2μm nominal tip radius [Tam 2006].

of large grained crystalline materials, since their behavior is dominant in the overall material response. Practically, however this is not always feasible, since this implies localizing the grain boundaries using a time–consuming pre–measure surface scan. In the case of small grained or nanocrystalline materials, one can hardly proceed in this manner anymore, since the size of the grains can be on the same order of magnitude, or smaller than the nanoindentation imprint size. Particularly for nanocrystalline materials the large volume fraction of grain boundaries is the deliberate result of material processing, resulting in advanced plastic properties [Delincé *et al.* 2006; Ebrahimi *et al.* 1999; Mirshams & Parakala 2004; Torre *et al.* 2002]. In this case the grain boundaries are not considered to have spurious effects, since their contribution to the behavior of the material is characteristic for the tested sample.

The indentation of quasi–brittle materials often results in sample damage by the propagation of cracks in the material instead of plastic deformation [Jang & Pharr 2008]. Damage is a dissipative phenomenon, which can result in easily recognizable displacement bursts in the load–displacement curve, but a smooth load–displacement curve similar to the ones of elastic–plastic material response can also be obtained (Fig.2.6). The sub–surface fracture can potentially influence the complete indentation response since by such damage the integrity of the material under the indentation zone is compromised. Depending on the assumptions of the nanoindentation post–treatment methods, they may not remain applicable to quasi–brittle materials (e.g. the post–treatment method of Ni et al. [Ni *et al.* 2004] developed for elastic–plastic material behavior). Moreover, since both plasticity and damage can have similar impact on load–displacement

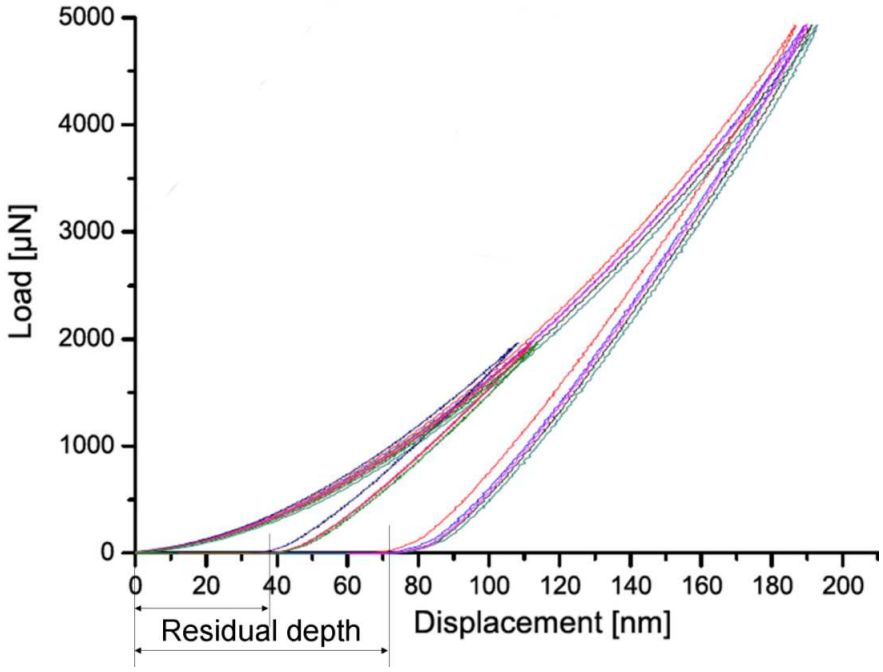

Figure 2.6: Residual deformation in nanoindentation of fused quartz with a Berkovich tip (sharp–edged pyramidal shape), potentially caused by brittle fracture, in spite of the similarity of the obtained load–displacement curve to an elastic–plastic material response. Load–displacement curves presented in Tam [2006].

curves of nanoindentation, it is unrealistic to expect a straightforward interpretation of nanoindentation results based solely on experimental load–displacement data, when no strongly motivated assumption on the behavior of the sample material is possible to make.
Advanced problems in nanoindentation, such as the characterization of multi–layer systems and substrates with thin coatings, where the interface between the various material layers is prone to fail, may present additional dispersion. The delamination of the applied coatings is a potential failure mechanism [Abdul-Baqi 2002; van den Bosch 2007], which works much like fracture in the bulk material, discussed before, only localized to the thin film interface. The understanding of the deformation and failure mechanisms of material systems composed of substrate material and thin layers with different material ductility remains one of the major issues of nanoindentation [van den Bosch 2007; Xu 2004].

Different material behaviors (ductile and brittle) can result in load–displacement curves with similar features. Following this line of thought it will be shown in Section 5.1 that similar load–displacement data can result from different material parameter sets using the same material model, and in Section 5.2 that the same indentation data can be reproduced by a rate–independent and a rate–dependent material model, while only the latter bears a physically motivated material parameter set for pure nickel.

Moreover, despite all experimental efforts there is no guarantee that a single material parameter set obtained by nanoindentation at a given depth could remain representative of the tested material's behavior in a wide range of indentation depths. The indentation response of a material may indeed be potentially dependent on the magnitude of the indenter penetration. This phenomenon is generally referred to as indentation size effects (ISE), and may take important proportions, leading to large variations in nanoindentation results.

2.3.1 Indentation size effects

Indentation size effects can originate from various sources, among which material–related and surface–roughness–related effects (referred to as geometrical size effects) are the most commonly considered. They result in an increase of the post–treated material nano–hardness value H_{nano}. In spite of its definition compacting all of the indentation parameters leading to a large freedom of interpretation (effects of the indenter geometry, surface roughness, material behavior), the nano–hardness value of a material is often used, as a characteristic of its resistance to deformation. A stiffer material response to indentation causes an increase in the load levels at fixed indentation depth, which leads to an increase of H_{nano}.

Such a stiffness increase in the sample response to indentation can be related to the high strain gradients in the sample material which therefore shows a size–dependent behavior [Al-Rub *et al.* 2007; Frick *et al.* 2008; Zhao *et al.* 2003]. Material size effects are recognized to be responsible for an increase in the nanohardness value of the same material by a factor as much as 2 to 5 when decreasing the deformed volume [Al-Rub 2007; Qu *et al.* 2006]. A reasonable explanation for size effects in crystalline materials comes from the plastic deformation procedure. Size effects are results of low–level phenomena issued from the scale of dislocation activity or as low as the atomic level, which appears on the nanoscale as an increase in the material hardening in the plastic behavior. Material size effects in crystalline materials are the subject of intensive research. They are often explained by the interaction of dislocations [Balint *et al.* 2008], which causes a stiffer response to deformation of a small volume of material than of the bulk. In nanoindentation, the localized severe deformation of a small material volume induces high strain gradients, which is responsible for the appearance of size effects. Three examples of testing procedures, other than indentation, where material size effects were observed are nanoscale bending [Stölken & Evans 1998; Wang *et al.* 2003], nanoscale torsion [Horstemeyer *et al.* 2001; Radi 2008], and the compression of small–scale pillars [Frick *et al.* 2008]. The material–related indentation size effects are stronger in the small indentation depth regime and weaken gradually with increasingly deep indentations [Tho *et al.* 2006]. In a numerical model, they are often taken into account by using a strain gradient plasticity formulation [Fleck & Hutchinson 1997, 2001; Qiu *et al.* 2003; Tho *et al.* 2006; Tymiak *et al.* 2001]. Depending

on the considered model, size effects are reproduced numerically in a phenomenological manner [Fleck & Hutchinson 2001], or based on physical quantities, such as the dislocation density in the sample [Evers 2003; Gao & Huang 2003; Gao *et al.* 1999; Qiu *et al.* 2003]. Higher order theories taking material size effects into account were however not considered in this work, the focus is set on other indentation–related phenomena.

Another interpretation of the indentation depth–dependent nanohardness is related to the presence of surface roughness. The energy necessary for the crushing of surface asperities was recognized to be a significant term in the energy balance in indentation depths comparable to the height of the surface asperities. With increasing indenter penetration, the relative contribution of the surface roughness deformation in the total work of indentation decreases and the contribution related to the the bulk deformation becomes dominant. In the literature indentation size effects depending on the surface topology have been associated to this phenomenon [Gao & Fan 2002; Kim *et al.* 2007; Qiu *et al.* 2003; Zhang *et al.* 2004], and denoted as geometrical indentation size effects (GISE), as will be discussed in Section 5.3. The common feature in material related and roughness related ISE is that their influence is strong in the small indentation depth regime and weakens with increasing indentation depths.

2.4 Discussion on the nanoindentation experiment

Nanoindentation is a testing procedure with a simple principle, well adapted to characterize the local behavior of bulk materials and thin films in working conditions. The result of a nanoindentation experiment is the load–displacement curve, being usually considered as the sample material response to indentation. Actually, it is composed of the convolution of various contributions: (i) the behavior of the material system (elastic–plastic [Cheng & Cheng 2004], rate–dependent [Bucaille *et al.* 2004; Chudoba & Richter 2001], size–dependent [Al-Rub *et al.* 2007; Al-Rub 2007; Frick *et al.* 2008; Mirshams & Pothapragada 2006; Qiu *et al.* 2003; Tho *et al.* 2006; Zhao *et al.* 2003], the effect of residual stresses [Warren & Guo 2006]), (ii) the geometry of the contact (sample surface topology and indenter geometry [Kim *et al.* 2005; Lu & Bogy 1995; Yu *et al.* 2004], (iii) the potential indenter tip deformation and misalignment [Jeong & Lee 2005; Pelletier *et al.* 2007]), and (iv) the effects of the contact interface behavior (adhesion, friction) [Cao *et al.* 2007]. Conversely to its major advantage of being a local and straightforward measurement, its main drawback is the difficulty of the deconvolution of a large number of potential contributions to the indentation response of the material system. Similar load–displacement data may result from samples with different material behaviors. Therefore the interpretation of load–displacement curves obtained in ideal conditions of a numerical model, without considering the majority of the experimental sources of dispersion is

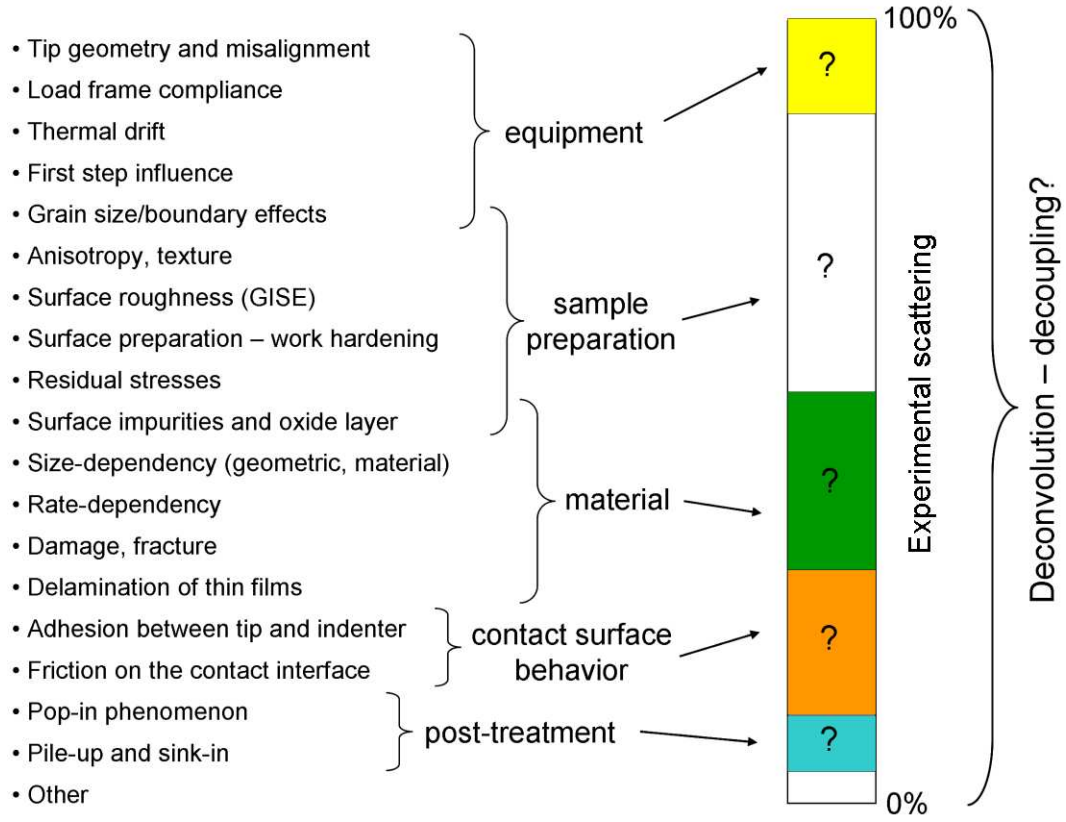

Figure 2.7: Different sources of scattering in nanoindentation.

already a complex task, let alone the challenge of interpreting experimental data. The problem of convoluted effects can be somewhat alighted with the careful choice of experimental conditions (e.g. when thin film material properties are addressed, the indentation depth usually does not exceed 10% of the film thickness [Cai & Bangert 1995; Hainsworth & Soh 2003; Kusano *et al.* 2003]). This however cannot be considered to be a generally feasible solution. Issues related to high inaccuracies and the compromised validity of simplifying assumptions of the post–treatment methods can result in varying degrees of success, particularly when indentations are made in small indentation depth.

A more detailed understanding of this testing method in relatively simple situations is therefore needed. An exhaustive study of issues in less complex nanoindentation setups is indeed useful to build a knowledge base allowing the interpretation of observed trends in more more complex systems. In view of the important interaction of experimental effects, this can be done efficiently when experiments are coupled to numerical models, where all parameters are freely adjustable. Numerical results obtained from such models can contribute to the interpretation of the experimental results, since the analytical background for the interpretation of the measures still lacks a full understanding of the physics encountered during the measurement process.
Experimental results are exposed to the convolution of different sources of scattering, that can be enhanced or decreased by the experimental parameters. They must be defined such as to

decrease to the minimum the effect of the sources of dispersion in nanoindentation, in order to ensure exploitable results. This leads to one of the major objectives of numerical simulations of nanoindentation: the identification of the dominant sources of scattering and the choice of the indentation parameters that can potentially contribute to their reduction.

These are the reasons why the development of an adapted numerical tool for the simulation of nanoindentation coupled to experiments was defined as a prime objective of the research work. The development of the numerical tools is the focus of the following two chapters of the thesis.

Chapter 3

Nanoindentation modeling on different scales

Numerical modeling can be useful in the understanding of the complex physics involved on small scales. Different numerical modeling strategies of nanoindentation, adapted to specific requirements are first presented in this chapter, leading to the particular choice of the numerical models applied in this thesis: (i) an atomic scale numerical model, and (ii) a continuum scale numerical model, using the finite element method. The atomic scale numerical model set up to investigate some features of the nanoindentation procedure linked to atomic scale mechanisms in very small indentation depth and its results are also discussed here.

In nanoindentation of thin film–substrate sandwiches if the indentation depth is too large the substrate influences the response of the film. As a result, very small indentation depths are required to characterize the mechanical properties of thin films. As a rule of thumb to avoid the effect of the substrate $1/10$ of the film thickness (under $1\mu m$ for thin films) is usually taken as maximum indentation depth. In the case of such shallow indents various artifacts of the load–displacement curve have been observed which cannot be reproduced by the 'classical' continuum theory, particularly the increased hardness due to size effects and appearance of pop–ins. Considering the small size of the deformed material volume, the material response in such an experiment is the combination of a behavior that can be described by continuum models and the one of individual atoms. The shallower the indent is the more the atomic level behavior of the material becomes dominant. Depending on the purpose of the simulation different aspects of the nanoindentation procedure are addressed in different numerical models. Any numerical modeling strategy is adapted to specific requirements, unfortunately it is rarely possible to directly compare the simulation results issued from different models. The reader can consult the review paper of Gouldstone [Gouldstone *et al.* 2007] considering different numerical models

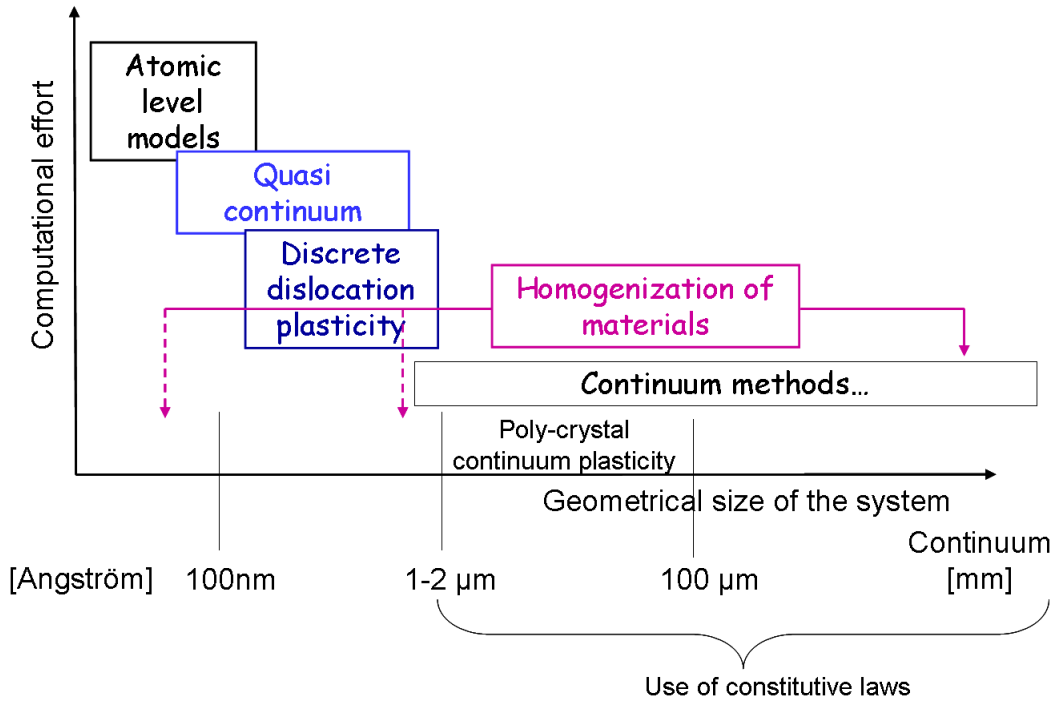

Figure 3.1: Domain of application and computational demand of the different numerical methods discussed in this section (an atomistic and a continuum scale numerical model were chosen to study the nanoindentation procedure).

and techniques applied at different length scales of nanoindentation for further details. When the numerical frame has to be coupled directly to experiments, the continuum models are most frequently preferred because of their computational efficiency. These models are well adapted to reproduce the overall average response of the material in nanoindentation and to conduct parametric studies addressing parameters which are difficult to access experimentally.

In order to describe the more complex physics of shallow nanoindentations where the size–dependent response of the material has to be taken into account, the continuum methods are specially adapted to microscale simulations, using higher order theories in a finite element setting [Fleck & Hutchinson 2001; Qu *et al.* 2006] for example. However, when the purpose of the numerical simulation is the understanding of the plastic deformation, models usually work on smaller scales. The descent to scales where continuum mechanics is not applicable anymore usually implies the use of computationally more expensive simulations. One of these computational numerical methods uses the discrete dislocation plasticity or dislocation dynamics models which focuses on the plastic deformation of the crystalline material considering only the slip planes without details on the positions of the atoms [Bulatov 2008; Kreuzer & Pippan 2004; Miller *et al.* 2003; Nicola *et al.* 2007; Shilkrot *et al.* 2004]. Experimental efforts are made in order to investigate the deformation mechanisms on the corresponding scale using adapted experimental techniques. The work of Kulkarni and Bhushan [Kulkarni & Bhushan 1996] considering nanoindentation with sharp tips used in atomic force microscopy (AFM) in very small

indentation depth (down to 25nm) should be mentioned. In Nibur & Bahr [2003] the activated slip systems of face–centered cubic (FCC) crystals in a microindentation setting is studied experimentally. Tanaka investigated the plastic zones and slip band formation around a crack tip in silicon, observed together with the produced dislocation structure [Tanaka *et al.* 2004]. Finally, the recent experimental work of Fujikane et al. gives insight into the elastic–plastic transition in GaN crystals [Fujikane *et al.* 2008].

When the details of the onset of the plastic deformation and the dislocation activity are in the focus of interest, atomistic simulations investigating the lowest scale can be used. Generally, atomistic models are used for system sizes smaller than $100nm$ (around the upper limit of the range of thin film nanoindentations), a scale from which other numerical methods are more appropriate to describe the behavior of the material [Gouldstone *et al.* 2007]. The atomic level models have the indisputable advantage of identifying the trends concerning the main physical variables of a problem and give qualitative information for the understanding of experimentally observed complex phenomena. The main handicap of purely atomistic models for mechanical applications is that they are computationally expensive. They therefore generally handle length (in the order of tens of nm) and time scales (some ps) many orders of magnitude smaller than in the experiments. Extending them is the main challenge of numerical modeling on the atomic scale. This results for example in molecular dynamics simulations where the prescribed indenter speed can reach $100m/s$ [Fang *et al.* 2003, 2006; Jian *et al.* 2006; Noreyan *et al.* 2005; Richter *et al.* 2000] due to computational limitations, as opposed to the experimental values in the range of some $\mu m/s$. Even though atomic level calculations are computationally expensive, the increase in computational power in recent years allowed the adaptation of atomic level models to interesting mechanical applications [Rafii-Tabar 2000]. Very large systems could be modeled using parallel computational techniques with several million atoms [Lee *et al.* 2005; Vashishta *et al.* 2006]. The computational effort, directly related to the quantity of information of atomic level models however still remains very large. Several numerical works using molecular dynamics in the domain of tribology considered the problem of nanoscratching [Komanduri *et al.* 2000; Noreyan & Amar 2008] or nanoscale machining [Lin *et al.* 2007]; and were used for the identification of different wear regimes [Zhang & Tanaka 1997] and for the explanation of tribological phenomena, like the nanoscale stick–slip [Cho *et al.* 2005] and adhesion [Song & Srolovitz 2006]. The possible qualitative comparison of the nanoscratch behavior of Au and Pt issued from the numerical model and the experimental data [Fang *et al.* 2006] also encourages the use of atomic level simulations for problems concerning nanocontact and friction [Harano 2004; Mate 2008].

Considering the modeling of the nanoindentation procedure, the review of Szlufarska [Szlufarska 2006] gives a general overview. The prime concern of such calculations is the understanding of the early stages of plastic deformation in the sample material (i.e. the determination

of a suitable criterion defining the onset of defect nucleation [Vliet *et al.* 2003]), the study of the dislocation nucleation [Kelchner *et al.* 1998; Lilleodden *et al.* 2003; Miller & Rodney 2008], the observation of the indenter–sample contact [Christopher *et al.* 2001] and the induced wear mechanism in the tip [Hagelaar *et al.* 2006]. From the point of view of the atomic scale simulations presented in the following, one of the most interesting papers presents the results of modeling the nanoindentation of pure nickel [Saraev & Miller 2006].
Finally, to complete this overview explaining the reasons of the particular choice of the numerical models applied in this work, the complex but very promising hybrid methods and methods using homogenization techniques have to be mentioned. These methods build a bridge between scales using suitable numerical methods on each scale. The higher scales are fed by the lower scale behavior allowing the seamless treatment of multiple scales. One member of this family of methods is the quasi-continuum method which considers atomic and structural scales simultaneously (using an adaptive FEM mesh [Knap & Ortiz 2001; Shenoy *et al.* 1999]) for the analysis of fracture and plasticity [Miller *et al.* 1998, 2003]. Coupling atomic level models to other methods can be addressed for problems with large geometrical size, e.g. discrete dislocation methods [Miller & Rodney 2008; Shilkrot *et al.* 2004], quasi–continuum methods [Vashishta *et al.* 2006], or advanced finite element models [Vliet *et al.* 2003]. The atomic scale model is used to catch precisely the local behavior of the material and the higher scale model to prescribe more realistic boundary conditions to the atomic scale model. It has to be noted however that finding the proper boundary conditions for each considered model (working potentially at different length scales) to assure the transition between the different scales is far from being obvious, especially in a multi–model numerical assembly. The main drawback of these models is their advanced complexity compared to single model approaches.

Taking into consideration the different aspects of the presented numerical methods, and that behavior of materials in nanoindentation stems from contributions of different scales, two numerical descriptions of the nanoindentation procedure have been used:

- a finite element model working on the continuum scale (a detailed description is given in Chapter 4)
  - applied to small, moderate and large indentation depth
  - to model the overall indentation response of the studied material on the continuum scale together with experiments, and taking into account experimental parameters
  - to study the influence of experimental parameters that are difficult to control in the real–life setup

- a single level purely atomistic numerical model (presented in detail in the following section)
  - to simulate the nanoindentation procedure at very small indentation depths
  - to contribute to the understanding of some features of the nanoindentation procedure linked to atomic scale mechanisms in very small indentation depth

3.1 A simple atomistic model of nanoindentation

In nanoindentation even for shallow indentation depths, the deformation of a very large volume of material has to be considered with respect to the atomic scale. A quantitative comparison with experimental results is thereby not possible in the context of this study considering the extremely large computational effort necessary to model indentation, even with very sharp AFM tips in indentation depths where the experimental scattering is small enough to obtain results with a reasonable accuracy for the comparison [Kulkarni & Bhushan 1996]. The purpose of this work is to gain some insight in the features of the nanoindentation in very small indentation depths linked to the atomic scale in a numerical study. From the experimental point of view, indents performed in nanoindentation are so small that they can be made inside a grain and the material properties corresponding to the ones of single crystals (with defects) can be measured. For the sake of simplicity and to be able to handle large system size calculations in a most efficient way, an atomic level numerical model using empirical potentials was chosen for the simulation task. In the model all atoms of the considered nickel lattice are represented, with three degrees of freedom of displacement corresponding to each atom. The choice of a quasi–static simulation of the nanoindentation procedure is taken, as in Hagelaar *et al.* [2006]; Miller & Rodney [2008], since the speed of the indenter can be considered to be negligible (varying between some tens of nm/s to some $\mu m/s$ in the experiment) with respect to the speed of the atom vibrations. This reduces the numerical problem to a *structural optimization* with quasi–static increments calculated by the 'NAMD Scalable Molecular Dynamics' software [NAMD 2008]. NAMD is a parallel molecular dynamics code openly distributed, designed for high-performance simulation of large biomolecular systems, with a quasi–static optimization feature. The choice of a molecular dynamics solution has been rejected to avoid using non–physically large indenter velocities, since it would be impossible to bridge the time scales between simulations and experiments, and for the sake of computational efficiency.

The surface adhesion forces and the forces applied to obtain plastic deformation of the sample

This section is based on P. Berke, M.-P. Delplancke-Ogletree, A. Lyalin, V.V. Semenikhina, A.V. Solov'yov, 'Simulation of the nanoindentation procedure on Nickel on the smallest length scale: a simple atomistic level model' published in Latest Advances in Atomic Cluster Collisions: structure and dynamics from the nuclear to the biological scale, edited by J.-P. Connerade and A.V. Solov'yov, Imperial College Press, London (2008)

in the nanoindentation experiment are basically of different order (the latter being more important). As a result, the surface adhesion forces are often neglected in the structural numerical simulation on the continuum scale. However this assumption is not satisfied generally anymore on smaller scales. In order to remain consistent with the physics on the considered scale, the rather rare choice is made to represent the diamond lattice of the indenter and the interaction between the tip and the sample is taken into account [Christopher *et al.* 2001; Lilleodden *et al.* 2003]. The atoms in the diamond lattice are frozen, the indenter is represented as an undeformable body. The interaction potentials of both the Ni–Ni and Ni–C interactions are modeled by Lennard–Jones type interaction potentials.

$$\phi_{LJ}(r) = \epsilon \left[(r_0/r)^{12} - 2(r_0/r)^6\right] \tag{3.1}$$

where ϵ [eV] is the energy well depth, r_0 [$\mathring{A}$] the equilibrium distance between two atoms, and r [$\mathring{A}$] the distance measured between two atoms. Even though this approximation might not be the best choice to describe the behavior of the nickel material and the contact interaction, it is the necessary implication of the use of NAMD code in one step of the simulation procedure (as described later). A major difficulty in atomic level models is the choice of the interaction potential and of its parameters to properly describe the behavior of the modeled material. An inaccurate choice indeed results in the non–physical response of the numerical model (issues of stability of the lattice, 'crushing' or 'explosion' of the lattice at indentation). Fortunately, Lennard–Jones type potentials seem to represent (in a limited, but satisfactory manner) the atomic interaction in FCC lattices, but the improvement of the model by using more adequate interaction potentials is recognized to be an important development step in a future work, before addressing more advanced systems. The two sets of Lennard–Jones potential parameters were calculated to fit the best possible the Morse type potentials obtained for Ni–Ni and Ni–C interactions, issued from density functional theory (DFT) calculations [Shibuta & Maruyama 2007], and used to describe the nanotribology of a small scale scratch test of nickel with a nanoindenter [Lin *et al.* 2007]. The parameter sets used for the Ni–Ni interactions and for the Ni–C interactions are: $\epsilon^{Ni-Ni} = 0.4245eV$, $r_0^{Ni-Ni} = 2.56\mathring{A}$ and $\epsilon^{Ni-C} = 0.1eV$, $r_0^{Ni-C} = 2.4\mathring{A}$. The indenter is constructed from 3308 carbon atoms in a diamond lattice (with the lattice parameter $a_{diam} = 3.56\mathring{A}$ [Kittel 1996]), the same material as in the experimental setting. Even though in reality the nanoindenter has a tip radius of $R = [100...800nm]$ for the sharpest tips, in this study a cono–spherical tip of $2nm$ radius has been considered due to computational limitations. The chosen tip size and geometry is in good agreement with other works using atomistic models of nanoindentation where the indenter tip radius ranges generally from $2nm$ [Fang *et al.* 2003; Lilleodden *et al.* 2003] to $18nm$ [Hagelaar *et al.* 2006]. The deformability of the indenter is not taken into account in this numerical work,. The indenter tip is modeled merely as a rigid body, which is a common assumption, since both its elastic modulus as well as its yield limit are orders of magnitude higher than those of nickel. A defect–free FCC lattice structure (with

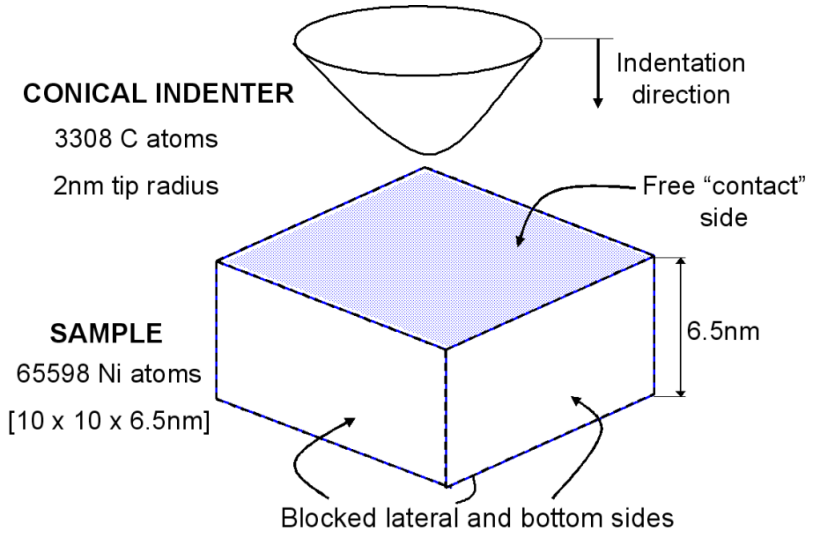

Figure 3.2: Applied boundary conditions in the atomic level simulation, the atoms in the indenter are frozen.

the lattice parameter $a_{Ni} = 3.52\mathring{A}$ [Kittel 1996]) of parallelepipedic shape with dimensions $10nm \times 10nm \times 6.5nm$ built from roughly 65600 atoms was considered for the nickel sample, corresponding to a defect–free single crystal indentation setup. The sample was constructed from unit cells with $[001]$ orientation. The variation of the lattice orientation of the nickel structure was not considered in this study, keeping in mind however the dependence of the material's response on the lattice orientation [Richter *et al.* 2000]. This size of the lattice was found to be sufficiently large with respect to the size of the diamond indenter with $2nm$ tip radius and the imposed displacement of $0.8nm$. The considered atomic scale model of nanoindentation uses simple ingredients, however this relative simplicity is balanced by a computational efficiency that allowed to reach a system size and an indentation depth comparable to other works in the field [Christopher *et al.* 2001; Lin *et al.* 2007]. The displacement of the atoms on the lateral and bottom sides of the nickel lattice are prescribed to be zero during the whole simulation, leaving only the upper contacting surface of the lattice and the enveloped volume to deform (Fig.3.2). During the numerical indentation the indenter moves downwards and comes into contact with the sample. The rigid indenter then deforms the sample volume and finally is retracted upwards to its final position. The holding period present in the experiments is omitted here, considering that the simulation is quasi–static. This methodology corresponds to a displacement controlled simulation. The nanoindentation simulation is divided into quasi–static increments; at the beginning of each increment the position of the rigid diamond indenter is updated and then an iterative structural optimization step using the structural optimization feature of the NAMD code is made recalculating the position of the free nickel atoms in order to minimize the total energy of the system. A program was created to drive the whole calculation as an external frame to the structural optimization step (communicating with the NAMD code

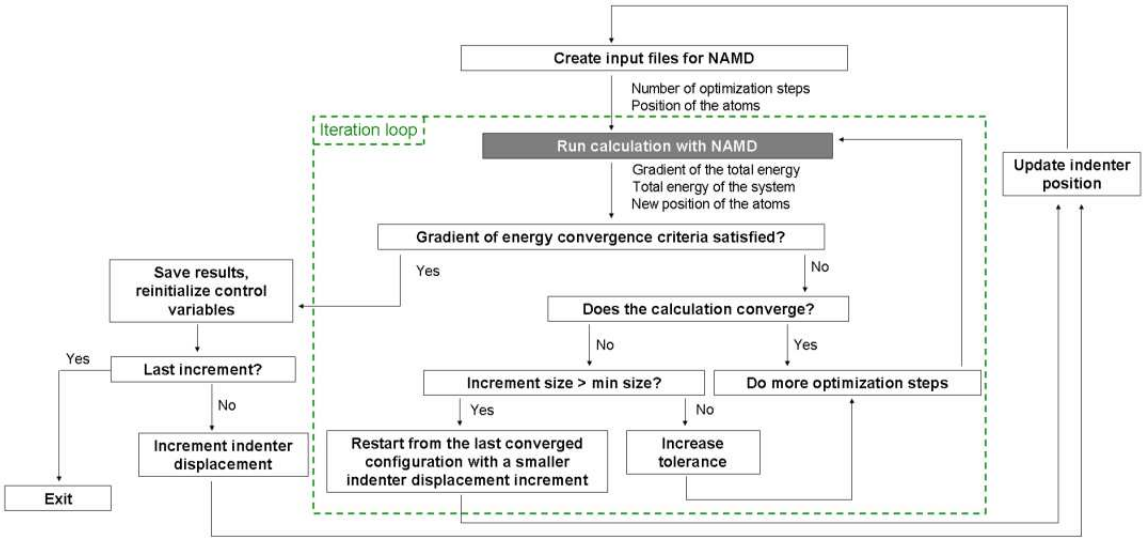

Figure 3.3: Programmed external frame mimics an incremental iterative solution scheme, used in nonlinear computations. This frame drives the computation, exploiting the structural optimization feature of the NAMD code in one step of the procedure.

through its standard input and output parameters) and to process the results of the structural optimization (Fig.3.3). The structural optimization feature of the NAMD code is driven using the following input parameters; the parameters of the Lennard–Jones type interaction potentials; the initial configuration of the position of the atoms; the number of optimization steps which are generated in an incremental iterative calculation scheme to solve the nonlinear indentation problem. The outputs of the structural optimization step, i.e. the optimized configuration with the updated position of the atoms; the total energy of the system; the gradient of the total energy of the system are used to create the total energy–indenter displacement curve and to decide on the convergence of the actual optimized configuration in the external frame.

An increment is considered converged when a gradient of the total energy satisfies the tolerance condition. The overall convergence of the indentation simulation is ensured by a 'bypass' procedure increasing the prescribed tolerance value when the increment size had reached the minimum prescribed value and the calculation still has not satisfied the convergence criteria after a large number of optimization steps. This numerical maneuver allows the continuation of the simulation and the configurations with a high tolerance value can be filtered out in the post–processing step. Note that considering a path–dependent indentation response, this introduces the assumption, that the converged configurations with a high tolerance still remain good approximations of the corresponding actual equilibrium state. The average displacement step of the indenter per increment in the simulation was $0.064\mathring{A}$, with a fixed minimum step size of $0.001\mathring{A}$.

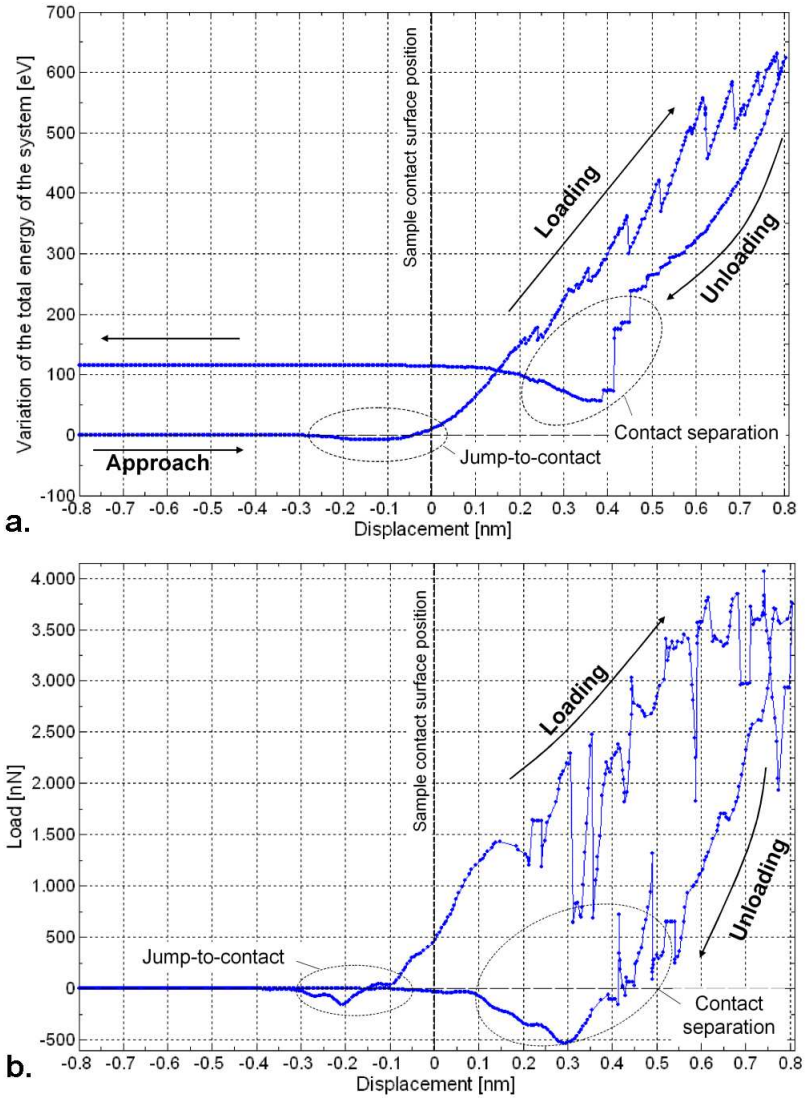

Figure 3.4: a. Variation of the total energy of the modeled system as a function of the indenter displacement b. Atomic level load–displacement curve derived from the total energy–displacement curve.

Numerical results and analysis

The main results obtained from the atomic scale numerical model of nanoindentation are presented here. The main outputs of the numerical simulation are the total energy of the structure as a function of the indenter displacement (Fig.3.4a), from which the atomic scale reaction force–displacement or load–displacement curve was computed (Fig.3.4b), and the positions of the atoms in the deformed configurations (Fig.3.5). Since the carbon atoms in the indenter are frozen, the change in the total energy of the structure is related to two contributions: the deformation of the sample volume and the contact interaction between the nickel and the carbon atoms on the indenter–sample interface. The zero reference energy level corresponds to the initial configuration with the defect–free, undeformed and relaxed perfect nickel lattice, and the

indenter sufficiently far so that there is no contribution of the sample–indenter interaction to the energy balance. The convention is taken that the zero value on the axis of the indenter displacement on all figures matches the position of the sample contact surface and negative values stand for separation between the contacting bodies in a geometrical sense.

In the *approach phase* the indenter moves towards the sample until contact is established. With diminishing separation distance (from $0.8nm$ to $0.1nm$) the total energy of the system first decreases (Fig.3.4a), the indenter and the sample volumes attract each other bulging up the nickel contact surface. In force–controlled simulations the above-mentioned attraction between the two surfaces may result in a jump–to–surface phenomenon, as mentioned in Hagelaar *et al.* [2006]; Szlufarska [2006]. An experimental manifestation of jump–to–surface is called pull–in in AFM experiments. This jump–to–surface, related to atomic attraction in the context of nanoindentation can only be observed experimentally with the condition (among others) of having to manipulate atomically clean surfaces. In experiments the major sources of attraction between the indenter tip and the sample are electrostatic forces [Lambert & Régnier 2006], capillary forces [Lambert 2007; Mate 2008] and Van der Waals forces [Israelachvili 1974; Mate 2008]. Further approaching the indenter to the sample (from the separation distance of around $0.1nm$ on), the interaction force between the indenter and the sample changes to repulsion, with an increase in the energy of the system.

The next phase of the numerical nanoindentation starts when the repulsive interaction force between the indenter and the sample *deforms the nickel lattice*, causing a global increase in the energy level of the system. In agreement with the theory of continuum solid mechanics, based on observations on the macroscale, the sample deformation is first elastic followed by an elastic–plastic regime. The transition corresponds to the start of the nucleation of dislocations in the sample volume [Vliet *et al.* 2003] causing the first large energy jump in Fig.3.4a, at around $0.24nm$ of indenter penetration. Until this point the elastic contact model of Hertz [Hertz 1882], considering the approximation of a deformable body with a flat surface and a rigid spherical body with $2nm$ of contact radius was applied to the problem, as in Lilleodden *et al.* [2003]. A good agreement between the Hertzian contact model with a sample's Young's modulus of $E_{sample} = 5000$GPa and the numerical results was obtained. This value is an order of magnitude higher than the macroscopically measured average of $E_{Ni} = 207$GPa [ASM 1990]. A peak contact pressure of 1300GPa was calculated at yield by the Hertzian contact model. This value is two orders of magnitude larger than the theoretical shear strength of the nickel crystal defined by $\tau_{max} = G/2\pi = 12$GPa [Vliet *et al.* 2003]. Deviations of the results of atomic scale numerical models from the predictions of continuum solid mechanics are often observed (explained by the complex stress condition under the indenter) but generally with considerably smaller magnitude. The large difference observed here is related to the (imposed) use of Lennard–Jones interaction potentials. The plastic yielding in the present numerical model

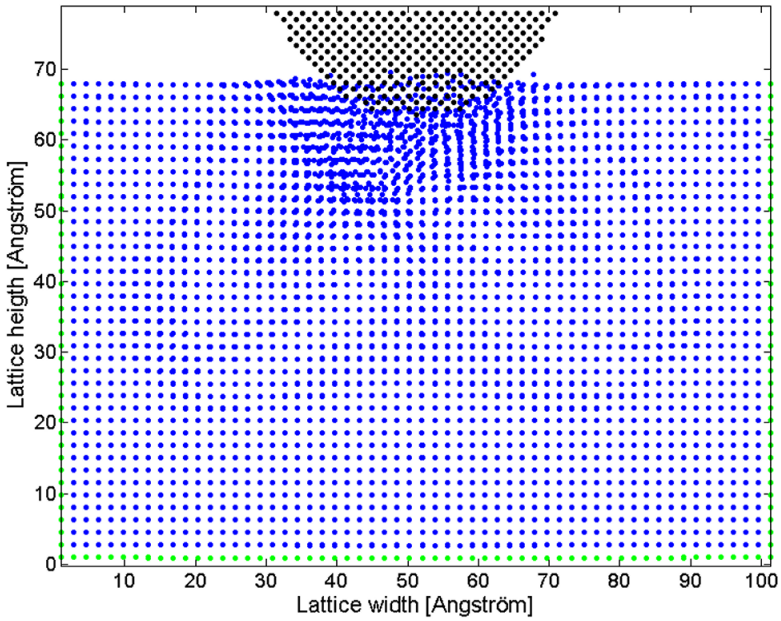

Figure 3.5: Snapshot in cut view of the deformed configuration of the nickel lattice in the numerical model during indentation at indenter penetration of 4.38$\mathring{A}$. The atoms on the left, right and bottom sides are blocked (in green), the indenter carbon atoms are represented in black.

seems to start off the symmetry axis of the indenter (Fig.3.5), in agreement with other atomic scale models [Lee *et al.* 2005], but contrary to the predictions of the continuum and the Hertzian contact model. With larger penetration of the indenter, up to the peak value of 0.8nm, the system response is composed of subsequent energy and force jumps. The spacing of these energy jumps on the total energy–indenter displacement curve is closer at larger indentation depths (passing from around 0.11nm to 0.07nm and their magnitude is also increasing at large penetration values (up to 62eV) showing the increasing plastic deformation of the nickel lattice (Fig.3.4a). The sharp falls in the total energy of the system indicate the plastic relaxation of the stresses in the lattice corresponding to the reorganization of the position of a larger number of atoms via dislocation activity. In agreement with experiments and the theory of continuum solid mechanics, the slope of the atomic scale load–displacement curve of indentation in the purely elastic domain is steeper than in the elastic–plastic deformation domain.

After reaching the maximum prescribed value of the indenter penetration, the indenter is retracted, corresponding to the beginning of the *unloading phase*. The initial decrease of the total energy during unloading can be explained by the elastic relaxation (to some extent) of the accumulated stresses in the nickel lattice. There are no significant energy and force jumps in the beginning of the unloading up to an indentation depth of around 0.6nm suggesting the mainly elastic nature of this nanoindentation phase (Fig.3.4a). The post–treatment method of nanoindentation proposed by Oliver and Pharr [Oliver & Pharr 1992], based on the assumption

of elastic contact unloading was applied to the numerical load–displacement curve in the unloading period and the following material properties have been obtained: a hardness $H^{OP}_{sample} =$ 646GPa, two orders of magnitude larger than the documented values for bulk nickel $H^{bulk}_{Ni} =$ 4GPa [Pauleau *et al.* 2006] and a Young's modulus $E^{OP}_{sample} =$ 4580GPa that matches well the value found by Hertzian elastic contact analysis of the loading curve (less than 10% of deviation). The source of the difference between the elastic moduli identified in the loading, and in the unloading period is the effect of the increased contact interaction in the deformed configuration, having a larger contact area. The fair agreement between the Young's modulus calculated by the Hertzian elastic contact approximation using the numerical loading curve and the value obtained by the Oliver–Pharr post–treatment method confirms the validity of its simplifying approximations, particularly when contact adhesion is low. Note the similar multiplicative factor of around two orders of magnitude of the initial yield strength and of the hardness of the material in the numerical model with respect to the macroscopic material properties of pure nickel. This can be explained by the dependence of H on the elastic–plastic behavior of the material.
The sample–tip interaction is mainly responsible for the energy jumps during the retraction of the indenter from penetration depth of $0.55nm$ on (Fig.3.4a), due to the rearrangement of a large number of nickel atoms on the sample surface during contact separation by these adhesive forces. This adhesive atomic interaction is witnessed again by the very similar shape of the final unloading portion of the curve compared to the approach phase. Contact separation between the indenter and the sample occurs at around $0.1nm$ of penetration depth, which can give an indication on the residual imprint depth. As expected, the final total energy of the system suffering permanent deformation after indentation is higher than the one corresponding to the initial defect–free configuration.

Conclusions and outlook

The numerical results issued from this simple atomic level model set up for nanoindentation in very shallow indentation depths are consistent with the physics of the problem, and the nature of the obtained total energy–displacement curve is in good agreement with other works considering the indentation in materials with FCC lattice [Jian *et al.* 2006; Lee *et al.* 2005; Lilleodden *et al.* 2003; Richter *et al.* 2000; Saraev & Miller 2006; Vliet *et al.* 2003].
In spite of some differences stemming from the scale on which the numerical model is formulated (i.e. important influence of contact adhesion) and all the simplifying assumptions that can be refined (Lennard–Jones interaction potentials) the overall response of the discrete model is in good agreement with the experimental trends and the theory of continuum solid mechanics. Conversely, this implies that the results of atomic scale numerical models, representative of the considered problem can be used to derive trends that are applicable on the continuum scale,

enforcing a potential practical interest of such low–scale simulations. Hence, by adequate scale transition assumptions, trends issued from atomistic numerical models can be used to formulate or verify constitutive relationships formats for higher scales.

Since no matching is obtained from a quantitative viewpoint, some aspects of the developed qualitative model are still to be revisited. The stiff response of the system is an inevitable result of the use of Lennard–Jones potentials. The outlook of this study includes the use of more realistic Embedded Atom Model (EAM) type potentials in order to describe the behavior of the modeled nickel monocrystal sample better.

Furthermore, to ensure that atomic scale models remain representative of the (mechanical) problems in the context of this research, their geometrical size should be further increased. Since the computational effort of the considered numerical model is relatively small the system size can be increased without particular difficulties in a future work. This can allow atomic scale models to address a number of advanced issues in the outlook of this thesis, linked to atomic scale phenomena, such as the study of thin film adhesion and delamination and material size effects [Nair *et al.* 2008].

For very shallow indentations the atomic scale numerical modeling revealed interesting features of the nanoindentation experiment concerning the plastic deformation of the sample (e.g. off–axis yielding). In order to study the plastic deformation mechanism in the nickel lattice a post–treatment method using the centrosymmetry parameter P, based on the property of central symmetry of the defect–free, undeformed FCC lattice can be implemented.

$$P = \sum_{i=1,6} |R_i + R_{i+1}|^2 \tag{3.2}$$

with R_i and R_{i+1} the vectors corresponding to six pairs of opposite nearest neighbors in the lattice. This would allow to study the influence of different tip geometries on the onset of plastic deformation, giving additional insight into the physics of the nanoindentation.

Finally it is noted, that despite the discrete nature of the model, the large scale transition and the influence of contact adhesion during unloading, the Oliver–Pharr post–treatment method of nanoindentation [Oliver & Pharr 1992] was applied to the numerical load–displacement curve, and was shown to perform well, resulting in a deviation of less than 10% with respect to the value obtained by the Hertz elastic contact analysis during loading. This method can be continued to be applied in future studies to numerical load–displacement curves issued from atomic scale simulations.

3.2 Continuum scale models of nanoindentation

Atomic level models are used generally for fundamental research aiming at the understanding of complex phenomena by a low–level description. Such models can reproduce qualitatively

the trends observed experimentally, potentially leading to the identification of the key physical parameters of the studied phenomena. However, when the numerical frame has to be coupled directly to experiments considering both qualitative and quantitative results on the scale of the experiments, continuum models are most frequently preferred to the low scale description of the material because of their computational efficiency.

The requirement of a direct coupling of the numerical model to experiments on a physical basis lead to considering the nanoindentation simulation on the continuum scale. Continuum scale numerical models have frequently proven their performance in the same context for problems such as: to develop more accurate post–treatment methods of nanoindentation [Ni *et al.* 2004]; to propose inverse methods of nanoindentation [Bolzon *et al.* 2004; Stauss *et al.* 2003]; to broaden the scope of material properties obtained from the experimental load–displacement curves [Bouzakis *et al.* 2001; Bouzakis & Michailidis 2004; Bucaille *et al.* 2004, 2003; Cao & Lu 2004; Giannakopoulos & Suresh 1999; Kramer *et al.* 1998; Ma *et al.* 2003; Zhao *et al.* 2006] on the basis of the comparison of numerically obtained trends with experimental results; to study the the influence of various contributions to the measured load–displacement curves [Jeong & Lee 2005; Walter *et al.* 2007; Youn & Kang 2005]; without aiming for an exhaustive overview.
The most frequently used discretization in continuum models is the finite element method because of its computational efficiency, its broad domain of application and high flexibility. The possibility of using a large variety of material behaviors (elastic–plastic material models, damage models), including higher order theories to model material size effects; its direct applicability to advanced problems, such as modeling the deformation and delamination of thin films and thin film sandwiches [Abdul-Baqi 2002; van den Bosch 2007; Xu 2004] using different interfacial and contact behaviors; and the possibility of coupled multi–physics simulations, using models that can be defined in terms of physically meaningful parameters are interesting and valuable features of the finite element method.

In the majority of the cited numerical works, the authors use commercial finite element packages for the sake of simplicity. Commercial finite element codes are interesting for prototyping of the potential need for a physical ingredient for example (unavailable in a research oriented code, but preprogrammed with a simple model in the commercial code). However, due to their often limited flexibility they potentially cannot always satisfy yet emerging demands of the research. This motivated the development of the continuum scale numerical tool using the finite element method presented in detail in the following chapter, with the objective of reaching a maximum flexibility and accuracy by the proper choice of the numerical ingredients, adapted for the problem of nanoindentation.

Chapter 4

Developed continuum scale numerical tool for large deformation contact

This chapter treats the development of the continuum scale numerical tool using the finite element method, applicable to problems involving frictional contact, and the finite elastic–plastic deformation of one of the bodies in contact. The main steps of the development consist of including (i) the corotational finite deformation description, (ii) isotropic hardening plasticity and (iii) normal and tangential contact constraints by the augmented Lagrangian formulation.

Contact deformation gives a large contribution in the applications considered in this work (nanoindentation and micromanipulation by contact), potentially inducing large elastic and plastic deformations. These are aspects that a numerical model must be able to describe. For this purpose a finite element code, programmed in MATLAB language, was further developed in order to include the following features:

- finite deformation description
- material plasticity
- normal and tangential contact constraints

to the original code, which initially contained an element library with linear elastic and damaging behavior in infinitesimal deformation description, and a nonlinear solver. The program development was made keeping in mind computational efficiency, robustness and an emphasis on maintaining a maximum degree of flexibility of the resulting code for future development of new features and material/interface behaviors.

In order to be able to describe large local deformations the original finite element code had to

be modified. The choice of the most adequate, efficient and robust numerical frame to describe finite deformations in finite element models remains an open and actual question. Two families of finite deformation descriptions are distinguished, e.g. hyperelastic [Areias *et al.* 2003; Liebe *et al.* 2003; Simo 1992] and hypoelastic formulations. The hyperelastic model uses a hyperelastic potential (functional), defined in terms of strains from which stresses are derived. This results in a formulation where the requirements of reversibility, of path–independence and of no energy dissipation in a closed elastic cycle are naturally satisfied. This formulation is frame invariant and therefore satisfies the strong objectivity criterion (stresses are only generated by strains without any contribution of rigid motion). When coupled to plasticity, this formulation uses the multiplicative decomposition of the deformation gradient (relating the initial and deformed configurations) in its elastic and plastic parts. The basis of the formulation of computational plasticity is the maximum plastic dissipation theorem. However, in spite of its merits the hyperelastic formulation has a major drawback when considering its flexibility for future developments, particularly including material size effects. Strain gradient plasticity (SGP) models coupled to hyperelastic formulations are very complex [Chambon *et al.* 2001, 2004; Fleck & Hutchinson 1997], whereas SGP models coupled to hypoelastic formulations are simpler [Fleck & Hutchinson 2001; Niordson & Redanz 2004] and perform well in reproducing phenomenologically material size effects, resulting in the more efficient choice from the code development point of view.

Hence a hypoelastic formulation was chosen to describe finite deformations in the finite element code. Hypoelasticity coupled to plasticity can be considered as a rather straightforward extension of the infinitesimal deformation theory, being a rate–type formulation. The main issue of hypoelastic formulations is the choice of objective rates and objective integration schemes of the rate equations, as explained later. In a purely elastic loading cycle, non–physical stresses may appear using hypoelastic formulations, but considering that for the aimed applications usually the plastic response of the material is dominant this is not considered to be a severely penalizing error. Moreover some additional developments can restore the energy conservation of an elastic cycle [Noels *et al.* 2004], if it is justified in the context of the considered applications by erroneous numerical results.
The corotational hypoelastic–plastic finite deformation formulation [Ponthot 1995, 2002] was implemented in the existing code with the following salient features:

- it is a trivially objective scheme, very efficient handling problems involving large rigid rotations,
- it introduces a full decoupling of the contributions of material and geometrical nonlinearities,

- an analytical expression exists for the evaluation of the consistent tangent stiffness matrix,
- it consists of a straightforward development from the infinitesimal displacement and deformation theory.

In the majority of industrial applications the loading of a structural element is transferred by contact (e.g. sheet metal forming [Zhang *et al.* 2003], tight interface fit [Yang *et al.* 2001], let alone the tire industry). In the context of the project involving nanoindentation the capability of describing contact conditions in a numerical model is obviously required. Including contact loading to the original code represents an essential step to be able to prescribe the evolving boundary conditions related to contact evolution (of both normal and tangential contact conditions).

The theory of contact mechanics is an interdisciplinary area, which via the coupling of structural and contact behaviors needs input from different research areas such as tribology, mathematics, computer science, mechanics, and for coupled multi–physics problems heat transfer [Idesman & Levitas 1994; Xing & Makinouchi 2002], or electromagnetism or plasticity and damage for example [Jefferson 2003; Stachowiak 2005]. Computational contact mechanics, sometimes also presented as the numerical branch of tribology, solves numerically contact problems and has become a vast domain of research. Indeed problems involving contact and friction are of utmost importance in most engineering applications and their complexity usually requires the use of numerical models for their understanding. In spite of the large number of contributions in the domain, the choice of the most efficient numerical method to treat contact constraints still remains an open and frequently discussed question.

In this work an augmented Lagrangian treatment of the normal and tangential contact constraints was added to the initial finite element code. This formulation was chosen considering its principal advantages:

- it satisfies both normal and tangential contact conditions exactly,
- it avoids numerical ill–conditioning (penalty method) and the use of an additional field of variables (Lagrange multiplier method),
- it introduces a full decoupling of the contact nonlinearities from other contributions.

Its major disadvantage from a theoretical point of view is the use of a generalized Newton method with a convergence rate which cannot be established rigorously at least in a general setting, when friction with Coulomb type law is considered.

Problems related to finite deformations and contact, using nonlinear, non–differentiable constitutive laws for the interface behavior lead to the use of advanced numerical methods. The salient features of the chosen numerical methods and some more detailed discussion related to

the major steps of the code development are presented in the following. Section 4.1 sketches the main developments needed to describe material plasticity in the corotational finite deformation frame, introducing the main ingredients related to the description of finite deformations. Section 4.2 gives basic notions of the general computational contact mechanics formulation, the chosen Coulomb friction model and the induced numerical difficulties to tackle. Then, the development of the required one–node contact element satisfying the normal and tangential contact constraints is presented. Finally, a discussion on the choice and performance of the numerical ingredients and on the development of the initial finite element code is given.

4.1 Modeling the elastic–plastic material behavior in a corotational finite deformation framework

Finite deformation formulations and related issues are treated in detail in several references the interested reader can consult for a more general overview [Belytschko *et al.* 2000; Laursen 1992; Ponthot 1995; Wriggers 2002; Zienkiewicz 2000]. The formulation presented in this section considers the work of Ponthot [Ponthot 1995, 2002], who introduced a unified stress update algorithm for elastic–plastic constitutive equations in a finite deformation framework using a *corotational formulation*, within an *updated Lagrangian scheme*.

4.1.1 Kinematics in finite deformation theory

Contrary to the infinitesimal deformation theory of continuous media, the finite deformation theory necessarily distinguishes between the initial and the deformed configuration. Hence the kinematics used to describe finite deformations have to be defined first.

The position of a material particle in the reference configuration of a body, corresponding to a time t_0 is denoted by $\mathbf{X}$ while its position in the deformed configuration of the body, corresponding to a time $t > t_0$ is noted by $\mathbf{x} = \mathbf{x}(\mathbf{X}, t)$. Note that considering an updated Lagrangian scheme, the initial configuration at t_0 corresponds to the last converged equilibrium configuration of the analysis. The deformation gradient relating the deformed configuration to the initial configuration is defined as

$$\mathbf{F} = \frac{\partial \mathbf{x}}{\partial \mathbf{X}} \tag{4.1}$$

By the polar decomposition theorem [Ponthot 1995] the stretch tensor $\mathbf{U}$ and the rotation tensor $\mathbf{R}$ can be uniquely defined by

$$\mathbf{F} = \mathbf{R}\,\mathbf{U} \quad \text{with} \quad \mathbf{R}^T\mathbf{R} = \mathbf{I} \quad \text{and} \quad \mathbf{U} = \mathbf{U}^T \tag{4.2}$$

with $\mathbf{I}$ representing the identity tensor. The spatial gradient of velocity $\mathbf{L} = \dot{\mathbf{F}}\mathbf{F}^{-1}$ (differentiation with respect to the actual configuration) can be decomposed into

$$\begin{aligned} \mathbf{D} &= \tfrac{1}{2}(\mathbf{L} + \mathbf{L}^T) \quad \text{the rate of deformation tensor} \\ \mathbf{W} &= \tfrac{1}{2}(\mathbf{L} - \mathbf{L}^T) \quad \text{the spin tensor} \end{aligned} \tag{4.3}$$

The rate equations used in modeling material plasticity are written in terms of the rate of deformation tensor $\mathbf{D}$ in the chosen finite deformation theory, which is decomposed to its elastic part $\mathbf{D}_e$ and plastic part $\mathbf{D}_p$ by

$$\mathbf{D} = \mathbf{D}_e + \mathbf{D}_p \tag{4.4}$$

This assumption is usually made in hypoelastic–plastic formulations, causing a negligible error for small elastic strains. This leads to a straightforward extension of the infinitesimal plasticity theory based on the additive decomposition of the elastic and plastic strains and strain rates.

4.1.2 Plasticity constitutive setting

One of the most developed theories of material nonlinearity is the mathematical theory of plasticity [Bushnell 1977; Hill 1956; Hult & Lemaitre 1981; Kachanov 1971], resulting in various models describing the nonlinear plastic behavior of materials. The reader can consult [Belytschko *et al.* 2000; Crisfield 1995; de With 1999] for a general view on the theory of plasticity. The common idea in all plasticity models is that the induced plastic deformation is irreversible. In a simple elastic behavior, the structure returns to its original configuration as soon as the loads are removed. Plastic behavior can be classified in two main groups: rate–dependent, and rate–independent theories. The former group includes phenomena such as creep or viscoplasticity [Bushnell 1977] where the magnitude of the irreversible deformation depends on the duration of the loading and on the strain rate. Such a model is considered in Section 5.2 to describe the behavior of pure nickel in nanoindentation.

The latter group corresponds to a particular case of the more general rate–dependent models with a simpler behavior of the material assumed to depend on the loading history only [Hugues 1984]. It is a common practice to use this type of material model to describe the plastic response of metallic materials, when their rate–dependent effects are assumed to vanish. For similar reasons a rate–independent plastic material model was implemented in the numerical tool.

In the theory of plasticity, contrary to the theory of elasticity, in which total elastic strains and stresses are directly related, the relationship between the rate of strains and the rate of stresses is postulated as

$$\hat{\boldsymbol{\sigma}} = \mathbf{H}_e \, (\mathbf{D} - \mathbf{D}_p) \tag{4.5}$$

where $\hat{\boldsymbol{\sigma}}$ is an objective rate (see below) of the Cauchy stress tensor $\boldsymbol{\sigma}$ and $\mathbf{H}_e$ the elastic stiffness tensor.

Detection of plastic straining, the yield function

Plastic deformation is triggered when stresses in the material reach a given limit. The physical origin of plastic straining in crystalline materials is the activation and propagation of dislocations generated by the applied stresses resulting in shear slip on a number of slip planes [Bowman 2004; de With 1999; Hill 1956]. In the material model, a mathematical function called yield function is used to detect an increase of plastic deformations. Yield functions define a surface, which envelops all physically possible stress states in rate–independent plasticity. Stress states inside this contour cause only elastic deformations, while stress states on this yield surface give rise to elastic–plastic deformations. By definition, in rate–independent plasticity stress states outside the yield contour f are not admissible. These conditions are expressed mathematically by the Kuhn–Tucker complementary conditions.

$$\begin{cases} \dot{\gamma} & \geq & 0 \\ f & \leq & 0 \\ \dot{\gamma}\, f & = & 0 \end{cases} \tag{4.6}$$

with γ the consistency parameter, which determines the magnitude of plastic strain. The dot superscript denotes the time derivative of the considered term.

The von Mises pressure–insensitive yield function for isotropic materials was chosen for the numerical tool. This yield criterion is frequently assumed for metals [de With 1999; Geers 2001; Hill 1956], furthermore it offers the numerical advantage that the gradients of the Von Mises yield surface, which are used for the numerical solution procedure, are always uniquely defined. Mathematically the von Mises contour is expressed as

$$f(\boldsymbol{\sigma}, \sigma_v) = \sqrt{\frac{1}{2}[(\sigma_1 - \sigma_2)^2 + (\sigma_2 - \sigma_3)^2 + (\sigma_3 - \sigma_1)^2]} - \sigma_v \tag{4.7}$$

where σ_1, σ_2 and σ_3 are the principal Cauchy stresses and σ_v is the current yield strength of the material, depending on its hardening behavior.

A Ludwik's law, with a power law expression is used together with the von Mises yield function to describe the hardening behavior of metallic materials in the simulation

$$\sigma_v(\kappa) = \sigma_0 + K\ \kappa^n \tag{4.8}$$

where $\sigma_v(\kappa)$ is the current yield stress, σ_0 stands for the elastic limit in uniaxial tension. The scalar valued hardening parameter κ is typically dependent on the strain history through invariants of the plastic strain tensor. K and n are curve fitting parameters, called hardening coefficient, and hardening exponent, respectively, chosen to fit (4.8) to experimental stress–strain data. Ludwik's law describes well experimental stress–strain data for the considered base materials, pure titanium and pure nickel well. Since the yield function depends on the loading

history only through a scalar–valued hardening parameter, the yield surface can only expand or shrink, but not translate or rotate in the stress space, i.e. no kinematic hardening is considered here.

Plasticity evolution laws and the flow rule

Considering the definition of a yield surface, plastic straining occurs when the stress point in the stress space is on the yield contour of a yield surface, and subsequently remains on this contour as the loading progresses. This is expressed by the consistency condition

$$\dot{f} = \frac{\partial f}{\partial \boldsymbol{\sigma}} \, \dot{\boldsymbol{\sigma}} + \frac{\partial f}{\partial \kappa} \, \dot{\kappa} = 0 \tag{4.9}$$

The evolution law of plastic deformation is defined by the flow rule

$$\mathbf{D}_p = \dot{\gamma} \, \mathbf{n} \qquad \text{with} \qquad \mathbf{n} = \frac{\partial f}{\partial \boldsymbol{\sigma}} \tag{4.10}$$

$\mathbf{n}$ is the unit outward normal to the yield surface in the case of associated plasticity.

4.1.3 The essence of the corotational formulation

The major challenge of integrating the above rate equations in the finite deformation framework is to respect *incremental objectivity* during a finite time step. The objectivity criterion means that a pure rotation or rigid translation transformation should not cause any increment of strain $\mathbf{D}$ and of stress $\delta\boldsymbol{\sigma}$.

To solve this problem the equations are first rewritten in a *corotational* moving frame [Ponthot 1995]. This corotational frame is generated using a skew–symmetric tensor $\boldsymbol{\Omega}$ = -$\boldsymbol{\Omega}^T$ in the following. A group of rotations $\mathbf{r}$ is generated by

$$\begin{cases} \dot{\mathbf{r}} &= \boldsymbol{\Omega} \, \mathbf{r} \\ \mathbf{r}(t_0) &= \mathbf{I} \end{cases} \tag{4.11}$$

This group of rotations implies a change of frame from the Cartesian reference axes to the corresponding rotating axes. In these rotated axes the Cauchy stress tensor transforms as

$$\boldsymbol{\sigma}^c = \mathbf{r}^{\mathbf{T}} \, \boldsymbol{\sigma} \, \mathbf{r} \tag{4.12}$$

and the rate of Cauchy stress is given by

$$\dot{\boldsymbol{\sigma}}^c = \mathbf{r}^{\mathbf{T}} \, (\dot{\boldsymbol{\sigma}} - \boldsymbol{\Omega} \, \boldsymbol{\sigma} + \boldsymbol{\sigma} \, \boldsymbol{\Omega}) \, \mathbf{r} = \mathbf{r}^T \, \hat{\boldsymbol{\sigma}}^c \, \mathbf{r} \tag{4.13}$$

with $\hat{\boldsymbol{\sigma}}^c$ a corotational objective stress rate (the Jaumann rate if $\boldsymbol{\Omega}$ = $\mathbf{W}$).

In the new (rotating) reference frame the evolution equations take a simple form, similar to the infinitesimal theory of plasticity

$$\hat{\boldsymbol{\sigma}}^c = \mathbf{H}_e^c \, (\mathbf{D}^c - \mathbf{D}_p^c) \tag{4.14}$$

with

$$\begin{cases} \mathbf{D}^c &= \mathbf{r^T}\ \mathbf{D}\ \mathbf{r} \\ \mathbf{n^c} &= \mathbf{r^T}\ \mathbf{n}\ \mathbf{r} \\ \mathbf{H}_e^c &= \mathbf{H}_e \end{cases} \tag{4.15}$$

and the scalar quantities remain unchanged.

Numerical solution by return mapping algorithm

The main difficulty in elastic–plastic computation is the calculation of stresses [Argon 1975], on which the internal forces and the global equilibrium of the system depend. The equations of the mathematical theory of plasticity have to be integrated [Matthies 1989; Ortiz & Popov 1985; Ortiz & Simo 1986] to obtain the stresses corresponding to the actual state of deformation. In a finite element study the stresses are calculated at each integration point of every element. The integration of the above rate equations is conducted using a return mapping algorithm [Simo & Taylor 1985] with an iterative forward Euler scheme. For more details on the numerical solution of problems in plasticity the reader can consult [Owen & Hinton 1980; Simo 1988; Sussmann & Bathe 1987]. Conceptually the return mapping schemes can be divided in an elastic predictor step and a plastic corrector step.

Elastic predictor step

First an elastic predictor is established starting from the last converged configuration assuming the total incremental deformation elastic in the *elastic trial step*

$$\boldsymbol{\sigma}_{tr}^c = \boldsymbol{\sigma}_0^c + \int_{t_0}^{t_1} \mathbf{H}_e\ \mathbf{D}^c dt \tag{4.16}$$

The trial stress $\boldsymbol{\sigma}_{tr}^c$ is back–transformed in the initial Cartesian frame

$$\boldsymbol{\sigma}_{tr} = \mathbf{r}_1^T\ \boldsymbol{\sigma}_{tr}^c\ \mathbf{r}_1 = \mathbf{r}_1^T \left[\mathbf{r}_0^T\ \boldsymbol{\sigma}_{tr}^0\ \mathbf{r}_0 + \int_{t_0}^{t_1} \mathbf{H}_e\ \mathbf{D}^c dt\right] \mathbf{r}_1 \tag{4.17}$$

Using the polar decomposition (4.2) and that $\mathbf{D} = \text{sym}\ (\mathbf{L})$

$$\mathbf{D}^c(t) = \mathbf{r}_1^T\ \mathbf{D}\ \mathbf{r}_1 = \frac{1}{2}\mathbf{r}_1^T\ \mathbf{R}\ [\dot{\mathbf{U}}\mathbf{U}^{-1} + \mathbf{U}^{-1}\dot{\mathbf{U}}]\ \mathbf{R}^T\ \mathbf{r}_1 \tag{4.18}$$

The following three assumptions are next introduced, as in Ponthot [2002] i.e. (i) that the reference configuration is the configuration at time t_0 (updated Lagrangian configuration) $\mathbf{r}_0 = \mathbf{I}$; (ii) we suppose $\mathbf{r}(t) = \mathbf{R}(t)$; and (iii) the following exponential map for $\mathbf{U}(t)$ is assumed

$$\mathbf{U}(t) = \exp\left[\frac{t - t_0}{\Delta t}\ \mathbf{C}\right] \tag{4.19}$$

with $\mathbf{C} = \ln\mathbf{U}$ the incremental natural strain tensor between the reference configuration and the actual configuration. Considering the above assumptions the trial stress tensor can be calculated as

$$\boldsymbol{\sigma}_{tr} = \mathbf{R}\,[\boldsymbol{\sigma}_0 + \mathbf{H}_e\,\mathbf{C}]\,\mathbf{R}^T \tag{4.20}$$

The major features of this formulation are, that:

- all kinematic quantities are based on the deformation gradient $\mathbf{F}$, which is derived in a straightforward manner in a finite element frame
- $\mathbf{R}$ is computed exactly from the polar decomposition
- the logarithmic strain tensor $\mathbf{C}$ can be computed exactly [Ponthot 1995]
- the scheme is trivially incrementally objective, since in the case of rigid body motion $\mathbf{C} = \ln\mathbf{U} = \mathbf{0}$ and the stress tensor is updated as $\boldsymbol{\sigma}_t = \mathbf{R}\ \boldsymbol{\sigma}_0\ \mathbf{R}^T$ for any finite rotation
- the formulation is not restricted to isotropic behavior, it constitutes a natural frame for anisotropy

Plastic corrector step

If the elastic trial step violates the yield condition a *plastic corrector step* is used to return to the evolving yield surface. The nonlinear system of equations to solve is:

$$\begin{cases} \mathbf{H}_e^{-1}\,(\boldsymbol{\sigma} - \boldsymbol{\sigma}_{tr}) + \mathbf{D}_p &= 0 \\ \mathbf{D}_p &= \dot{\gamma}\left(\dfrac{\partial f}{\partial \boldsymbol{\sigma}}\right) \\ f(\boldsymbol{\sigma}, \kappa) &= 0 \\ \dot{\kappa} &= \dot{\gamma} \end{cases} \tag{4.21}$$

The linearization of this system of equations for the Newton–Raphson local iteration procedure can be written as

$$\begin{bmatrix} \boldsymbol{\sigma}^{(k+1)} \\ \\ \kappa^{(k+1)} \end{bmatrix} = \begin{bmatrix} \boldsymbol{\sigma}^{(k)} \\ \\ \kappa^{(k)} \end{bmatrix} - [\mathbf{J}_p(\boldsymbol{\sigma}^{(k)}, \kappa^{(k)})]^{-1}\,\mathbf{M}^{(k)} \begin{pmatrix} \boldsymbol{\sigma}^{(k)} \\ \\ \kappa^{(k)} \end{pmatrix} \tag{4.22}$$

where the superscripts in parentheses (k) represent the current iteration number. $\mathbf{J}_p(\boldsymbol{\sigma}^{(k)}, \kappa^{(k)})$ is the Jacobian matrix of the system (4.21), and $\mathbf{M}^{(k)}(\boldsymbol{\sigma}^{(k)}, \kappa^{(k)})$ stands for the matrix of residuals at the k-th iteration of a given increment of the local Newton–Raphson procedure.

Consistent tangent stiffness matrix of the return mapping

The notion of the tangent stiffness matrix $\mathbf{H}_t$ consistent with the integration algorithm of the constitutive equations was introduced in Simo & Taylor [1985]. The local tangent stiffness matrix calculated at the integration points of the elements used in the assembly of the global structural tangent stiffness matrix has to be consistent with the chosen algorithm of integration of system (4.21) to keep the asymptotically quadratic rate of convergence of the global iteration on the structural level, which is necessary for computational efficiency. The derivation of $\mathbf{H}_t$ (if possible by an analytical expression) is essential to guarantee an efficient calculation.
The elastic–plastic operator *consistent* with the stress integration algorithm is defined by the relation [Ponthot 1995; Simo & Taylor 1985]

$$\mathbf{H}_t = \lim_{\mathbf{D}_n^{(i\to i+1)}\to 0} \frac{\boldsymbol{\sigma}_n^{(i+1)} - \boldsymbol{\sigma}_n^{(i)}}{\mathbf{D}_n^{(i\to i+1)}} \tag{4.23}$$

with subscripts n, and superscripts in parentheses (i) corresponding to the increment number and the iteration number of the local iteration loop, respectively. $\mathbf{D}_n^{(i\to i+1)}$ and $(\boldsymbol{\sigma}_n^{(i+1)} - \boldsymbol{\sigma}_n^{(i)})$ are the increment of strain and stress between non–equilibrium iterations (i) and $(i+1)$.
After some straightforward manipulations the Jacobian matrix $\mathbf{J}_{p\,n}^{(k)}$ issued from the linearization of the nonlinear system of equations to solve at the k-th iteration of the increment n can be expressed

$$\mathbf{J}_{p\,n}^{(k)} = \begin{bmatrix} [\mathbf{H}_e]^{-1} + \dot{\kappa}_n^{(k)} \left(\dfrac{\partial^2 f}{\partial^2 \boldsymbol{\sigma}}\right)_n^{(k)} & \left(\dfrac{\partial f}{\partial \boldsymbol{\sigma}}\right)_n^{(k)} + \dot{\kappa}_n^{(k)} \left(\dfrac{\partial^2 f}{\partial \boldsymbol{\sigma}\, \partial \kappa}\right)_n^{(k)} \\ \left(\dfrac{\partial f}{\partial \boldsymbol{\sigma}}\right)_n^{(k)^T} & \left(\dfrac{\partial f}{\partial \kappa}\right)_n^{(k)} \end{bmatrix} \tag{4.24}$$

The upper 3×3 matrix of the inverse of the Jacobian matrix $\mathbf{J}_p^{-1}$ is the tangent stiffness matrix consistent with the stress update integration algorithm $\mathbf{H}_t$ [Simo & Taylor 1985]. The tangent stiffness matrix consistent with the stress integration scheme is used in the code on local and global levels for the sake of rapid convergence and efficiency. Once the local iteration converged, $\mathbf{H}_t$ is further used to construct the material stiffness matrix (see below) of the global structural iteration.

4.1.4 Evaluation of the structural consistent tangent stiffness matrix

As pointed out in the previous section, in order to guarantee the asymptotically quadratic rate of convergence of the Newton–Raphson iteration loop on the structural level, the structural tangent stiffness matrix consistent with the stress integration scheme $\mathbf{K}_s$ has to be used. An interesting feature of the corotational finite deformation formulation is that an analytical expression of this

matrix $\mathbf{K}_s$ can be given by direct linearization. By definition, this stiffness matrix is given by

$$\dot{\vec{f}}^{\,(i)}_{int\,n} = [\mathbf{K}_s]^{\,(i)}_{n}\; d\dot{\vec{x}}^{\,(i)}_{n} \tag{4.25}$$

at increment n and at iteration (i). From here on the superscript in parentheses (i) referring to the iteration number is omitted for the sake of a less complex notation, keeping in mind however, that the consistent tangent operator is defined between two non–equilibrated iterations.

In the current deformed configuration at time t the internal forces of a node I of the discretized structure, in the direction i are evaluated using Einstein's notation convention as

$$f_{int\,Ii} = \int_{V(t)} B_{Ij}\;\sigma_{ji}\;dV \tag{4.26}$$

with $B_{Ij} = \dfrac{\partial N_I}{\partial x_j}$, N_I being the interpolation function of the finite element. The expression of the the consistent tangent operator is

$$\dot{f}_{int\,Ii} = \mathbf{K}_{s\,IJik}\;\dot{x}_{Jk} \tag{4.27}$$

where the uppercase letters relate to nodes and lowercase letters correspond to directions. The time derivative of (4.26) can be written as

$$\dot{f}_{int\,Ii} = \int_{V} [B_{Ij}\;\dot{\sigma}_{ji}\;dV + \dot{B}_{Ij}\;\sigma_{ji}\;dV + B_{Ij}\;\sigma_{ji}\;d\dot{V}] \tag{4.28}$$

The first term on the right side of (4.28) expresses the influence of the change of stress (the traditional notion of the stiffness matrix in infinitesimal theory) and the second and third term describes the influence of the change in the geometry on the internal forces.

The expression of $\dot{\sigma}_{ji}$ depends on the chosen objective rate of stress. It was shown in Ponthot [1995] that the Jaumann objective rate is consistent with corotational formulation considered here. By the appropriate mathematical developments the expression of $\mathbf{K}_s$ can be established as [Ponthot 1995]

$$\begin{cases} \mathbf{K}_{s\,IJik} &= \displaystyle\int_V B_{Ij}\;B_{Jl}\;\mathbf{T}_{ijkl}\;dV \qquad \text{with} \\ \\ \mathbf{T}_{ijkl} &= \mathbf{K}^{mat}_{ijkl} + \sigma_{ij}\delta_{kl} - \dfrac{1}{2}\sigma_{il}\delta_{kj} - \dfrac{1}{2}\sigma_{ik}\delta_{jl} + \dfrac{1}{2}\sigma_{lj}\delta_{ik} - \dfrac{1}{2}\sigma_{kj}\delta_{il} \end{cases} \tag{4.29}$$

with δ_{nm} denoting the Kronecker delta. $\mathbf{K}^{mat}_{ijkl}$ is the contribution to the structural stiffness matrix related to the material behavior (defined in the constitutive law), in our case it is obtained from $\mathbf{H}_t$ presented previously. The other terms of $\mathbf{T}_{ijkl}$ can be condensed in a matrix $\mathbf{K}^{geo}_{ijkl}$ which represents the contribution related to changes in the geometry.

Note, that in the case of infinitesimal displacement and deformation theory $\mathbf{K}^{geo}$ does not exist, since the initial and deformed configurations are assumed to be similar. Equation (4.29) indeed degenerates to the stiffness matrix of linear elasticity when $\boldsymbol{\sigma}$ = **0** is taken and $\mathbf{K}^{mat}$ is replaced by the elastic tensor of Hooke. The corotational formulation considered here has the major advantage of fully decoupling the treatment of material and geometric nonlinearities, leading to a high degree of flexibility for the choice of the material behavior.

4.1.5 Conclusion

In this section the necessary ingredients of the corotational finite deformation formulation and of mathematical plasticity used during the implementation of the finite deformation plastic behavior in the finite element code were presented.

The programmed elements use the von Mises yield function with isotropic nonlinear hardening behavior. The necessary incremental iterative solution procedure was introduced. The notion of the elastic–plastic tangent stiffness matrix consistent with the stress integration algorithm was recalled. The latter, determined on the level of the integration points of the elements was used in the global iteration algorithm for the construction of the material stiffness matrix $\mathbf{K}^{mat}$.

The finite deformation scheme used here is trivially incrementally objective, and the contribution related to changes in the geometry to the structural stiffness matrix $\mathbf{K}^{geo}$, being specific to finite deformation formulations can be determined analytically. The structural stiffness matrix is defined as $\mathbf{K}_s = \mathbf{K}^{mat} + \mathbf{K}^{geo}$ showing a full decoupling of material and geometric nonlinearities, being an interesting feature of the formulation.

In spite of the material and geometric nonlinearities considered in the formulation the asymptotically quadratic rate of convergence of both the global and the integration point–level iterations was ensured. The plastic element set was assessed using several benchmark problems, among others, some presented in AFNOR [1990]. The simulations were successful for the considered problems, the obtained results correspond to the analytical results of the benchmarks.

4.2 Computational contact mechanics using augmented Lagrangian formulation

Several recent publications [Chabrand *et al.* 2005; Stadler 2007] and books [Meguid *et al.* 2004; Stachowiak 2005; Wriggers 2002; Wriggers & Zavarise 2004] are dedicated to experimental and computational tribology and related issues. The reader can consult them for a more general overview of the subject. Modeling contact conditions and contact evolution in a numerical model is required to represent the evolving boundary and loading conditions of problems involving contact. In this work, contact problems with the following assumptions were addressed:

- rigid (undeformable) body–deformable body contact in two dimensions,
- the rigid body is described by parametric curves,
- whenever friction is assumed on the contact interface, a Coulomb model is used.

In the following subsections, basic notions of contact mechanics are first introduced, with constitutive laws for frictionless normal contact and frictional behavior. The chosen Coulomb friction model, coupled to normal contact conditions is finally discussed. This introduction is followed by the presentation of the main steps of the developments necessary to include a one–node node–to–facet contact element in the finite element code.

4.2.1 Contact mechanics

Contact kinematics

To put the problem in a general context, all contact relations will be formulated for finite deformations, for problems in which two bodies approach each other and come into contact on parts of their boundaries. Two bodies B_1 and B_2 are considered with boundaries Γ_1 and Γ_2 respectively in a structural analysis framework. The body B_1 will represent a rigid body, and body B_2 will be considered deformable. When boundary conditions are applied on the bodies $B_i\ ;\ i = 1, 2$, namely surface tractions on Γ_2, body forces, and forced displacements; displacement/strain and stress fields are generated as a response.

The rigid body is represented by a single or interconnected two–dimensional convex parametric curves, which implies that the contact variables (see below) describing the contact kinematics are well defined [Heegaard & Curnier 1995]. The assumption of neglecting the deformation of one of the bodies can be adopted in many engineering applications. Apart from the obvious example of nanoindentation, this assumption could be performed even for materials in contact with similar elastic moduli if they exhibit plastic yielding with strongly different yield strengths

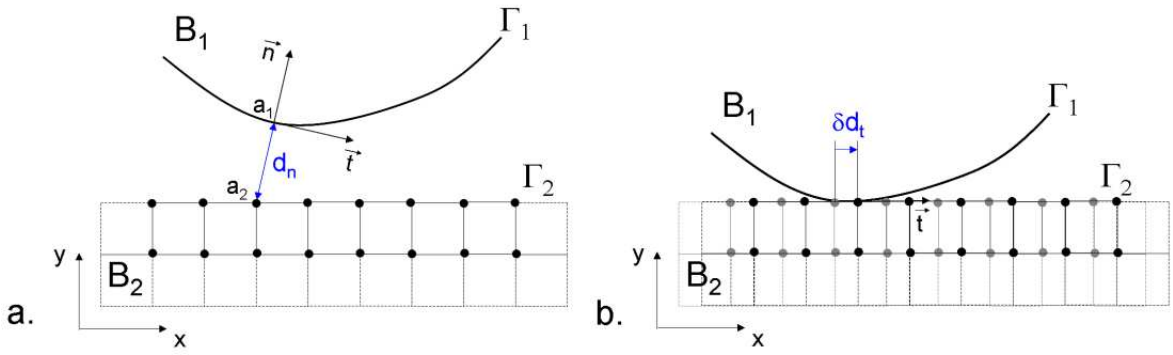

Figure 4.1: Definition of the contact variables for a. unilateral and b. tangential contact.

(in that case the low yield limit material is prone to suffer the majority of the deformation if it enters the plastic domain during indentation while the other material remains elastic). If the normal $\vec{n}(x_1, y_1)$ at a point $a_1(x_1, y_1)$ of surface Γ_1 passes through the point $a_2(x_2, y_2)$ of the surface Γ_2, then the distance $\parallel a_1 a_2 \parallel$ is minimal. The point $a_1(x_1, y_1)$ is the normal projection of point $a_2(x_2, y_2)$. The choice of the point a_1 is not unique in general, unless B_1 is convex. The signed normal distance d_n can be defined as

$$d_n(a_2) = \vec{n}(x_1, y_1)\ [\vec{x}(a_2) - \vec{x}(a_1(a_2))]\ \forall a_2 \in \Gamma_2 \tag{4.30}$$

with $\vec{x}$ denoting the position vector in the two–dimensional space. If d_n is positive the two bodies do not inter–penetrate. Making the assumption of the quasi–static evolution of the contact variables the relative contact velocities $\delta\vec{d}$ at time t can be written as

$$\delta\vec{d}(a_2, t) = \delta\vec{x}(a_2, t) - \delta\vec{x}(a_1, t) \tag{4.31}$$

$\delta\vec{d_t}$ is the projection of $\delta\vec{d}$ on the tangent vector space to Γ_1 representing the vector field of tangential relative velocities. The normal contact distance d_n and the tangential relative contact velocity δd_t are linear functions of the displacement vector $\vec{u}$.

Unilateral contact conditions

Frictionless normal contact, or *unilateral contact* conditions are usually characterized by the following conditions:

- solids can separate, but not pull each other (since surface adhesion forces and contact forces necessary for surface deformation are usually of different order – the latter being more important),
- solids can press, but not penetrate each other,

which are classically expressed mathematically at a given point of the contact surface using variables d_n and f_n, representing respectively the normal separation distance and normal contact

forces between the contacting solids:

$$d_n \geq 0;\ f_n \leq 0;\ f_n\, d_n = 0 \tag{4.32}$$

These conditions are also referred to as the Hertz–Signorini–Moreau conditions in contact mechanics [Alart & Curnier 1991; Meguid *et al.* 2004]. Such conditions coincide with Kuhn–Tucker complementary conditions in the theory of optimization.

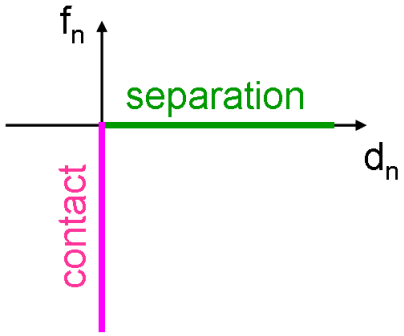

Figure 4.2: Unilateral contact conditions, multivalued contact law.

The contact law relating f_n to d_n (Fig.4.2) is a non–smooth, multivalued function (it is not differentiable and can take an infinite number of values at the origin). Even simple, frictionless contact problems are therefore difficult to formulate and solve numerically, since a weak form of the contact mechanics problem is usually needed.

Friction contact laws

Practically all real–life contact problems involve frictional effects. Friction is a particularly complex phenomenon that stems from and bridges multiple scales, from atomic level (atomic interactions in Section 3.1) to the macroscale. Friction potentially depends on a variety of parameters of the contact, i.e. the normal contact force, the relative sliding speed, the temperature, the humidity, the lubrication, the surface roughness, possible wear and particle detachment forming a third body layer, etc. [Stachowiak 2005; Wriggers 2002].

This results in a large number of friction models with varying complexity, developed and adapted for different types of problems. In this work dry friction conditions (without lubrication) were considered, since the aimed applications work usually in these conditions. The most well–known and most widely applied dry friction model is the simplest one, defined by one parameter μ (usually referred to as the coefficient of friction), the quotient of the normal and the tangential forces on the contact surface, separating the states of sliding and sticking under constant normal force. It is generally known as the model of Coulomb, or Amontons [Mate 2008; Wriggers & Zavarise 2004]. Although this model is based on a phenomenological

description of the frictional behavior on the macro–scale it has a vast field of application, and it was shown to perform well in complex situations as well [Nosonovsky & Bhushan 2007]. Even though other, more complex constitutive laws may better describe the frictional behavior of the contact interface on the considered micro-and nanoscale [Carpick *et al.* 1996, 1997, 2001; Deshpande *et al.* 2007; Mate 2008; Nosonovsky & Bhushan 2007], the Coulomb's law remains the most frequently adopted law for friction in the literature (concerning the modeling of nanoindentation, see [Antunes *et al.* 2006, 2007; Bolzon *et al.* 2004; Bressan *et al.* 2005; Bucaille *et al.* 2004, 2003; Cao *et al.* 2007; Cao & Lu 2004; Carlsson *et al.* 2000; Habbab *et al.* 2006; Mata & Alcalà 2004; Mesarovic & Fleck 1999; Qin *et al.* 2007; Taljat & Pharr 2004; Wang *et al.* 2007b]). It was therefore chosen in order to allow the results to be compared to other works. However, the developments were performed such that other laws for friction can be accounted for in future works.

This model is first presented for the particular case of solids in contact under constant normal load (f_n = const). The relative sliding speed between the solids and the tangential contact force at a given point of the contact surface are represented by δd_t and f_t, respectively. Two tangential contact states can be distinguished:

- the state of stick: the tangential forces are under a limit value $\| f_t \| < k$, there is no relative movement between the solids in contact $\delta d_t = 0$,
- the state of slip: the tangential forces are equal to the limit value $\| f_t \| = k$, and the solids are in relative movement $\| \delta d_t \| > 0$.

Keeping the limit value for stick k constant, the similarity of the Coulomb contact conditions to the formulation of perfect plasticity is easily recognizable. The Coulomb contact law relating f_t to d_t (Fig.4.3) is a non–smooth, multivalued function. For similar reasons as in the case of unilateral contact, this leads to difficulties in formulating and solving the tangential contact problem in a numerical scheme.

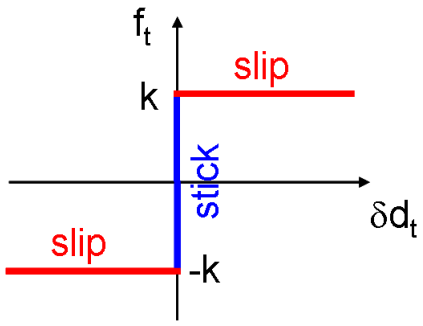

Figure 4.3: Tangential contact conditions of the Coulomb friction model at constant normal contact force, multivalued contact law.

Coupling Coulomb friction law and unilateral contact conditions

The stick limit k is not a fixed value in the classical Coulomb friction model, but on the contrary, it depends on the magnitude of the normal force via the coefficient of friction μ by the relation: $k = \mu\ f_n$. This results in a coupling between the unilateral and the tangential contact laws, as illustrated in Fig.4.4.

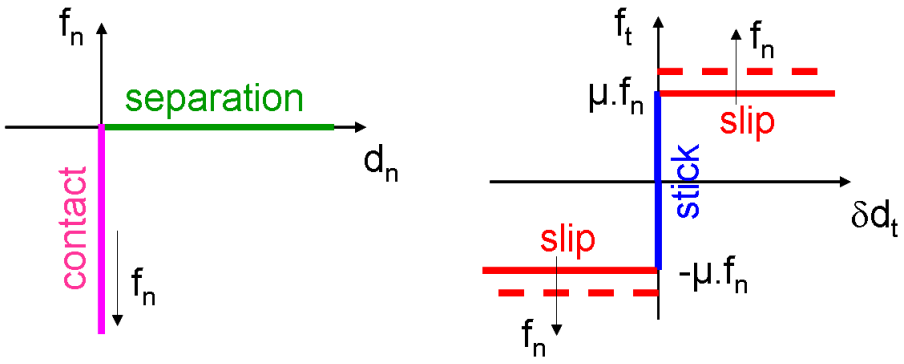

Figure 4.4: Unilateral and tangential contact conditions resulting from the coupling of Coulomb friction law and unilateral contact constraints.

Three contact states are thus to be considered:

$$\begin{array}{lllll} \text{gap:} & d_n > 0 & f_n = 0 & f_t = 0 & \\ \text{stick:} & d_n = 0 & f_n < 0 & \| f_t \| < \| \mu f_n \| & \delta d_t = 0 \\ \text{slip:} & d_n = 0 & f_n < 0 & \| f_t \| = \| \mu f_n \| & \| \delta d_t \| > 0 \end{array} \tag{4.33}$$

The use of non–smooth, multivalued functions and the coupling of normal and tangential contact behavior are the reason for which even the simplest Coulomb friction model requires advanced solution methods in computational contact mechanics.

4.2.2 Numerical modeling of contact by an augmented Lagrangian formulation

Analytical solutions of contact problems are restricted to simple load cases with elementary geometries [Hertz 1882] thereby calling for numerical simulations in most practical cases. The most obvious change taking place when two surfaces come into contact is related to the fact that their displacements have to satisfy some restrictions on the contact surface, and that contact stresses appear in the contact zone. Starting from this observation, contact mechanics, in its first interpretation, can be considered as a particular set of boundary conditions that vary within the analysis, rendering the overall structural problem nonlinear independently from the constitutive law used to model the material behavior.

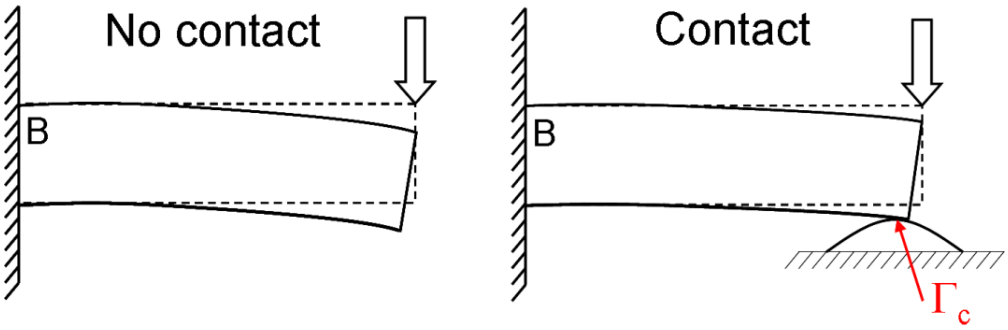

Figure 4.5: As opposed to classical problems (left), when considering contact (right) the displacements of body B have to satisfy contact conditions defined by the contact laws on the contact surface Γ_c.

The nonlinear nature of the problem makes a proper consideration of these constraints not straightforward, hence iterative algorithms are needed. A method based on minimization principle was considered in this work. For a summary and a detailed description of the applicable computational methods to contact mechanics problems the reader can consult [Meguid *et al.* 2004; Wriggers 2002; Wriggers & Zavarise 2004].

Search for equilibrium as an optimization problem

Without any loss of generality as for the treatment of the contact problem the assumption will be made, that the mechanical equilibrium of the system without contact conditions can be defined by the minimization of a functional $\Pi(\vec{u})$ (the free energy potential for example). This allows the description of the continuum mechanics equilibrium problem as an optimization (minimization) problem [Meguid *et al.* 2004]. The solution of the equilibrium problem of the two discretized bodies in the absence of any contact can be expressed as

$$\vec{u}^{\,*} = \text{argmin}\,[\Pi(\vec{u})] \;\longleftrightarrow\; \Pi(\vec{u}^{\,*}) \leq \Pi(\vec{u})\;\forall \vec{u} \tag{4.34}$$

where $\Pi(\vec{u})$ is for example a hyperelastic or elastic–plastic functional [Lemaitre & Chaboche 1985] in terms of the global displacement vector $\vec{u}$, and the notation $y^* = \text{argmin}\; f(y)$ denotes the particular point y^* which realizes the minimum of the function $f(y)$. A necessary condition for $\vec{u}^{\,*}$ to be a solution of the problem (which becomes sufficient if $\Pi(\vec{u})$ is strictly convex) is [Heegaard & Curnier 1993; Pietrzak & Curnier 1999]

$$\nabla\Pi(\vec{u}^{\,*}) = \vec{f_{int}}(\vec{u}^{\,*}) - \vec{f_{ext}} = \vec{0} \tag{4.35}$$

where ∇ denotes the gradient operator, $\vec{f_{int}}(\vec{u})$ is the internal force vector and $\vec{f_{ext}}$ the externally applied force vector. Note that in elasticity any continuum problem can be formulated as a minimization problem. This is based on the fact that the total potential energy realizes a minimum

at the solution point. This is no longer valid in plasticity, where another functional has to be introduced if one wishes to convert the problem of the search for equilibrium to a minimization problem [de Borst & Mühlhaus 1992; Lemaitre & Chaboche 1985].

Including contact constraints

Contact conditions add new and potentially evolving kinematic constraints to the original problem. These constraints can be divided in two classes: the unilateral contact problem [Burguera & Viano 1994; Chen 2001; Han & Sofonea 2000; Sofonea 1997] and frictional contact problem [Alart & Curnier 1991; Baillet & Sassi 2003; Feng *et al.* 2004; Kim *et al.* 2000; Kontoleon & Baniotopoulos 2000; Kontoleon *et al.* 1999; Laursen & Simo 1993; Lin & Tseng 1998; Meyer *et al.* 1991; Serpa & Iguti 2000; Wriggers 2002; Wriggers & Zavarise 2004; Yang *et al.* 2005]. The former restrains the normal components of the displacement at the interface of the contacting bodies to avoid inter–penetration, while the latter condition describes the tangential (e.g. stick–slip) behavior in the contact zone. From the conceptual point of view, a mechanical contact problem can be considered as a 'classical' mechanical problem (search for equilibrium by minimizing a functional $\Pi(\vec{u})$) with additional contact features related to the inequality constraints [Barber & Ciavarella 2000; Wriggers 2002; Wriggers & Zavarise 2004]. The constrained optimization problem of finding $\vec{u}^*$ subject to contact constrains transforms to an *unconstrained* optimization problem using a generalized functional

$$\Phi(\vec{u}) = \Pi(\vec{u}) + C_n(f_n,\ d_n(\vec{u})) + C_t(f_t,\ \delta d_t(\vec{u})) \tag{4.36}$$

where $C_n(f_n,\ d_n(\vec{u}))$ and $C_t(f_t,\ \delta d_t(\vec{u}))$ stand for functionals representing normal and tangential contact conditions.

With the assumption made that the equilibrium of the analyzed system is the minimum of a functional, the solution of the structural – contact mechanics problem becomes from a mathematical point of view an inequality–constrained minimization problem. It has to be realized that the major difficulties in the algorithmic treatment of contact problems are related to adding the inequality constraints C_n and C_t and to the non–differentiability of normal contact and friction terms. To overcome these difficulties, different formulations were developed, the best choice still remains an open and frequently discussed question of computational contact mechanics.

The minimization problem is solved here using a primal–dual method, which means that practically the saddle point of an augmented Lagrangian function $\Phi^{AL} = \Pi(\vec{u}) + C^{AL}$ (having conceptually a form similar to (4.36)) is searched for with a Newton type continuous multiplier update procedure [Arora *et al.* 1991; Heegaard & Curnier 1995; Pietrzak & Curnier 1999]. $C^{AL} = C_n^{AL} + C_t^{AL}$ is expressed using augmented Lagrangian multipliers (see below). Such a solution procedure can be used, the gradients of individual contact constraints are available.

The augmented Lagrangian formulation is the convolution of the classical penalty and Lagrange multiplier optimization methods [Nocedal 2000; Wriggers 2002], bearing the prime advantages of both, however without inheriting their respective disadvantages.

In the penalty method, a penalty term is used to enforce the contact conditions. This method can be preferred because only the primal displacement variables enter the formulation, which leads also to a straightforward implementation. However, since this method is a regularization method based on the penalty principle, this implies that constraints are exactly satisfied only at an infinite value of the penalty parameter. As a result, there is a compromise between satisfying the contact conditions and numerical ill–conditioning.

Enforcing the contact constraints using Lagrange multipliers results in the exact satisfaction of the contact conditions. At equilibrium the values of the Lagrange multipliers correspond to the unknown contact forces. Conversely to this advantage, its numerical drawback is that in this method the field of Lagrange multipliers and the displacement field both have to be discretized (using interpolation functions for the Lagrange multipliers and kinematic contact variables) [Wriggers 2002]. As a result the total number of unknowns is increased with respect to the unconstrained problem, and has to be adapted when the contact interface varies during the loading process.

The augmented Lagrange multiplier method is the combination of penalty and Lagrange multiplier methods, including a Lagrange multiplier term (λ, the dual variable) as well as a penalty term: $g_n = \lambda_n + r_n d_n$ and $g_t = \lambda_t + r_t \delta d_t$. Contact is detected with a linear combination of primal and dual variables. Note that when the Lagrange multiplier terms are zero the expressions of g_n and g_t correspond to the penalty method. This method ensures the accurate satisfaction of the contact constraints, at the same time the regularization parameters r_t and r_n penalizing d_n and δd_t, respectively, take small values (usually $r_t = r_n =$ 10 to 100 was used), allowing to avoid numerical ill–conditioning. This formulation allies the prime advantages of the penalty and Lagrange multiplier methods, i.e. simple implementation and accurate solution, resulting in an efficient and accurate computational contact mechanics method. Multiplier methods are discussed in the context of a general constrained optimization problem (for equality and inequality constraints), and its solution in Arora *et al.* [1991].

Before considering the complete mechanical problem, the focus on the additional terms C_n^{AL} and C_t^{AL} related to contact constraints are first introduced. This would correspond to contact configurations with rigid bodies only (i.e. without the functional $\Pi(\vec{u})$ describing the mechanical behavior of the contacting solids).

Contact contribution to the Augmented Lagrangian for unilateral contact conditions (C_n^{AL})

For the sake of simplicity in a first step the unilateral contact problem is investigated (the assumption is made that there is no friction between the contacting surfaces). It was shown in Alart & Curnier [1991] that a functional C_n^{AL} expressing the frictionless, normal contact conditions can take the following form:

$$C_n^{AL}(\lambda_n,\ d_n(\vec{u})) = -\frac{1}{2\ r_n} \parallel \lambda_n \parallel^2 + \frac{1}{2\ r_n}\text{dist}^2[g_n,\ \mathbf{R}_+] \tag{4.37}$$

where $\text{dist}[p,\ \mathbf{C}] = \min_{y\in\mathbf{C}} \parallel p - y \parallel$; $g_n = \lambda_n + r_n d_n$ is the augmented Lagrange multiplier for normal contact; and $\mathbf{R}_+$ is the space of positive real numbers.
This form of the functional C_n^{AL} for normal contact in the augmented Lagrangian Φ^{AL} satisfies the normal contact conditions exactly, moreover it has the advantage that an analytical expression of the consistent tangent stiffness matrix can be derived from it, which ensures that the global structural iteration loop keeps its asymptotically quadratic rate of convergence when unilateral contact conditions are prescribed [Alart & Curnier 1991].

Contact contribution to the Augmented Lagrangian for pure friction conditions (C_t^{AL})

When pure friction conditions are considered (the assumption is made that the normal force remains constant, implying that the stick limit value k = const.), a functional C_t^{AL} expressing the corresponding contact conditions can take the following form [Alart & Curnier 1991; Pietrzak & Curnier 1999]:

$$C_t^{AL}(\lambda_t,\ \delta d_t(\vec{u})) = \lambda_t\ \delta d_t + \frac{r_t}{2} \parallel \delta d_t \parallel^2 - \frac{1}{2\ r_t}\text{dist}^2[g_t,\ \mathbf{K}] \tag{4.38}$$

where $g_t = \lambda_t + r_t \delta d_t$ is the augmented Lagrange multiplier for tangential contact, and $\mathbf{K}$ is a segment of $\mathbf{R}$ defined by the constant stick limit value k, as $\mathbf{K} = [-k \quad k]$.
This form of the functional C_t^{AL} for tangential contact at fixed stick limit k in the augmented Lagrangian Φ^{AL} satisfies the corresponding contact conditions exactly. If considering this particular form of friction law with a constant stick limit value (which can potentially be used to model micro-and nanoscale contact behavior [Carpick *et al.* 1996, 1997, 2001]), it is possible to derive an analytical expression of the consistent tangent stiffness matrix.

Augmented Lagrangian for Coulomb friction conditions between deformable bodies

The complete form of the functional Φ^{AL} is now used including the functional $\Pi(\vec{u})$ describing the mechanical behavior of the contacting bodies. The final form of the contact functional C^{AL} for Coulomb friction in the augmented Lagrangian Φ^{AL} used in the finite element code is the combination of the expression used to describe unilateral contact conditions C_n^{AL} and the one describing tangential contact conditions C_t^{AL}, taking however the dependence of the stick limit on the normal force into account.

$$\begin{aligned}\Phi^{AL}(\vec{u},\ \lambda_n,\ \lambda_t) \ = \ \Pi(\vec{u}) \ & -\frac{1}{2\ r_n} \parallel \lambda_n \parallel^2 + \frac{1}{2\ r_n}\text{dist}^2[g_n,\ \mathbf{R}_+] \\ & +\lambda_t\ \delta d_t + \frac{r_t}{2} \parallel \delta d_t \parallel^2 - \frac{1}{2\ r_t}\text{dist}^2[g_t,\ \mathbf{K}_\mu]\end{aligned} \tag{4.39}$$

where $\mathbf{K}_\mu$ is a segment defined by $\mathbf{K}_\mu = [-\mu g_n \quad \mu g_n]$, depending on the coefficient of friction μ and the augmented Lagrange multiplier of unilateral contact g_n. It must be stressed that finding the saddle point of the augmented Lagrangian $\Phi^{AL} = \Pi(\vec{u}) + C^{AL}$ is not a standard optimization problem, but only a quasi–optimization problem, since the convex set $\mathbf{K}_\mu$ depends on the solution $\vec{u}$ through λ_n. The augmented Lagrangian is continuously differentiable with respect to $\vec{u}$, λ_n and λ_t if $\Pi(\vec{u})$ is continuously differentiable with respect to $\vec{u}$ [Alart & Curnier 1991]. Consequently, the saddle–point of the augmented Lagrangian, $(\vec{u}^{\,*}, \lambda_n^*, \lambda_t^*)$ is unique, resulting from the strict convexity of $\Pi(\vec{u})$. The necessary condition for $(\vec{u}^{\,*}, \lambda_n^*, \lambda_t^*)$ to be the saddle point of Φ^{AL}, i.e. to be the solution of the constrained optimization problem, is the satisfaction of:

$$\left\{\begin{array}{lllllll} \nabla_{\vec{u}}\ \Phi^{AL} & = & \nabla_{\vec{u}}\ \Pi(\vec{u}) & +\nabla_{\vec{u}}\ C^{AL} & = & 0 \\ \nabla_{\lambda_n}\Phi^{AL} & = & & +\nabla_{\lambda_n}\ C^{AL} & = & 0 \\ \nabla_{\lambda_t}\Phi^{AL} & = & & +\nabla_{\lambda_t}\ C^{AL} & = & 0 \end{array}\right. \tag{4.40}$$

The contact constraints in the discretized problem are applied through a set of one–noded, node–to–facet type contact elements on the predetermined contact surface. For the sake of clarity and simplicity the detailed development of the terms entering (4.40) is *restricted to the additional terms due to contact constraints* C^{AL}, considering one contact element in the following. In order to calculate the involved gradients of the terms representing the contact constraints it is recalled that the distance of a given point $p \in \mathbf{P}$ to a convex set $\mathbf{C}$ can be expressed in accordance with the projection theorem [Heegaard & Curnier 1993] as:

$$\text{dist}[p,\ \mathbf{C}] = \parallel p - \text{proj}_{\mathbf{C}}\ (p) \parallel \tag{4.41}$$

where $\text{proj}_{\mathbf{C}}\ (p)$ is the projection of p on $\mathbf{C}$. Moreover, the projections on $\mathbf{C}$ and on its complementary set $\overline{\mathbf{C}}$ (for example $\mathbf{R}_+ = \overline{\mathbf{R}_-}$) satisfy

$$p = \text{proj}_{\mathbf{C}}\ (p) + \text{proj}_{\overline{\mathbf{C}}}\ (p) \tag{4.42}$$

This formula is the generalization of the decomposition of a vector on two orthogonal subspaces. Combining (4.41) and (4.42), the following expression can be written [Heegaard & Curnier 1993]:

$$\nabla_p \left(\frac{1}{2} \text{dist}^2[p,\ \mathbf{C}] \right) = \text{proj}_{\overline{\mathbf{C}}}\ (p) \tag{4.43}$$

The *contact contribution* in the system of equations expressing the saddle point necessary conditions (4.40) can be rewritten for one contact node as

$$\begin{cases} \nabla_{\vec{u}}\ C^{AL} &= (\nabla_{\vec{u}}\ d_n)^T \text{proj}_{\mathbf{R}_-}\ (g_n) + (\nabla_{\vec{u}}\ \delta d_t)^T \text{proj}_{\mathbf{K}_\mu}\ (g_t) \\ \nabla_{\lambda_n} C^{AL} &= -\dfrac{1}{r_n}(\lambda_n - \text{proj}_{\mathbf{R}_-}\ (g_n)) \\ \nabla_{\lambda_t} C^{AL} &= -\dfrac{1}{r_t}(\lambda_t - \text{proj}_{\mathbf{K}_\mu}\ (g_t)) \end{cases} \tag{4.44}$$

It has to be noted that, since $\mathbf{K}_\mu$ is a segment with variable length, depending on both λ_n and $d_n(\vec{u})$ through $\mathbf{K}_\mu = [-\mu\ (\lambda_n + r_n d_n(\vec{u})) \quad \mu\ (\lambda_n + r_n d_n(\vec{u}))]$, obtaining the above expressions using the projection defined in (4.43) requires the assumption that $\mathbf{K}_\mu$ is constant. This is necessary, because the dependence of $\mathbf{K}_\mu$ on λ_n and $\vec{u}$ cannot be given by analytical expressions. This has implications on the rate of convergence of the computation when frictional sliding is involved, the convergence is not asymptotically quadratic anymore. However, a fast convergence is kept if the contact variables are updated at every iteration of the solution procedure [Alart & Curnier 1991], this frequent update minimizes the error made by the assumption of $\mathbf{K}_\mu$ = const. As pointed out before, the asymptotically quadratic rate of convergence of the global iteration loop can be restored when a constant stick limit k, independent of the normal contact force is chosen (if k is supposed to be an intrinsic property of the contact interface), since in this case the expressions in (4.44) can be evaluated consistently.

Contact forces and generalized contact Jacobians on the level of a single contact element for the three contact states (i.e. gap, stick, slip) are derived from (4.44). At the element level the contact operator $\mathbf{F^e}$ derived from C^{AL} can be written

$$\mathbf{F^e} = \begin{bmatrix} \vec{f}^e_{cont} \\ \lambda^e_n \\ \lambda^e_t \end{bmatrix} = \begin{cases} \mathbf{F}^e_{gap} &= \begin{bmatrix} \vec{0} \\ -\lambda_n / r_n \\ -\lambda_t / r_t \end{bmatrix} \\ \mathbf{F}^e_{stick} &= \begin{bmatrix} g^e_n [\nabla_{\vec{u}}\ d^e_n(\vec{u})]^T + g^e_t [\nabla_{\vec{u}}\ \delta d^e_t(\vec{u})]^T \\ d^e_n \\ \delta d^e_t \end{bmatrix} \\ \mathbf{F}^e_{slip} &= \begin{bmatrix} g^e_n [\nabla_{\vec{u}}\ d^e_n(\vec{u})]^T - \text{sign}\ \mu g^e_n\ [\nabla_{\vec{u}}\ \delta d^e_t(\vec{u})]^T \\ d^e_n \\ -(1/r_t)(\lambda^e_t + \text{sign}\ \mu g^e_n) \end{bmatrix} \end{cases} \tag{4.45}$$

with

$$\text{sign} = \begin{cases} +1 & \text{if} \quad g_t^e > 0 \\ -1 & \text{if} \quad g_t^e < 0 \end{cases} \tag{4.46}$$

taking into account that frictional forces point in the opposite direction to the direction in which the relative movement occurs. This contact element contribution combined with the structural finite elements leads to a mixed formulation of the contact problem in the sense that both primal $\vec{u}$ and dual λ_n and λ_t quantities are independent variables.

The usual system of equations in a structural finite element analysis (4.35) has to be modified to take into account the contribution of the contact elements (the enforcement of the contact constraints). Let us consider the two–dimensional deformable body, B_2 described in a numerical model, discretized with n degrees of freedom. Adding a number c of contact elements, the system has to be extended to $n + 2c$ equations, since two dual variables λ_n and λ_t are added at each contact node.

$$\vec{f_{int}}(\vec{u}) - \vec{f_{ext}} - \vec{f_{cont}} = \vec{0} \tag{4.47}$$

where $\vec{f_{int}}(\vec{u}) = \{\{f_{int}^n\}, \{0^{2c}\}\}^T$, $\vec{f_{ext}} = \{\{f_{ext}^n\}, \{0^{2c}\}\}^T$ are the internal force vector and the vector of externally applied forces, both of increased dimension $n + 2c$. $\{0^{2c}\}$ represents the $2c$–dimensional zero vector. The $n+2c$ dimensional contact force vector is assembled from the contact operators $\mathbf{F^e}$ determined on the element level for the c number of contact elements

$$\vec{f_{cont}} = \bigcup_c \mathbf{F^e} \tag{4.48}$$

with $\bigcup_c$ representing the assembly operator of the contact element generalized forces.

4.2.3 Numerical solution of the contact problem - generalized Newton method

To solve numerically (4.47), the system of equations defining the saddle point necessary conditions (4.40) giving the solution to the general problem has to be linearized. Since operators for normal and tangential contact are piecewise linear, they are not differentiable everywhere. They possess a weak notion of derivative, called the generalized Jacobian [Alart & Curnier 1991; Pietrzak & Curnier 1999]. An extension of Newton's scheme to non–differentiable but continuous equations is

$$\vec{u}_n^{(i+1)} = \vec{u}_n^{(i)} - [\mathbf{K_s}_n^{(i)} + \mathbf{J_c}_n^{(i)}]^{-1}\{\vec{f_{int}} - \vec{f_{ext}} - \vec{f_{cont}}\}_n^{(i)} \quad \mathbf{J_c}_n^{(i)} \in \partial \vec{f_{cont}}(\vec{u}_n^{(i)}) \tag{4.49}$$

with subscripts n, and superscripts in parentheses (i) corresponding to the increment number and the iteration number of the *structural loop*, respectively. $\partial \vec{f_{cont}}(\vec{u}_n^{(i)})$ is a generalized Jaco-

bian of $\vec{f_{cont}}$ at $u^{(i)}_n$, assembled from the contact Jacobians of the contact elements.

$$\mathbf{J^e}_{\vec{u},\lambda_n,\lambda_t} = \begin{bmatrix} \nabla_{\vec{u},\vec{u}}\, C^{AL} & \nabla_{\vec{u},\lambda_n} C^{AL} & \nabla_{\vec{u},\lambda_t} C^{AL} \\ \nabla_{\lambda_n,\vec{u}}\, C^{AL} & \nabla_{\lambda_n,\lambda_n} C^{AL} & \nabla_{\lambda_n,\lambda_t} C^{AL} \\ \nabla_{\lambda_t,\vec{u}}\, C^{AL} & \nabla_{\lambda_t,\lambda_n} C^{AL} & \nabla_{\lambda_t,\lambda_t} C^{AL} \end{bmatrix} \tag{4.50}$$

The contact Jacobian of each contact element depends on the contact state of the particular contact element, according to

$$\begin{cases} \mathbf{J^e_{gap}} = \begin{bmatrix} 0 & 0 & 0 \\ 0 & -(1/r_n) & 0 \\ 0 & 0 & -(1/r_t) \end{bmatrix} \\ \mathbf{J^e_{stick}} = \begin{bmatrix} \mathbf{N_{stick}} + \mathbf{T_{stick}} & (\nabla_{\vec{u}}\, d_n)^T & (\nabla_{\vec{u}}\, \delta d_t)^T \\ \nabla_{\vec{u}}\, d_n & 0 & 0 \\ \nabla_{\vec{u}}\, \delta d_t & 0 & 0 \end{bmatrix} \\ \quad \text{with } \mathbf{N_{stick}} = r_n(\nabla_{\vec{u}}\, d_n)^T(\nabla_{\vec{u}}\, d_n) + g_n(\nabla^2_{\vec{u}}\, d_n) \\ \quad \text{and } \mathbf{T_{stick}} = r_t(\nabla_{\vec{u}}\, \delta d_t)^T(\nabla_{\vec{u}}\, \delta d_t) + g_t(\nabla^2_{\vec{u}}\, \delta d_t) \\ \mathbf{J^e_{slip}} = \begin{bmatrix} \mathbf{N_{slip}} + \mathbf{T_{slip}} & (\nabla_{\vec{u}}\, d_n)^T - \text{sign}\, \mu(\nabla_{\vec{u}}\, \delta d_t)^T & 0 \\ \nabla_{\vec{u}}\, d_n & 0 & 0 \\ -\text{sign}\, \mu \nabla_{\vec{u}}\, d_n & -\text{sign}\, \mu/r_t & -1/r_t \end{bmatrix} \\ \quad \text{with } \mathbf{N_{slip}} = r_n(\nabla_{\vec{u}}\, d_n)^T(\nabla_{\vec{u}}\, d_n) + g_n(\nabla^2_{\vec{u}}\, d_n) \\ \quad \text{and } \mathbf{T_{slip}} = -\text{sign}\, \mu r_n(\nabla_{\vec{u}}\, d_n)^T(\nabla_{\vec{u}}\, \delta d_t) + g_n(\nabla^2_{\vec{u}}\, \delta d_t) \end{cases} \tag{4.51}$$

Thereby the structural iteration loop, solved by a Newton–Raphson method transforms to a generalized Newton solution scheme when contact constraints are added. This formulation introduces a full decoupling of the contributions of contact constraints from other material (plasticity) and geometrical (finite deformation) nonlinearities, keeping a high degree of flexibility and the modular structure of the resulting finite element code.

4.2.4 Discussion

Aiming for the most efficient, most accurate and reliable algorithm, this augmented Lagrangian formulation for the Coulomb friction model was integrated in the numerical tool, bearing in mind to keep the necessary flexibility for further development. The chosen formulation introduces a full decoupling of the contributions of contact constraints from other material and geometrical nonlinearities related to the structural behavior. Adding other friction laws in the code is possible, and planned in a future work. Particularly, a relatively easy development promising valuable results is the use of a fixed value of the stick limit k, for micro-and nanoscale contacts. The 'classical' alternate treatment of the primal and dual variables results in a solution scheme

with multiple loops [Wriggers 2002]. Here the simultaneous treatment of both variables in the structural iteration loop is considered, referred to as a continuous multiplier update procedure [Alart & Curnier 1991], promising a more efficient computation. Even though the convergence of the generalized Newton method, applied to non–differentiable, but continuous equations was not established in a general manner, in practice the method was observed to be robust [Pietrzak & Curnier 1999].

In agreement with Alart & Curnier [1991]; Pietrzak & Curnier [1999] the unilateral contact problem was found to converge in practice for all considered cases. When friction is involved the rate of convergence of the global iteration loop is asymptotically quadratic in the state of stick, but cycling between stick and slip states can occur. The resulting decrease in the rate of convergence depends on the number of cycling contact elements and the coefficient of friction μ. These convergence issues can be decreased by the choice of the penalty parameters $0 < r < 2\ \lambda_{min}(\mathbf{K})$, with $\lambda_{min}(\mathbf{K})$ the smallest eigenvalue of the complete stiffness matrix of the system $\mathbf{K} = \mathbf{K_s} + \mathbf{J_c}$ as proposed in Pietrzak & Curnier [1999]. Slip state shows the slowest rate of convergence, stemming from the approximation that the contact forces and Jacobians are determined for a fixed value of stick limit in an iteration.

The contact element has been assessed using simple benchmarks on the element level (particularly for the frictional case), and more complex benchmarks considering coupled structural–contact problems [Hertz 1882; Simo & Laursen 1992]. The simulations were successful, the obtained numerical results and trends correspond to the analytical and numerical results given for the benchmark problems. With the above verifications we can conclude that the implementation of the contact element was successful.

4.3 General discussion on the model development

A finite deformation description with plasticity and computational contact mechanics features were incorporated within an existing nonlinear finite element code. A 2D elastic–plastic element set with 4–noded linear and 8–noded quadratic elements using plane strain, plane stress and axisymmetric assumptions in the corotational finite deformation frame was created together with a one–node contact element that ensures the exact satisfaction of both normal and tangential contact constraints on the element level. In the simulations, the contact elements correspond to the nodes of structural elements on the predetermined contact surface. A special care was taken for the choice of the numerical ingredients that are the most adapted, precise and efficient with an emphasis on keeping the maximum degree of flexibility of the resulting code.

The finite deformation framework uses the corotational formulation [Ponthot 1995, 2002], which has the advantage to be trivially incrementally objective and hence to be capable of handling arbitrary large rigid rotations. Contact constraints on the contact interface were taken

into account using the high–precision augmented Lagrangian method [Alart & Curnier 1991; Heegaard & Curnier 1995; Pietrzak & Curnier 1999] with a Newton type continuous multiplier update procedure.

All sources of nonlinearities (material - plasticity, geometric - finite deformation and contact) are fully decoupled in the resulting code keeping its high degree of modularity. In spite of all involved nonlinearities, the asymptotically quadratic rate of convergence of the computation is ensured when frictionless contact is considered. Including frictional contact constraints decreases the rate of convergence, however keeping it reasonable. This drawback is compensated to a certain extent by the relatively simple form of the contact formulation and the efficient one–step continuous multiplier update procedure. The convergence of the coupled structural–frictional contact problem was obtained for all considered cases, even though the general convergence of the generalized Newton method cannot be stated rigorously. Consequently the performance of the resulting numerical tool is considered satisfying.

Both the developed structural element set and the contact element were verified using benchmark problems and were shown to perform as expected. An example of the validation of the the programmed features through the problem of the extrusion of an aluminum cylinder with elastic–plastic material behavior with friction on the contact interface is presented in the Appendix A.2. Thereby the developed numerical tool satisfies the predefined requirements of accuracy, robustness, efficiency and flexibility and thus can be applied for modeling purposes. It can be currently applied to problems involving frictional or frictionless contact and the elastic–plastic finite deformation of one of the contacting bodies, with a behavior approximated by a power law hardening and using the von Mises yield criterion.

Chapter 5

Application to the nanoindentation interpretation and to the micro–manipulation

The aim of this chapter is to apply the continuum scale modeling tool described previously to material characterization by nanoindentation and to micromanipulation. The focus of the $m\mu n$ project, the work presented in this thesis is part of, was set on potentially biocompatible materials. The following sections address different aspects of nanoindentation, i.e. (i) a study of the influence of the variation in the indentation parameters on the dispersion in nanoindentation results, (ii) an investigation of the rate–dependent plastic behavior of pure nickel in nanoindentation, (iii) an evaluation of the dispersion in nanoindentation results due to the coupled effect of sample surface roughness and friction. Finally, the numerical tool is used for the estimation of the variation of contact adhesion due to the plastic flattening of surface asperities during micromanipulation.

In all research works in this thesis the studied material was pure nickel. This choice was made considering the potential bio–compatibility of small scale devices made of pure nickel or a coated nickel substrate; and in view of the large quantity of available experimental information and numerical studies on this material on the nanoscale, compared to titanium. The numerical tool using the finite element method, presented in Chapter 4 was used entirely, or partly in the majority of the research. The appropriate choice of the numerical ingredients, specially adapted for the considered applications (among other requirements of numerical–experimental consistency) allowed to conduct a coupled experimental–numerical study, and ensured the necessary confidence in the obtained numerical results and trends.

The following sections address different aspects of nanoindentation and micromanipulation, with a special attention given, so that all presented works allow to draw conclusions that are

important from both a modeling and an experimental point of view. For this purpose, in the research work considering the problem of nanoindentation via numerical modeling, the post–treatment tool (Section 2.2) was systematically applied to numerical results, with an emphasis to simulate the complete experimental measuring procedure ending in the evaluation of the elastic modulus of the tested material. This enforced the practical interest and applicability of the results of purely numerical studies.

Sections 5.1 to 5.4 relate to the problem of nanoindentation with a special attention to consistency between numerical simulations and experimental conditions. Section 5.1 can be considered as a preliminary study evaluating the influence of some indentation parameters on nanoindentation results of pure nickel, using a 'classical' rate–independent material model (i.e. the material behavior is independent from the rate of strain). The obtained trends pointed out the need for a rate–dependent material behavior for the sake of consistency with experimental results, as explained in Section 5.2. Numerical simulations dedicated to the rate–dependent behavior of pure nickel coupled to nanoindentation experiments conducted at various indentation depths and at different loading rates on pure nickel are studied in Section 5.2. The study parameters are carefully chosen to ensure a priori the closest possible conditions between the experiments and the numerical simulations. It is shown that a good agreement between the experimental and the numerical results can be obtained for both the load levels and the so–called indentation creep phase (displacement–time curves in the holding period) when taking into account a simple model with rate–dependent material behavior, and using a material parameter set that is in the acceptable domain for metals. Results of Section 5.1 and 5.2 show that a variation in the considered indentation parameters influences the dispersion in the elastic modulus identified by the post–treatment methods of nanoindentation. In the same line of thought, the objective of Section 5.3 is the numerical evaluation of the dispersion in shallow nanoindentation results due to the effects of sample surface roughness and friction on the contact interface. The simultaneous account for sample surface roughness and friction in the context of nanoindentation modeling was apparently not performed yet. It shows the important cumulative effect of the two considered contributing terms of surface effects in shallow indentation depth. The line of studies dedicated to nanoindentation ends with a short discussion on the performance of the considered post–treatment methods in the previously studied indentation configurations in Section 5.4. The attention is then shifted to the problem of micromanipulation in Section 5.5 aiming for a contribution to the understanding of the adhesive electrostatic effects and an estimation of their variation due to the plastic flattening of surface asperities in the gripper–manipulated object contact. A rate–independent material law for pure nickel is used in this study, because the strain rates are assumed to be small, as opposed to nanoindentation. The observed effect in the numerical model clearly gives a contribution to the difficulty to release objects when the squeezing manipulation force is removed.

5.1 Influence of testing conditions on conical nanoindentation of nickel with a rate–independent material model

The response to nanoindentation of a material is the convolution of a large number of contributions, which potentially cause variations in the resulting load–displacement curve. An important general issue of the nanoindentation procedure is the interpretation of the results and the identification of the sources of their potential variation.

The purpose of the numerical study presented in this section is the evaluation of the effects of indentation parameters and how they influence nanoindentation results of pure nickel in a simple numerical model with the particular choice of a rate–independent material model. Considering the identification of the key parameters of the general nanoindentation problem and the effects of various material parameters, the reader can consult [Zhang *et al.* 2008] and the review article of [Cheng & Cheng 2004]. A parametric study in realistic nanoindentation conditions (inspired from the coupled experimental–numerical study of Section 5.2) is conducted here, with the possibility of addressing each considered indentation parameter separately to evaluate their deconvoluted effect on both raw and post–treated nanoindentation results. The influences of the variation of the elastic (Section 5.1.1), and of the plastic material parameters (Section 5.1.2), and the most frequently considered geometric inaccuracy, the influence of a variation in the indenter tip radius R were investigated.

The numerical tool, presented in detail in Chapter 4, using the finite element method is used for this purpose. The considered indentation setup and numerical model correspond to the ones used in Section 5.2 for the simulation of conical nanoindentations in a pure nickel sample material. The modeling assumptions are:

- The conical diamond indenter, with $2\mu m$ nominal radius is modeled as a rigid body. The assumption of neglecting the indenter deformation can be a source of error for very hard sample materials where the overall deformation in the contact is taken partly by the sample and partly by the indenter [Jeong & Lee 2005]. In the case of the pure nickel sample however, the assumption that the indenter can be modeled as a rigid body holds because both its elastic modulus as well as its yield limit are orders of magnitude lower than those of diamond.

- The contact between the indenter and the sample surface is assumed to be frictionless. Since the focus here is set on the influence of the variation of material parameters and contact geometry, for the sake of deconvolution friction is neglected. Frictional effects are treated in detail in Section 5.3.

- The contact surface of the sample is perfectly flat and smooth, the surface roughness is neglected. The effects of surface roughness are treated in Section 5.3.

- The sample material is assumed to be homogeneous and to obey isotropic hardening with a Ludwik's evolution law, recalled here as

$$\sigma_v = \sigma_0 + K\kappa^n$$

where σ_v is the current yield stress, determined here using the von Mises yield function, σ_0 stands for the elastic limit in uniaxial tension. κ is the scalar valued hardening parameter depending on the strain history, K and n are curve fitting parameters, called hardening coefficient, and hardening exponent, respectively, chosen such as to fit Ludwik's law to experimental stress–strain data of pure polycrystalline nickel extracted from uniaxial tension measurements [Kovács & Vörös 1996]. The following parameter set was calculated by this fit: E = 207GPa, ν = 0.31, σ_0 = 59MPa, K = 1165MPa, and n = 0.56.
The error made by the power law approximation is reasonably small, the obtained hardening curve fits the experimentally measured behavior well. The obtained elastic and plastic parameter set has been compared to other works [ASM 1990; Hollang *et al.* 2006; Nayer 1997; Ross 1992; Torre *et al.* 2002] and are found to be in good agreement. It is recognized that the grain size has an impact on the hardening behavior of nickel [Ebrahimi *et al.* 1999; Li & Weng 2007]. However, even for grain sizes of $10\mu m$ that are much smaller than the experimentally observed value, the power law model seems to fit the data well. Note that the initial yield strength σ_0 of pure nickel with nano–sized grains [Hollang *et al.* 2006], and that of nickel alloys can be many times higher.
The material model is rate–independent, which means that no viscous effects are included, the material response is independent of the strain rate, being a common assumption in numerical simulations of nanoindentation in metallic materials [Antunes *et al.* 2006; Bressan *et al.* 2005; Pelletier 2006], while it will be challenged in Section 5.2.

- Considering the axial symmetry of the indentation problem, stemming from the above mentioned assumptions it is described in the numerical model using 8 noded axisymmetric elastic–plastic elements (in the corotational finite deformation framework).

The finite element mesh is refined in the contact zone (Fig.5.1), and consists of more than 14000 degrees of freedom to be able to reproduce with high precision the stress and plastic strain evolution during the quasi–static simulation. The geometrical size of the mesh in all cases is chosen sufficiently large such that a homogeneous stress distribution at the boundary of the model is obtained for the imposed maximum indenter penetration of $430nm$. The side nodes of the mesh are constrained in the horizontal direction. The deformable body is prescribed to move upward to come into contact with the rigid indenter which has a fixed position in space.
The two experimentally used post–treatment methods presented in Section 2.2 (and in Appendix A.1) were applied to the numerical results to evaluate the influence of the variation of the considered material and contact parameters (E, ν, σ_0, K, n and R) on the post–treated elastic modulus

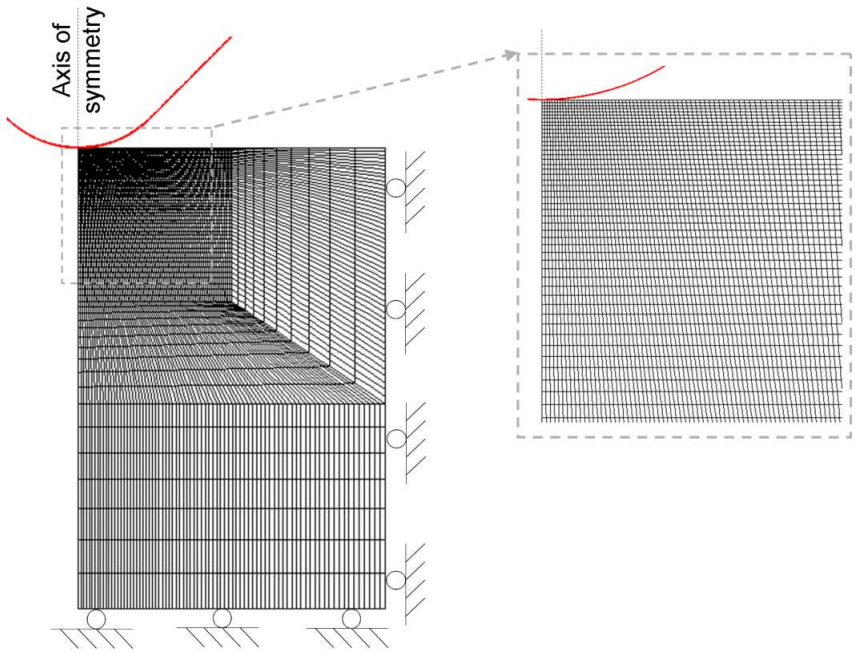

Figure 5.1: Finite element mesh used in the parametric study with zoom on the refined region near the indenter tip. The continuous curve represents the conical indenter with $2\mu m$ nominal tip radius modeled as a rigid body.

[Ni *et al.* 2004; Oliver & Pharr 1992]. The combination of these material parameters resulted in the numerical indentations, described in Tab.5.1. It is recalled, that material parameters obtained from nanoindentation data are relative values compared to a predefined value associated to the indentation of a material with known properties, measured in the calibration step of the experiments [Baker 1997; Fischer-Cripps 2006]. There may appear thus naturally a difference between the input material parameters and the ones identified as output by the post–treatment procedures. Different post–treatment methods may result in different values of the output elastic modulus for the same load–displacement curve. It is emphasized that their relative variation with respect to the reference value of the chosen method holds the only meaningful information. This variation is defined by:

$$\Delta E^{method} = \frac{E^{method}_{out} - E^{method}_{ref}}{E^{method}_{ref}} = \frac{E^{method}_{out}}{E^{method}_{ref}} - 1 \tag{5.1}$$

with E^{method}_{out} the Young's modulus identified from the load–displacement curves by the considered post–treatment method. The elastic modulus obtained for the indentation with the reference indentation parameter set ($R = 2000nm$, E = 207GPa, ν = 0.31, σ_0 = 59MPa, K = 1165MPa, n = 0.56) gives the reference value for each of the considered post–treatment methods:

$$E^{OP}_{ref} = 261.5\text{MPa} \qquad \text{and} \qquad E^{Ni}_{ref} = 318.2\text{MPa}.$$

Note, that since pure nickel has a low yield limit the indentation response was observed to be essentially plastic from the early stages of indentation. This low value of the yield limit

has particular implications on the influence of different material parameters on nanoindentation results. First the elastic material properties are considered.

$E_{input}\,[GPa]$	ν	$\sigma_0\,[MPa]$	$K\,[MPa]$	n	$\Delta E_{out}^{OP}\,[\%]$	$\Delta E_{out}^{Ni}\,[\%]$
103.5	0.31	59	1165	0.56	-50	-50
414	0.31	59	1165	0.56	+102	+98
207	**0.25**	59	1165	0.56	-3	-4
207	**0.35**	59	1165	0.56	+3	+3
207	0.31	**29.5**	1165	0.56	-3	-2
207	0.31	**118**	1165	0.56	+3	+1
207	0.31	59	**582.5**	0.56	+4	0
207	0.31	59	**2330**	0.56	-3	-1
207	0.31	59	1165	**0.28**	+5	+2
207	0.31	59	1165	**1**	-2	-3

Table 5.1: Nanoindentations with varying elastic and plastic input material parameters (highlighted items in the upper and in the lower half of the table, respectively). ΔE_{out}^{OP} and ΔE_{out}^{Ni} represent the variation of the post–treated Young's modulus (the decimals are rounded off) with respect to reference values of the post–treatment method of Oliver and Pharr and of Ni et al., respectively.

5.1.1 Elastic material properties

In this section the influence of the elastic material properties, E and ν on nanoindentation results is studied. Two additional values, representing a variation of 50% in the input elastic modulus of the sample were considered (Tab.5.1). The variation in the Poisson's ratio ν of the material is rarely considered in numerical studies. Furthermore, there is no efficient experimental procedure to measure the value and the potential variation of ν on the nanoscale. Here two additional values of the Poisson's ratio were studied 0.25 and 0.35. The raw output data in nanoindentation experiments, the resulting load–displacement curves are analyzed first. Pure nickel, being a low yield limit material shows only a low sensitivity of the load levels to elastic material properties, since the material response to indentation is plastic from nearly the beginning of the loading period.

However, considering the post–treated elastic modulus, the variation in the input elastic modulus gives the most pronounced effect, independently of the post–treatment method considered (Tab.5.1). The relative variation in the output Young's modulus is observed to be practically equal to the relative variation in the input Young's modulus, when it is the only varied parame-

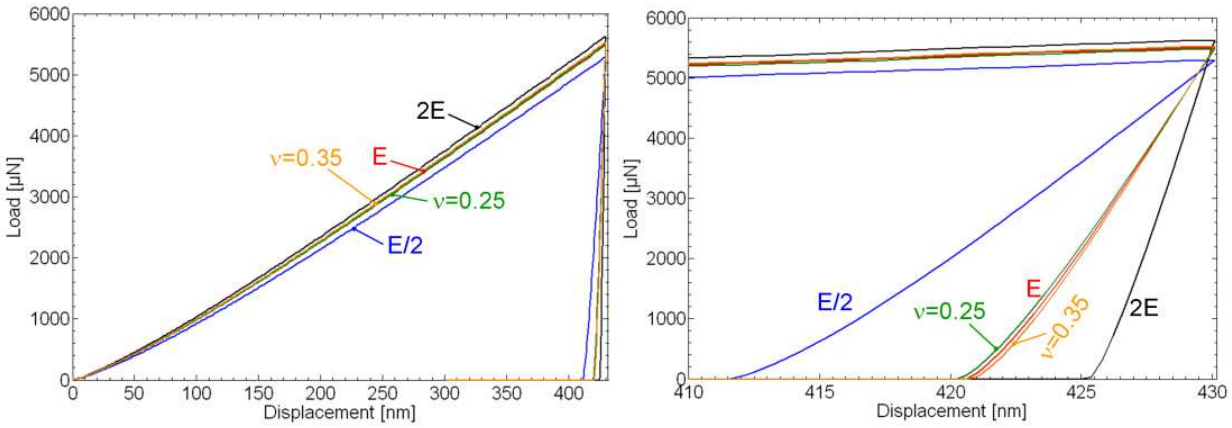

Figure 5.2: Influence of the elastic properties E and ν on the load–displacement curves. Right: zoom on the unloading period.

ter, independently of the post–treatment method.

$$\gamma^{AB}_{input} = \frac{E^A_{input}}{E^B_{input}} = \gamma^{AB}_{output} = \frac{E^A_{output}}{E^B_{output}} \tag{5.2}$$

This result was expected, it shows that the post–treatment methods considered here satisfy their primary goal. The slope of the unloading curve is highly sensible to the input elastic modulus (Fig.5.2), which explains the good performance of the Oliver and Pharr post–treatment method, mainly based on the unloading period of the load–displacement curve. Note that this is observed on both the continuum scale as well as on the atomic scale (Section 3.1).
Ideal post–treatment methods would be sensible only to the variation in the material property at which they are aimed. The main issue of nanoindentation experiments is the potentially simultaneous variation of a large number of experimental conditions and material parameters, other than the Young's modulus of the sample, to which post–treatment methods potentially show a spurious sensibility. The Poisson's ratio of the material is recognized to be a parameter of small importance since only a small variation in the post–treated elastic modulus (around 3% for pure nickel for both considered post–treatment methods) was found, as reported in Tab.5.1. All effects related to the elastic behavior of the material are most pronounced in the unloading period. Conversely, the plastic material properties, treated in the following are prone to have the largest effect on the load levels considering that the indentation response is practically plastic from the beginning.

5.1.2 Plastic material properties

A variation in the plastic material properties may influence the material response to nanoindentation as well. Here the sensitivity of the nanoindentation results to: the initial yield limit σ_0; the hardening coefficient K; and the hardening exponent n of the hardening law is examined.

Initial yield limit σ_0

The initial yield limit or yield strength σ_0 defines the boundary between the elastic and the plastic domain of the material for the initial yielding. An increase in the yield limit shifts higher the curve of the stress–strain relationship of the model material on the vertical axis in Fig.5.3. Naturally nanoindentation is highly sensitive to this parameter, as it influences the balance of the elastic and the plastic material response to indentation. In this parametric study two values of σ_0 were chosen to demonstrate its effects.

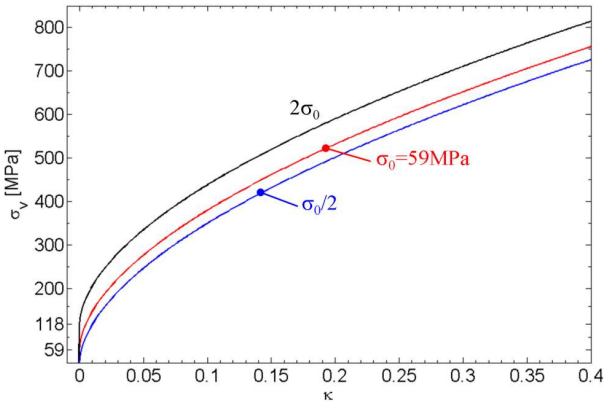

Figure 5.3: Effect of the variation of σ_0 on the material law. The von Mises equivalent stress σ_v is plotted as a function of the cumulated plastic strain measure κ.

As expected, the increase in σ_0 results in the increase in the indentation load levels, since the elastic response of the material to deformation is significantly stiffer than the plastic one. The highest yield limit considered here $\sigma_0 = 118$MPa still remains a relatively low value for nickel–based metallic materials used in common engineering applications. The yield limit of nickel alloys and of pure nickel with nano–sized grains can be considerably higher [ASM 1990; Ebrahimi *et al.* 1999; Hollang *et al.* 2006].

A relatively moderate increase in the initial yield limit of the model material results in a significant increase in the indentation load levels, without however a significant effect on the post–treated Young's modulus. Indeed, the unloading curve, the primary information for the post–treatment method of Oliver and Pharr, is rather insensitive to the variation of the initial yield limit of the material. Considering that the unloading of the indenter–sample contact is generally assumed elastic this trend is not surprising.

In the case of the post–treatment method proposed by Ni et al., taking into account the complete load–displacement curve (both loading and unloading periods), a larger dispersion in the identified Young's modulus could be expected. It has to be recalled however, that this more advanced post–treatment method was specifically designed to decrease the scattering in the post–treated Young's modulus related to variations in the plastic material parameters, based on the results of

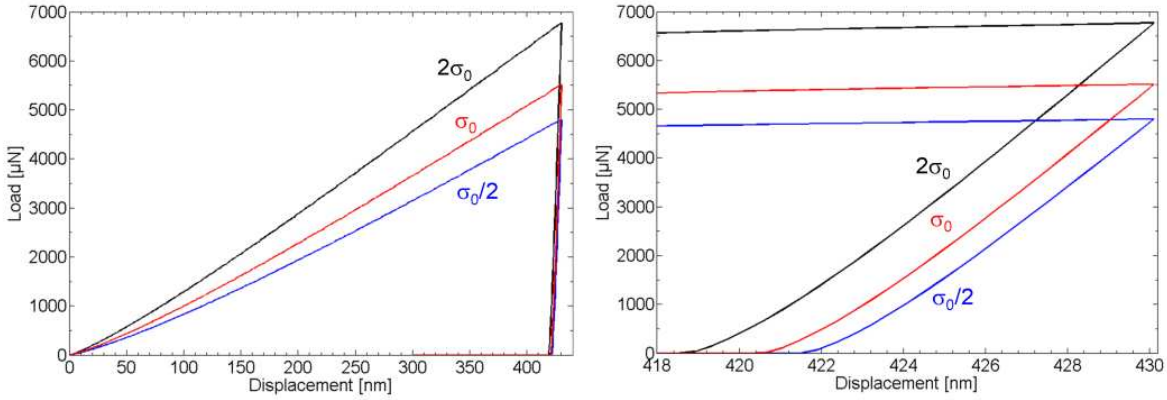

Figure 5.4: Influence of the initial yield limit σ_0 on the load–displacement curves. Right: zoom on the unloading period.

finite element simulations with the same assumptions on the material behavior. This is the reason why the dispersion related to the variation in the initial yield limit of the material remains rather low for both post–treatment methods considered here (Tab.5.1).

Hardening coefficient K

To clarify the meaning of the hardening coefficient K, the example of the frequently adopted linear hardening model is the most adequate. In such a model, generally chosen for its simplicity, since it can be defined using only two material parameters, σ_0 and K (a linear hardening assumption implies $n = 1$), K defines the slope of the linear hardening law.

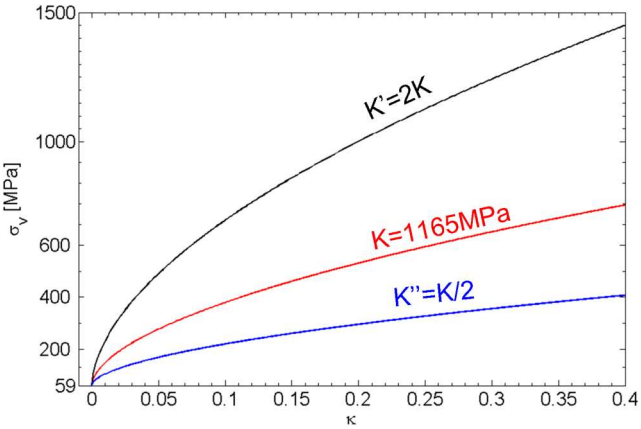

Figure 5.5: Effect of the variation of the hardening coefficient K on the material law. The von Mises equivalent stress σ_v is plotted as a function of the cumulated plastic strain measure κ.

In this parametric study a power–law describes the isotropic hardening of the model material, the effect of varying K on the stress–strain law is less straightforward to see, as sketched in

Fig.5.5. It has to be emphasized that the highest value of $K = 2330$MPa alters significantly the hardening behavior of the model material. Indeed, the area under the stress–strain curve in the plastic deformation domain is related to the energy dissipation due to plastic deformation in the material. In the large deformation domain this area is roughly doubled with respect to the material with the initial parameter set. An increase in the indentation load levels, shown in Fig.5.6, due to the increasing material hardening as a result of a higher value of K can be foreseen. However, much like the initial yield strength, and for the same reasons, i.e. the unloading tangent is relatively insensitive to the value of K (Fig.5.6); and because the post–treatment method of Ni et al. corrects variations of the output Young's modulus due to plastic material parameters, a variation in the hardening coefficient does not induce considerable variations in the post–treated Young's modulus (Tab.5.1), this independently of the post–treatment method considered.

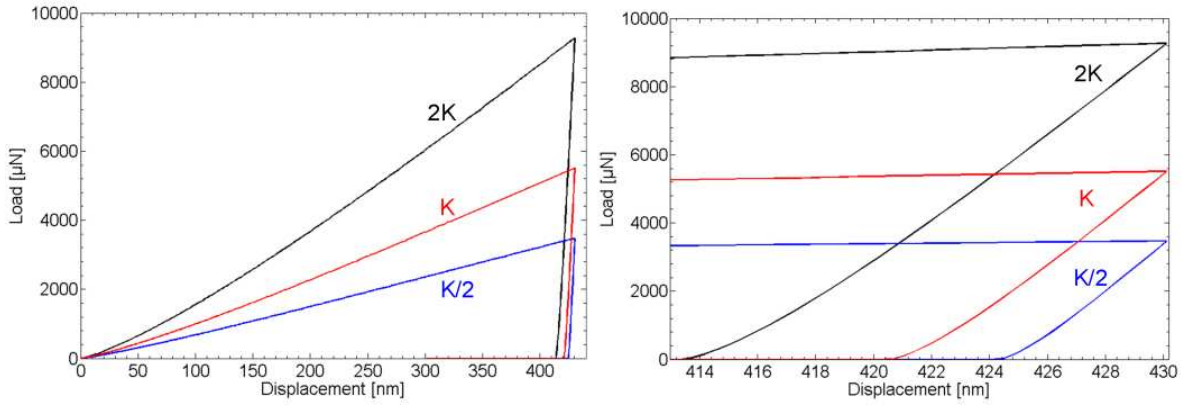

Figure 5.6: Influence of the initial yield limit K on the load–displacement curves. Right: zoom on the unloading period.

Hardening exponent n

The hardening exponent, n defines the shape of the hardening law, when all other parameters are kept the same (Fig.5.7). Consequently it plays also an important role in the essentially plastic indentation response. Moreover in Kim *et al.* [2006] the value of n is related to predictions on the pile–up and sink–in behavior of the material. This aspect was not considered here, since the contact depth was calculated by the standard assumptions of the Oliver–Pharr method, as in the actual experimental procedure. The focus is set on its influence on the load–displacement curves and on the post–treated Young's modulus.

Much like the hardening coefficient K, the hardening exponent plays a determinant role in the hardening law of the model material (Fig.5.7). The lowest value of $n = 0.28$ describes a more drastic hardening, compared to the material with the initial parameter set. A significant influence of n on the load levels can be predicted. The unloading curve is rather insensitive to a

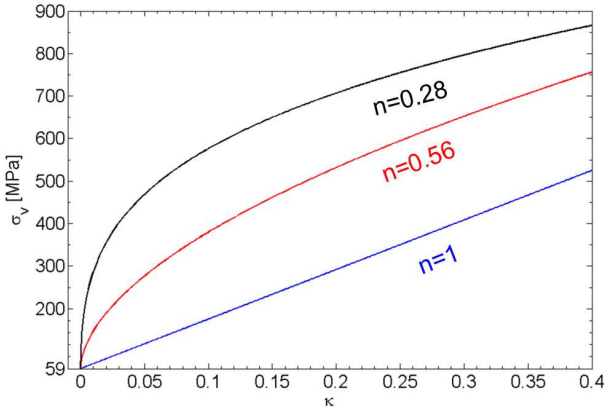

Figure 5.7: Effect of the variation of the hardening exponent n on the material law ($n \leq 1$ is assumed). The von Mises equivalent stress σ_v is plotted as a function of the cumulated plastic strain measure κ.

variation in the value of n (Fig.5.8). As all plastic material properties, the variation of n has only a relatively small influence on the post–treated Young's modulus (Tab.5.1), for the reasons exposed earlier.

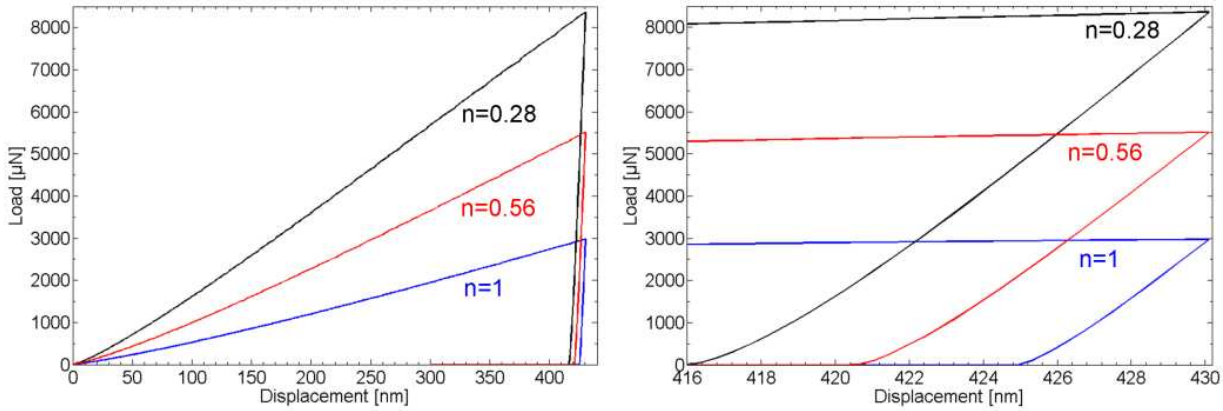

Figure 5.8: Influence of the initial yield limit n on the load–displacement curves. Right: zoom on the unloading period.

5.1.3 Tip radius effect

The most frequently considered geometrical inaccuracy in nanoindentation is a variation in the tip geometry [Kim *et al.* 2005; Lu & Bogy 1995; Wang *et al.* 2007b; Warren & Guo 2006; Youn & Kang 2005]. In the experimental work related to this thesis conical indenters were used exclusively for the sake of consistency between the experimental conditions and the numerical model having an axial symmetry. Consequently the focus is set on the evaluation of the effect of a variation in the radius of curvature of the considered conical tip having a spherical cap of

$2\mu m$ radius. A variation of 10% in the value of the nominal radius of curvature was considered, resulting in two additional simulations with $1800nm$ and $2200nm$ tip radius.

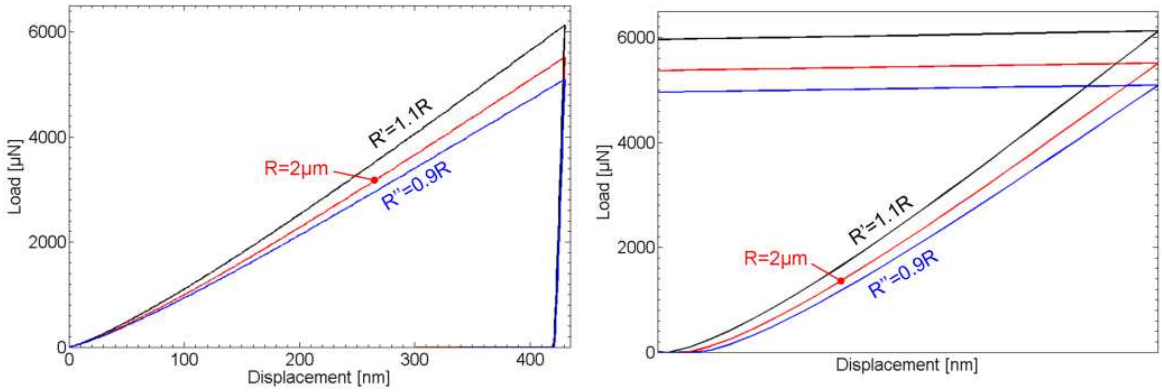

Figure 5.9: Influence of a 10% variation in the tip radius of the indenter R on the load–displacement curves. Right: zoom on the unloading period.

An increase in the tip radius, due to tip deformation or potential tip wear, results in the deformation of a larger volume of sample material at a given imposed indenter penetration. Consequently the applied force necessary to reach the same indentation depth with a blunter tip is higher, as shown in Fig.5.9. For the same reasons, an indenter tip with a smaller tip radius, due to fabrication inaccuracies penetrates deeper at the same load level. Indentations with blunter tips at a given load level induce less severe loading conditions than sharp tips, which cause more easily plastic deformation. The indentation load–displacement curve, keeping all material parameters constant is shown to be very sensitive to variations in the tip radius. Since it alters the size of the deformed volume and the volume fraction of domains with elastic and plastic response under the indenter it has naturally an influence on the unloading contact stiffness. The variation in the post–treated elastic modulus of the sample as a consequence of tip radius change is reported in Table 5.2. Two cases are distinguished, corresponding to two experimental situations:

- The indenter geometry had varied (irreversible deformation, tip wear) since the last calibration, and this variation has not been detected. The area function determined in the last calibration, corresponding to a tip radius of $2\mu m$ is considered in the post–treatment procedure.

- The indenter geometry is approximated in a calibration step first before starting the experiments, the actual indenter geometry is taken into account in the post–treatment method (marked with a star superscript in Tab 5.2)

The numerical results considering the variation of the tip radius emphasize the necessity of frequent repetition of the tip calibration step preceding the actual nanoindentation measures, since

it reduces significantly the dispersion related to the non–perfect tip geometry and its potential variation (Tab.5.2).

$R[nm]$	$\Delta E_{out}^{OP}\,[\%]$	$\Delta E_{out}^{OP*}\,[\%]$	$\Delta E_{out}^{Ni}\,[\%]$	$\Delta E_{out}^{Ni*}\,[\%]$
1800	-6	-1*	-7	-1*
2200	+8	+1*	+8	+2*

Table 5.2: Influence of the indenter tip radius on the post–treated Young's modulus is represented by ΔE_{out}^{OP} and ΔE_{out}^{Ni} (the decimals are rounded off), calculated with respect to reference indentations ($R = 2000nm$) of the post–treatment method of Oliver and Pharr and of Ni et al., respectively. *Values with a star superscript are computed with the actual tip radius in the post–treatment procedures, making the assumption that the variation in the tip radius was measured in a calibration step.

5.1.4 Concluding remarks

The results of the parametric study, considering the variation of the indentation parameters in a rate–independent material model with isotropic hardening allow to draw the following salient conclusions.

- The elastic material parameters have a small influence on the load levels of indentations considering the pure nickel low yield limit material.

- The variation in the input Young's modulus has the far most significant influence on the post–treated Young's modulus issued from the numerical load–displacement curves, independently of the considered post–treatment method. The relative variation in the input Young's modulus γ_{input} results in a practically same relative variation in the post–treated Young's modulus $\gamma_{output} = \gamma_{input}$ for both post–treatment methods considered here.

- The variation of the post–treated Young's modulus due to variations in the material properties, other than the input Young's modulus is considered as dispersion in the results. These material parameters, considered separately were shown to have only a slight influence on the value of the post–treated Young's modulus (under 6% of relative variation). It has to be emphasized, that the results of this study cannot however lead to a conclusion about the effect of their simultaneous variation, which might induce more important variations.

- The indentation load levels are sensitive to a variation in the plastic material parameters σ_0, K, and n. The results of Section 5.1.2 imply that the same load–displacement curves

can be reproduced by different combinations of the plastic material parameters, i.e. the same load levels at the considered indentation depth can be reached [Cheng & Cheng 2004]. It can be shown that by a purely numerical manipulation (but lacking a physically sound motivation) by increasing the initial yield limit to four times its value $\sigma_0^{'} = 4 \times \sigma_0$ or by doubling the value of the hardening coefficient $K^{'} = 2 \times K$ the same load levels, corresponding to the experimental indentation data are reached. Special care has thus to be taken if the identification of plastic material properties from complete load–displacement indentation data is aimed for as in [Bouzakis & Michailidis 2004; Bucaille *et al.* 2004, 2003; Cao & Lu 2004; Zhao *et al.* 2006], since various plastic parameter sets can reproduce the same load–displacement curves.

- Geometrical issues related to the actual tip geometry and its variation influence both the load levels at a given indentation depth significantly and the unloading slope (thereby the contact stiffness, used in the post–treatment methods). Consequently this results in a variation in the post–treated elastic modulus of the sample. The dispersion this generates can be reduced by a systematic verification of the actual indenter geometry in calibrations steps preceding the nanoindentation measure.

5.2 Rate–dependent behavior of pure nickel in conical nanoindentation

This contribution investigates the rate–dependent plastic behavior of pure nickel in nanoindentation through a coupled experimental–numerical study based on the consistency of experimental and numerical conditions. The rate–dependent plastic behavior of non–metallic materials [He & Swain 2007], of metals [Goodall & Clyne 2006] and of some thin films [Fang *et al.* 2007] was already observed during indentation. The rate–dependent behavior of aluminum films was documented in Wang *et al.* [2007a]. The creep of titanium during nanoindentation was presented recently in [He & Swain 2007]. For the present study, the most interesting references to experimental work describe the rate–dependent behavior of nickel with micron–sized grains [Chudoba & Richter 2001; Goodall & Clyne 2006] and nano–sized grains [Mirshams & Pothapragada 2006; Yin *et al.* 2001]. Based on published experimental results, mainly for polymer materials, rate–dependent material laws have been used in numerical models of indentation. In Kermouche *et al.* [2007] the viscoplastic behavior of a sample material without work hardening and a conical indenter with a perfectly sharp idealized geometry is considered. Gomez and Basaran analyzed the effect of viscoplasticity on the nanoindentation of Pb/Sn solder alloys in a numerical study under small strain and small displacement assumptions with an idealized sharp conical indenter geometry [Gomez & Basaran 2006], in which a good agreement between numerical and experimental results was found.

In the present work, the correlation between the response of a numerical model and the experimental nanoindentation results of pure nickel is investigated, with a specific attention for the need to account for the rate–dependent plastic behavior of nickel. Considering the complexity of the nanoindentation experiment involving many convoluted effects, special care has been taken to ensure the best possible decoupling of the effects related to the viscoplastic behavior of nickel from other potential spurious contributions. This special effort to ensure the best consistency between modeling assumptions and experiments allowed the use of a relatively simple numerical model defined by a limited number of parameters; yet still performing well at the task of describing qualitatively the studied features of the experiment. Keeping the number of assumptions in the numerical model relatively low, with a physically sound basis, and the consistency between the experimental conditions and the assumptions of the numerical simulations, constitutes the main argument supporting the incorporation of the rate–dependent plastic behavior of nickel.

This section is based on P. Berke, E. Tam, M.-P. Delplancke, T.J. Massart, 'Study of the rate–dependent behavior of pure nickel in conical nanoindentation through numerical simulation coupled to experiments' accepted for publication in Mechanics of Materials (DOI: 10.1016/j.mechmat.2008.09.003)

The experimental procedure and its results, performed by E. Tam, are presented first, in Section 5.2.1. The description of the numerical model and the comparison of the experimental and numerical results are treated in Section 5.2.2, followed by a discussion on the need for including rate–dependency in the material model and its implication on the determination of the elastic modulus obtained from nanoindentation data. Finally the conclusions of this work are presented.

5.2.1 Experimental procedure and results

Choice of the cono–spherical indenter tip

A conical indenter tip with a nominal curvature radius of $2\mu m$ was chosen for the nanoindentation experiments. This choice is made to avoid modeling indenter shapes without an axial symmetry, as well as to decrease as much as possible any effect of large strain gradients in the sample in the region near the tip.

Non–axisymmetric indenters, like the popular Berkovich and the Vickers geometry are described in numerical simulations using either a 3D model [Antunes *et al.* 2006; Warren & Guo 2006] resulting in a computationally demanding calculation, or alternatively with an equivalent axisymmetric geometry based on the projected area to depth ratio equivalence [Lichinchi *et al.* 1998]. The significant influence of the size effects related to high strain gradients generated at the edges of non–axisymmetric indenters on the global variables of indentation (load level, indenter displacement) was not confirmed in a coupled numerical–experimental study. However, numerical research works using higher order strain gradient plasticity formulations were performed in Al-Rub *et al.* [2007]; Al-Rub [2007]; Tho *et al.* [2006] to account for the depth related size effect obtained in shallow indentation. A reasonable agreement was found between experimental data and the results of numerical simulations making simplifying assumptions on the indenter geometry. Here, the choice of a conical indenter was made to avoid using any assumption on the subsurface stress and strain behavior in the numerical model with respect to the experiments.

Sample preparation procedure

Samples were cut from $3mm$ thick pure nickel plates. The surface preparation aimed at minimizing surface roughness, to approximate an ideally smooth surface. The sample surfaces were polished first and then etched to remove the work–hardened surface layer. Finally, the samples were annealed to relieve any residual stresses and to eliminate possible anisotropy due to the fabrication and preparation procedures.

The average grain size of the nickel sample after surface preparation (around $100\mu m$) turned out

to be much larger than the imprint size (of a few micrometers in diameter). As a consequence, all indentations have been performed in the middle of the grains with arbitrary orientation so as to avoid any grain boundary effects and to have an average, grain orientation–independent material response. Experimental results are thus considered to be an average response of pure nickel for conical indentation with a cono–spherical tip of $2\mu m$ radius.

Machine calibration and monitoring of the experimental conditions

The compulsory tests of machine calibration, the verification of the extent of the thermal drift and the thermal drift correction were performed before each set of indentations to ensure the accuracy and good reproducibility of the measurements.
The load–displacement curve of a nanoindentation experiment especially in the small indentation depth regime may be affected by the surface roughness and more generally by the contact geometry of the indenter–sample surface contact [Berke & Massart 2006; Bouzakis *et al.* 2001; Wang *et al.* 2007b; Warren & Guo 2006; Yu *et al.* 2004]. The measurement of the surface roughness as well as the verification of the actual indenter geometry are therefore of crucial importance. The surface scan showed that the arithmetic mean roughness value (Ra) of the undeformed surfaces was in the order of $1nm$, and it was confirmed that the conical tip was proper and that the curvature radius was approximately $2\mu m$.

Experimental test conditions

The experimental test conditions address the problem of rate–dependent material behavior of pure nickel. It is recalled that the experiments followed a predefined loading sequence in which the applied force was specified as a function of time. Generally, three parts of the loading sequence are distinguished: the loading period where the applied force is increased up to a peak value, the holding period where for a prescribed amount of time this peak load is maintained, and finally the unloading period where the applied force is decreased to zero.
During the holding period, the indenter displacement may be different from zero. This phenomenon is called indentation creep in nanoindentation experiments [Fischer-Cripps 2004], and is clearly related to a rate–dependent feature of the materials response [Goodall & Clyne 2006]. The length of this displacement plateau observed during the holding period together with the load levels obtained in the load–displacement curves are the focus of interest of this study.
In order to investigate the rate–dependence of pure nickel a first set of indentations with a maximum load of $2000\mu N$ was conducted at different loading rates ($1000\mu N/s$, $400\mu N/s$ and $100\mu N/s$, with a holding time of $10s$) and different holding times ($10s$ and $50s$ with a loading rate of $400\mu N/s$). A further increase in the holding time was not considered because of the

increasing influence of thermal drift for long holding periods.
In order to observe the potential influence of the size effects in nanoindentation, two new sets of experiments were defined: one resulting in shallow indents and one in the large indentation depth regime (with maximum load levels of $1000\mu N$ and $9000\mu N$, respectively). In these experiments, the loading, holding and unloading times ($5s$–$10s$–$5s$, respectively) have been kept constant resulting in two additional loading rates ($200\mu N/s$ and $1800\mu N/s$, respectively). It should be recalled that the indentation size effects are recognized to be stronger in the small indentation depth regime and weaken gradually with increasingly deep indentations [Tho *et al.* 2006]. If any, their influence is thus expected to be larger in nanoindentations with $1000\mu N$ and $2000\mu N$ peak loads (corresponding to a $54nm$ and a $100nm$ indentation depth) than on the $9000\mu N$ indentations (with $430nm$ penetration). However, a significant variation of the size effects with increasing indentation depths in the considered range could not be clearly confirmed by the obtained experimental results.
The combination of these test conditions therefore resulted in six sets of nanoindentation experiments.

Discussion

The experimental results of the six sets of nanoindentations with 6 to 8 indentations per set are shown in Fig.5.10 to Fig.5.13. Note that for the case of shallow indentations the pop–in phenomenon is quite frequently observed, which increases significantly the scattering in the experimental results. The scattering is the smallest for the deepest indentations, as expected. An important observation is that the variation of the loading rate in the studied range (from $100\mu N/s$ to $1000\mu N/s$ for the experiments with $2000\mu N$ peak load) does not seem to have an influence on the loading curves (Fig.5.12). More generally, the loading period of all load–displacement curves obtained at different maximum loads and at different loading rates (up to $1800\mu N/s$) are found to coincide at small and moderate indentation depths (Fig.5.10). At first this could suggest that the deformation process involved during nanoindentation is rate–independent as in Schwaiger *et al.* [2003], at least in the range investigated in the present study. However a displacement plateau always appears in the load–displacement curves (Fig.5.10) during the holding period, which on the contrary suggests a rate–dependent behavior of the pure nickel material. This holding displacement plateau can be further analyzed, based on Fig.5.11, 5.12 and 5.13 which depict the obtained indenter displacement as a function of time during the holding period, as performed for instance in Chudoba & Richter [2001] for different values of the the holding period length, of the loading rate, and of the peak load, respectively. Fig.5.11 allows the identification of the effect of the holding period length, with other parameters fixed (peak load kept at $2000\mu N$ with $400\mu N/s$ loading rate). The average indenter displacement

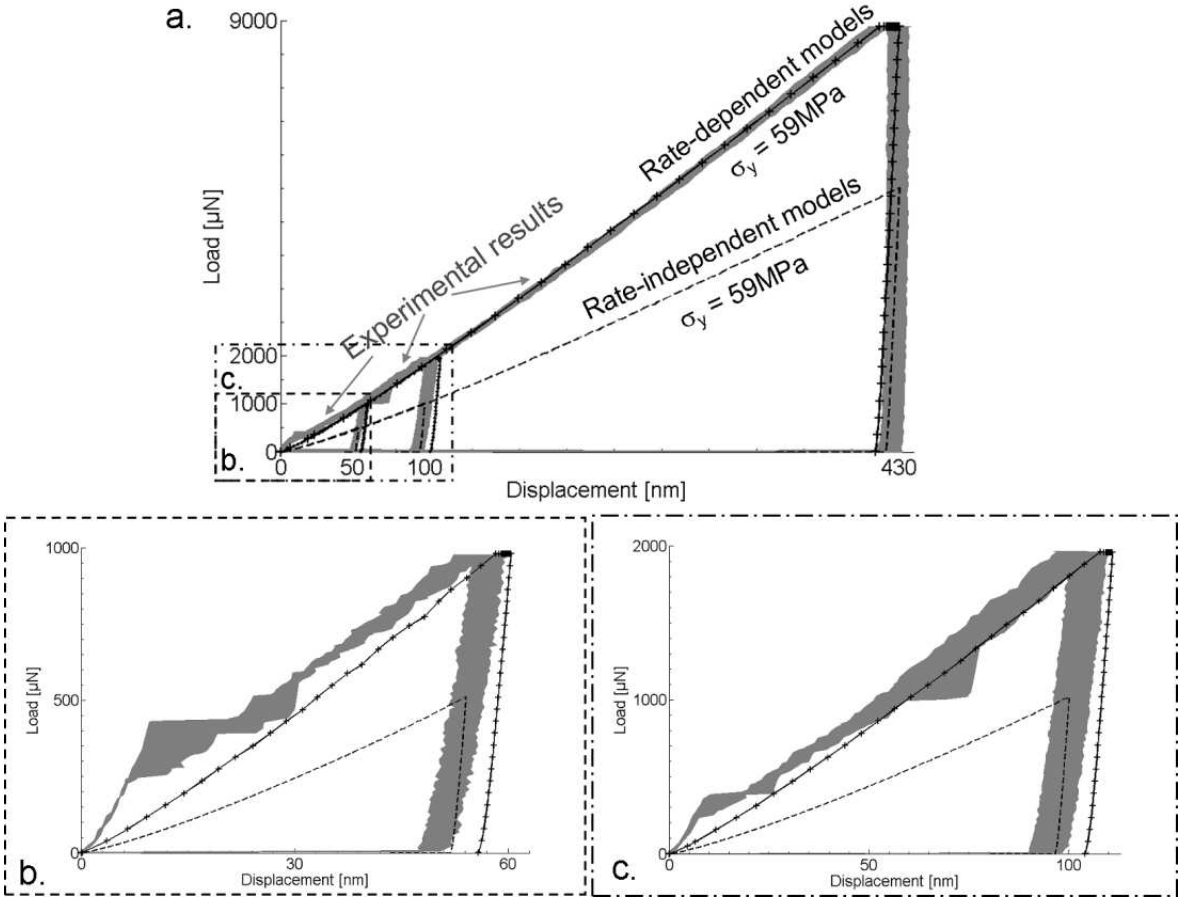

Figure 5.10: Experimental and numerical results for three series of indentations at different loading rates and different indentation depths. Solid curves represent the results of a numerical rate–dependent material model, dashed curves represent the results of the numerical rate–independent material model of Section 5.1.

during the holding period is increased by a factor of approximately 1.7 when the holding period is increased by a factor of 5 in the measurements. The loading rate also has an influence on the holding plateau length, as can be seen from Fig.5.12. For a fixed peak load of $2000\mu N$ and holding time of $10s$, an increase in the loading rate from $100\mu N/s$ to $400\mu N/s$ and to $1000\mu N/s$ results in an increase of the plateau length by a factor of approximately 1.2 and 2 respectively. Finally, the effect of the peak load can be observed in Fig.5.13 which respectively match $1000\mu N$, $2000\mu N$, and $9000\mu N$ peak load, keeping the holding time $10s$. The holding plateau length increases by a factor of approximately 1.8 and 6 when the peak load is increased from $1000\mu N$ to $2000\mu N$ and $9000\mu N$, respectively. Note that even though the loading rate effect is convoluted in this increase, the peak load effect remains clearly recognizable since the observed variation is much more important than when varying the loading rate alone.

Therefore, considering the presence of the displacement plateau, another interpretation of the observations is that the material has a viscoplastic response for which the rate effect has already saturated at the applied strain rates. The saturation of the viscoplastic effects implies that there

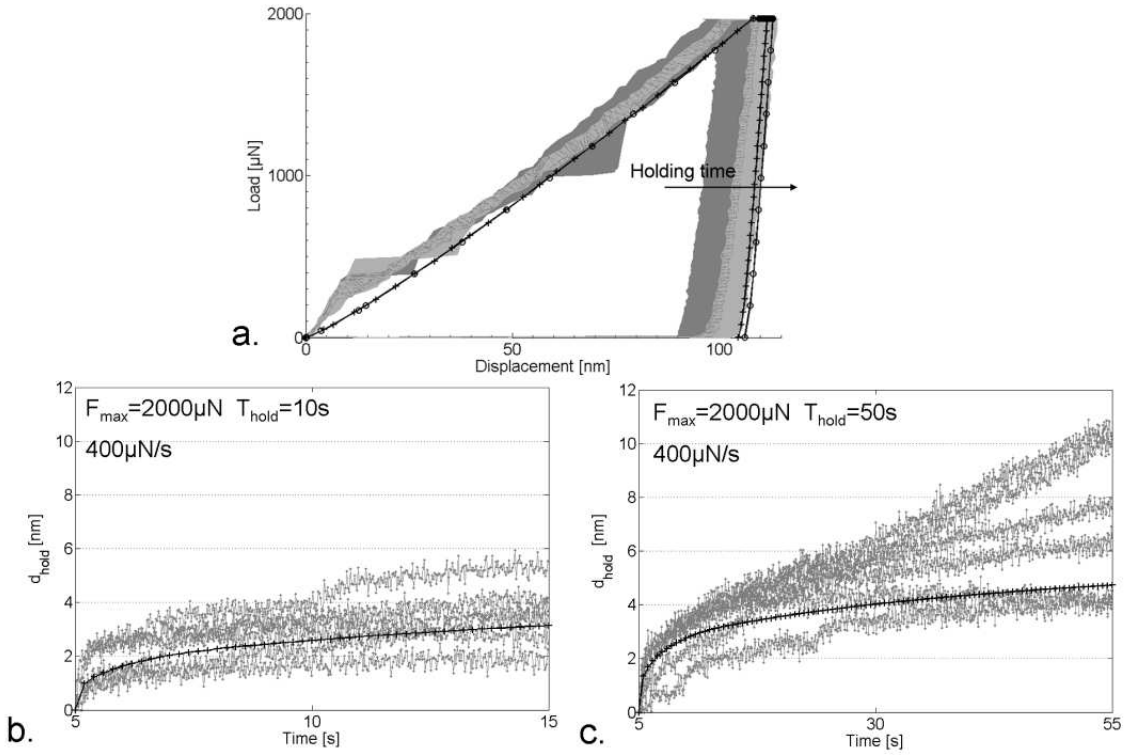

Figure 5.11: Influence of the holding time: experimental and numerical results for nanoindentation at 2000μN peak load. a. Load–displacement curves; the dark grey patch and the curves with plus marks represent the experimental and numerical results, respectively for $T_{hold} = 10s$; the light grey patch and the curves with plus marks represent the experimental and numerical results, respectively for $T_{hold} = 50s$ b. to c. Experimental (grey) and numerical (black plus marks) displacement–time curves during holding period.

is no significant increase in the stresses in the sample (thus no gain in the reaction force) with a further increase in the strain rate. This is why the rate–dependent effects on the global response are potentially masked during the loading period. In other words, significant viscoplastic deformations are only observed experimentally during the holding period, where the strain rates are relatively small.

5.2.2 Numerical analysis of rate–dependency

The motivation of the numerical simulations is to confirm this interpretation of experiments by investigating whether the rate–dependent behavior of pure nickel indentation can be reproduced using a simple viscoplastic law.

Modeling a nanoindentation experiment is a task requiring to take into account complex physical phenomena such as contact evolution and the elastic–plastic deformation in a finite deformation setting, since the globally small deformation of the sample volume leads to locally large deformations and rigid rotations. The first requirement is needed to simulate the experimental,

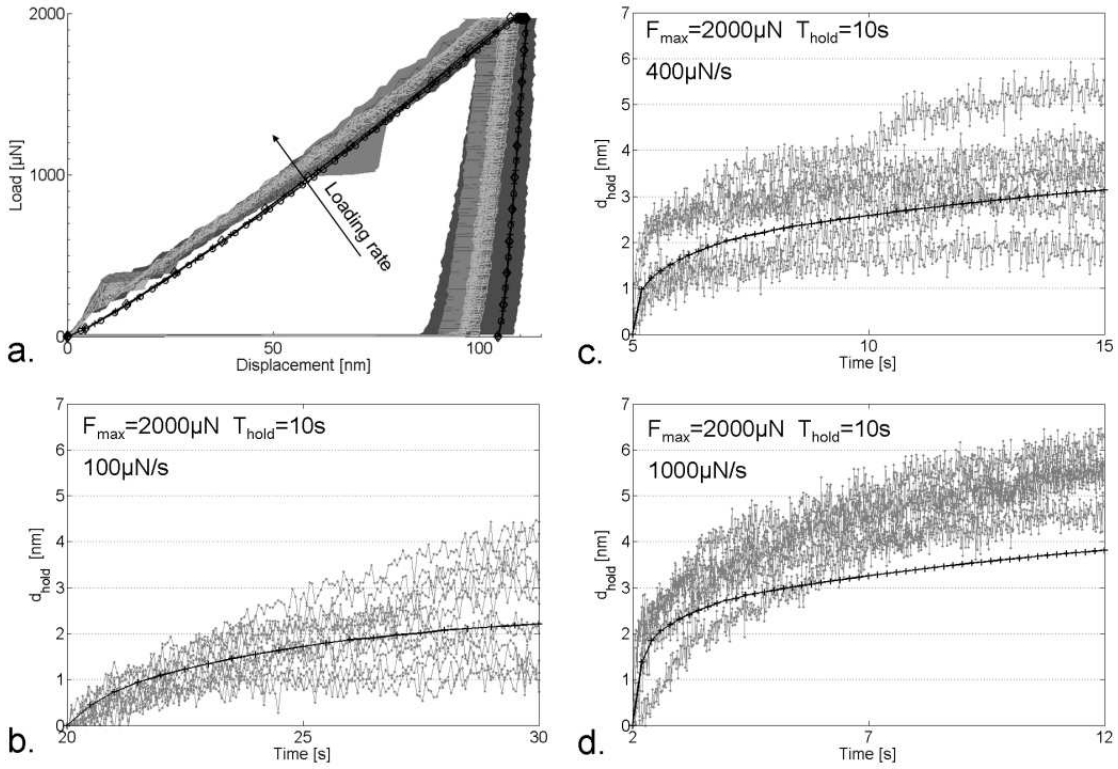

Figure 5.12: Influence of the loading rate: experimental and numerical results for the indentation experiment at constant 2000μN peak load with 10s holding time. a. Load–displacement curves; the dark grey patch and the curves with circle marks represent the experimental and numerical results, respectively at 100$\mu N/s$; the light grey patch and the curves with diamond marks represent the experimental and numerical results, respectively at 1000$\mu N/s$; the patch with the intermediate shade and the curves with plus marks represent the experimental and numerical results, respectively at 400$\mu N/s$ b. to d. Experimental (grey) and numerical (black plus marks) displacement–time curves during holding period.

yet idealized evolving boundary conditions and the latter to account for the correct behavior of the material in the model.

General assumptions of the model

The diamond indenter is modeled as a conical rigid body (since both the elastic modulus and the yield limit of pure nickel are orders of magnitude lower than those of diamond) having a spherical cap with a 2μm radius of curvature as verified by microscopy.
With all of the precautions taken in the experiments to avoid the presence of work–hardened layers, residual stresses, and potential anisotropy due to sample preparation, it is assumed that the response obtained is the nanoindentation of pure nickel only. In the numerical model a homogeneous sample material with isotropic hardening is assumed. This assumption is generally

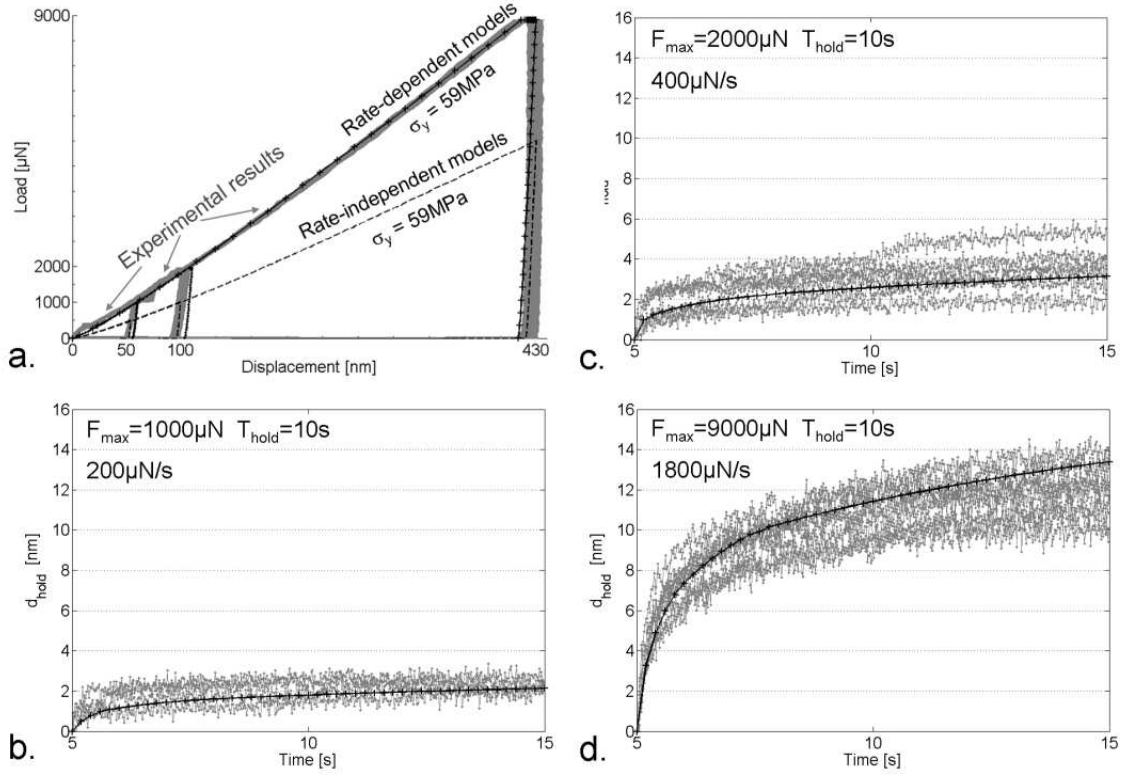

Figure 5.13: Influence of the holding force (convoluted to the loading rate effect): experimental (grey) and numerical (black solid curves) results for nanoindentation at 1000μN, 2000μN and 9000μN peak load. a. Load–displacement curves b. to d. Experimental (grey) and numerical (black plus marks) displacement–time curves during holding period.

used for FCC metals, which have a large number of slip planes. As in Section 5.1 using a rate–independent material model, an isotropic hardening behavior for pure nickel obeying Ludwik's law, was considered in this work

$$\sigma_v = \sigma_0 + K\kappa^n$$

where σ_v [MPa] stands for the current yield limit, σ_0 [MPa] the initial yield stress, K [MPa] the hardening coefficient, κ the cumulative plastic strain measure and n the hardening exponent. The simulations with the rate–dependent material model were conducted using the general purpose SAMCEF finite element package (the contact conditions are treated using Lagrange multipliers). Due to the limitations of this code the viscoplastic material model can only be combined with a linear hardening behavior, i.e. $n = 1$). Considering the shape of the experimental stress–strain curve (approximated in the rate–independent material model of Section 5.1 by the parameter set E = 207GPa, ν = 0.31, σ_0 = 59MPa, K = 1165MPa, and n = 0.56), the chosen material parameter set σ_0 = 59MPa, K = 2230MPa of this linear approximation imposed by SAMCEF needs justification. The initial yield strength σ_0, playing a major role in the indentation response of the material, was kept the same as the measured value of 59MPa for the sake of consistency. Consequently, the hardening coefficient K is the only free material parameter

to be adjusted in the linear fit of the material law obtained from [Kovács & Vörös 1996]. This coefficient K defines the tangent of the linear hardening law in Fig.5.14. It was chosen such as to find a suitable approximation to the experimental stress–strain curve taking into account the range of the magnitude of the cumulative viscoplastic deformation measure during indentation. By this approximation the imposed linear hardening is not a severely penalizing assumption of the rate–dependent material model.

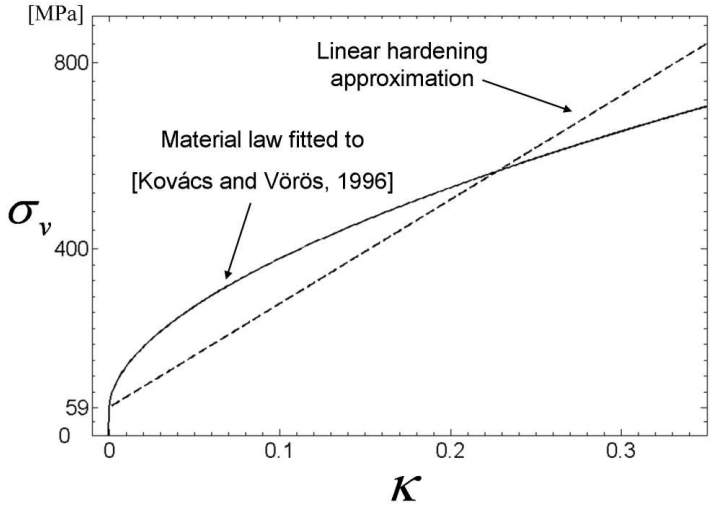

Figure 5.14: Material law for pure nickel: the von Mises equivalent stress σ_v is plotted as a function of the cumulated plastic strain measure κ. Solid line: power law fit to uniaxial tension measurements [Kovács & Vörös 1996] used in the rate–independent material model; Dashed line: linear hardening approximation used in the rate–dependent material model.

Note that high strain gradients promoted by nanoindentation could also be responsible for a potential difference between the experimental results and the numerical predictions knowing that the numerical model used here does not take into account the dependence of hardening on the strain gradients.

The experimental indentation geometry was chosen so as to exhibit an axial symmetry. The sample is therefore described in the numerical model using 8–noded axisymmetric elastic–plastic elements using a finite deformation theory. The contact surface of the sample is assumed perfectly flat and smooth. Three meshes were created for the three different indentation depths (corresponding to three different peak loads of $1000\mu N$, $2000\mu N$ and $9000\mu N$) observed in the experiments: $54nm$, $100nm$ and $430nm$. Each consisted of more than 14000 degrees of freedom to be able to reproduce with high precision the stress and plastic strain evolution during the simulation. The geometrical size of the mesh in all cases was chosen sufficiently large such that a homogeneous stress distribution at the boundary of the model was obtained. The side nodes of the mesh were constrained in the horizontal direction and the displacement of the bottom nodes was prescribed in the vertical direction. Friction on the contact interface was neglected

in the numerical model to keep the focus on the rate–dependent material effects.

$Numerical\,ind.$	$F_{max}\,[\mu N]$	$Load.rate\,[\mu N/s]$	$T_{hold}\,[s]$
1	1000	200	10
2	2000	100	10
3	2000	400	10
4	2000	400	50
5	2000	1000	10
6	9000	1800	10
*7	1000	400	10
*8	9000	400	10
*9	9000	900	10

Table 5.3: Studied sets of nanoindentation configurations in the simulations. Cases marked with a star were added to study the effect of the viscoplastic material parameters.

Rate–dependent constitutive model

A rate–dependent material behavior was incorporated in a numerical model to attempt to reproduce the experimental results with a special attention to both the loading and holding period. The applied loading conditions respect the experimental loading sequence (i.e. the duration of each period).

It is emphasized that all of the experimental curves for all different loading rates are superimposed in the small indentation depth regime. This suggests the use of a viscoplastic model with a saturation behavior at high strain rates (i.e. for which a further increase in the strain rate does not influence the flow properties anymore). Taking this into consideration, a Perzyna–type viscoplastic behavior [Ponthot 1995] was chosen to incorporate the rate–dependent behavior of pure nickel.

The relation between the variation of stresses and strains is written as:

$$\hat{\boldsymbol{\sigma}} = \mathbf{H}_e\,(\mathbf{D} - \mathbf{D}_{vp}) \tag{5.3}$$

with $\hat{\boldsymbol{\sigma}}$ an objective rate of stress, $\mathbf{D}$ the total and $\mathbf{D}_{vp}$ the viscoplastic strain rate, and $\mathbf{H}_e$ the elastic stiffness tensor. The yield function that defines the viscoplastic domain for the Perzyna model is given by:

$$f = \overline{\sigma} - \sigma_v - \sigma_c(\mathbf{D}_{vp})^{1/n_{vp}} = 0 \tag{5.4}$$

with $\overline{\sigma}$ [MPa] the calculated equivalent von Mises stress, σ_c [MPa.s$^{1/n_{vp}}$] the comparative stress or viscosity parameter, and n_{vp} the viscosity exponent. σ_v [MPa] is the current yield stress determined from the linear hardening law.

The viscoplastic parameters of the Perzyna–type model were determined in an iterative procedure adjusting both σ_c and n_{vp} simultaneously such that the numerical curve fits both the loading and holding periods of the 430nm deep experimental nanoindentation data (reaching 9000μN peak load), as reported in Fig.5.10 and Fig.5.13. An iterative parameter search was necessary because of the coupled and nonlinear effect of both viscoplastic parameters on the response of the material in the numerical indentation: σ_c has a major influence on the load levels of indentation and changes slightly the displacement–time curves, while n_{vp} has an important effect on indentation creep (displacement–time curves in the holding period) and influences the load levels as well. The purpose of choosing the deepest indentation for the identification of the viscoplastic material parameter set was the relative decrease of the material size effects appearing in shallow indentation depths, resulting in the best possible decoupling of the rate–dependent effects. The uniqueness of the proposed viscoplastic parameter set $\sigma_c = 265\text{MPa.s}^{1/n_{vp}}$ and $n_{vp} = 65$ can however not be stated, and a number of sets in the vicinity of the proposed pair may also perform well. However, the obtained parameter set seems a fair approximation in view of the good agreement of the numerical and experimental results for both the load levels (Fig.5.10) and the indentation creep (Fig.5.11, 5.12, and 5.13). The values of σ_c and n_{vp} are in the acceptable domain for metals [Ponthot 1995]. A low value of n_{vp} would correspond to a highly viscous material whereas the rather high value of the viscosity exponent determined for pure nickel shows a material behavior with less pronounced rate–dependent effects, which might mask rate–dependent effects of the behavior in some cases [Schwaiger *et al.* 2003].

5.2.3 Numerical results and discussion

Comparison with experimentally obtained load levels and indentation creep

Two aspects of the viscoplastic behavior nickel were investigated, which have equally important implications on the results of the nanoindentation procedure: (i) the load levels in nanoindentation, represented in Fig.5.10; and (ii) indentation creep, represented in the displacement–time curves plotted during the holding period (Fig.5.11, 5.12, and 5.13).

The loading period of the numerical load–displacement curves matches the experimental data for all six experiments with the chosen parameter set. The effect of saturation (observed experimentally) is reproduced by the Perzyna law: all curves with loading rates ranging from 100$\mu N/s$ to 1800$\mu N/s$ (Fig.5.10 and Fig.5.12) are nearly superimposed in the shallow and moderate indentation depth domain. The slightly stiffer response in the experimental loading curves at the small and moderate indentation depths (Fig.5.10) might be attributed to size effects at shallow indentation depths, and to a potential local variation in the actual indenter tip radius due to fabrication inaccuracy. Indeed, an important issue in modeling the shallow nanoindentation experiment is related to the high strain gradients in the sample material resulting from

the penetration, resulting in a size–dependent behavior at this scale [Al-Rub *et al.* 2007; Al-Rub 2007; Frick *et al.* 2008; Zhao *et al.* 2003]. Due to its size and symmetry, the selected tip reduces strain and strain gradient effects at the indentation depths considered [Mirshams & Pothapragada 2006]. If in a rigorous sense these effects cannot be neglected, their influence is larger at small indentation depths and can be felt even for the case of spherical indentation according to [Qu *et al.* 2006]. However, these size effects were not taken into account in the present numerical model since the focus is on rate–dependent material behavior. The stiffness of the experimental curves in the displacement domain up to $430nm$ was found to vary only slightly (Fig.5.10); whereas at large indentation depths the influence of size effects should be relatively smaller. Therefore no significant variation in the size effects with increasing indentation depth could be deduced from experimental results, which seems to show that neglecting size effects was indeed a sensible assumption.

The computed displacement–time curves of the numerical model are inside the envelope defined by the experimental results, except for Fig.5.12 where the numerical prediction of the final plateau length for $1000\mu N/s$ loading rate is slightly under the experimentally measured values. The length of the plateau formed during the holding period in all six series of experiments is well approximated by the numerical simulations (Fig.5.11 to 5.13) using the same parameter set that describes the gain in hardening due to rate–dependent effects in nickel. The simple viscoplastic model reproduces the experimental trends well, when the experimental parameters are varied similar to the testing procedure. The computed indenter displacement during the holding period is 1.5 times larger, compared to a factor of roughly 1.7 in the experimental average values, when the holding period is increased by a factor of 5 (Fig.5.11). When the loading rate is increased from $100\mu N/s$ to $400\mu N/s$ and to $1000\mu N/s$ for a fixed peak load of $2000\mu N$ and holding time of $10s$ (Fig.5.12), the numerical model predicts an increase of the holding plateau length by a factor of approximately 1.4 and 1.7, respectively. These values approximate reasonably well the increase in the experimental average value of 1.2 and 2, respectively. Similar to the experimental trends, the holding plateau length is found to be the most sensitive in the numerical model to variations in the peak load. When the peak load is increased from $1000\mu N$, to $2000\mu N$, and to $9000\mu N$, keeping the holding time at $10s$ (Fig.5.13) the computed holding plateau length increases by a factor of approximately 1.5 and 6.3, respectively, compared to an increase in the experimental average values of 1.8 and 6. The peak load effect remains clearly recognizable from both the experimental and the numerical data since the observed variation is much more important than when varying the loading rate alone. The length of the holding plateau is found to be directly proportional to the maximum applied load, which is in agreement with the experimental trend. The magnitude of the applied peak load necessary to reach a given indentation depth is related to the stresses in the sample material. Since the viscoplastic strain rate is directly proportional to the magnitude of the overstress in the used viscoplastic model,

the result is a high sensitivity of the holding plateau length (being related to the time integral of the viscoplastic strain rate) on the value of the peak load.
This fair agreement between the predictions of the numerical model and the experimental results was reached, resulting from fitting the parameters of the viscoplastic material model to experimental data in a single testing condition corresponding to the deepest considered nanoindentation. Even though the simplest viscoplastic model was used, it was shown to perform rather well in all other considered testing conditions as well, concerning both indentation load levels, displacement–time curves plotted in the holding period and holding plateau length. The results suggest that the rate–dependent behavior of pure nickel has to be taken into account to remain consistent with the physics encountered during nanoindentation experiments [Chudoba & Richter 2001]. The reason for this is merely the nature of the experiment itself; causing large local deformations in the sample material near the indenter tip at high strain rates, as opposed to classical applications in which the strain rates are much lower.

On the need of rate–dependency

Even though it is obvious that a rate–independent material model cannot reproduce the holding plateau considering the rate–dependent nature of this feature of the measurement, it was pointed out, based on experimental results, that rate–dependent effects are potentially masked during the loading period. As a result, rate–independent material models were often used in nanoindentation simulations without taking the creep phenomenon into account [Antunes *et al.* 2006; Bressan *et al.* 2005; Pelletier 2006]. Following this idea simulations with a rate–independent material behavior using the same spatial discretization were conducted (corresponding to the study in Section 5.1) to evaluate how well the load levels during the loading period using an experimentally measured constitutive law for pure nickel agree with the experimental ones.
It can be seen from Fig.5.10 that the load levels obtained in a simulation using an experimentally measured constitutive law for pure nickel, with a rate–independent material model (presented in Section 5.1) are lower by 40% to 50% than the experimental ones at large indentation depth ($430nm$) and at small ($54nm$) to medium ($100nm$) indentation depths, respectively. The reason for this large difference here is clearly the lack of the description of a key physical feature of the experiment in the numerical model (i.e. the rate dependent effect). As shown previously, the slope of the load–displacement curve in the loading period depends on the combination of the plastic parameters (keeping the Young's modulus of the material constant), thus the same loading curve can be obtained with different rate–insensitive plastic parameter sets; and the load levels of the numerical loading curve can be increased to fit the experimental data in various ways, by simply adjusting the material parameters.
The initial yield limit and the hardening behavior have the largest influence on the loading

period of the load–displacement curves in nanoindentation of nickel using a rate–independent material model (Section 5.1). Therefore, an obvious (but poorly physically motivated) choice would consist in varying the corresponding material parameters so as to fit the numerical results. A fairly good agreement between the loading period of the experimental and the numerical curves could be reached with such a numerical manipulation by increasing the initial yield stress to four times its initial value ($\sigma_0^{'}$ = $4 \times \sigma_0 = 236$MPa) or by doubling the hardening coefficient ($K^{'}$ = $2 \times K$). However, the low yield limit $\sigma_0 = 59$MPa is a physically–based value for the studied pure nickel material [ASM 1990; Hollang *et al.* 2006; Kovács & Vörös 1996]. Moreover, increasing K to the double of its initial value would change the hardening behavior of the modeled material significantly. As a consequence, an agreement between experimental and numerical results using a rate–independent material model can only be reached by a drastic increase in the considered plastic material parameters, a manipulation which is clearly difficult to motivate from a physical point of view.

Note that changing the frictionless contact assumption to even very large values of the experimental friction coefficient on the contact interface would not explain the observed difference between the experimental and the numerical data with the rate–independent material model.

In light of this, it is apparent that the viscoplastic effects presented above should be considered, as it allows to account for both the load levels and the holding plateau present in the experiments, and avoids non physically motivated numerical manipulations.

On experimental post–processing procedures

It has to be noted that the viscoplastic behavior alone potentially influences the post–treated Young's modulus, even though it has a considerably smaller effect than the variation of elastic material properties.

The detection of the point of initial unloading and the numerical curve fitting to the unloading curve used in the post–treatment procedures influence the post–treated elastic modulus (as explained in Appendix A.1). This can be referred to as 'nanoindentation dispersion related to the post–treatment procedure', and can be felt particularly in the case of long holding periods. With a special attention to decrease these effects, the variation of the post–treated Young's modulus issued from the results of the numerical model with rate–dependent material behavior for the six sets of indentations considered in the experiments was $\Delta E_{out}^{OP} = ^{+7\%}_{-8\%}$ for the Oliver–Pharr post-treatment method. Note that this remains in the order of magnitude of the scattering observed experimentally. The post–treatment method of Ni et al. performed better with $\Delta E_{out}^{Ni} = ^{+4\%}_{-2\%}$.

Finally, the implications of these findings on advanced post–treatment methods for the identification of plastic material parameters should be emphasized. In post–treatment methods using the complete load–displacement curves (such as the energy based methods), the potentially

rate–dependent plastic behavior of the tested material is included in a natural way in the experiment. Therefore, care should be taken in the choice of the material model to avoid identifying overestimated rate–independent material parameters.

5.2.4 Conclusions

It has been shown through coupled experimental–numerical investigation that the rate–dependent behavior of pure nickel may be important in conical nanoindentation. An experimental program has been set up to study the material response of pure nickel with a specific selection of experimental conditions to decouple rate–dependent effects from other potential spurious contributions, and to investigate the agreement between a numerical model using the finite element method and the experimental data.

A simple material model taking into account rate–dependent effects in plasticity was chosen in the simulations reproducing the experimental nanoindentation program. The material parameters governing the viscoplastic behavior were obtained by fitting the numerical load–displacement curve to the experimental results at the deepest indentation, and are situated in a physically acceptable domain for metallic materials. The rate–dependent numerical model for nickel seems to describe the experiments rather well, based on the good agreement between both the loading and holding periods of the numerical and the experimental load–displacement curves, and indentation creep obtained for all considered experimental data. The experimentally observed trends concerning the variation of the testing conditions are reproduced in the numerical simulations for all considered cases.

5.3 Coupled friction and roughness surface effects in shallow spherical nanoindentation

When nanoindentation is used for thin film characterization, the penetration of the indenter is usually limited to shallow indents to avoid the spurious effect of the substrate, a regime in which the surface effects, related to the contact behavior are the most pronounced. Therefore, the variation in the obtained mechanical properties due to surface effects may wrongly be attributed to the thin film mechanical behavior. A numerical study is conducted with the intention to investigate how frictional and surface roughness effects interact in a numerical model of nanoindentation of pure nickel and their influence on the output data. In this numerical study two major mechanical contributions to surface effects are distinguished and investigated: *frictional* and *sample surface roughness* effects.

In the majority of the experiments only an estimation of the frictional behavior is postulated and its influence on the output data is unknown. Moreover friction cannot be easily varied experimentally in dry friction conditions keeping the same contacting material pair. This motivates numerical modeling efforts having the objective to evaluate the influence of friction and its variation on indentation problems. Numerical studies having this objective are mostly considering *a perfectly smooth sample surface* and result in varying conclusions. Friction is recognized to have the largest influence when using sharp indenters [Bucaille *et al.* 2004, 2003; Qin *et al.* 2007] in indentation depths comparable to or larger than the curvature radius of the indenter [Cao *et al.* 2007]. The importance of frictional effects also depends on the choice of the sample material model, for example the indentation of an elastic–perfectly plastic material is rather insensitive to friction when considering high friction [Wang *et al.* 2007b]. This has lead to some dispersion in the conclusions of works considering the global effect of friction on the indentation results: some conclude that the global indentation behavior is unaffected by friction on the contact interface [Antunes *et al.* 2006; Carlsson *et al.* 2000; Wang *et al.* 2007b], while other findings show that friction can be a significant source of scattering [Cao *et al.* 2007; Habbab *et al.* 2006; Mata & Alcalà 2004].

As a second surface effect, a special attention in the literature is given to issues related to indentations on rough surfaces, both with experimental and numerical approaches, since roughness is recognized to give a significant contribution to the indentation response. A large number of experimental works evaluated its influence on the nanoindentation results [Kumar *et al.* 2006; Qasmi & Delobelle 2006; Wai *et al.* 2004], sometimes with the aim to propose post–treatment corrections allowing to decrease the dispersion in the output data due to surface roughness

This section is based on P. Berke, F.E. Houdaigui, T.J. Massart, 'Coupled friction and roughness surface effects in shallow spherical nanoindentation' submitted for publication

[de Souza *et al.* 2005, 2006]. The influence of the surface roughness is found to be the most important in small and moderate indentation depths, comparable to the height of the surface asperities. This indentation–depth–dependent effect is sometimes interpreted as an indentation–size–effect depending on the contact geometry [Gao & Fan 2002; Kim *et al.* 2007; Qiu *et al.* 2003; Zhang *et al.* 2004].
In numerical approaches, this effect is observed to be significant even for low average roughness (with respect to the considered nanoscale), assuming that the energy balance of indentation is constituted from two contributions: the elastic–plastic deformation of the surface asperities and of the bulk material [Kim *et al.* 2007], without taking frictional effects into account. Numerical studies incorporating the roughness of the contact surfaces in indentation problems use almost exclusively *frictionless* models. The rough sample surface topology is described in two–dimensions [Bobji & Biswas 1999] or three–dimensions [Bobji *et al.* 1999; Zahouani & Sidoroff 2001] with fractal–based [Bora *et al.* 2005; Tao *et al.* 2001] and polynomial [Tao *et al.* 2001] modeling assumptions. The reader can consult [Persson 2006] for a more detailed review on rough surface contact mechanics. Even with a frictionless contact assumption, a good *qualitative* (if not quantitative) agreement can be found with experimental trends in the increase of the dispersion in the results due to surface roughness [Walter *et al.* 2007].

The demanding computational effort of simulating numerically the problem of multiple frictionless contacts with a rough surface, coupled to the extrapolation of the conclusions of some of the previous works, showing a negligible frictional effect in indentation problems on perfectly flat surfaces, resulted in the fact that references analyzing both surface effects simultaneously are scarce. Even though the observed dispersion is solely attributed to surface roughness effects, the frictional effects are obviously naturally convoluted with the effect of surface roughness in the experiments. Therefore the present study investigates surface effects in nanoindentation convoluting the effects of the sample surface roughness and friction on the contact interface. In order to illustrate the coupled effect of friction and roughness practically, an estimation of the scattering in the post–treated elastic material properties due to surface effects is calculated by the two considered post–treatment methods presented in Section 2.2.

The numerical model of indentation used in this study is described first. The issues of indenting on a flat surface considering friction on the contact interface and indenting on a frictionless rough surface are revisited in Section 5.3.1. The attention is then shifted to the evaluation of the coupled effect of friction and surface roughness on nanoindentation results in Section 5.3.2. This is achieved by conducting a numerical parametric study using a simplified description of the surface topology in a first step. A more realistic description of the surface topology is then used to confirm the obtained results. This contribution ends with the conclusions involving a

discussion focusing on the implications of the findings on the interpretation of the nanoindentation output data, and on the contribution of the frictional energy dissipation on the contact interface.

Numerical modeling of the indentation setups

The main purpose being to contribute to the understanding of surface effects in nanoindentation, a model of the experimental setup and program in which such effects play a significant role needs to be considered. A special attention was therefore given to the definition of the numerical indentation parameters, in order to use quantities consistent with a real–life experimental setup used for the characterization of thin films. The modeled situation is the nanoindentation of pure nickel material with depths ranging from 0 to 45nm, using a cube corner indenter. The loading sequence considered here is 5s–0s–5s loading, holding and unloading time respectively.

Such shallow indents are generally imposed in experiments following the rule of thumb of making indents not deeper than one tenth of the thickness of the deposited thin film to avoid spurious effects of the substrate [Cai & Bangert 1995; Hainsworth & Soh 2003; Kusano *et al.* 2003]. The surface roughness of thin films can become comparable to the imposed penetration [Barshilia & Rajam 2002; Fang *et al.* 2007; Kumar *et al.* 2006; Qasmi & Delobelle 2006], which motivates the choice of roughness input parameters used here and emphasizes the practical interest of this numerical study. A non–perfect, realistic cube–corner indenter geometry is

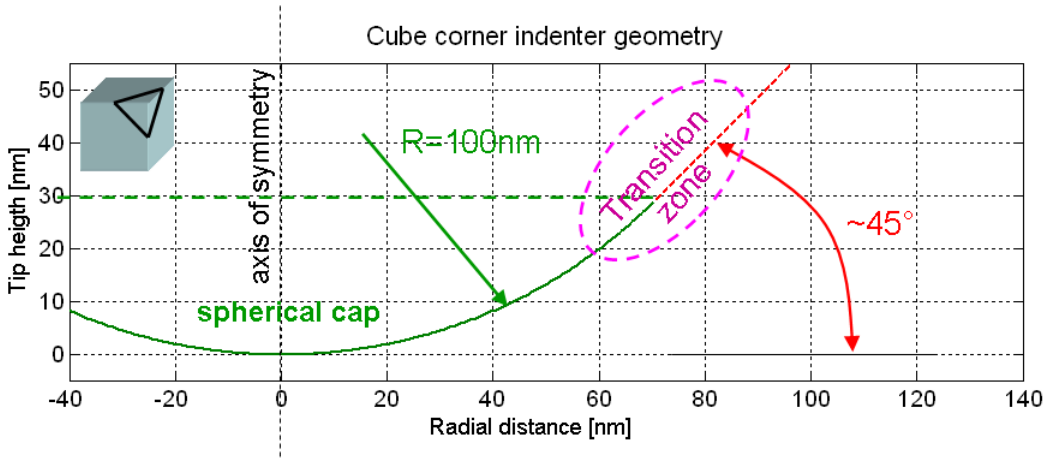

Figure 5.15: Schema of the cube corner nanoindenter tip geometry approximated in this study by a rigid sphere of 100nm radius.

considered with a nominal curvature radius of 100nm (Fig. 5.15). The sharp–edged cubic geometry transforms in a 30–35nm high smooth spherical cap at the tip of the diamond indenter. This assumed indenter geometry is approximated by a rigid spherical body in all simulations,

since the considered indentation depth of $45nm$ is comparable to the height of the spherical cap. The transition zone between the cubic and the spherical geometry potentially triggers material effects related to high strain gradients [Al-Rub *et al.* 2007; Al-Rub 2007; Mirshams & Pothapragada 2006; Qiu *et al.* 2003; Tho *et al.* 2006; Zhao *et al.* 2003]. It is here smoothened out by the spherical shape assumption.

Since the main concern here are surface effects, the potentially present material size–effects in shallow indentations are not considered, however keeping in mind their importance in the case of a direct comparison between experimental and numerical data. The behavior of the tested pure nickel material is modeled as elastic–viscoplastic, using the constitutive model and the material parameter set obtained in Section 5.2 in all simulations.

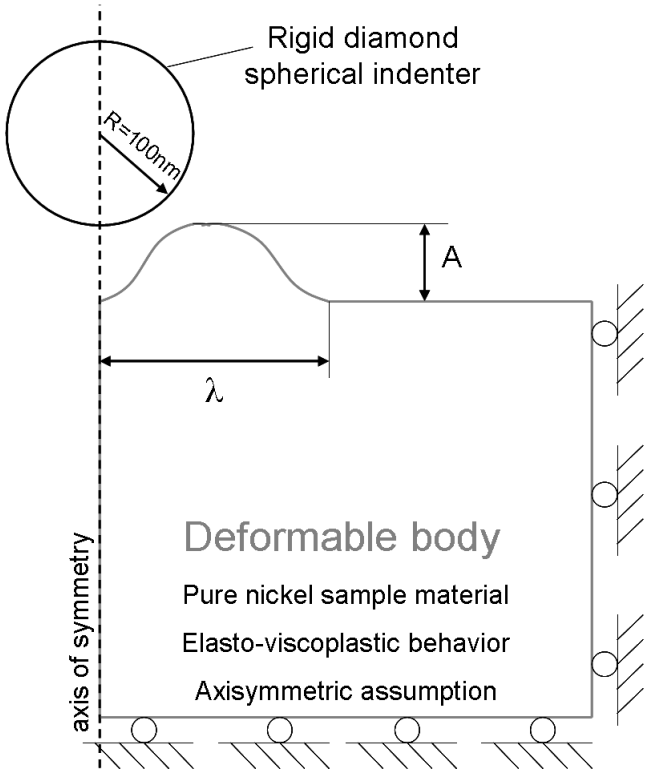

Figure 5.16: The boundary conditions of the considered axisymmetric numerical models and the parameters defining the geometry of the model surface asperity (A, λ).

The numerical work is conducted using the general purpose commercial finite element code SAMCEF, taking into account the material and geometric nonlinearities due to local finite deformation and contact evolution. For each studied case, different 2D finite element meshes of 8 noded quadratic quadrilateral elements were used, consisting of more than 48000 degrees of freedom each, with up to 160 nodes in the estimated contact area to be able to reproduce with high precision the stress and plastic strain evolution during the simulation. The frictional contact problem is solved using a Lagrange multipliers approach. The geometrical size of the mesh in all cases is chosen sufficiently large such that a homogeneous stress distribution is obtained at the lower and side boundaries of the model. The side nodes and the bottom nodes of the

mesh are constrained in the horizontal and in the vertical direction, respectively. The indenter is prescribed to reach a penetration of $45nm$ in the deformable sample which has a fixed position in space in the displacement controlled numerical indentations (Fig.5.16).

Each studied configuration was calculated using both plane strain and axisymmetric modeling assumptions, providing respectively a lower and an upper bound of the frictional effects. Indeed, considering the plane strain assumption, the modeled problem corresponds to the indentation of a deformable half–space with a rigid cylinder. Friction only acts in the in–plane direction, as unidirectional forces pointing to the center line of the contact area, which gives the lower bound of frictional effects. The axisymmetric model implicitly incorporates a three–dimensional effect of both radial and tangential friction, which describes well the indentation of a perfectly flat surface. When the indentation of rough surfaces is considered, the roughness profile is naturally described in the axisymmetric model by concentric circular rings showing a stiffer response to indentation than the real three–dimensional surface with randomly distributed surface asperities in the contact area. This lateral stiffening effect is particularly important when indenting in the middle of a roughness ring, which results in an increase in the normal contact forces. When combined with a Coulomb type friction law, this results in the increase of the friction forces, giving an upper bound of the frictional effects. By default, all simulations presented in this section are performed using an an axisymmetric assumption. The qualitative comparison of the predictions of the plane–strain and axisymmetric models will however be used to verify the agreement of the obtained trends concerning frictional and surface roughness effects.

5.3.1 Uncoupled surface effects in shallow indentation regime

The influence of friction on the numerical indentation of pure nickel considering a perfectly flat sample surface and the influence of surface roughness in a frictionless indentation are considered in this section applied to the particular case of cube corner nanoindentation of pure nickel material in shallow indentation depth. The trends observed considering first the uncoupled effect of friction and of surface roughness help the interpretation of the results issued from the more complex coupled models of Section 5.3.2.

Effect of friction on a flat surface indentation

The nanoindentation on a perfectly flat surface with a cube–corner indenter of $100nm$ tip radius in pure nickel is first considered with a special focus on the effects of friction on the results. A simple Coulomb friction model as presented in Section 4.2, is the most frequently adopted law for friction in the literature concerning the modeling of nanoindentation [Antunes *et al.* 2006, 2007; Bolzon *et al.* 2004; Bressan *et al.* 2005; Bucaille *et al.* 2004, 2003; Cao *et al.* 2007;

Cao & Lu 2004; Carlsson *et al.* 2000; Habbab *et al.* 2006; Mata & Alcalà 2004; Mesarovic & Fleck 1999; Qin *et al.* 2007; Taljat & Pharr 2004; Wang *et al.* 2007b]. The same contact law is assumed on the contact interface with a perfectly flat surface in the following simulations.

Generally, friction is shown to have a considerable influence on the local variables [Antunes *et al.* 2006; Carlsson *et al.* 2000; Mesarovic & Fleck 1999], while a lower impact is observed for the global variables, e.g. the indentation load. The main evidence of frictional effects in the considered simulations are:

- Variation of the imprint topology, and therefore of the pile–up magnitude [Bolzon *et al.* 2004; Bucaille *et al.* 2003; Mata & Alcalà 2004; Mesarovic & Fleck 1999; Taljat & Pharr 2004], influencing the contact depth h_c used in the Oliver–Pharr post–treatment method. Although the real contact depth could be obtained in a straightforward manner from simulation results, no correction will be used here, to remain consistent with the contact depth calculated by the standard assumptions of the Oliver–Pharr method, as in any actual experimental procedure. This feature is thus not considered in more detail here, focusing rather on variations of the load–displacement curves and their implications.

- Change in the load–displacement curves load levels [Cao *et al.* 2007], and the possible change in the initial unloading segment of the load–displacement curves [Tsou *et al.* 2005], inducing a variation (an increase) in the post–treated material properties.

The most obvious effect of friction observed on the load–displacement curves is an increase in the load level necessary to reach a given indenter penetration in the loading phase, compared to the frictionless numerical indentation, as shown in Fig.5.17a. This stiffening of the load–displacement curve is however triggered only after reaching some value of the indenter penetration (around $25nm$ on Fig.5.17a) for axisymmetric simulations, from which on this frictional effect seems to exhibit a monotonic increase. The size of the area formed between the loading curve of a frictionless indentation and one considering friction is related to the frictional energy dissipation on the contact interface, increasing with deeper indents. A considerable variation, up to 20% in the load levels of spherical nanoindentation due to friction is documented in [Cao *et al.* 2007], stating that the frictional effects are the most important when the penetration of the indenter h becomes comparable to the radius of the indenter R, i.e., from $h/R = 0.3$ on. The results reported in Fig.5.17a are in reasonable agreement with this statement, since the indentation configuration in the curves even surpasses the stated h/R ratio.
The magnitude of frictional effects in indentation on the load–displacement curves, as well as on the material properties obtained by post–treatment methods (Fig.5.17b) is strongly related to the friction coefficient μ. In agreement with the observations in Bucaille *et al.* [2003]; Carlsson *et al.* [2000]; Habbab *et al.* [2006], for values of μ larger than a given threshold (around $\mu =$

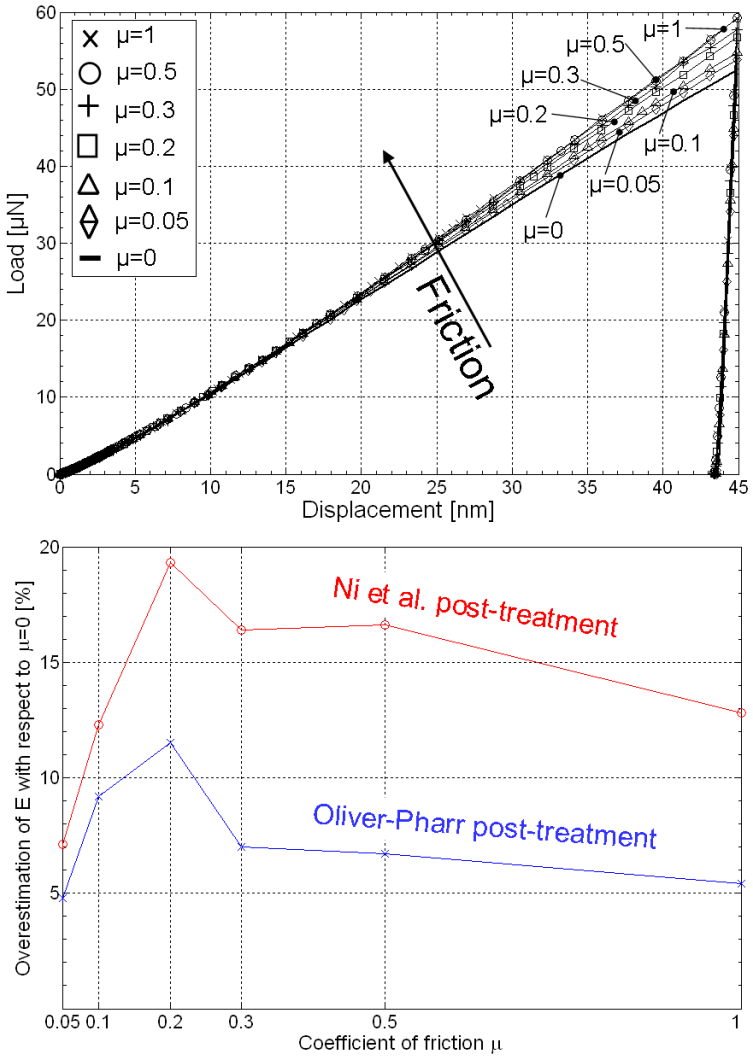

Figure 5.17: a. Load–displacement curves computed for the nanoindentation of pure nickel with a $100nm$ spherical rigid body considering friction on the perfectly flat sample surface with different coefficients of friction μ, with an axisymmetric modeling assumption. b. Variation of the post–treated Young's modulus with respect to the reference value, as a function of the coefficient of friction μ on the contact interface considering the Oliver–Pharr post–treatment method [Oliver & Pharr 1992] (dot marks) and the one proposed by Ni et al. [Ni *et al.* 2004] (hollow circle marks).

0.3 in Fig.5.17a) no essential difference can be observed between the load–displacement curves obtained for higher values of the coefficient of friction, i.e. a saturation appears in the frictional effect. From a practical point of view, the frictional effects responsible for the increase in the load levels are thus relatively independent of the actual value of the coefficient of friction for $\mu > 0.3$. As expected the same trends are observed when a plane strain assumption is adopted in the numerical model, even though the effect of friction on the load level obtained is slightly less important. As a result of the post–processing procedure, although keeping the same input material properties in the numerical model, a variation in the load–displacement curves due to

friction induces variations in the post–treated material properties, as depicted in Fig.5.17b. The post–treated material properties obtained from the numerical indentation satisfying the assumptions of the considered post–treatment methods (flat, frictionless sample surface) are considered as reference values. The simulation of the indentation in pure nickel with a perfectly flat frictionless surface yields the following Young's modulus values $E_{ref}^{OP} = 229\text{GPa}$ and $E_{ref}^{Ni} = 260\text{GPa}$, respectively for the classical Oliver–Pharr post–treatment method and for the work–of–indentation based post–treatment method proposed by Ni et al.

Unsurprisingly the work–of–indentation based post–treatment method of Ni et al. [Ni *et al.* 2004], considering the entire load–displacement curve is the most sensitive to frictional effects resulting in a variation in the output Young's modulus, defined by

$$\gamma_{fric}^{flat} = \frac{E_{fric}^{flat}}{E_{ref}} - 1 \tag{5.5}$$

up to nearly 20% with respect to the reference value E_{ref}^{Ni}. Note that even though less sensitive to purely frictional effects, the classical post–treatment method of Oliver and Pharr also shows an overestimation γ_{fric}^{flat} up to more than 10% of the reference value E_{ref}^{OP}. It is also worth noting that the largest variation in the post–treated material properties is observed at a moderate value of $\mu = 0.2$, lower than the values assumed to correspond to a purely adhesive contact, for both considered post–treatment methods.

These results point out that friction indeed affects significantly the results of nanoindentation of pure nickel in the considered configuration with a perfectly flat sample surface.

Effect of surface roughness without friction

In order to evaluate the related physical trends and to set the scene for a coupled study of friction and roughness, in this section the issue of indentation on a frictionless rough surface is revisited in a parametric study. Obviously deactivating friction ($\mu = 0$) on the contact interface, just like in the cited references in the introductory section, aims at evaluating the variation in the nanoindentation response related to the sample surface roughness only. This manipulation is of course only feasible in numerical simulations conducting virtual indentations. In practice, the surface roughness of thin films can reach average values of 30-40nm [Barshilia & Rajam 2002; de Souza *et al.* 2005, 2006; Fang *et al.* 2007; Kumar *et al.* 2006] which becomes comparable to the imposed indentation depth, limited by the film thickness. In this work, the considered indentation setup potentially falls in this category of shallow indentations.

A brief review of the rough surface models is presented in order to better motivate the choice of the simple representation used here. The roughness of a real surface has a multi–level nature calling for multiscale description in the numerical models. In a most general fashion a rough-

ness profile can be considered as the convolution of single profiles with various wavelengths and different amplitude to wavelength ratios. The description of the experimentally observed surface roughness in a numerical model depends on the physics involved. One family of models uses the fractal description of the surface roughness. This latter has been applied for example to the surface of polycrystalline Si for MEMS applications [Bora *et al.* 2004, 2005] and for ns–C films [Buzio *et al.* 2003]. Another type of models consider a single level or multi–level description using asperities with statistical height distribution, like initially proposed in Greenwood & Williamson [1966]. Some numerical works considering rough surface contact address the problem of cross–property connections [Sevostianov & Kachanov 2008], such as the variation of contact conductance [Ciavarella *et al.* 2008]. Most frequently, in the mechanical simulation of rough surface deformation, a purely elastic response of the material is considered [Bell *et al.* 1998; Sevostianov & Kachanov 2008], and depending on the modeled problem a fair agreement between experimental and numerical results can be found. In many numerical models considering the plastic behavior of rough contact, the interaction between neighboring asperities is not taken into account in order to reduce the computational effort.

For the mechanical behavior studied here, the surface roughness is chosen to have the simplest representation, considering only the first level of a protuberance–on–protuberance type roughness description, similar to [Jackson & Streator 2006; Kumar *et al.* 2006] for the sake of computational efficiency and easy interpretation of the resulting trends. Furthermore, the assumption is made that the shape of a single roughness profile i can be well approximated by a sine function

$$y_i(x) = \frac{A_i}{2} \sin\left(\frac{2\pi}{\lambda_i}\, x + \theta_i\right) \tag{5.6}$$

with A_i the peak to peak amplitude, λ_i the wavelength and θ_i the phase shift of the profile. In this section only a single roughness asperity is considered on the sample surface, placed as shown in Fig.5.16 to reduce the computational effort. This means that the influence of the interaction between the neighboring asperities of a real rough surface is not taken into account. The response of the surface roughness to deformation has been shown to depend on the shape of the roughness asperities experimentally [Buzio *et al.* 2003]. In order to cover a large range of roughness asperity shapes from relatively sharp to smooth geometries, the amplitude $A =$ [5...30nm] and the wavelength $\lambda =$ [100...800nm] of the profile was varied in physically sound ranges, resulting in 16 different surface asperity geometries.

Surface roughness can have a twofold effect resulting in either a higher or a lower contact stiffness depending on whether the indentation is performed in a roughness valley or on the tip of an asperity, respectively. This aspect, and the way the sample surface roughness affects the load–displacement curves as a function of the position of the indent is shown later in Section 5.3.2 considering a more representative case with a more realistic roughness description. A variation

in the resistance to deformation as well as a change in both the loading and unloading contact stiffnesses due to the presence of surface roughness, which affects the indentation response is thus expected. Despite keeping the same input model material parameters, when indenting on a rough surface a change in the post–treated results is found, and is illustrated in Fig.5.18a for the Oliver–Pharr and Ni et al. post–treatment methods for the axisymmetric simulations. These maps are created by interpolating between the calculated grid point values corresponding to the 16 simulated configurations. On these maps the variation of the output Young's modulus with respect to the reference values, defined by:

$$\gamma_{rough}^{\mu=0} = \frac{E_{rough}^{\mu=0}}{E_{ref}} - 1 \tag{5.7}$$

is represented as a function of the non–dimensional parameters defining the initial geometry of the asperity, A/R and λ/R. The indentations made on the rough surfaces with various geometries result in an overestimation of up to $\gamma_{rough}^{\mu=0} = 10\%$ of the reference value E_{ref}^{OP} using the Oliver–Pharr post–treatment method, which is highly sensitive to the variation in the unloading contact stiffness. As expected, the largest overestimation with respect to the reference value is obtained for the surface asperities for which the indenter and the sample contact interfaces form well–conforming surfaces, resulting in a high contact stiffness. Unsurprisingly, the lowest variation with respect to the reference value of the Young's modulus (calculated from the frictionless indentation on a flat surface) is observed for asperity shapes with large wavelengths and small amplitudes, i.e., the flattest profiles for both post–treatment methods.
Contrary to the Oliver–Pharr post–treatment method, the one proposed by Ni et al. shows a general tendency to underestimate the Young's modulus with respect to the reference value E_{ref}^{Ni} for the same input material parameter set. This underestimation is the most important for sharp asperities, reaching a value of $\gamma_{rough}^{\mu=0} =$ -15%. Unlike for the Oliver–Pharr method, here the wavelength of the initial asperity shapes λ seems to be a dominant parameter affecting significantly the post–treated results, forming vertically oriented bands on the map of Fig.5.18a. The amplitude A is observed to have a less important influence. The interpretation of these trends is not straightforward, considering the large amount of compacted information processed in the work–of–indentation based methods. The results based on the complete load–displacement curve implicitly incorporate the balance of the elastic vs. the history–dependent plastic deformation of the sample, as well as effects related to the contact evolution during indentation.

The presented trends are independent from the modeling assumption (axisymmetric or plane strain), and results are consistent with the other works [Qasmi & Delobelle 2006; Walter *et al.* 2007]. The surface roughness in frictionless indentations in small indentation depth is shown to affect significantly the results of nanoindentation. A dispersion of $\gamma_{rough}^{\mu=0} =$ 10-15% is found in the post–treated Young's modulus due to the roughness effect, depending on the post–treatment

method. The largest variation is observed for initial asperity shapes with wavelengths λ comparable to the radius of the indenter tip R.

5.3.2 Effect of friction on rough surface nanoindentation

In indentation experiments conducted on rough surfaces, the variation of the indentation response is usually attributed to the effect of the contact geometry only, even though the effects of surface roughness and friction are naturally coupled. Adding friction on the rough contact interface in the simulations should thus lead to a more realistic modeling of nanoindentation. The convolution of both effects considered separately until now may enhance the global surface effects, thereby affecting the scattering of nanoindentation results. This motivates the numerical study presented in this section considering the indentation on rough surfaces with friction on the contact interface, i.e. friction and surface roughness are combined. First, the single asperity surface roughness model used before (Fig.5.16) is updated by incorporating friction on the contact interface. As a subsequent step an attempt is made to model the indentation of pure nickel considering friction with a more realistic surface roughness representation.

Frictional effects in a contact with one surface asperity - a parametric study

From a practical viewpoint, the frictional effects were found to be relatively independent of the actual value of the coefficient of friction as soon as $\mu > 0.3$ in the previous section. The value of the coefficient of friction between two surfaces in micro–and nanoscale applications is generally measured by so–called scratch tests [Lafaye *et al.* 2008; Li & Weng 2007]. Such tests however have the drawback of lacking a straightforward interpretation as the plastic behavior is convoluted with the frictional effect, especially when pile–up is present [Bellemare *et al.* 2007, 2008]. Since a single parameter is used to model the complex multiscale frictional behavior between two surfaces, being potentially dependent on the actual contact area, on the relative tangential velocity and many other quantities, this leads to large dispersions in the value of this parameter. For these reasons, the variation of the imposed coefficient of friction of the Coulomb friction model in numerical simulations of nanoindentation in the literature is important and ranges from 0.1 [Bressan *et al.* 2005; Bucaille *et al.* 2004; Cao & Lu 2004] to 1 [Wang *et al.* 2007b], chosen more or less arbitrarily. Here the value of $\mu = 0.5$ is assumed for the coefficient of friction, which is a physically sound approximation for dry friction between a diamond and a clean metal surface for the previously adopted phenomenological model of Coulomb [Guidry 1999; Kojima *et al.* 2007; Lafaye *et al.* 2008; Noreyan & Amar 2008]. The previously discussed effects of friction (increase in the load levels with respect to the frictionless case resulting in variations in the post–treated material properties) are confirmed in the case of indentations of the single roughness asperity model when adding friction on the contact inter-

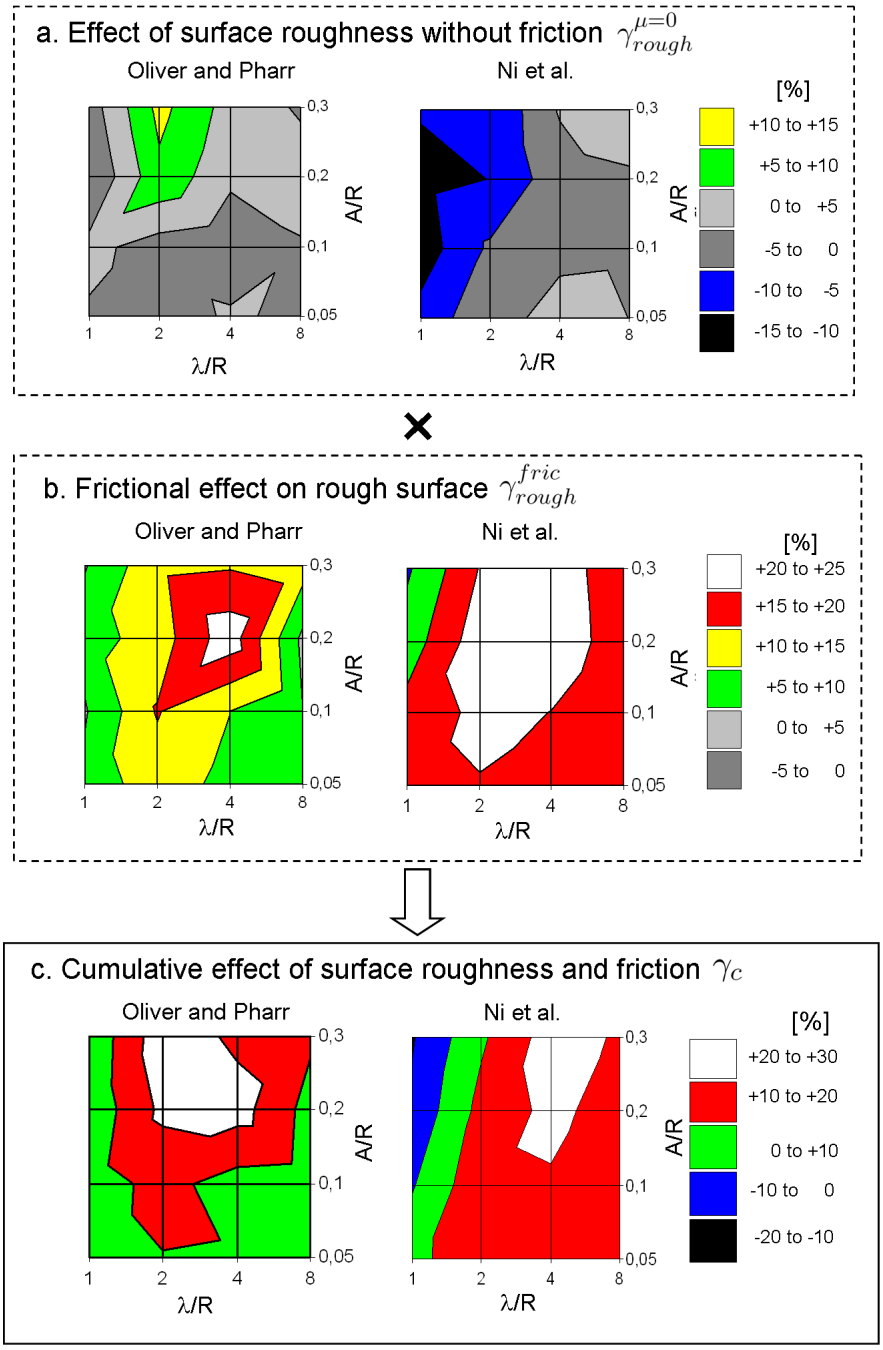

Figure 5.18: Map of the variation of the post–treated Young's modulus issued from the axisymmetric simulations for a. $\gamma_{rough}^{\mu=0}$, b. γ_{rough}^{fric}, c. γ_c as a function of the parameters defining the initial geometry of the single roughness asperity in frictionless indentation for the Oliver–Pharr post–treatment method [Oliver & Pharr 1992] and the one proposed by Ni et al. [Ni *et al.* 2004].

face. Focusing first on the post–treated results, coupled frictional and surface roughness effects are illustrated in the maps plotted in Fig.5.18c representing the variation of the post–treated Young's modulus with respect to the reference value for both post–treatment methods, defined by:

$$\gamma_c = \frac{E_{rough}^{\mu=0.5}}{E_{ref}} - 1 \tag{5.8}$$

The cumulated dispersion γ_c stemming from the convoluted effect of rough surface indentation $\gamma_{rough}^{\mu=0}$ and frictional effects is reaching nearly 30%, much higher than in the case of the frictionless assumption, confirming that frictional effects increase the scattering in the nanoindentation results.

$$\gamma_c = \gamma_{rough}^{\mu=0} \times \gamma_{rough}^{fric} > \gamma_{rough}^{\mu=0} \tag{5.9}$$

The frictional effects on the rough surface indentation considered here in terms of the output material properties can be characterized by:

$$\gamma_{rough}^{fric} = \frac{E_{rough}^{\mu=0.5}}{E_{rough}^{\mu=0}} - 1 \tag{5.10}$$

corresponding to the variation in the post–treated Young's modulus due to friction only with respect to the values obtained from the frictionless indentation of the surface asperities. Unsurprisingly the influence of friction alone γ_{rough}^{fric} on the post–treated material parameters is observed to be dependent on the contact geometry, i.e. the initial topography of the considered surface asperity (Fig.5.18b.) An increase up to $\gamma_{rough}^{fric} =$ 20-25% in the output material parameters independently of the choice of the post–treatment method is shown, emphasizing the need of taking *the cumulative effect of friction and surface roughness* into account. Note, that in agreement with the findings in the previous section, friction is shown to increase the value of the post–treated Young's modulus with respect to the frictionless case (Fig.5.18b).

Frictional effects in indentation on a realistic rough surface

The use of a simple roughness model may restrain the domain of validity of the obtained trends, which motivates the consideration of a more realistic surface roughness representation. The surface profile of the sample, depicted in Fig.5.19 is described by the sum of four sine functions with different amplitudes, wavelengths and phase shifts, to reproduce qualitatively the nature of real surface profiles for a mechanical problem. In the adopted roughness model increasing amplitudes are associated to increasing wavelengths. The previously used Coulomb friction model is assumed here, with a coefficient of friction of $\mu = 0.5$. Eight different indentation positions were considered, plotted in Fig.5.19. The indentation depth of $45nm$ after initial contact is prescribed in each case.

The obtained load–displacement curves for the axisymmetric assumption, shown in Fig.5.20a are highly sensitive to the position of the indent. The significant variation in the load levels of the load–displacement curves is due to the convolution of the surface roughness and friction effects. In order to evaluate the effect brought by friction separately, the set of indentations was performed for the same geometries in a frictionless numerical setup (Fig.5.20b). The conclusions are similar to Section 5.3.1, i.e., frictional effects strongly depend on the contact geometry defined by the initial surface topology. For some configurations, friction plays an important role

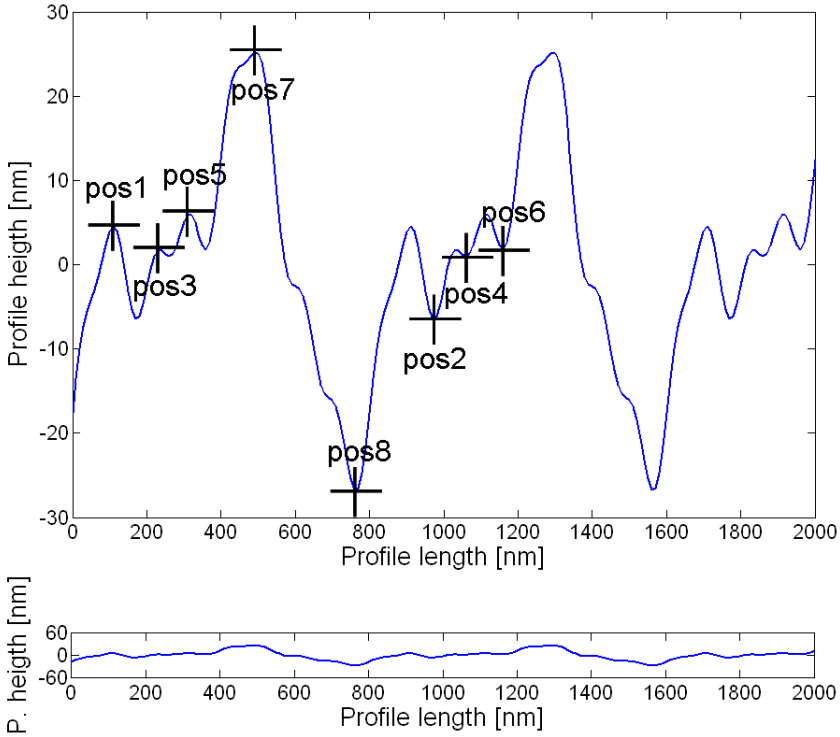

Figure 5.19: Representation of the surface roughness used for modeling a real–life indentation program. The marks correspond to the considered indentation positions. Note that the scale of the profile height on the top figure is amplified for the sake of clarity with respect to actual profile shown in the bottom figure.

in the load–displacement curves (Positions 6, 8 on Fig.5.20), whereas in other cases it only has a minor influence on the nanoindentation response (e.g. Position 7 on Fig.5.20). The sample surface roughness can have a twofold effect: it either increases or decreases the contact stiffness during indentation depending on the position of the indent, affecting the load levels necessary for reaching a given indentation depth. In agreement with the physics of nanoindentation, the highest load level is obtained when indenting in the deepest roughness valley forming a well conforming contact surface with the indenter (Position 8 on Fig.5.19). Conversely, the indentation on the highest roughness peak shows the most deformable response (Position 7 on Fig.5.19).

These trends are observed independently of the modeling assumption (plane strain or axisymmetric). The only noticeable difference is the expected larger influence of surface effects in the axisymmetric models (as pointed out before). The dispersion in the maximum force levels of the load–displacement curves stemming from the convoluted effect of friction and surface roughness is around 40% in the axisymmetric simulations, larger than in the previous parametric study on a single asperity. The post–treated average Young's modulus is shifted to $E^{OP} = 248.1GPa^{+33.6GPa}_{-70.7GPa}$ and $E^{Ni} = 292.7GPa^{+72.3GPa}_{-55.1GPa}$ with respect to the reference values, with a dispersion of $\Delta E^{OP} =^{+13.5\%}_{-28.5\%}$ and $\Delta E^{Ni} =^{+24.7\%}_{-18.8\%}$.

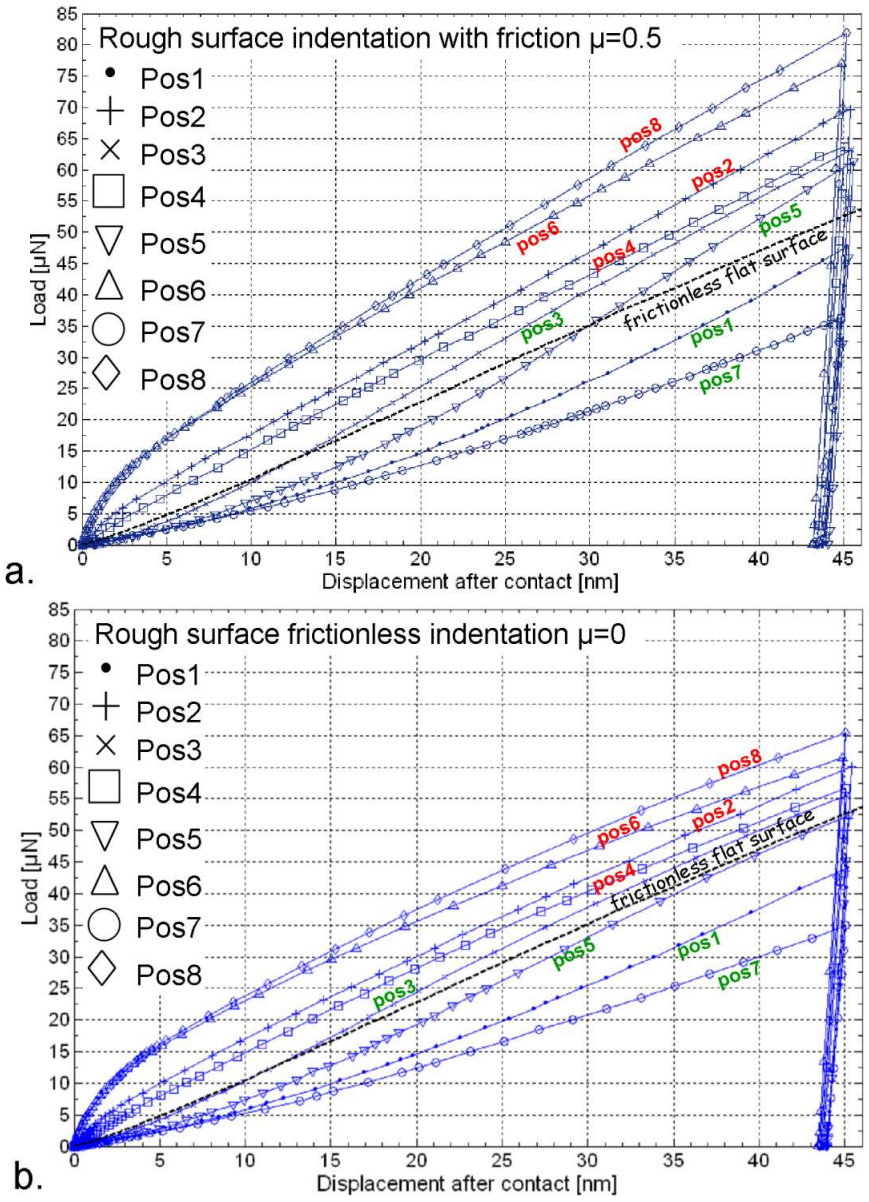

Figure 5.20: Load–displacement curves obtained for the indentations in the predefined eight positions in Fig.5.19 for the axisymmetric models (a.) considering friction and (b.) for the frictionless case Note the increase in the dispersion of the load levels when considering friction.

It is emphasized that the parameters of the presented set of numerical indentations are defined to respect the best possible the experimental conditions of an eventual real–life setup, and have not been fine–tuned with the intention to obtain the most significant surface effects. Nonetheless, the obtained scattering in the post–treated results which is exclusively related to the convoluted effect of friction and roughness is found to be considerably high, and in good agreement with experimental observations in Qasmi & Delobelle [2006]. The cumulative effect of friction and surface roughness on the scattering in the raw (Fig.5.20) and post–treated (Fig.5.21) nanoindentation results was confirmed in this set of simulations with a more realistic description of the sample surface roughness.

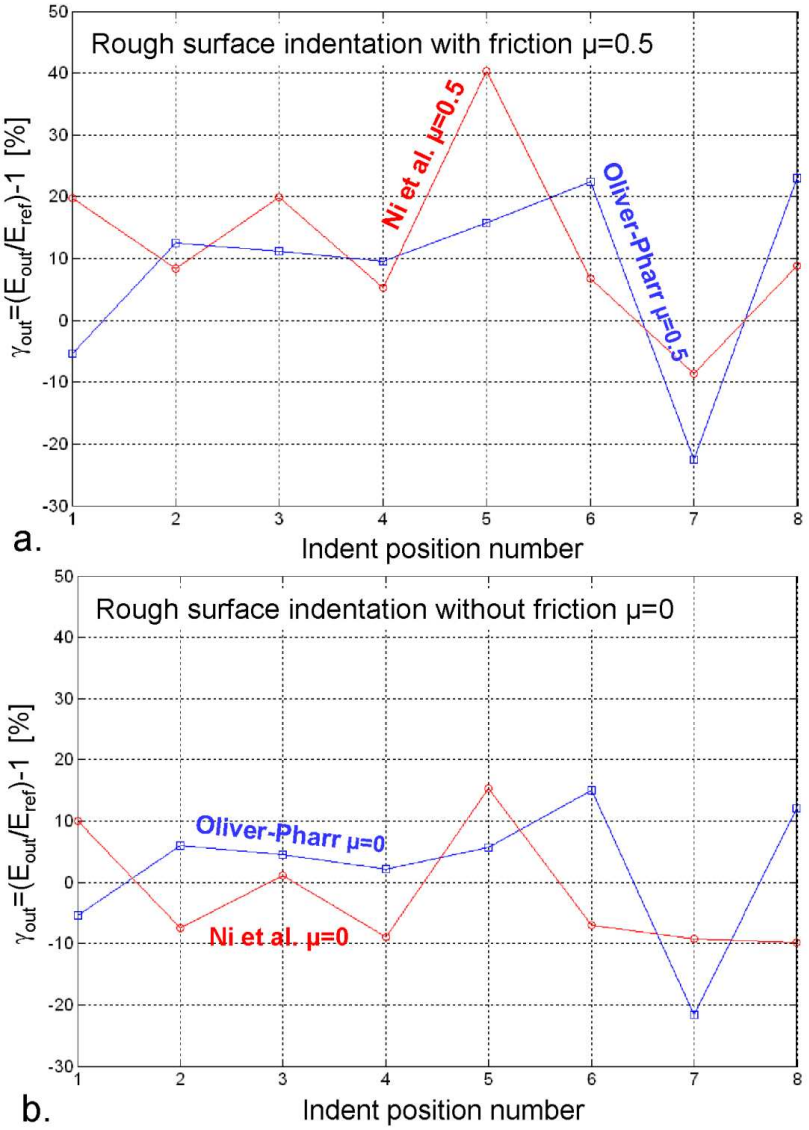

Figure 5.21: Variation of the output Young's modulus with respect to the reference value for cases a. with friction; and b. without friction as a function of the indentation position i defined in Fig.5.19 for the Oliver–Pharr post–treatment method [Oliver & Pharr 1992] (square marks) and the one proposed by Ni et al. [Ni *et al.* 2004] (hollow circle marks).

5.3.3 Concluding remarks

In this numerical study considering indentations on rough surfaces, the effect of friction on nanoindentation results is found significant, yielding a scattering level comparable to the one met in experiments [Qasmi & Delobelle 2006]. Surface effects stemming from friction and surface roughness were found to depend on the initial surface topology, partly because of the high sensitivity of the frictional effects on the shape of the indented asperity and partly due to the variation of the deformability of the asperities with different shapes. The results show a strong interaction between these two contributing terms to surface effects and allow to draw the following salient conclusions.

- Their effect on the dispersion of nanoindentation raw and post–treated results is found to be cumulative: considering friction in a numerical model with roughness increases the scattering in both the force levels of the load–displacement curves (Fig.5.20) for a given indentation depth, and in the post–treated elastic material parameters (Fig.5.21). Friction should thus be included in a thorough description of rough surface nanoindentation.

- Surface effects were found to shift the average value of the identified material parameter. If surface effects are not considered, the large dispersion and this shift in the post–treated average elastic modulus could be wrongly interpreted in terms of variations of the material behavior, or of other potential sources of nanoindentation scattering. The numerically obtained range of dispersion may give an indication to whether this interpretation of the results can be assumed or not.

- The predictions of the simple single asperity roughness model considered in the parametric study and the results from the simulation on a more realistic surface roughness description agree well, leading to interesting conclusions from a practical point of view. The results of the single asperity surface roughness model showing the most pronounced surface effects for wavelengths λ comparable to the radius of the indenter tip R may be used as a simple/basic guideline for surface preparation steps when they are not prescribed by the fabrication procedure otherwise.

- Surface effects contribute to the energy balance of the indentation problem. The surplus energy necessary for the crushing of surface asperities has already been recognized to be a significant term in the energy balance in small indentation depth and size–effects depending on the surface topology have been associated to it [Gao & Fan 2002; Kim *et al.* 2007; Qiu *et al.* 2003; Zhang *et al.* 2004]. The dissipative frictional effects depending on the contact geometry are also found to be considerable here.

- For the same reasons the work–of–indentation based methods [Beegan *et al.* 2005; Kusano & Hutchings 2003] are more sensible to surface effects. In particular, if the parameters of the plastic behavior of thin films is intended to be identified [Cao & Lu 2004; Giannakopoulos & Suresh 1999; Ma *et al.* 2003; Zhao *et al.* 2006], the dispersion in the post–treated results as a consequence of the surface roughness and friction is expected to be even more important.

In order to avoid a misinterpretation of the presented numerical results, the trends concerning surface effects have been verified with plane strain simulations. The same trends were observed for both modeling assumptions in all considered configurations confirming the significant influence of the interaction of friction and surface roughness effects in nanoindentation based on similar observations on the load–displacement curves.

5.4 Discussion on the performance of nanoindentation post–treatment methods for the prediction of the sample elastic modulus

The presented two post–treatment methods of nanoindentation (Section 2.2) were applied systematically in all nanoindentation simulations (Sections 5.1 to 5.3). The variation of the post–treated elastic modulus due to variations in the indentation parameters, other than the input elastic modulus is considered as dispersion in the nanoindentation results. This leads to an important general issue of the nanoindentation procedure addressed here, i.e. the evaluation of the performance of post–treatment methods.

As expected, both methods perform well when the post–treatment assumptions are satisfied. It is noted, that a simple calculation, presented in Appendix A.1 showed, that the Oliver–Pharr method was rather insensitive to effects of pile–up and sink–in in the indentation configurations studied in Section 5.2, with a conical indenter with $2\mu m$ nominal radius. Both methods considered here are sensitive to an undetected variation in the tip geometry (radius), which results in a similar dispersion. The corresponding dispersion can be efficiently reduced by a systematic evaluation of the actual tip geometry preceding the experiments (Section 5.1).

On one hand the post–treatment method proposed by Ni et al. shows a lower sensitivity to changes in the plastic properties of the sample material when the elastic–plastic material behavior is rate–independent (Section 5.1), and particularly when the material behavior is elastic–viscoplastic (Section 5.2). On the other hand, this work–of–indentation based post–treatment method is more sensitive to frictional effects (Section 5.3), since frictional energy dissipation W_{fric} potentially alters the ratio of the reversible elastic W_e, and of the total work $W_t = W_e + W_p + W_{fric}$. This was observed for nanoindentations on both flat and rough surfaces.

The contact stiffness of indentations, determined on the unloading portion intervenes in both post–treatment methods, therefore they are sensitive to potential variations in the unloading curve. Since the contact stiffness of indentations on rough surfaces may vary, this can result in a considerable dispersion in the post–treated elastic modulus for both methods (Section 5.3). Note that a potential viscoelastic material behavior [Cheng & Cheng 2005; Ovaert *et al.* 2003; Zhang *et al.* 2008] may influence the unloading slope of the load–displacement curves as well. When taking frictional effects into account in nanoindentation of rough surfaces, due to the coupled effect of friction and surface roughness the resulting dispersion increases significantly (as shown in Section 5.3), reaching very important proportions.

The overall performance of the two post–treatments methods is similar (the method of Ni et al.

was found more accurate when the plastic material properties were varied, and the Oliver–Pharr method performs better for the coupled effect of friction and surface roughness). In view of the comparable performance of the two methods for identifying the elastic modulus, the use of the post–treatment method proposed by Oliver and Pharr [Oliver & Pharr 1992] remains advisable, considering its simplicity, which allows a more straightforward interpretation.

Indeed, the main drawback of the work–of–indentation based post–treatment method is the difficult interpretation of the potential variation in the output elastic modulus, considering the large amount of compacted information. The results based on the complete load–displacement curve implicitly incorporate a larger number of potentially spurious contributions (material plasticity and damage, contact evolution and behavior, etc.) than methods based solely on the unloading portion showing a relative independence on the contributions influencing principally the loading period of indentation.

However, when material parameters related to the plastic behavior of the material are aimed for, work–of–indentation based methods are usually applied [Cao & Lu 2004; Giannakopoulos & Suresh 1999; Ma *et al.* 2003; Zhao *et al.* 2006]. It was shown that the same indentation data can be achieved numerically for different material parameter sets, and the significant variation in the load–displacement curves as a consequence of rate–dependent material effects, friction and surface roughness was demonstrated. Care should therefore be taken when using such methods in the choice of the material model to allow identifying parameters consistent with the underlying physics, and in the interpretation of the (potentially non–unique) resulting parameter set and its variation.

5.5 Variation of the adhesion due to the deformation of surfaces roughness during micromanipulation

In this contribution the continuum scale numerical tool (presented in Chapter 4, satisfying the particular requirements for the simulation of nanoindentation) is applied to the problem of manipulation of objects on the microscale. The manipulation of objects between $10\mu m$ and $1mm$ is often disturbed by the adhesion between the contacting surfaces [Carpick *et al.* 2001, 2002]. The spurious adherence between the manipulating equipment and the object can lead to the impossibility of releasing the handled object. It is therefore of high interest to study the forces responsible for these perturbations and which, although negligible at macroscopic scale, are of great importance at microscale/nanoscale. This originates from the different balance between surface and volume forces on the microscale/nanoscale: the surface-to-volume ratio is indeed much more important on the small scales.

Various surface forces can be identified as potential sources of adhesion, i.e. capillary forces [Lambert 2007; Mate 2008], van der Waals forces [Israelachvili 1974; Mate 2008] electrostatic forces [Lambert & Régnier 2006] and the chemical bonding of surfaces. This numerical study focuses on the electrostatic forces because they are the most significant for grasping and manipulating parts of micrometer size [Fearing 1995], since their magnitude is such that they alone can be important enough to perturb the manipulation. These long–range forces are active for separation distances in the order of the radius of the manipulated object.
A significant decrease in the magnitude of surface forces was observed [Bhushan 2003; Lhernould *et al.* 2007; Rabinovich *et al.* 2000] due to the presence of surface roughness. Conversely the change in the surface topology by the flattening of the asperities during micromanipulation can give rise to an increase of the contact adhesion. Indeed, when the handled object is in contact with the gripper it is unavoidable that the asperities on the contacting surfaces are crushed to some extent due to the grasping force. The prime purposes of this work are to contribute to the understanding of how the induced deformation of the contacting rough surfaces influences the electrostatic adhesive forces, and to give some insight into the physics of the evolution of adhesion during micromanipulation through an adapted multi–physics numerical study. The computational work can be divided into two parts coupled unilaterally (Fig.5.22). The first one involves the computation of the elastic–plastic deformation of surface asperities on the gripper arm during micromanipulation with the numerical tool presented in Chapter 4. The assumption is made that the deformation of the gripper arm surface gives the main contri-

This section is based on M. Sausse Lhernould, P. Berke, T.J. Massart, S. Régnier, P. Lambert, 'Variation of the adhesive electrostatic forces on a rough surface due to the deformation of roughness asperities during micromanipulation of a spherical rigid body' submitted for publication

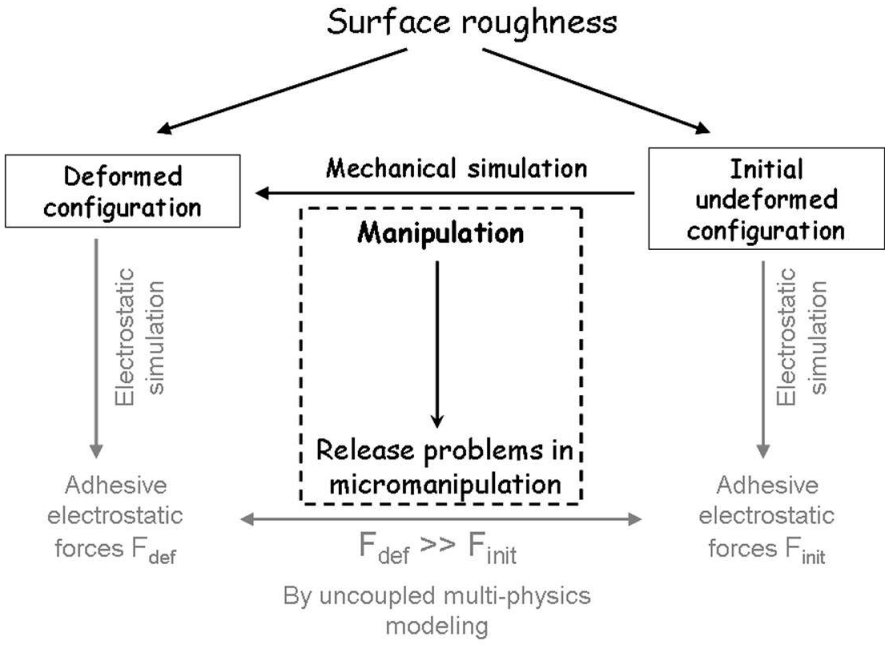

Figure 5.22: Scheme of the uncoupled multi–physics simulation investigating the effect of surface roughness deformation on adhesive electrostatic forces during micromanipulation.

bution to the considered physics. The second part aims at the evaluation of the variation of the contact adhesion during micromanipulation based on the computed deformation of the surface asperities using an electrostatic numerical model. This part of the work was performed by M. Sausse Lhernould. This unilateral coupling of the electrostatic simulations introduces the assumption that the electrostatic force levels are much smaller than the ones necessary to deform the surface asperities, therefore that the electrostatic forces and their variations do not influence the obtained deformation (this will be confirmed later on). The adhesive electrostatic forces on the surface asperities in the initial, undeformed and in the final deformed configuration are calculated and compared to evaluate the variation of their magnitude during micromanipulation.

This study is structured as follows. Section 5.5.1 deals with the mechanical problem of the deformation of the gripper arm during micromanipulation on the scale of the object (the macroscale) and on the scale of the surface roughness asperities (the microscale). In Section 5.5.2 the results of the electrostatic simulations working on the microscale are presented and discussed. The increase of the adhesive electrostatic force during micromanipulation is found to be significant in all studied cases. Finally the assumptions used in this study, and their implication on the obtained results and trends are discussed, explaining why the observed effect seems to be a lower bound of the real one.

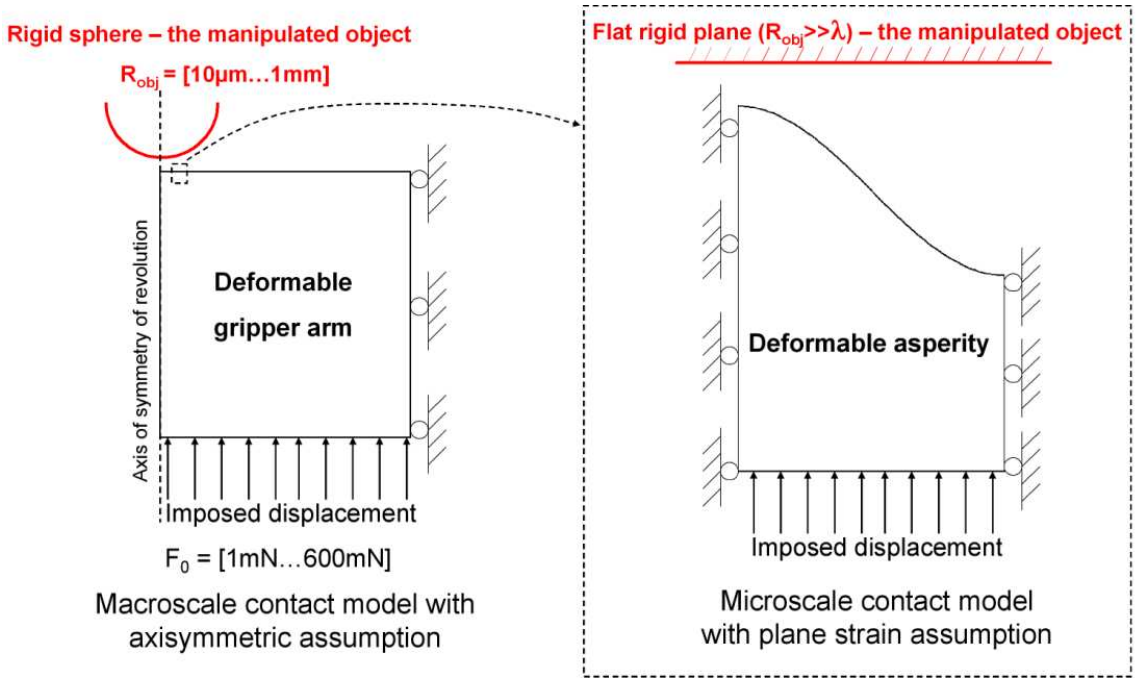

Figure 5.23: The two considered contact models working on different scales. Left: macroscale model of the micromanipulation considering realistic loading conditions and an axisymmetric description with the manipulated object modeled as an undeformable body. F_0 is the manipulating force, R_{obj} the radius of the manipulated object. Right: microscale contact model of the flattening of one surface asperity on the surface of the gripper arm, using a plane strain assumption. λ is the wavelength of the sine function describing the asperity shape, the manipulated object is modeled as a rigid flat plane in view of $R_{obj} = [10\mu m...1mm] >> \lambda$.

5.5.1 Contact deformation modeling

This part of the work addresses the problem of the evaluation of the deformation of a pure nickel gripper arm during manipulation using the numerical tool presented in in Chapter 4. Two numerical models have been set up on two different scales for this purpose.

- The macroscale contact model working on the scale of the manipulated object is used to evaluate the deformation of the gripper arm when a realistic squeezing force is applied to grab spherical objects with sizes ranging from $10\mu m$ to $1mm$. The magnitude of the obtained macroscopic deformation gives an indication for the deformation level to be applied on the surface roughness asperities in the microscale model.

- The microscale model is used to determine the deformed shapes of the roughness asperities considering the chosen deformation level. The results of the microscale model are the input data for the electrostatic simulations that determine the adhesive electrostatic forces in the contact.

This separation of scales was indispensable merely to allow the calculation of the considered problem.

Macroscopic contact model of micromanipulation: surface roughness deformation estimate

This numerical model works on the scale of the manipulated object, which is assumed to have a perfect spherical geometry with a radius varying in the range of sizes of the potentially manipulated objects $R_{obj} = [10\mu m...1mm]$ [Agnus *et al.* 2004]. For the sake of simplicity and computational efficiency the roughness of both surfaces of the gripper arm and of the manipulated object is neglected on the macrolevel.
At this macroscale the gripper arm is considered to be made of pure nickel and is modeled as a deformable body having a perfectly flat frictionless contact surface. Frictional effects are not taken into account in this study in order to reduce the complexity of the numerical models and to ensure the computational efficiency. In the numerical model the isotropic rate–independent hardening behavior of pure nickel, used in Section 5.1 is assumed, because the strain rates are assumed to be small, as opposed to nanoindentation.
The manipulated spherical object is considered to be undeformable and is modeled by a rigid body (this assumption will be validated later).
The applied squeezing force varies in the range of the real manipulation force $F_0 = [1mN...600mN]$ [Agnus *et al.* 2004].
Considering the symmetry of the problem the finite element meshes are two dimensional (Fig.5.23) and built from 8 noded elastic–plastic *axisymmetric* elements capable of handling finite deformations. The models consisted of more than 33500 degrees of freedom to be able to reproduce with high precision the stress and plastic strain evolution during the simulation. During the simulation the side nodes of the mesh are constrained in the horizontal direction, the deformable body is prescribed to move upwards to come into contact with the rigid object having a fixed position in space. The nodes on the bottom side of the model are not constrained in the horizontal direction. The geometrical size of the meshes in all cases is chosen sufficiently large such that a homogeneous stress distribution at the boundary of the model is obtained.
Two extreme contact configurations were analyzed on the macro level:

- **A.** The largest manipulated object $R_{max} = 1mm$ is combined with the smallest manipulation force $F_0^{min} = 1mN$. This macroscopic contact generates the smallest contact stresses and corresponds to the least severe loading conditions. The behavior of the material remains mainly *elastic*, with a contact area radius of $a_{macro} = 1{,}653\mu m$ close to the elastic contact radius approximation by the theory of Hertz [Hertz 1882]. The obtained penetration of the rigid body is $h_{macro} = 2.3nm$.

- **B.** The smallest object $R_{min} = 10\mu m$ is manipulated with the largest force level $F_0^{max} = 600mN$. In this case the contact response is dominated by the *plastic* deformation of the gripper arm due to the high contact stresses. The calculated macroscopic contact radius is $a_{macro} = 10\mu m$, almost 4 times the elastic approximation by the theory of Hertz. The penetration of the rigid body is also strongly increased and becomes comparable to the radius of the sphere with $h_{macro} = 10\mu m$.

In both of the studied theoretical contact cases the finite deformation of the gripper arm was observed. In micromanipulation it is necessary to squeeze objects in order to hold them firmly. Case **A.** taking the largest object with the smallest gripping force most probably gives a lower bound to the contact stresses and the deformation of the gripper arm in the macroscopic level model with respect to the real configuration.

Microscopic rough contact model

The objective of this series of numerical simulations is the modeling of the deformation of the surface roughness of the gripper arm made of pure nickel during micromanipulation. For this a numerical model has been defined on the scale of the surface roughness asperities, i.e. on the microscale.

The surface roughness is chosen to have the simplest representation in this work approximated by a sine function $y_i(x) = A_i \sin\left(\frac{2\pi}{\lambda_i}x\right)$, considering only the first level of a protuberance-on-protuberance type roughness description, as in Section 5.3. For the sake of simplicity the amplitude A_i and the wavelength λ_i of each asperity i of the surface roughness composed of n interconnected asperities are defined to be the same in this study. In order to cover a large scope of roughness asperity shapes considering their sinusoidal description, the ratio between the amplitude and the wavelength of the sine function is varied. In the model the wavelength of the asperities has been kept fixed $\lambda_i = \lambda = 200nm$ and 13 different values of the amplitude (Tab.5.4) were chosen in the range $A_i/\lambda =$ [0.01...0.85] from the bluntest to the sharpest profiles (Fig.5.24).
In the multi–level description of the surface roughness, the shape of the asperities can potentially change on different levels. The considered model describing the surface asperities with sine functions has the advantage to be easily adaptable in studies for such multi–level representations or for a fractal description. From the point of view of electrostatic simulations, the same choice of a sinusoidal representation of the geometry was made in Kostoglou & Karabelas [1995] to compute the electrostatic repulsive energy between two rough colloidal particles.

The assumption that the size of the manipulated object is much larger than the wavelength of the roughness profiles

$$R_{obj} = [10\mu m...1mm] >> \lambda = 200nm \tag{5.11}$$

on the microscale generally holds for the majority of practical cases [Jamari & Schiper 2007]. As a consequence, in view of (5.11) some simplifying assumptions can be applied to the microscale numerical model, such as:

- The contact radius of the manipulated object is considered to be infinite in the microscale numerical contact model, and this object is thus modeled as a rigid flat plane on this scale.
- The neighboring roughness peaks are assumed to deform homogeneously in the vicinity of a chosen roughness asperity.

If every roughness peak is assumed to deform in the same way on the considered scale as performed in Kumar *et al.* [2006], the characterization of the behavior of one roughness peak is sufficient using a periodicity condition at the boundary of the model. Consequently, the interaction between asperities is neglected in this study, which is a common practice used to achieve a reasonable computational efficiency in numerical models of rough surface contact [Bora *et al.* 2005; Larsson *et al.* 1999]. Note that the results of some experimental works investigating the difference in the response of single and multi–asperity contact on small scales show that this assumption may alter the overall response of the contact, particularly for cases when the contact penetration is comparable to the height of the asperities [Buzio *et al.* 2003; Kumar *et al.* 2006; Nicola *et al.* 2007; Rajendrakumar & Biswas 1997]. Considering the finite deformation of the gripper arm on the macroscale with realistic loading conditions, the flattening d_i of a modeled roughness asperity i in the microscale model using the periodicity condition was chosen to be $d_i/A_i = 2/3$ corresponding to a moderate deformation on scale of the surface roughness.

This set of assumptions, based on (5.11) on the microscale thus introduces the assumption of a *full separation of the length scales* of the manipulated object (the macro scale) from those defining the conditions of the contact between the roughness peak and the object (the micro scale) as shown in Fig.5.23.

In the numerical model the geometry is two–dimensional with a *plane strain* assumption. Only the half of the sinusoidal profile is considered due to the symmetry of its shape. All thirteen finite element meshes with different A_i values are built from 8 noded elastic–plastic plane strain elements in the corotational finite deformation description with more than 14800 degrees of freedom. The geometrical size of the meshes is chosen such that a homogeneous stress distribution is found on the bottom side of the model. The left and right sides of the deformable

body are blocked in the horizontal direction in order to represent the above-mentioned periodicity condition. The bottom side of the body is free in the horizontal direction and moves upwards in the vertical direction by the value of $d_i = 2A_i/3$ (the prescribed flattening) using a displacement–controlled simulation. Unilateral contact conditions without friction are used between the contact nodes on the top side of the deformable body and a rigid horizontal plane representing the manipulated object. The same elastic–plastic rate—independent constitutive law with isotropic hardening is used for the nickel deformable body as before.

In a contact setting, both contacting objects often suffer both elastic and plastic deformations due to the high contact stresses. The assumption that the handled object can be considered undeformable was verified to hold. This was achieved by simulating the microscale contact problem with a deformable object made of S45C carbon steel ($E^{S45C} = 205$GPa, $\sigma_0^{S45C} = 400$MPa) using the SAMCEF commercial finite element code. Indeed, the plastic deformation is found to take place only in the nickel roughness peak, because of the lower elastic limit of pure nickel. In the considered contact although the elastic properties of both materials are similar, due to the lower yield limit of pure nickel, it reaches the plastic domain, while the carbon steel still shows an elastic contact response. Moreover the elastic deformation of the carbon steel object is also confirmed to be negligible. The rigid body modeling of the handled object appears thus reasonable for objects made of materials with substantially higher yield limit than the nickel base material of the gripper arm. The initial and deformed shapes of the considered profiles are presented in Fig.5.24. The reaction force per roughness peak generated by the imposed flattening of the asperities in the microscale contact simulations are depicted on Fig.5.25. Note the nonlinear variation of the response of the roughness peaks as a function of their shape. The *elastic springback*, i.e. the difference between the profile geometry at maximum load level and

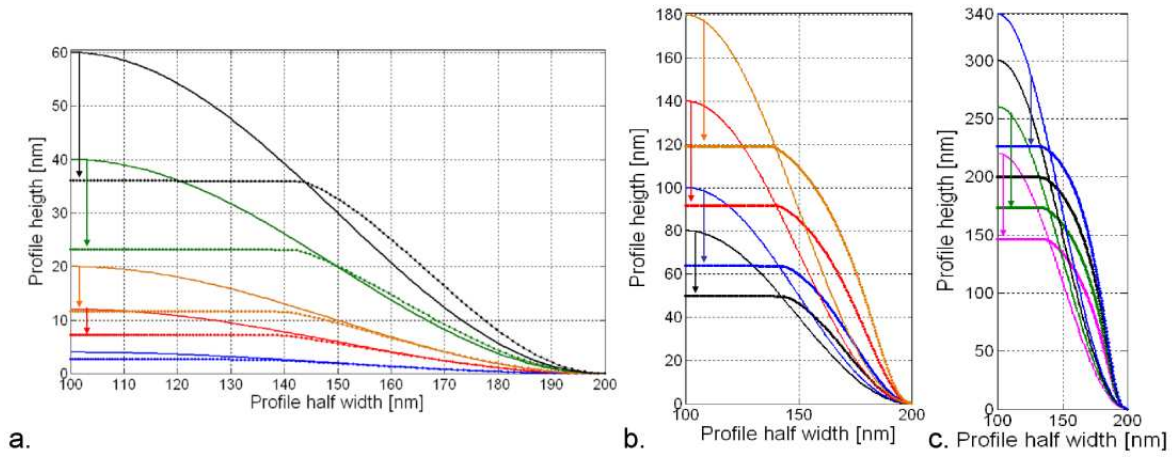

Figure 5.24: Studied asperity shapes in the initial and in the deformed configuration at peak load. a. blunt asperities $A_i/\lambda = [0.01..015]$, b. sharper asperity shapes $A_i/\lambda = [0.2..045]$, c. sharpest asperity shapes $A_i/\lambda = [0.55..085]$.

after unloading due to the elastic relaxation of the material, was analyzed for all considered geometries and was found small from the mechanical point of view.

Linking the microscale and the macroscale contact models

The results of the microscale model were obtained for a chosen crushing of the roughness profiles d_i, being function of the initial amplitude A_i. It is possible to show using a simple assumption that the chosen flattening of the surface asperities on the microscale gives reaction forces in the same order of magnitude as the manipulating force on the macroscale. The essence of the method is to check whether by filling uniformly the projected contact area A_{macro} obtained from the macroscopic scale model with deformed sinusoidal roughness peaks of the microscale model at the prescribed crushing, the induced reaction force is in the order of magnitude of the macroscopic manipulating force.

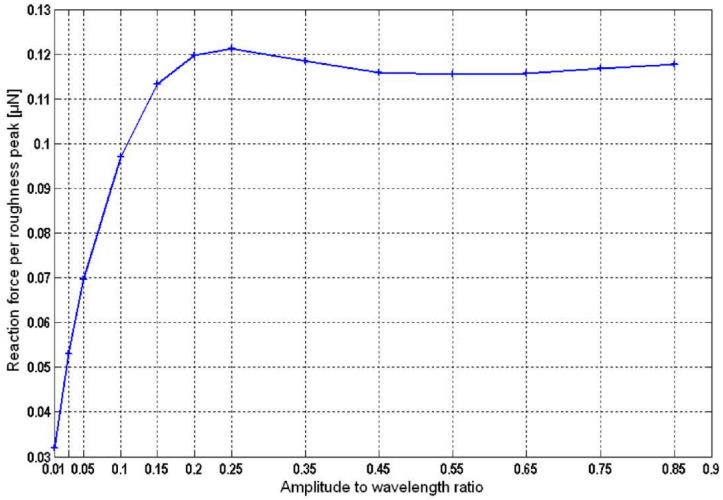

Figure 5.25: Reaction forces per roughness peak generated by the flattening of the asperities in the microscale model as a function of the A_i/λ_i ratio of their initial shapes.

This relation is expressed by (5.12). Note that the approximation of having a uniformly crushed surface roughness in the contact area A_{macro} limited by the macroscopic contact radius corresponds to the cylindrical rigid flat punch of the rough surface with an imposed crushing d_i.

$$F^{\Sigma}_{micro} = \sum_{A_{macro}} R_i = N_{asperity} \times R_i = o\left(F_0^{macro}\right) \tag{5.12}$$

Applying the above linking assumption to

- case **A.** of the macroscale simulations (object–gripper contact working mainly in the elastic domain), the overall reaction forces $F^{\Sigma}_{micro} = [1.37mN...5.2mN]$ of the 4.3×10^4 deformed peaks filling the macroscopic contact area are in the same order of magnitude as the macroscopic manipulating force. This suggests that the assumed plastic deformation

in the microscale contact problem matches the order of magnitude of the real plastic deformation of the roughness peaks. It is emphasized that the loading conditions in the case **A.** (largest object seized with the smallest manipulating force) are probably less severe than the practically used ones.

- case **B.** (object–gripper contact showing mainly plastic response on the macro scale), the overall reaction forces $F^{\sum}_{micro} = [50mN...190mN]$ of the 1.57×10^6 peaks filling the macroscopic contact area are lower than the macroscopic manipulation force. This means that the roughness peaks are crushed in average much more severely in reality than in the microlevel model. This interpretation is confirmed by the deep penetration of the object of around $10\mu m$ calculated in the macroscale contact model. Consequently, considering the generally large contact stresses in the macroscopic level micromanipulation model, most of the surface asperities in the contact area can be assumed severely crushed. Unlike in works reporting surface asperity persistence at considerably smaller relative penetration with respect to the height of the surface asperities (and sometimes in lubricated contact conditions) [Jamari & Schiper 2007; Larsson *et al.* 1999; Rajendrakumar & Biswas 1997], in the considered micromanipulation setup the surface roughness is probably practically flattened, as in Azushima *et al.* [2006].

The force levels obtained from the microscopic scale computation and upscaled by the considered simple cylindrical flat punch assumption remain for all considered cases almost in the same order of magnitude as the macroscopic manipulation force. However, the assumed number of contact points in the contact zone with similar asperity densities as on a Si polycrystalline surface [Carpick *et al.* 2002] is an order of magnitude larger than computed in Carpick *et al.* [2002], thereby resulting in an overall reaction force also an order of magnitude higher. This means that the plastic deformation of the surface asperities in the microscale problem is most probably a lower bound with respect to the real micromanipulation setting, and the obtained numerical results can be considered to give a lower bound to the surface asperity flattening.

i	1	2	3	4	5	6	7	8	9	10	11	12	13
A_i/λ	0.01	0.03	0.05	0.10	0.15	0.20	0.25	0.35	0.45	0.55	0.65	0.75	0.85
$A_i[nm]$	2	6	10	20	30	40	50	70	90	110	130	150	170
$d_i[nm]$	1.34	4	6.67	13.34	20	26.67	33.34	46.67	60	73.34	86.67	100	113.34
$R_i[\mu N]$	0.0320	0.0530	0.0696	0.0970	0.1132	0.1198	0.1212	0.1184	0.1158	0.1154	0.1156	0.1168	0.1178
$l_i^{peak}[nm]$	76.2	77.2	80.1	84.6	85.6	87.6	87	81.4	75	72.8	69.6	68.2	67.2
$l_i^{unload}[nm]$	69.8	69	70.2	65.8	63	64	66.2	66.2	63	58.8	57.8	55.4	54.8
$F_{init}[\mu N/m]$	9.1	5.1	3.9	2.8	2.3	1.9	1.7	1.5	1.3	1.1	1.0	1.0	0.9
$F_{def}^{peak}[\mu N/m]$	24.6	23.3	23.5	24.0	24.6	24.8	24.6	23.1	21.5	20.8	20.1	19.7	19.4
$F_{def}^{unload}[\mu N/m]$	22.8	21.4	21.3	21.1	21.2	21.4	21.4	20.4	19.1	18.3	17.7	17.3	17.0

Table 5.4: Studied roughness and related results – simulations on the microscale with a plane strain assumption. A_i is the initial amplitude, $\lambda = 200nm$ the wavelength, d_i the prescribed flattening of the asperities, R_i the generated reaction force per roughness peak, l_i^{peak} and l_i^{unload} are the plateau length at peak load and in the unloaded configuration respectively. F_{init}, F_{def}^{peak} and F_{def}^{unload} stand for the electrostatic force on the asperity for the initial shape, for the deformed shape at peak load and for the deformed shape in the unloaded configuration respectively for a potential difference of $0.1V$.

5.5.2 Analysis of the results of the uncoupled multi–physics numerical model

As mentioned before, the output of the microscale mechanical simulations (the deformed shapes of the roughness asperities) was used for the numerical evaluation of the adhesive electrostatic force between the gripper and the object, both conductors at the release of the manipulated object (performed by M. Sausse Lhernould). At contact some models (JKR [Johnson *et al.* 1971; Mate 2008], DMT [Derjaguin *et al.* 1975; Mate 2008]) provide closed form expressions of the adhesive force due to the interactions occurring in the contact area of rough *elastic* contacts. These theories are obviously no longer valid in the considered problem of micromanipulation, which induces significant plastic deformation of the surface roughness on the gripper arm.
To avoid these oversimplifying assumptions, the electrostatic numerical calculations are coupled (unilaterally) to the mechanical simulations of the surface roughness deformation described in the previous section. The adhesive electrostatic forces in the contact are considered to have no influence on the deformation of the surface roughness. When two dissimilar metal objects

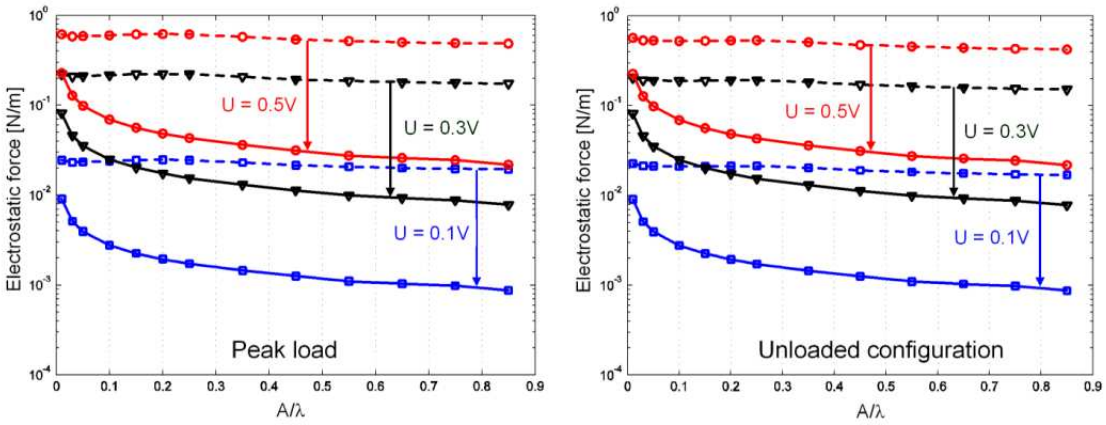

Figure 5.26: Results of the electrostatic simulation. Adhesive electrostatic forces before (solid lines) and after deformation (dotted lines) as a function of the A/λ ratio of the initial asperity profiles. Square marks stand for an applied voltage of $0.1V$, triangle marks for $0.3V$ and circle marks for $0.5V$. Left: for deformed shapes at peak load. Right: for the unloaded configuration.

are brought closer to each other, electrical interaction generates a contact potential difference, ranging usually for metals from U= $0V$ to $0.5V$ Bowling [1986], which depends on the properties of the considered conducting materials. The result is an attractive (or repulsive) electrostatic pressure. The electrostatic forces between two conductors are governed by the potential difference (materials), the permittivity (surrounding environment) and the area of contact (contact geometry). The electrostatic simulations here were performed at contact, i.e. at a chosen small separation distance (e.g. $z = 0.4nm$, as in Bowling [1986] to evaluate the electrostatic adhesion between the gripper and the object.

The numerical results are manifold considering the distribution of charges and the electrostatic force levels before and after the deformation of the roughness peak. The initial shape of the surface roughness was observed to have a significant influence both on the mechanical response to deformation (Fig.5.24) and on the magnitude of the generated electrostatic forces on the asperity surface (Fig.5.26). Electrostatic forces decrease with the increase of the amplitude A (for sharp geometries). The main concern of this study, i.e. the variation of the electrostatic force as a consequence of surface roughness deformation is considered in the following. The multiplicative factor γ between the electrostatic forces acting on the undeformed rough profile F_{init} and on the deformed profile F_{def} was found to be in the range $\gamma = \frac{F_{def}}{F_{init}} = [2...20]$ for the considered cases depending on the ratio of the amplitude A/λ of the initial profiles (Fig.5.27).

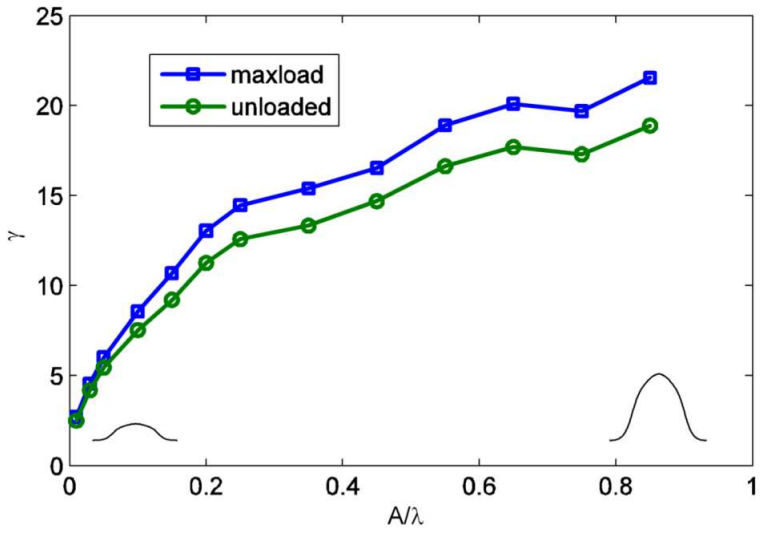

Figure 5.27: Variation of the multiplicative factor γ of the initial electrostatic force in the deformed configuration as a function of the amplitude to wavelength ratio A/λ of the initial asperity shape.

For the initially flattest peak the attractive electrostatic force before and after deformation is already doubled, and the most significant increase is observed for the sharpest asperities (with increasing A_i/λ). The significant increase in the adhesive electrostatic forces is related to the change in the distribution of the charges on the initial and on the deformed shape of the surface asperities.

Figure 5.28 depicts the typical electrostatic force and charge distribution in the initial and in the deformed configuration (for profile number 5 of Tab.5.4). The electrostatic forces are concentrated at the peak of the undeformed asperity. The deformed shape however has a portion with an almost flat surface (plateau) where the forces are uniformly distributed. Since electrostatic forces rapidly decrease with the separation distance, in the majority of cases the sides of the profile have almost no influence on the total adhesive electrostatic force. Consequently the

length of the formed plateau is a major parameter determining the overall electrostatic force in the deformed configuration. An exception is formed for blunt profiles with values of $A_i/\lambda < 0.01$ where the side effects cannot be neglected anymore.

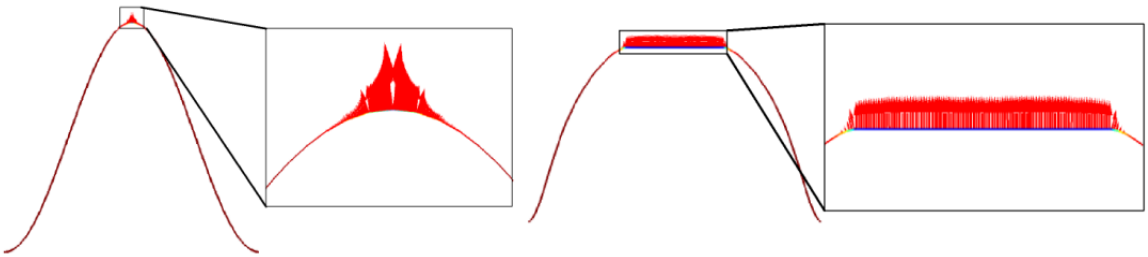

Figure 5.28: Charge and electrostatic force distribution in the undeformed (left) and in the deformed (right) configuration of profile number 5. In the undeformed configuration the charges are concentrated on the tip of the asperity, after deformation they are quasi uniformly distributed on the formed flat surface.

Considering the relatively simple charge and electrostatic force distribution in the initial and in the deformed configuration observed in the numerical model, two closed–form expressions can be proposed for the evaluation of the overall adhesive electrostatic force.

- In the undeformed configuration, the electrostatic force acting on the sinusoidal profile is evaluated using an analytical approximation for a cylinder–plane contact [Smythe 1968].
- In the deformed configuration the analytical expression is derived from the model for contact between two infinite planes [Fearing 1995], adding the length of the plateau l as parameter.

Taking the highest point of a roughness profile a_{top}, the plateau l is defined by all the points within a vertical cutoff distance of $0.4nm$ from a_{top}. The results are given both at peak load and in the unloaded configuration. The unloaded profiles slightly differ due to the elastic springback, a difference which influences the resulting electrostatic forces, especially for the blunt asperities. The length of the plateau at peak load l_i^{peak} increases until A_i/λ reaches 0.2 and then decreases while the length of the plateau in the unloaded configuration l_i^{unload} taking into account the elastic springback globally decreases with increasing A_i/λ values (Tab.5.4). The prediction of the numerical simulations and of the analytical approximations are in good agreement (Fig.5.29). The results of the geometrical approximation in the initial configuration are more reliable for small ratios of A/λ since the approximation of using a circle matches better the sinusoidal profiles in that case. The error remains less than 10% for profiles with $A/\lambda < 0.4$. There is less than 5% error for most ratios A_i/λ in the deformed configuration at peak load. The geometrical approximation becomes unreliable only for $A_i/\lambda < 0.01$ due to side effects (non–negligable contribution of the sides of the profile to the electrostatic forces) on

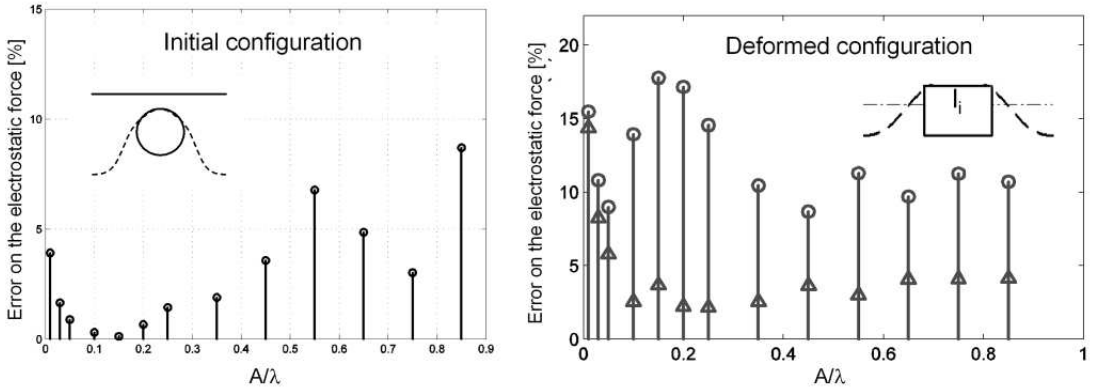

Figure 5.29: Comparison between the analytical expression and the numerical model predictions. Left: for initial profile shapes. Right: in the deformed configuration for maximum load (triangle marks) and in the unloaded configuration (circle marks).

the blunt profile. The error is of course larger in the unloaded configuration due to the elastic springback which slightly curves the plateau on the sides. Indeed the plateau length definition is less accurate in this configuration but the side effects are also more important. From the above approximations it is possible to estimate with a rather good accuracy the magnification factor γ of the electrostatic forces on the surface asperities in the initial configuration and after deformation, knowing the shape of the initial profiles and the length of the formed plateau.

$$\gamma = \frac{2l}{\lambda}\sqrt{\frac{2A}{z}} \tag{5.13}$$

with l the length of the plateau, λ and A the wavelength and amplitude of the sine approximation, respectively and z the separation distance. The good agreement between the analytical expression and the numerical predictions in both cases confirms that for most profiles the presence of *the plateau plays the significant role* and the side effects can be neglected.

5.5.3 Concluding remarks

The important effect of surface roughness deformation was demonstrated using an uncoupled multi–physics numerical model, since the initial electrostatic forces on the asperities are magnified by a factor $\gamma = [2...20]$ after plastic deformation. The small magnitude of the electrostatic interaction forces with respect to the mechanical forces necessary to deform the asperities (Tab. 5.4) confirms the unilateral coupling of the electrostatic model to the microscale contact model.

The observed effect clearly gives a contribution to the difficulty to release objects when the squeezing manipulation force is released. The key role of the flat surface formed on the deformed profiles on the increase of electrostatic forces was identified and confirmed using a closed form approximation of the electrostatic forces based on the plateau length.

The obtained magnifying factor of the electrostatic forces related to the plastic deformation effect $\gamma = [2...20]$ seems merely a lower bound of the effect of the surface roughness deformation on electrostatic adhesion. As pointed out before the imposed flattening in the microscale model of $d_i = 2A_i/3$ gives probably a lower bound to the magnitude of the deformation of the surface asperities with respect to the real micromanipulation setting. Moreover, in the case of real surfaces, considering the predictions of the numerical model used for the evaluation of the electrostatic forces the charges would concentrate on the tip of asperities of the highest order roughness, thereby further decreasing the initial electrostatic forces. During deformation more than one level of asperities (considering the protuberance-on-protuberance model) can be crushed and γ could reach even higher values than the ones reported here.

These observations lead to the conclusion that decreasing the plastic deformation of surface asperities could substantially contribute to decrease release problems related to electrostatic forces in micromanipulation by contact (e.g. application of coatings with elastic behavior in a more extended range).

Chapter 6

Conclusion and perspectives

The objective of the conducted research work was to build a more complete understanding of the behavior of surfaces and of the nanoindentation as one of its characterization tools. The corresponding experience can be used as a set of information for the interpretation of the nanoindentation experiment. Numerical models were set up on different levels and were shown to give insight into the physics of some of the phenomena related to the behavior of pure nickel material on the nanoscale. Valuable information can be obtained from numerical models, since all parameters are accessible and can be freely varied, which becomes particularly advantageous when numerical simulations are coupled to experiments. However, care has to be taken to keep physically–based arguments for such models.
In the present work, adapted numerical tools were developed to study the behavior of pure nickel.

- The atomic level model of quasi–static nanoindentation of pure nickel has the interesting feature of being a natural frame for the identification of physically based trends. The main drawback of lacking the possibility of a direct comparison with the experiments (impossibility of bridging the different time and length scales) is balanced by this prime advantage. A relatively efficient computation was conducted in Section 3.1 due to the simplifying assumptions.

- The continuum scale model, presented in Chapter 4 is applicable to a large variety of metallic materials, and has the major advantage of being directly comparable to the experiments. Hence a good qualitative and quantitative agreement with the experimental data can be searched for, allowing trends and dominant sources of scattering to be identified using coupled experimental–numerical studies. The model development required adding nonlinear material behavior (plasticity) and transforming the initial infinitesimal deformation description to a corotational finite deformation formulation to represent the

material behavior correctly. Furthermore normal and tangential contact constraints of the Coulomb dry friction model were included in an augmented Lagrangian formulation solved using a continuous multiplier update scheme to represent the experimental evolving contact conditions. These developments satisfy the predefined requirements of efficiency, relatively simple implementation and flexibility. Flexibility is ensured since all sources of nonlinearities are fully decoupled in the resulting program, which implies that changing the material or contact behavior or the finite deformation formulation, leads to changing the corresponding building block only.

The prime objectives of the research work were reached, since important contributions to the understanding of pure nickel material were given on the material characterization level (nanoindentation)

- different contributions to the atomic scale response were identified using the atomic scale discrete model,
- taking into account the rate–dependent plastic behavior of pure nickel in nanoindentation was shown to be a physically–based need by a coupled experimental–numerical study using a continuum scale model,
- the large influence of the coupled effect of friction and sample surface roughness was identified and evaluated in a numerical study using a continuum scale model.

On the level of microscale applications (microgripper) the large influence of irreversible surface asperity deformation on the increase of electrostatic–based adhesion between the gripper and the object was identified and the factor of increase evaluated.
Additional results with a practical interest are the evaluation of the performance of the considered nanoindentation post–treatment methods in realistic indentation configurations.

Outlook and perspectives

The numerical developments necessary for obtaining the above results required using advanced numerical methods. The logical order of constructing a basis of knowledge starting from the analysis of simple cases before advancing to more complex subjects had to be respected considering the complexity of the numerical developments and the difficulty of interpreting experimental results even for simple configurations. The acquired experience for the considered simple cases could be extended for more advanced applications in a future work.
Additional studies to conduct and numerical building blocks to be added can be identified from the results presented here, to broaden the field of application of the developed numerical tools. The most relevant ones of this context are presented in the following without however constituting an exhaustive list.

- The presented numerical models were set up on the smallest (atomic level discrete model) and on the largest (continuum description) scales. The description of the nanoindentation experiment on an intermediate scale, potentially building a bridge between the studied atomic and continuum scales (by dislocation dynamics [Widjaja *et al.* 2007], or the quasi–continuum methods for example) could allow exploiting results issued from small scales on larger scales on a physically sound basis.

- The present study should be extended on pure titanium (having a hexagonal crystalline structure, implying a different material and frictional response) to confirm a potential generalization of the results for all considered metallic substrate materials in the project $m\mu n$, having a potential biomedical application. Since the experimental results are available and the numerical tools are directly applicable to the case of pure titanium on the continuum scale, this study is readily feasible.

- The study of the rate–dependent material behavior and its influence on nanoindentation results [Cheng & Cheng 2005; Ovaert *et al.* 2003] can be continued. Including a rate–dependent plastic model in the existing code will result in the more representative description of the behavior of the considered metallic materials.

- In view of the potential significant influence of material size effects in small indentation depth (potentially used for thin film characterization), including a material model with size–dependent plastic behavior [Evers 2003; Gao & Huang 2003; Gao *et al.* 1999; Gao & Fan 2002; Qiu *et al.* 2003] in the continuum model, in convolution with a coupled experimental–numerical study aiming for the identification of material size effects in the considered metallic materials can be of interest. Two main issues of this development step were identified: (i) definition of an experimental program that sheds light to material size effects of the considered metallic materials, and (ii) choice and implementation of the adequate gradient plasticity formulation, which can be potentially included in the present numerical scheme.

- Frictional effects in nanoindentation of rough surfaces were found to be significant in the numerical study of Section 5.3. This trend could be verified experimentally in controlled indentation configurations in a future work. Experimentally the variation of the friction in the indenter–sample contact can be obtained by applying a thin silver coating on the sample surface to reduce friction. This first step sketched here is prone to lead to an extensive coupled experimental–numerical investigation of frictional effects in nanoindentation.

- In the present study the phenomenological Coulomb friction law was used. More adapted friction models for the considered scale can be included in the continuum model to study

the influence of the tangential contact behavior in a future work. As pointed out in Chapter 4 a tangential contact law, independent of the normal contact force seems in some cases to describe the nanoscale contact behavior well [Carpick *et al.* 1996, 1997, 2001]. Including such a contact law in the numerical tool can be considered as 'downgrading' the present Coulomb friction model. This manipulation is straightforward and has an additional beneficial effect on the convergence rate of the computation. The procedure of identifying the value of the constant stick limit parameter remains however to be discussed. The trends obtained from the numerical study could be verified in an experimental program.

- The analysis of the behavior of thin films and multi–layer sandwiches [Xu 2004], to help the interpretation of the experimental data compacting all experimental effects are among the most important extensions of the present study from the point of view of practical applications. An important branch of this step is the study of the deformation and delamination of thin films both on the continuum level [Abdul-Baqi 2002; Geng *et al.* 2007; van den Bosch 2007] and on the atomic (or some intermediate) scale to identify major physical trends [Nair *et al.* 2008]. For this purpose an increase in the size of the atomic scale model and the use of more realistic potentials to describe inter–atomic interactions are necessary in the first place, to obtain a better representation of the physics of nanoindentation. The continuum numerical model should incorporate interface elements capable of representing this type of damage in a finite displacement and deformation theory, leading to a relatively complex formulation [van den Bosch 2007].

- A future goal is to broaden the scope of the identified material parameters (particularly the ones related to the plastic material behavior) by implementing more advanced work–of–indentation based post–treatment methods of nanoindentation [Cao & Lu 2004; Ma *et al.* 2003; Zhao *et al.* 2006] in the numerical post–treatment tool. In a parametric numerical study the performance of some of these methods could be addressed, which could potentially contribute to the interpretation and a deeper understanding of nanoindentation results.

- The development of an advanced multi–physics finite element model, including adhesive effects (stemming from electrostatic, van der Waals, and capillary forces) in mechanical simulations for applications of micromanipulation is also of interest, allowing a direct and coupled treatment of the mechanical deformation and the contact adhesion. The resulting numerical tool could have a large domain of application on small scales. It would be particularly useful for the study of pull–off effects in AFM experiments, for which the coupled effect of plastic deformation and adhesion are probably responsible.

All listed aspects can be addressed based on the research work summed up in this thesis. The further development of the present numerical tools, and potentially the exploration of the intermediate scales by adapted numerical methods are among the main challenges of the future work. Similarly to the present research, the in–depth investigation of the mechanical behavior of materials and single–or multi–layered material sandwiches will be best ensured by experiments coupled to numerical simulations.

Bibliography

Abdul-Baqi, A. 2002. *Failure of Brittle Coatings on Ductile Metallic Substrates*. Ph.D. thesis, Technical University of Delft.

AFNOR. 1990. *Guide de validation de progiciels de calcul de structures*. AFNOR Technique.

Agnus, J., Clévy, C., Urushima, Y., & Perez, R. 2004. A micromanipulation station based on a new integrated microprehensile microrobot on a chip (mmoc). *In: Proc. of the 35th Int. Symposium on Robotics - ISR 2004, Paris, France.*

Aifantis, K.E., & Ngan, A.H.W. 2007. Modeling dislocation-grain boundary interactions through gradient plasticity and nanoindentation. *Mat. Sci. Eng. A*, **459**, 251–261.

Al-Rub, K.R. Abu, Voyiadjis, G.Z., & Bammann, D.J. 2007. A thermodynamic based higher-order gradient theory for size dependent plasticity. *Int. J. Sol. Struct.*, **44**, 2888–2923.

Al-Rub, R.K. Abu. 2007. Prediction of micro and nanoindentation size effect from conical and pyramidal indentation. *Mech. Mat.*, **39**, 787–802.

Alart, P., & Curnier, A. 1991. A mixed formulation for frictional contact problems prone to Newton like solution methods. *Comp. Meth. Appl. Mech. Eng.*, **92**, 353–375.

André, N., Coulombier, M., Longueville, V. De, Fabrègue, D., Gets, T., Gravier, S., Pardoen, T., & Raskin, J.-P. 2007. Microfabrication-based nanomechanical laboratory for testing the ductility of submicron aluminium films. *Microelectronic Eng.*, **84**, 2714–2718.

Antunes, J.M., Menezes, L.F., & Fernandes, J.V. 2006. Three-dimensional numerical simulation of Vickers indentation tests. *Int. J. Sol. Struct.*, **43**, 784–806.

Antunes, J.M., Fernandes, J.V., Menezes, L.F., & Chaparro, B.M. 2007. A new approach for reverse analysis in depth-sensing indentation using numerical simulation. *Acta Mat.*, **55**, 69–81.

ARC(04/09-310). 2003. *Miniaturization of Micromanipulators by characterizing and modeling Nanomaterials, Action de Recherche Concertée (ARC) Convention 04/09-310*.

Areias, P.M.A., de Sá, J.M.A. César, & António, C.A. Conceição. 2003. A gradient model for finite strain elastoplasticity coupled with damage. *Fin. Elem. Analys. Design*, **39**, 1191–1235.

Argon, A.S. 1975. *Constitutive equations in plasticity*. M.I.T. Press.

Arora, J.S., Chahande, A.I., & Paeng, J.K. 1991. Multiplier methods for engineering optimization. *Int. J. Num. Meth. Eng.*, **32**, 1485–1525.

ASM. 1990. *ASM handbook: Volume 2 : Properties and selection : nonferrous alloys and special-purpose materials 10. ed.* Materials Park, OH, ISBN: 0-87170-378-5.

Azushima, A., Kuba, S., Tani, S., & Olsson, D.D. 2006. Direct observation of asperity deformation of specimens with random rough surfaces in upsetting and indentation processes. *Wear*, **260**, 258–264.

Baillet, L., & Sassi, T. 2003. Mixed finite element formulation in large deformation frictional contact problem. *In: Proc. 7th International Conference on Computational Plasticity, Complas, Barcelona*.

Baker, S.P. 1997. Between nanoindentation and scanning force microscopy: measuring mechanical properties in the nanometer regime. *Thin Sol. Films*, **308-309**, 289–296.

Baker, S.P. 2001. *Encyclopedia of Materials: Science and Technology*. Elsevier Science Ltd. Chap. Nanoindentation techniques.

Balint, D.S., Deshpande, V.S., Needleman, A., & der Giessen, E. Van. 2008. Discrete dislocation plasticity analysis of the grain size dependence of the flow strength of polycrystals. *Int. J. Plas.*, **24**, 2149–2172.

Barber, J.R., & Ciavarella, M. 2000. Contact Mechanics. *Int. J. Sol. Struct.*, **37**, 29–43.

Barshilia, H.C., & Rajam, K.S. 2002. Characterization of Cu/Ni multilayer coatings by nanoindentation and atomic force microscopy. *Surf. Coat. Tech.*, **155**, 195–202.

Beegan, D., Chowdhury, S., & Laugier, M.T. 2005. Work of indentation methods for determining copper film hardness. *Surf. Coat. Tech.*, **192**, 57–63.

Bell, T., Mao, K., & Sun, Y. 1998. Surface engineering design: modelling surface engineering systems for improved tribological performance. *Surf. Coat. Tech.*, **108-109**, 360–368.

Bellemare, S., Dao, M., & Suresh, S. 2007. The frictional sliding response of elasto-plastic materials in contact with a conical indenter. *Int. J. Sol. Struct.*, **44**, 1970–1989.

Bellemare, S.C., Dao, M., & Suresh, S. 2008. Effects of mechanical properties and surface friction on elasto-plastic sliding contact. *Mech. Mat.*, **40**, 206–219.

Belytschko, T., Liu, W.K., & Moran, B. 2000. *Nonlinear Finite Elements for Continua and Structures*. John Wiley & Sons, Ltd., ISBN 471-98774-3.

Berke, P., & Massart, T.J. 2006. Numerical simulation of the nanoindentation experiment: influence of the experimental uncertainties. *Pages 963–965 of: Proc. of the Third International Conference Multiscale Material Modeling, Freiburg, Germany*.

Bhushan, B. 2003. Adhesion and stiction: mechanisms, measurement techniques, and methods for reduction. *J. Vacuum Sci. Tech. B*, **21**, 2262–2296.

Bobji, M.S., & Biswas, S.K. 1999. Hardness of a surface containing uniformly spaced pyramidal asperities. *Trib. Lett.*, **7**, 51–56.

Bobji, M.S., Shivakumar, K., Alehossein, H., Venkateshwarlu, V., & Biswas, S.K. 1999. Influence of surface roughness on the scatter in hardness measurements - a numerical study. *Int. J. Rock Mech. Mining Sci.*, **36**, 399–404.

Bolzon, G., Maier, G., & Panico, M. 2004. Material model calibration by indentation, imprint mapping and inverse analysis. *Int. J. Sol. Struc.*, **41**, 2957–2975.

Bora, C.K., Plesha, M.E., Flater, E.E., Street, M.D., & Carpick, R.W. 2004. Multi-scale roughness of MEMS surfaces. *In: Proc. of the 2004 ASME/STLE Joint International Tribology Conference, Long Beach CA*.

Bora, C.K., Flater, E.E., Street, M.D., Redmond, J.M., Starr, M.J., Carpick, R.W., & Plesha, M.E. 2005. Multiscale roughness and modeling of MEMS interfaces. *Trib. Lett.*, **19**, 37–48.

Bouzakis, K.-D., Michailidis, N., & Erkens, G. 2001. Thin hard coatings stress-strain curve determination through a FEM supported evaluation of nanoindentation test results. *Surf. Coat. Tech.*, **142-144**, 102–109.

Bouzakis, K.D., & Michailidis, N. 2004. Coating elastic-plastic properties determined by means of nanoindentations and FEM–supported evaluation algorithms. *Thin Sol. Films*, **469-470**, 227–232.

Bowling, R.A. 1986. A theoretical review of particle adhesion. *Page 129 of: Proc. of Symposium on particles on surfaces 1: Detection, Adhesion and Removal, San Francisco*.

Bowman, K. 2004. *Mechanical Behavior of Materials*. John Wiley & Sons, Inc.

Bressan, J.D., Tramontin, A., & Rosa, C. 2005. Modeling of nanoindentation of bulk and thin film by finite element method. *Wear*, **258**, 115–122.

Bucaille, J.-L., Stauss, S., Schwaller, P., & Michler, J. 2004. A new technique to determine the elastoplastic properties of thin metallic films using sharp indenters. *Thin Sol. Films*, **447-448**, 239–245.

Bucaille, J.L., Stauss, S., Felder, E., & Michler, J. 2003. Determination of plastic properties of metals by instrumented indentation using different sharp indenters. *Acta Mat.*, **51**, 1663–1678.

Bulatov, V.V. 2008. *Materials Issues for Generation IV Systems Status, Open Questions and Challenges*. Springer Science + Business Media B.V. 2008, ISBN: 978-1-4020-8423-2. Chap. Crystal Plasticity from Dislocation Dynamics, pages 275–284.

Burguera, M., & Viano, J.M. 1994. Numerical solving of frictionless contact problems in perfectly plastic bodies. *Comp. Meth. Appl. Mech. Eng.*, **121**, 303–322.

Bushnell, D. 1977. A strategy for the solution of problems involving large deflections, plasticity and creep. *Int. J. Num. Meth. Eng*, **11**, 682–708.

Buzio, R., Boragno, C., & Valbusa, U. 2003. Contact mechanics and friction of fractal surfaces probed by atomic force microscopy. *Wear*, **254**, 917–923.

Cai, X., & Bangert, H. 1995. Hardness measurements of thin films - determining the critical ratio of depth to thickness using FEM. *Thin Sol. Films*, **264**, 59–71.

Cao, Y., Qian, X., & Huber, N. 2007. Spherical indentation into elastoplastic materials: Indentation-response based definitions of the representative strain. *Mat. Sci. Eng. A*, **454-455**, 1–13.

Cao, Y.P., & Lu, J. 2004. A new method to extract the plastic properties of metal materials from an instrumented spherical indentation loading curve. *Acta Mat.*, **52**, 4023–4032.

Carlsson, S., Biwa, S., & Larsson, P.-L. 2000. On friction effects at inelastic contact between spherical bodies. *Int. J. Mech. Sci.*, **42**, 107–128.

Carpick, R.W., Agraït, N., Ogletree, D.F., & Salmeron, M. 1996. Measurement of interfacial shear (friction) with an ultrahigh vacuum atomic force microscope. *J. Vac. Sci. Technol. B*, **14**, 1289–1295.

Carpick, R.W., Ogletree, D.F., & Salmeron, M. 1997. Lateral stiffness: A new nanomechanical measurement for the determination of shear strengths with friction force microscopy. *Appl. Phys. Lett.*, **70**, 1548–1550.

Carpick, R.W., Langedon, J. R. Van, Wilson, E. H., & Sridharan, K. 2001. Nanocontacts: Fabrication, characterization, and nanotribology studies (p.725). *In: Proc. of the SEM VII International Congress and Exposition on Experimental and Applied Mechanics*.

Carpick, R.W., Flater, E.E., Langendon, J.R. Van, & de Boer, M.P. 2002. Friction in MEMS: from single to multiple asperity contact. *Page 282 of: Proc. of the SEM VIII International Congress and Exposition on Experimental and Applied Mechanics*.

Chabrand, P., Dubois, F., Graillet, D., Boman, R., & Ponthot, J.P. 2005. Numerical simulation of tribological devices used as a set of benchmarks for comparing contact algorithms. *Fin. El. Analys. Design*, **41**, 637–665.

Chambon, R., Caillerie, D., & Tamagnini, C. 2001. A finite deformation second gradient theory of plasticity. *C. R. de l'Acad. Sci. - Série IIB - Mech.*, **329**, 797–802.

Chambon, R., Caillerie, D., & Tamagnini, C. 2004. A strain space gradient plasticity theory for finite strain. *Comp. Meth. Appl. Mech. Eng.*, **193**, 2797–2826.

Chen, Z. 2001. On the augmented Lagrangian approach to Signorini elastic contact problem. *Numer. Math.*, **88**, 641–659.

Cheng, Y.-T., & Cheng, C.-M. 2004. Scaling, dimensional analysis, and indentation measurements. *Mat. Sci. Eng. R*, **44**, 91–149.

Cheng, Y.-T., & Cheng, C.-M. 2005. Relationships between initial unloading slope, contact depth and mechanical properties for spherical indentation in linear viscoelastic solids. *Mat. Sci. Eng. A*, **409**, 93–99.

Cho, M.H., Kim, S.J., Lim, D.S., & Jang, H. 2005. Atomic scale stick–slip caused by dislocation nucleation and propagation during scratching of a Cu substrate with a nanoindenter: a molecular dynamics simulation. *Wear*, **259**, 1392.

Christopher, D., Smith, R., & Richter, A. 2001. Nanoindentation of carbon materials. *Nucl. Instrum. Meth. Phys. Res. B*, **180**, 117.

Chudoba, T., & Richter, F. 2001. Investigation of creep behaviour under load during indentation experiments and its influence on hardness and modulus results. *Surf. Coat. Tech.*, **148**, 191–198.

Ciavarella, M., Dibello, S., & Demelio, G. 2008. Conductance of rough random profiles. *Int. J. Sol. Struc.*, **45**, 879–893.

Crisfield, M.A. 1995. *Non linear finite elements analysis of solids and structures - Volume 2: Advanced topics*. Wiley and Sons.

de Borst, R., & Mühlhaus, H.-B. 1992. Gradient-dependent plasticity formulation and algorithmic aspects. *Int. J. Num. Meth. Eng.*, **35**, 521–539.

de Souza, G.B., Foerster, C.E., da Silva, S.L.R., Serbena, F.C., Lepienski, C.M., & dos Santos, C.A. 2005. Hardness and elastic modulus of ion-nitrided titanium obtained by nanoindentation. *Surf. Coat. Tech.*, **191**, 76–82.

de Souza, G.B., Foerster, C.E., da Silva, S.L.R., & Lepienski, C.M. 2006. Nanomechanical properties of rough surfaces. *J. Mat. Res.*, **9**, 159–163.

de With, G. 1999. *Structure, Deformation, and Integrity of Materials*. Wiley-VCH Verlag GmbH & Co. KGaA, ISBN 0-471-24317-5.

Delincé, M., Jacques, P.J., & Pardoen, T. 2006. Separation of size-dependent strengthening contributions in fine-grained Dual Phase steels by nanoindentation. *Acta Mat.*, **54**, 3395–3404.

Derjaguin, B.V., Muller, V.M., & Toporov, Y.P. 1975. Effect of contact deformations on the adhesion of particles. *J. of Colloid and Interface Sci.*, **53**, 314–326.

Deshpande, V.S., Balint, D.S., Needleman, A., & der Giessen, E. Van. 2007. Size effects in single asperity frictional contacts. *Mod. Sim. Mat. Sci. Eng.*, **15**, S97–S108.

Ebrahimi, F., Bourne, G.R., Kelly, M.S., & Matthews, T.E. 1999. Mechanical properties of nanocrystalline nickel produced by electrodeposition. *Nanostruct. Mat.*, **11**, 343–350.

Evers, L.P. 2003. *Strain Gradient Plasticity Based on Dislocation Densities*. Ph.D. thesis, Technical University of Eindhoven.

Fang, T.-H., Weng, C.-I., & Chang, J.-G. 2003. Molecular dynamics analysis of temperature effects on nanoindentation measurement. *Mat. Sci. Eng. A*, **357**, 7.

Fang, T.-H., Chang, W.-J., & Weng, C.-I. 2006. Nanoindentation and nanomachining characteristics of gold and platinum thin films. *Mat. Sci. Eng. A*, **430**, 332.

Fang, T.-H., Chang, W.-J., & Lin, C.-M. 2007. Nanoindentation characterization of ZnO thin films. *Mat. Sci. Eng. A*, **452–453**, 715–720.

Fearing, R.S. 1995. Survey of sticking effects for micro parts handling. *Pages 212–217 of: Proc. of IEEE/RSJ Conf. on Intelligent Robots and Systems*.

Feng, Z.Q., Magnain, B., Cros, J.M., & Joli, P. 2004. Energy dissipation by friction in dynamic multibody contact problems. *In: World Congress of Computational Mechanics, WCCM VI in conjunction with APCOM'04, Beijing, China*.

Fischer-Cripps, A.C. 2004. A simple phenomenological approach to nanoindentation creep. *Mat. Sci. Eng. A*, **385**, 74–82.

Fischer-Cripps, A.C. 2006. Critical review of analysis and interpretation of nanoindentation test data. *Surf. Coat. Tech.*, **200**, 4153–4165.

Fleck, N.A., & Hutchinson, J.W. 1997. Strain gradient plasticity. *Adv. App. Mech.*, **33**, 295–361.

Fleck, N.A., & Hutchinson, J.W. 2001. A reformulation of strain gradient plasticity. *J. Mech. Phys. Sol.*, **49**, 2245–2271.

Frick, C.P., Clark, B.G., Orso, S., Schneider, A.S., & Arzt, E. 2008. Size effect on strength and strain hardening of small-scale [1 1 1] nickel compression pillars. *Mat. Sci. Eng. A*, **489**, 319–329.

Fujikane, M., Leszcznski, M., Nagao, S., Nakayama, T., Yamanaka, S., Niihara, K., & Nowak, R. 2008. Elastic–plastic transition during nanoindentation in bulk GaN crystal. *J. Alloys Compounds*, **450**, 05–411.

Gao, H., & Huang, Y. 2003. Geometrically necessary dislocation and size–dependent plasticity. *Script. Mat.*, **48**, 113–118.

Gao, H., Huang, Y., Nix, W.D., & Hutchinson, J.W. 1999. Mechanism–based strain gradient plasticity - I. Theory. *J. Mech. Phys. Sol.*, **47**, 1239–1263.

Gao, Y.X., & Fan, H. 2002. A micro-mechanism based analysis for size-dependent indentation hardness. *J. Mat. Sci.*, **37**, 4493–4498.

Geers, M.G.D. 2001. *Grasmech Course on Plasticity*. Tech. rept. Technical University of Eindhoven.

Geng, K., Yang, F., Druffel, T., & Grulke, E.A. 2007. Nanoindentation-induced delamination of submicron polymeric coatings. *Polymer*, **48**, 841–848.

Giannakopoulos, A.E., & Suresh, S. 1999. Determination of elastoplastic properties by instrumented sharp indentation. *Scripta Mat.*, **40**, 1191–1198.

Gomez, J., & Basaran, C. 2006. Nanoindentation of Pb/Sn solder alloys: experimental and finite element simulation results. *Int. J. Sol. Struct.*, **43**, 1505–1527.

Goodall, R., & Clyne, T.W. 2006. A critical appraisal of the extraction of creep parameters from nanoindentation data obtained at room temperature. *Acta Mat.*, **54**, 5489–5499.

Gouldstone, A., Chollacoop, N., Dao, M., Li, J., Minor, A. M., & Shen, Y.-L. 2007. Indentation across size scales and disciplines: Recent developments in experimentation and modeling. *Acta Mat.*, **55**, 4015–4039.

Greenwood, J.A., & Williamson, J.B.P. 1966. Contact of nominally flat surfaces. *Proc. R. Soc. London A*, **295**, 300–319.

Guidry, D.J. 1999. *Tribological behavior of nanostructured nickel*. M.Phil. thesis, Louisiana State University.

Habbab, H., Mellor, B.G., & Syngellakis, S. 2006. Post-yield characterisation of metals with significant pile-up through spherical indentations. *Acta Mat.*, **54**, 1965–1973.

Hagelaar, J.H.A., Bitzek, E., Flipse, C.F.J., & Gumbsch, P. 2006. Atomistic simulations of the formation and destruction of nanoindentation contacts in tungsten. *Phys. Rev. B*, **73**, 045425.

Hainsworth, S.V., & Soh, W.C. 2003. The effect of the substrate on the mechanical properties of TiN coatings. *Surf. Coat. Tech.*, **163–164**, 515–520.

Han, W., & Sofonea, M. 2000. Numerical analysis of a frictionless contact problem for elastic-viscoplastic materials. *Comp. Meth. Appl. Mech. Eng.*, **190**, 179–191.

Harano, T. 2004. A fundamental study on friction and wear behavior between metals by MD simulation (20041126). *In: Proc. MPT Fukuoka : the JSME international conference on motion and power transmissions, The Japan Society of Mechanical Engineers*.

He, L.H., & Swain, M.V. 2007. Enamel - a ”metallic-like” deformable biocomposite. *J. Dentistry*, **35**, 737–743.

Heegaard, J.-H., & Curnier, A. 1993. An augmented Lagrangian method for discrete large-slip contact problems. *Int. J. Num. Meth. Eng.*, **36**, 569–593.

Heegaard, J.H., & Curnier, A. 1995. Geometric properties of 2D and 3D unilateral large slip contact operators. *Comp. Meth. Appl. Mech. Eng.*, **131**, 263–286.

Hertz, H. 1882. Über die Berührung fester elastischer Körper. *J. reine und angewandte Mathematik*, **92**, 156–171.

Hill, R. 1956. *The mathematical theory of plasticity*. University Press,Oxford.

Hollang, L., Hieckmann, E., Brunner, D., Holste, C., & Skrotzki, W. 2006. Scaling effects in the plasticity of nickel. *Mat. Sci. Eng. A*, **424**, 138–153.

Horstemeyer, M.F., Baskes, M.I., & Plimpton, S.J. 2001. Length scale and time scale effectsnext term on the plastic flow of fcc metals. *Acta Mat.*, **49**, 4363–4374.

Hugues, T.J.R. 1984. *Numerical implementation of constitutive models: rate independent deviatoric plasticity*. Marinus Nijhof Publishers, Doordrecht, The Nederlands.

Hult, J., & Lemaitre, J. 1981. *Physical non–linearities in structural analysis*. I.U.T.A.M. Symposium Springer–Verlag.

Hysitron. 2008. *Hysitron Triboindenter, www.hysitron.com*.

Idesman, A.V., & Levitas, V.I. 1994. Finite element procedure for solving contact thermoplastic problems at large strains, normal and high pressures. *Comp. Meth. Appl. Mech. Eng.*, **126**, 39–66.

Israelachvili, J. N. 1974. The nature of van der Waals forces. *Contemporary Phys.*, **15**, 159–177.

Jackson, R.L., & Streator, J.L. 2006. A multi–scale model for contact between rough surfaces. *Wear*, **261**, 1337–1347.

Jamari, J., & Schiper, D.J. 2007. Deformation due to contact between a rough surface and a smooth ball. *Wear*, **262**, 138–145.

Jang, J.-I., & Pharr, G.M. 2008. Influence of indenter angle on cracking in Si and Ge during nanoindentation. *Acta Mat.*, **56**, 4458–4469.

Jefferson, A.D. 2003. Craft - a plastic-damage-contact model for concrete. I. Model implementation with implicit return-mapping algorithm and consistent tangent matrix. *Int. J. Sol. Struct.*, **40**, 6001–6022.

Jeong, S.-M., & Lee, H.-L. 2005. Finite element analysis of the tip deformation effect on nanoindentation hardness. *Thin Sol. Films*, **492**, 173–179.

Jian, S.-R., Fang, T.-H., Chuu, D.-S., & Ji, L.-W. 2006. Atomistic modeling of dislocation activity in nanoindented GaAs. *Appl. Surf. Sci.*, **253**, 833–840.

Johnson, K.L., Kendall, K., & Roberts, A.D. 1971. Surface energy and the contact of elastic solids. *In: Proc. R. Soc. London Series A 324: 301*.

Kachanov, L.M. 1971. *Foundations of the theory of plasticity*. North–Holland Publication company.

Kelchner, C.L., Plimpton, S. J., & Hamilton, J. C. 1998. Dislocation nucleation and defect structure during surface indentation. *Phys. Rev. B*, **58**, 11085.

Kermouche, G., Loubet, J.L., & Bergheau, J.M. 2007. Cone indentation of time-dependent materials: The effects of the indentation strain rate. *Mech. Mat.*, **39**, 24–38.

Kim, J.-Y., Lee, B.-W., Read, D.T., & Kwon, D. 2005. Influence of tip bluntness on the size-dependent nanoindentation hardness. *Scripta Mat.*, **52**, 353–358.

Kim, J.-Y., Kang, S.-K., Lee, J.-J., Jang, J., Lee, Y.-H., & Kwon, D. 2007. Influence of surface-roughness on indentation size effect. *Acta Mat.*, **55**, 3555–3562.

Kim, N.H., Choi, K.K., Chen, J.S., & Park, Y.H. 2000. Meshless shape design sensitivity analysis and optimization for contact problem with friction. *Comp. Mech.*, **25**, 157–168.

Kim, S.H., Lee, B.W., Choi, Y., & Kwon, D. 2006. Quantitative determination of contact depth during spherical indentation of metallic materials—A FEM study. *Mat. Sci. Eng. A,* **415**, 59–65.

Kittel, C. 1996. *Introduction to Solid State Physics, 7th edn*. John Wiley and Sons.

Knap, J., & Ortiz, M. 2001. An analysis of the quasicontinuum method. *J. Mech. Phys. Sol.*, **49**, 1899–1923.

Kojima, Y., Shimab, M., Motodac, T., Jibikib, T., & Sugawarab, T. 2007. An estimation of friction from the indentation of metals by acute-angled conical indenters. *Tribology Int.*, **40**, 1479–1483.

Komanduri, R., Chandrasekaran, N., & Raff, L.M. 2000. MD simulation of indentation and scratching of single crystal aluminum. *Wear*, **240**, 113.

Kontoleon, M.J., & Baniotopoulos, C.C. 2000. Computational aspects on the frictional unilateral contact problem arising on steel base plate connections. *Comp. Struct.*, **78**, 303–309.

Kontoleon, M.K., Mistakidis, E.S., Baniotopoulos, C.C., & Panagiotopoulos, P.D. 1999. Parametric analysis of the structural response of steel base plate connections. *Comp. Struct.*, **71**, 87–103.

Kostoglou, M., & Karabelas, A.J. 1995. Effect of roughness on energy of repulsion between colloidal surfaces. *J. Colloid Interface Sci.*, **171**, 187–199.

Kovács, I., & Vörös, G. 1996. On the mathematical description of the tensile stress-strain curves of polycrystalline face centered cubic metals. *Int. J. Plas*, **12**, 35–43.

Kramer, D., Huang, H., Kriese, M., Robach, J., Nelson, J., Wright, A., Bahr, D., & Gerberich, W.W. 1998. Yield strength predictions from the plastic zone around nanocontacts. *Acta Mat.*, **47**, 333–343.

Kreuzer, H.G.M., & Pippan, R. 2004. Discrete dislocation simulation of nanoindentation: the effect of moving conditions and indenter shape. *Mat. Sci. Eng. R*, **387-389**, 254–256.

Kulkarni, A.V., & Bhushan, B. 1996. Nanoscale mechanical property measurements using modified atomic force microscopy. *Thin Sol. Films*, **290**, 206.

Kumar, A.K. Nanda, Kannan, M.D., Jayakumar, S., Rajam, K.S., & Raju, V.S. 2006. Investigations on the mechanical behaviour of rough surfaces of TiNi thin films by nanoindentation studies. *Surf. Coat. Tech.*, **201**, 3253–3259.

Kusano, Y., & Hutchings, I.M. 2003. Analysis of nano-indentation measurements on carbon nitride films. *Surf. Coat. Tech.*, **169-170**, 739–742.

Kusano, Y., Barber, Z.H., Evetts, J.E., & Hutchings, I.M. 2003. Influence of inert gases on ionized magnetron plasma deposition of carbon nitride thin films. *Surf. Coat. Tech.*, **174-175**, 601–605.

Labilloy, F. 2006. *Simulation numérique d'un contact avec prise en compte du frottement par la méthode du Lagrangien augmenté*. M.Phil. thesis, Université Libre de Bruxelles, BATir Dept., director: T.J. Massart, supervisor: P. Berke.

Laconte, J., Iker, F., Jorez, S., André, N., Proost, J., Pardoen, T., Flandre, D., & Raskin, J.-P. 2004. Thin films stress extraction using micromachined structures and wafer curvature measurements. *Microelectronic Eng.*, **76**, 219–226.

Lafaye, S., Gauthier, C., & Schirrer, R. 2008. Analyzing friction and scratch tests without in situ observation. *Wear*, **265**, 664–673.

Lambert, P. 2007. *Capillary Forces in Microassembly*. Springer, ISBN: 978-0-387-71088-4.

Lambert, P., & Régnier, S. 2006. Surface and contact forces models within the framework of microassembly. *J. Micromechatronics*, **3**, 123–157.

Larsson, J., Biwa, S., & Strøakers, B. 1999. Inelastic flattening of rough surfaces. *Mech. Mat.*, **31**, 29–41.

Latella, B.A., Gan, B.K., & Li, H. 2007. Fracture toughness and adhesion of thermally grown titanium oxide on medical grade pure titanium. *Surf. Coat. Tech.*, **201**, 6325–6331.

Laursen, T.A. 1992. *Formulation and Treatment of Frictional Contact Problems Using Finite Elements*. Ph.D. thesis, Standford University, USA.

Laursen, T.A., & Simo, J.C. 1993. A continuum–based finite element formulation for the implicit solution of multibody, large deformation frictional contact problems. *Int. J. Num. Meth. Eng.*, **36**, 3451–3485.

Lee, Y., Park, J.Y., Kim, S.Y., Jun, S., & Inn, S. 2005. Atomistic simulations of incipient plasticity under Al(1 1 1) nanoindentation. *Mech. Mat.*, **37**, 1035.

Lemaitre, J., & Chaboche, J. 1985. *Mécanique des matériaux solides*. Dunod, Paris.

Lhernould, M. Sausse, Delchambre, A., Régnier, S., & Lambert, P. 2007. Electrostatic forces in micromanipulations: review of analytical models and simulations including roughness. *Appl. Surf. Sci.*, **253**, 6203–6210.

Li, J., & Weng, G.J. 2007. A secant-viscosity composite model for the strain-rate sensitivity of nanocrystalline materials. *Int. J. Plas.*, **23**, 2115–2133.

Lian, J., Garay, J.E., & Wang, J. 2007. Grain size and grain boundary effects on the mechanical behavior of fully stabilized zirconia investigated by nanoindentation. *Script. Mat.*, **56**, 1095–1098.

Lichinchi, M., Lenardi, C., Haupt, J., & Vitali, R. 1998. Simulation of Berkovich nanoindentation experiments on thin films using finite element method. *Thin Sol. Films*, **312**, 240–248.

Liebe, T., Menzel, A., & Steinmann, P. 2003. Theory and numerics of geometrically non–linear gradient plasticity. *Int. J. Eng. Sci.*, **41**, 1603–1629.

Lilleodden, E.T., Zimmerman, J.A., Foiles, S.M., & Nix, W.D. 2003. Atomistic simulations of elastic deformation and dislocation nucleation during nanoindentation. *J. Mech. Phys. Sol.*, **51**, 901.

Lin, F.H., & Tseng, A.A. 1998. A finite element analysis of elasto-plastic contact problems in metal forming. *Mat. Design*, **19**, 99–108.

Lin, Z.-C., Huang, J.-C., & Jeng, Y.-R. 2007. 3D nano–scale cutting model for nickel material. *J. Mat. Proc. Tech.*, **192**, 27.

Lu, C.-J., & Bogy, D.B. 1995. The effect of tip radius on nano-indentation hardness tests. *Int. J. Sol. Struc.*, **32**, 1759–1770.

Ma, D., Ong, C.W., Lu, J., & He, J. 2003. Methodology for the evaluation of yield strength and hardening behavior of metallic materials by indentation with spherical tip. *J. Appl. Phys.*, **94**, 288–294.

Maneiro, M.A. Garrido, & Rodriguez, J. 2005. Pile–up effect on nanoindentation tests with spherical–conical tips. *Script. Mat.*, **52**, 593–598.

Mata, M., & Alcalà, J. 2004. The role of friction on sharp indentation. *J. Mech. Phys. Sol.*, **52**, 145–165.

Mate, C.M. 2008. *Tribology on the Small Scale*. Oxford University Press.

Matthies, H.G. 1989. A decomposition method for the integration of the elastic-plastic rate problem. *Int. J.Num. Meth. Eng.*, **28**, 1–11.

Meguid, S.A., Czekanski, A., & Silva-Gomes, J.F. 2004. *Advances in Computational Contact Mechanics*. Saxe-Coburg Publications. Pages 219–245.

Mesarovic, S.D., & Fleck, N.A. 1999. Spherical indentation of elastic-plastic solids. *Proc. R. Soc. Lond. A*, **455**, 2707–2738.

Meyer, D.W., Plesha, M.E., & Cooper, R.F. 1991. A contact friction algorithm including non-linear viscoelasticity and a singular yield surface provision. *Comp. Struct.*, **42**, 913–925.

Miller, R., Ortiz, M., Phillips, R., Shenoy, V., & Tadmor, E.B. 1998. Quasicontinuum models of fracture and plasticity. *Eng. Frac. Mech.*, **61**, 427–444.

Miller, R.E., & Rodney, D. 2008. On the nonlocal nature of dislocation nucleation during nanoindentation. *J. Mech. Phys. Sol.*, **56**, 1203–1223.

Miller, R.E., Shilkrot, L.E., & Curtin, W.A. 2003. A coupled atomistics and discrete dislocation plasticity simulation of nanoindentation into single crystal thin films. *Acta Mat.*, **52**, 271–284.

Mirshams, R.A., & Parakala, P. 2004. Nanoindentation of nanocrystalline Ni with geometrically different indenters. *Mat. Sci. Eng. R*, **372**, 252–260.

Mirshams, R.A., & Pothapragada, R.M. 2006. Correlation of nanoindentation measurements of nickel made using geometrically different indenter tips. *Acta Mat.*, **54**, 1123–1134.

Nagy, P.M., Horváth, P., Aranyi, D., & Kálmán, E. 2006. Relaxation issues in nanoindentation experiments. *Curr. Appl. Phys.*, **6**, 154–160.

Nair, A.K., Parker, E., Gaudreau, P., Farkas, D., & Kriz, R.D. 2008. Size effects in indentation response of thin films at the nanoscale: A molecular dynamics study. *Int. J. Plas.*, **24**, 2016–2031.

NAMD. 2008. *NAMD Scalable Molecular Dynamics, www.ks.uiuc.edu/Research/namd/*.

Nayer, A. 1997. *The Metals Databook*. McGraw-Hill Companies, New York, ISBN: 0070460884.

Ni, W., Cheng, Y.-T., Cheng, C.-M., & Grummon, D.S. 2004. An energy-based method for analyzing instrumented spherical indentation experiments. *J. Mat. Res.*, **19**, 149–157.

Nibur, K.A., & Bahr, D.F. 2003. Identifying slip systems around indentations in FCC metals. *Script. Mat.*, **49**, 1055.

Nicola, L., Bower, A.F., Kim, K.-S., Needleman, A., & der Giessen, E. Van. 2007. Surface versus bulk nucleation of dislocations during contact. *J. Mech. Phys. Sol.*, **55**, 1120–1144.

Niordson, C.F., & Redanz, P. 2004. Size–effects in plane strain sheet–necking. *J. Mech. Phys. Sol.*, **52**, 2431–2454.

Nocedal, J. 2000. *Numerical methods in optimization (graduate course)*. Tech. rept. University of British Columbia, Department of Computer Science.

Noels, L., Stainier, L., & Ponthot, J.-P. 2004. On the use of large time steps with an energy momentum conserving algorithm for non–linear hypoelastic constitutive models. *Int. J. Sol. Struc.*, **41**, 663–693.

Noreyan, A., & Amar, J.G. 2008. Molecular dynamics simulations of nanoscratching of 3C SiC. *Wear*, **265**, 956–962.

Noreyan, A., Amar, J.G., & Marinescu, I. 2005. Molecular dynamics simulations of nanoindentation of β-SiC with diamond indenter. *Mat. Sci. Eng. B*, **117**, 235–240.

Nosonovsky, M., & Bhushan, B. 2007. Multiscale friction mechanisms and hierarchical surfaces in nano- and bio-tribology. *Mat. Sci. Eng. R*, **58**, 162–193.

Oliver, W.C., & Pharr, G.M. 1992. An improved technique for determining hardness and elastic modulus using load and displacement sensing indentation measurements. *J. Mat. Res.*, **7**, 1564–1583.

Ortiz, M., & Popov, E.P. 1985. Accuracy and stability of integration algorithms for elasto–plastic constitutive relations. *Int. J. Num. Meth. Eng.*, **21**, 1561–1576.

Ortiz, M., & Simo, J.C. 1986. An analysis of a new class of integration algorithms for elasto-plastic constitutive relations. *Int. J. Num. Meth. Eng.*, **23**, 353–366.

Ovaert, T.C., Kim, B.R., & Wang, J. 2003. Multi–parameter models of the viscoelastic/plastic mechanical properties of coatings via combined nanoindentation and non–linear finite element modeling. *Progress Org. Coat.*, **47**, 312–323.

Owen, D.R.J., & Hinton, E. 1980. *Finite Elements in Plasticity: Theory and Practice*. Pineridge Press, Swansea.

Pauleau, Y., Kukielka, S., Gulbinski, W., Ortega, L., & Dub, S.N. 2006. Structure and physical properties of nickel films deposited by microwave plasma-assisted cathodic sputtering. *J. Phys. D: Appl. Phys.*, **39**, 2803–2808.

Pelletier, C.G.N., Dekkers, E.C.A., Govaert, L.E., den Toonder, J.M.J., & Meijer, H.E.H. 2007. The influence of indenter-surface misalignment on the results of instrumented indentation tests. *Polymer Test.*, **26**, 949–959.

Pelletier, H. 2006. Predictive model to estimate the stress–strain curves of bulk metals using nanoindentation. *Tribology Int.*, **39**, 593–606.

Persson, B.N.J. 2006. Contact mechanics for randomly rough surfaces. *Surf. Sci. Rep.*, **61**, 201–227.

Pietrzak, G., & Curnier, A. 1999. Large deformation frictional contact mechanics: continuum formulation and augmented Lagrangian treatment. *Comp. Meth. Appl. Mech. Eng.*, **177**, 351–381.

Ponthot, J.P. 1995. *Traitement Unifié de la Mécanique des Milieux Continus Solides en Grandes Transformations par la Méthode des Eléments Finis, ISSN 0075-9333*. Ph.D. thesis, Université de Liège.

Ponthot, J.P. 2002. Unified stress update algorithms for the numerical simulation of large deformation elasto-plastic and elasto-viscoplastic processes. *Int. J. Plas.*, **18**, 91–126.

Qasmi, M., & Delobelle, P. 2006. Influence of the average roughness R_{ms} on the precision of the Young's modulus and hardness determination using nanoindentation technique with a Berkovich indenter. *Surf. Coat. Tech.*, **201**, 1191–1199.

Qin, J., Huang, Y., Hwang, K.C., Song, J., & Pharr, G.M. 2007. The effect of indenter angle on the microindentation hardness. *Acta Mat.*, **55**, 6127–6132.

Qiu, X., Huang, Y., Wei, Y., Gao, H., & Hwang, K.C. 2003. The flow theory of mechanism-based strain gradient plasticity. *Mech. Mat.*, **35**, 245–258.

Qu, S., Huang, Y., Pharr, H.M., & Hwang, K.C. 2006. The indentation size effect in the spherical indentation of iridium: A study via the conventional theory of mechanism-based strain gradient plasticity. *Int. J. Plas.*, **22**, 1265–1286.

Rabinovich, Y.I., Adler, J.J., Ata, A., Singh, R.K., & Moudgil, B.M. 2000. Adhesion between nanoscale rough surfaces I. Role of asperity geometry. *J. Colloid Interface Sci.*, **232**, 10–16.

Radi, E. 2008. On the effects of characteristic lengths in bending and torsion on Mode III crack in couple stress elasticity. *Int. J. Sol. Struc.*, **45**, 3033–3058.

Rafii-Tabar, H. 2000. Modelling the nano–scale phenomena in condensed matter physics via computer–based numerical simulations. *Phys. Rep.*, **325**, 239.

Rajendrakumar, P.K., & Biswas, S.K. 1997. Deformation due to contact between a two–dimensional rough surface and a smooth cylinder. *Trib. Letters*, **3**, 297–301.

Richter, A., Ries, R., Smith, R., Henkel, M., & Wolf, B. 2000. Nanoindentation of diamond, graphite and fullerene films. *Diam Relat. Mat.*, **9**, 170.

Ross, R.B. 1992. *Metallic Materials Specification Handbook, 4th ed.* Springer, ISBN: 0412369400.

Saraev, D., & Miller, R.E. 2006. Atomic–scale simulations of nanoindentation–induced plasticity in copper crystals with nanometer–sized nickel coatings. *Acta Mat.*, **54**, 33.

Schwaiger, R., Moser, B., Dao, M., Chollacoop, N., & Suresh, S. 2003. Some critical experiments on the strain-rate sensitivity of nanocrystalline nickel. *Acta Mat.*, **51**, 5159–5172.

Serpa, A.L., & Iguti, F. 2000. Contact with friction using the augmented Lagrangian method: a conditional constrained minimization problem. *J. Brazilian Soc. Mech. Sci.*, **22**(2), 273–289.

Sevostianov, I., & Kachanov, M. 2008. Contact of rough surfaces: A simple model for elasticity, conductivity and cross–property connections. *J. Mech. Phys. Sol.*, **56**, 1380–1400.

Shenoy, V.B., Miller, R., Tadmor, E.B., Rodney, D., Phillips, R., & Ortiz, M. 1999. An adaptive finite element approach to atomic–scale mechanics - the Quasicontinuum method. *J. Mech. Phys. Sol.*, **47**, 611–642.

Shibuta, Y., & Maruyama, S. 2007. Bond–order potential for transition metal carbide cluster for the growth simulation of a single–walled carbon nanotube. *Comp. Mat. Sci*, **39**, 842.

Shilkrot, L.E., Miller, R.E., & Curtin, W.A. 2004. Multiscale plasticity modeling: coupled atomistics and discrete dislocation mechanics. *J. Mech. Phys. Sol.*, **52**, 755–787.

Simo, J.C. 1988. A framework for finite strain elastoplasticity based on maximum plastic dissipation and the multiplicative decomposition. Part II: Computational aspects. *Comp. Meth. Appl. Mech. Eng.*, **68**, 1–31.

Simo, J.C. 1992. Algorithms for static and dynamic multiplicative plasticity that preserve the classical return mapping schemes of the infinitesimal theory. *Comp. Meth. Appl. Mech. Eng.*, **99**, 61–112.

Simo, J.C., & Laursen, T.A. 1992. An augmented Lagrangian treatment of contact problems involving friction. *Comp. Struc.*, **42**, 97–116.

Simo, J.C., & Taylor, R.L. 1985. Consistent tangent operators for rate independent plasticity. *Comp. Meth. Appl. Mech. Eng.*, **48**, 101–118.

Smythe, W.R. 1968. *Static and dynamic electricity*. Mc Graw-Hill, New-York.

Sofonea, M. 1997. On a contact problem for elastic–viscoplastic bodies. *Nonlin. Analys.*, **29**, 1037–1050.

Song, J., & Srolovitz, D.J. 2006. Adhesion effects in material transfer in mechanical contacts. *Acta Mat.*, **54**, 5305.

Stachowiak, G.W. 2005. *Wear, Materials, Mechanisms and Practice*. John Wiley & Sons, Ltd.

Stadler, G. 2007. Path–following and augmented Lagrangian methods for contact problems in linear elasticity. *J. Comp. Appl. Math.*, **203**, 533–547.

Stauss, S., Schwaller, P., Bucaille, J.-L., Rabe, R., Rohr, L., Michler, J., & Blank, E. 2003. Determining the stress–strain behavior of small devices by nanoindentation in combination with inverse methods. *Microelectr. Eng.*, **67-68**, 818–825.

Stölken, J.S., & Evans, A.G. 1998. A microbend test method for measuring the plasticity length scale. *Acta Mat.*, **46**, 5109–5115.

Sussmann, T., & Bathe, K.J. 1987. A finite element formulation for nonlinear incompressible elastic and inelastic analysis. *Comp. Struct.*, **29**, 357–409.

Szlufarska, I. 2006. Atomistic simulations of nanoindentation. *Mat. Today*, **9**, 42.

Taljat, B., & Pharr, G.M. 2004. Development of pile-up during spherical indentation of elastic-plastic solids. *Int. J. Sol. Struc.*, **41**, 3891–3904.

Tam, E. 2006. *Caractérisation des propriétés mécaniques de surface par nanoindentation*. M.Phil. thesis, Université Libre de Bruxelles, Chemicals and Materials Department.

Tanaka, M., Higashida, K., & Haraguchi, T. 2004. Microstructure of plastic zones around crack tips in silicon revealed by HVEM and AFM. *Mat. Sci. Eng. A*, **433**, 387.

Tao, Q., Lee, H.P., & Lim, S.P. 2001. Contact mechanics of surfaces with various models of roughness descriptions. *Wear*, **249**, 539–545.

Tho, K.K., Swaddiwudhipong, S., Hua, J., & Liu, Z.S. 2006. Numerical simulation of indentation with size effect. *Mat. Sci. Eng. A*, **421**, 268–275.

Torre, F. Dalla, Swygenhoven, H. Van, & Victoria, M. 2002. Nanocrystalline electrodeposited Ni: microstructure and tensile properties. *Acta Mat.*, **50**, 3957–3970.

Tripathy, S. 2005. *Nanoindentaion: influence of surface morphology*. M.Phil. thesis, Université Libre de Bruxelles, Chemicals and Materials Department.

Tsou, C., Hsu, C., & Fang, W. 2005. Interfaces friction effect of sliding contact on nanoindentation test. *Sensors and Actuators A*, **117**, 309–316.

Tymiak, N.I., Kramer, D.E., Bahr, D.F., Wyrobek, T.J., & Gerberich, W.W. 2001. Plastic strain and strain gradients at very small indentation depths. *Acta Mat.*, **49**, 1021–1034.

van den Bosch, M. 2007. *Interfacial delamination in polymer coated metal sheet*. Ph.D. thesis, Technical University of Eindhoven.

Vashishta, P., Kalia, R.K., & Nakano, A. 2006. Multimillion atom simulations of dynamics of oxidation of an aluminum nanoparticle and nanoindentation on ceramics. *J. Phys. Chem. B*, **110**, 3727.

Vliet, K.J. Van, Li, J., Zhu, T., Yip, S., & Suresh, S. 2003. Quantifying the early stages of plasticity through nanoscale experiments and simulations. *Phys. Rev. B*, **67**, 104105.

Wai, S.W., Spinks, G.M., Brown, H.R., & Swain, M. 2004. Surface roughness: Its implications and inference with regards to ultra microindentation measurements of polymer mechanical properties. *Polymer Test.*, **23**, 501–507.

Walter, C., Antretter, T., Daniel, R., & Mitterer, C. 2007. Finite element simulation of the effect of surface roughness on nanoindentation of thin films with spherical indenters. *Surf. Coat. Tech.*, **202**, 1103–1107.

Wang, F., Huang, P., & Xu, K. 2007a. Strain rate sensitivity of nanoindentation creep in polycrystalline Al film on Silicon substrate. *Surf. Coat. Tech.*, **201**, 5216–5218.

Wang, T.H., Fang, T.-H., & Lin, Y.-C. 2007b. A numerical study of factors affecting the characterization of nanoindentation on silicon. *Mat. Sci. Eng. A*, **447**, 244–253.

Wang, W., Huang, Y., Hsia, K.J., Hu, K.X., & Chandra, A. 2003. A study of microbend test by strain gradient plasticity. *Int.J.Plas.*, **19**, 365–382.

Warren, A.W., & Guo, Y.B. 2006. Machined surface properties determined by nanoindentation: Experimental and FEA studies on the effects of surface integrity and tip geometry. *Surf. Coat. Tech.*, **201**, 423–433.

Widjaja, A., Needleman, A., & der Giessen, E. Van. 2007. The effect of indenter shape on sub-micron indentation according to discrete dislocation plasticity. *Mod. Sim. Mat. Sci. Eng.*, **15**, S121–S131.

Wriggers, P. 2002. *Computational Contact Mechanics*. John Wiley and Sons Ltd.

Wriggers, P., & Zavarise, G. 2004. *Computational Contact Mechanics*. John Wiley and Sons. Chap. 6, pages 195–221.

Xing, H.L., & Makinouchi, A. 2002. Three dimensional finite element modeling of thermo-mechanical frictional contact between finite deformation bodies using R–minimum strategy. *Comp. Meth. Appl. Mech. Eng.*, **191**, 4193–4214.

Xu, Z.-H. 2004. *Mechanical Characterization of Coatings and Composites – Depth–Sensing Indentation and Finite Element Modelling*. Ph.D. thesis, Royal Institut of Technology, Stockholm, Sweden, Department of Materials Science and Engineering.

Yang, B., Laursen, T.A., & Meng, X. 2005. Two dimensional mortar contact methods for large deformation frictional sliding. *Int. J. Num. Meth. Eng.*, **62**, 1183–1225.

Yang, G.M., Coquille, J.C., Fontaine, J.F., & Lambertin, M. 2001. Influence of roughness on characteristics of tight interference fit of a shaft and a hub. *Int. J. Sol. Struc.*, **38**, 7691–7701.

Yin, W.M., Whang, S.H., Mirshams, R., & Xiao, C.H. 2001. Creep behavior of nanocrystalline nickel at 290 and 373K. *Mat. Sci. Eng. A*, **301**, 18–22.

Youn, S.W., & Kang, C.G. 2005. FEA study on nanodeformation behaviors of amorphous silicon and borosilicate considering tip geometry for pit array fabrication. *Mat. Sci. Eng. A*, **390**, 233–239.

Yu, N., Polycarpoua, A.A., & Conry, T.F. 2004. Tip-radius effect in finite element modeling of sub-50 nm shallow nanoindentation. *Thin Sol. Films*, **450**, 295–303.

Zahouani, H., & Sidoroff, F. 2001. Rough surfaces and elasto-plastic contacts. *Different Faces of Tribology*, **IV**, 709–715.

Zhang, J., Niebur, G.L., & Ovaert, T.C. 2008. Mechanical property determination of bone through nano- and micro-indentation testing and finite element simulation. *J. Biomech.*, **41**, 267–275.

Zhang, L., & Tanaka, H. 1997. Towards a deeper understanding of wear and friction on the atomic scale–a molecular dynamics study. *Wear*, **211**, 44.

Zhang, S., Hodgson, P.D., Cardew-Hall, M.J., & Kalyanasundaram, S. 2003. A finite element simulation of micro-mechanical frictional behavior in metal forming. *J. Mat. Proc. Tech.*, **134**, 81–91.

Zhang, T.-Y., Xu, W.-H., & Zhao, M.-H. 2004. The role of plastic deformation on rough surfaces in the size-dependent hardness. *Acta Mat.*, **52**, 57–68.

Zhao, M., Slaughter, W.S., Li, M., & Mao, S.X. 2003. Material-length-scale-controlled nanoindentation size effects due to strain-gradient plasticity. *Acta Mat.*, **51**, 4461–4469.

Zhao, M., Ogasawara, N., Chiba, N., & Chen, X. 2006. A new approach to measure the elastic-plastic properties of bulk materials using spherical indentation. *Acta Mat.*, **54**, 23–32.

Zienkiewicz, O.C. 2000. *The finite element method Volume 2 - Solid mechanics*. Butterworth Heinemann, Linacre House, Jordan Hill, Oxford. Chap. 10 - Geometrically nonlinear problems - finite deformation.

Zong, Z., & Soboyejo, W. 2004. Indentation size effects in face centered cubic single crystal films. *Mat. Sci. Eng. A*, **404**, 281–290.

Appendix A

A.1 Post–treatment methods of nanoindentation

The focus is set here on how material properties are extracted from the raw nanoindentation data, the load–displacement curves. Two frequently used post–treatment methods for nanoindentation data are considered in this work. These experimentally applied methods were implemented in a numerical tool that allows the post–treatment of indentation data issued both from experiments and from numerical simulations. Both post–treatment methods have the goal to identify the Young's modulus E, and the nano–hardness value H_{nano} of the tested material with high accuracy and a low sensitivity to a variation in the experimental conditions (surface roughness, friction, etc.) and in the material properties other than they are designed to evaluate. Since the nano–hardness is not an intrinsic material property generally defined as the ratio of the peak load and the projected area at contact depth h_c: $H_{nano} = \frac{F_{max}}{A_{proj}(h_c)}$, the focus was rather set on the value and the variation of the post–treated Young's modulus E_{out}. Material parameters obtained from nanoindentation data are relative values compared to a reference value associated to the indentation of a material with known properties, measured in the calibration step of the experiments [Baker 1997; Fischer-Cripps 2006].

The Young's modulus of the sample can be evaluated from nanoindentation data is various ways. The first post–treatment method considered here is the most widely spread method, proposed by Oliver and Pharr [Oliver & Pharr 1992], and used for its simplicity and its broad range of application. This method is based on the assumption of purely elastic unloading of the indenter–sample frictionless contact. It only uses the unloading segment of the load–displacement curve of nanoindentation to compute the contact stiffness for further processing. Conversely to its simplicity, it has the corresponding drawback that a geometrical quantity called contact depth h_c, defined on an actual deformed contact configuration (depending on potential pile–up or sink–in phenomena), has to be reasonably well–known. The contact depth is calculated from the maximum indentation depth h_{max} by making simplifying assumptions. Even though the measure of the indent profile can give additional information about the deformation procedure during indentation [Bolzon *et al.* 2004; Nagy *et al.* 2006], and is helpful for a better approxi-

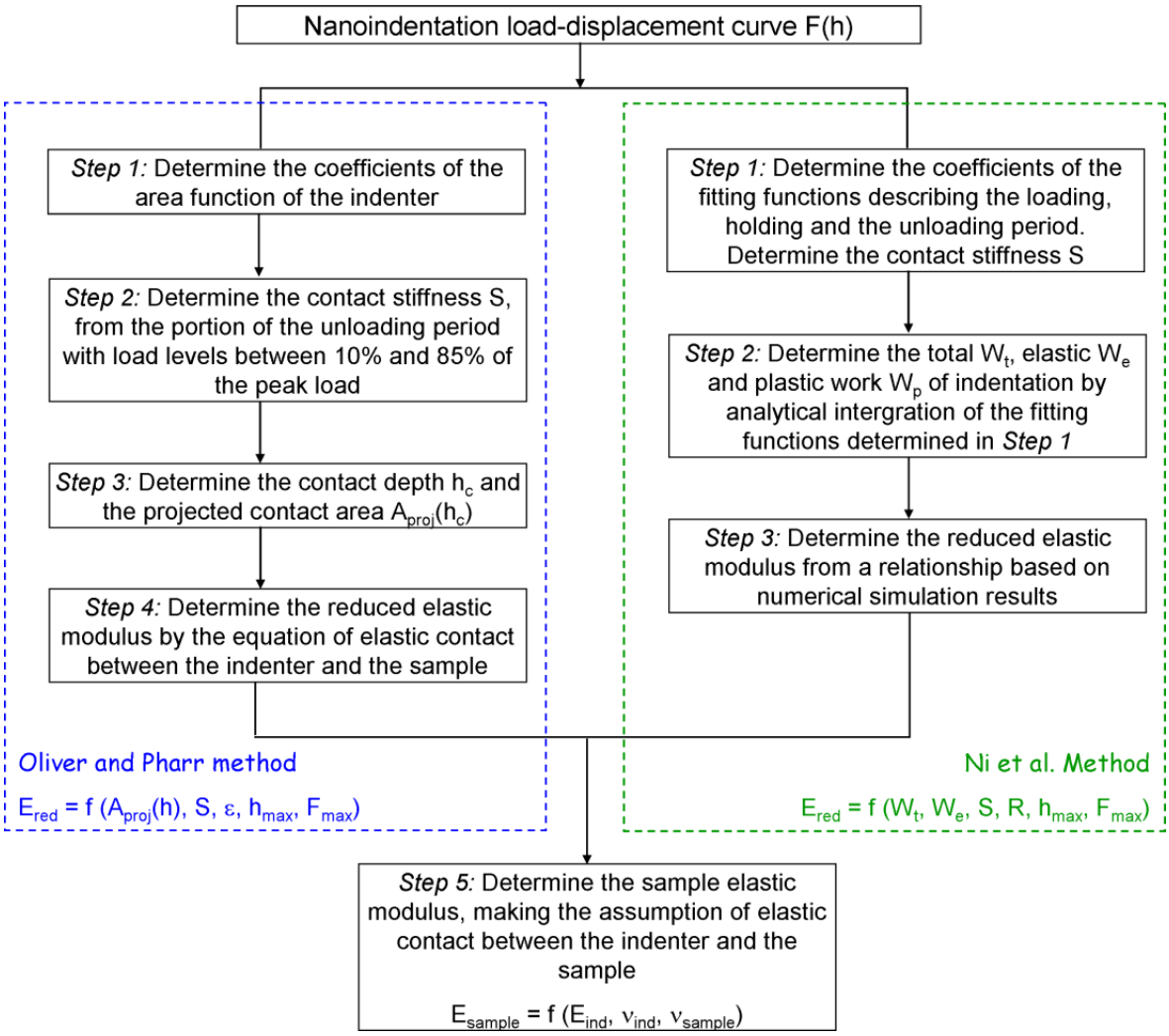

Figure A.1: Flowchart of the two post–treatment methods of nanoindentation considered in this work.

mation of h_c, it is a complex and time consuming procedure, and thereby it is rarely performed systematically after nanoindentation tests.

The second post–treatment method, proposed by Ni et al. [Ni *et al.* 2004] has the goal to overcome the main disadvantage of the Oliver and Pharr method; by avoiding the evaluation of the contact depth potentially leading to a higher accuracy. This post–treatment method is developed for the case of spherical nanoindentation. It is based on trends identified by numerical simulations of nanoindentation using the finite element method. Based on the numerical results, non–dimensional functions of the indentation problem were set up defined in terms of the unloading stiffness S, the total work W_t and the elastic work of indentation W_e, corresponding to the area under the loading and the unloading portion of the load–displacement curve respectively. These functions are used for the evaluation of the Young's modulus of the tested material. The corresponding drawback is that this method is much more sensible to changes in any portion of the curve and to the variations in the load levels affecting directly the integrated work quantities.

A numerical tool was set up for the post–treatment the nanoindentation results issued from experiments and simulations, aiming for a large flexibility in their assessment. The code is such that the user can intervene, and adjust some otherwise unaccessible parameters of the post–treatment methods considered here, if necessary. It also allows to follow step–by–step the post–treatment procedure.

Oliver and Pharr method, based on the unloading slope

Some assumptions are common to both considered nanoindentation post–treatment methods. These are recalled here:

- flat and smooth sample contact surface,
- frictionless contact between the indenter tip and the sample,
- the behavior of the indenter–sample contact in the unloading period is elastic and rate–independent. This means that potential viscoelastic effects of the material [Cheng & Cheng 2005; Ovaert *et al.* 2003; Zhang *et al.* 2008] are not taken into account; but also that a rate–dependent effect of the contact behavior itself is disregarded,
- the values of the Poisson's ratio of both the sample ν_{sample} and the indenter material ν_{ind} are known, or approximated.

In addition, the projected area A_{proj} of the tip as a function of the indenter penetration h, depends on the actual geometry of the indenter. It is approximated by a polynomial function in *Step 1*, determined in the calibration step of the experiments.

$$A_{proj}(h) = c_1 h^2 + c_2 h + c_3 h^{1/2} + c_4 h^{1/4} + c_5 h^{1/8} \tag{A.1}$$

For the sake of clarity, a simple example of the definition of the projected area is given. In the case of a spherical indenter, at a height $h^{'}$ from the tip, the projected area is defined as $A_{proj}(h^{'}) = \pi \left(\frac{d(h^{'})}{2} \right)^2$, with $d(h^{'})$ the diameter of the spherical tip at height $h^{'}$.
Moreover, for the approximation of h_c (in *Step 2*), the shape of the indenter is taken into account by a coefficient ϵ that varies as a function of the tip geometry.

Post–treatment procedure

Step 1

Determine the coefficients c_1 to c_n of the area function of the indenter. The coefficients in (A.1) are fitted to describe the shape of the indenter. When load–displacement curves issued from numerical simulations are treated, an ideal shape with a given nominal radius is considered.

Step 2

Determine the contact stiffness S from the unloading curve of nanoindentation. For this the point of initial unloading is identified first. Note that, particularly in the presence of rate–dependent effects, the choice of the point of initial unloading may potentially vary depending on the prescribed tolerance of detection, as shown in Fig.A.2.

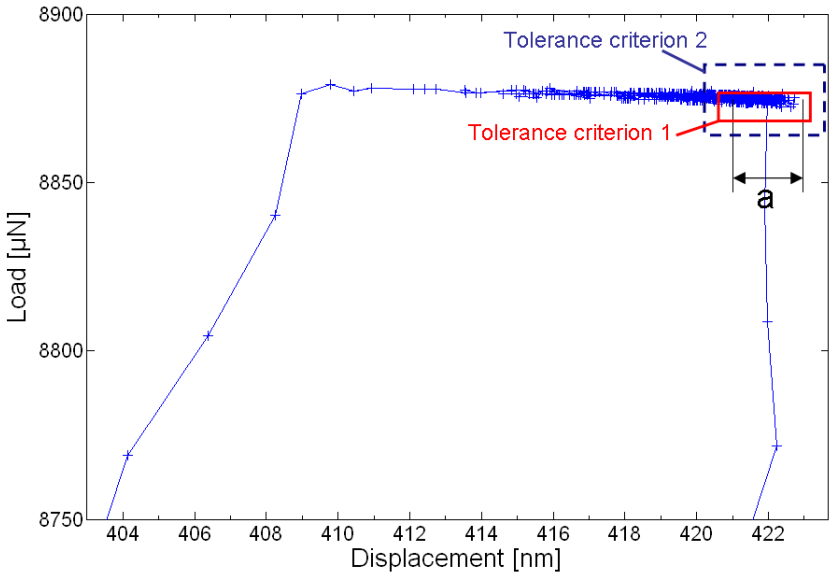

Figure A.2: Zoom on an experimental load–displacement curve of nanoindentation of pure nickel with a conical indenter of $2\mu m$ nominal radius. The size of the rectangular envelop depends on the tolerance values used to detect the point of initial unloading. The segment 'a' of the holding period is constituted of points that can potentially be identified as the point of initial unloading, satisfying 'Tolerance criterion 1'.

Then a function with the following form is fitted to the unloading curve.

$$F_{unload}(h) = s_1(h - s_2)^{s_3} \tag{A.2}$$

This fit uses weighting coefficients, such that the points of the unloading curve with load levels between 10% to 85% of the peak load have the largest influence for the sake of accuracy. Indeed the initial part of the unloading segment (down to load levels of around 90% of the peak load) can be subject to variations related to friction between the indenter and the sample [Tsou *et al.* 2005]. The user can adjust freely the domain of interpolation of high influence, if this becomes necessary. The contact stiffness S is then evaluated at the indentation depth, where the unloading begins, by:

$$S = s_1 s_3 (h_{unload} - s_2)^{(s_3 - 1)} \tag{A.3}$$

The position of the point of initial unloading, together with the curve fit influences the value of the contact stiffness S, and thereby the post–treated elastic modulus. Such effects can be considered as nanoindentation *dispersion related to the post–treatment procedure*.

These effects can be decreased by adapting the parameters of the automatic fitting procedure, being an available option in the programmed tool.

Step 3

The contact depth h_c and the projected area at contact depth $A_{proj}(h_c)$ are evaluated by the approximation:

$$h_c = h_{max} - \epsilon \frac{F_{max}}{S} \tag{A.4}$$

where h_{max} and F_{max} stand for the maximum indentation depth and the peak load level, respectively. ϵ is a model parameter depending on the indenter shape $\epsilon = 0.75$ for spherical and parabolic indenter geometries and $\epsilon = 0.72$ for conical indenters. The main drawback of this simple approximation is that it does not take into account potential pile–up and sink–in phenomena, which depend on the plastic behavior of the sample material [Habbab *et al.* 2006; Maneiro & Rodriguez 2005; Taljat & Pharr 2004]. This can lead to post–treatment errors, whose magnitude varies as a function of the indenter geometry and the sample material. In the case of the cono–spherical indenter geometry with $2\mu m$ nominal tip radius used in Sections 5.1 and 5.2 the influence of the variation of the contact depth for indentations in pure nickel at $1000\mu N$, $2000\mu N$, and $9000\mu N$ peak loads (corresponding to $55nm$, $100nm$, and $430nm$ indenter penetration, respectively) was found to be very low with respect to other potential sources of scatter

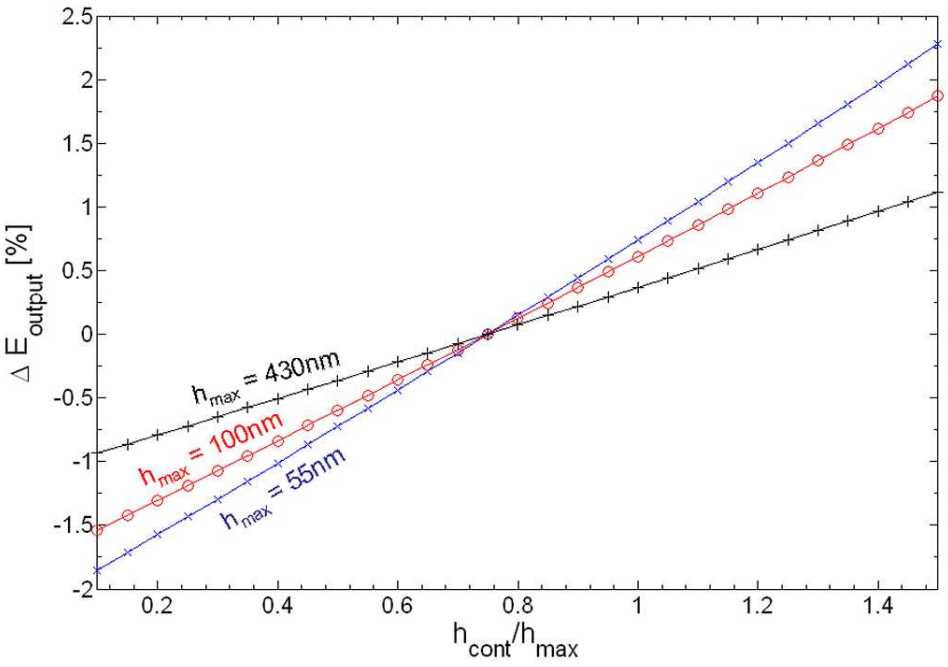

Figure A.3: Effect of potential sink–in and pile–up, resulting in variation in the value of $\epsilon = \frac{h_c}{h_{max}}$ on the post–treated elastic modulus of the sample for different indentation depths of cono–spherical nanoindentation of pure nickel with a tip of $2\mu m$ nominal radius. . Note the very large range of variation of ϵ, resulting in a small variation of $\Delta E_{output} = \frac{E^{\epsilon}_{output}}{E^{\epsilon=0.75}_{output}} - 1$.

(Fig.A.3). $A_{proj}(h_c)$ is evaluated using (A.1) substituting the value of h_c.

Step 4

The reduced modulus E_{red} of the contact is evaluated in this last step of the post–treatment procedure. The assumption of the elastic contact unloading between the sample and the indenter is used here. The reduced modulus is a quantity related to the elastic contact between the indenter and the sample materials and is calculated using the following approximation [Oliver & Pharr 1992]:

$$E_{red} = \frac{S}{2}\left(\frac{\pi}{A_{proj}(h_{cont})}\right)^{1/2} \tag{A.5}$$

Step 5

Finally the Young's modulus of the sample E_{sample} can be determined from the reduced modulus E_{red} making the assumption of an elastic contact behavior.

$$E_{sample} = \frac{E_{red}\,(1-\nu_{sample}^2)}{(1-\frac{E_{red}}{E_{ind}})\,(1-\nu_{ind}^2)} \tag{A.6}$$

Generally a reasonable approximation of the Poisson's ratio of the sample ν_{sample} is made when its value is not available in the literature. The Poisson's ratio of the diamond indenter material is most frequently taken $\nu_{ind} = 0.07$. The values of the Poisson's ratio have a small influence on the value of E_{sample}, therefore the potential inaccuracy in their values is not significantly penalizing, as shown in Fig.A.4. The elastic modulus of the indenter in the post–treatment pro-

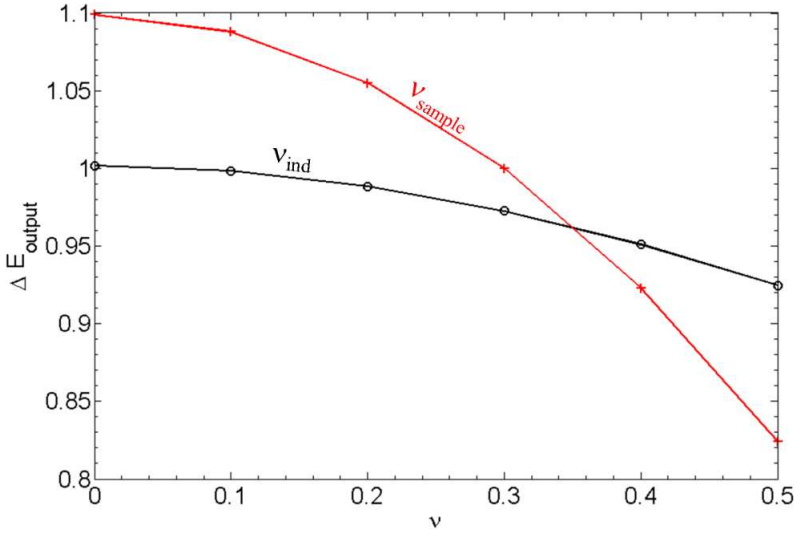

Figure A.4: Influence of the Poisson's ratio of the sample ν_{sample} (red crosses) and of the indenter material ν_{ind} (black circles) on the post–treated Young's modulus in (A.6), keeping the reduced elastic modulus E_{red} and the elastic modulus of the indenter material E_{ind} constant. $\Delta E_{sample} = \frac{E_{output}}{E_{ref}}$ with E_{ref} determined for $E_{red} = 260$GPa, $E_{ind} = 1040$GPa, $\nu_{sample} = 0.3$, and $\nu_{ind} = 0.07$.

cedure is taken to be very large when indentation results issued from numerical simulations are evaluated, since the indenter is modeled as a rigid body in the numerical model. Otherwise the value of the diamond material E_{ind} = 1140GPa is used.
To sum up, this post–treatment method of nanoindentation depends on the following functions, and parameters: $A_{proj}(h)$, S, ϵ, h_{max}, F_{max}, and in the final step, common to both methods considered here: ν_{sample}, ν_{ind}, and E_{ind}.

Method of Ni et al., based on the work of indentation

The post–treatment method proposed by Ni et al. [Ni *et al.* 2004] is based on the trends identified from finite element simulations of spherical nanoindentation. This implies that the post–treatment method performs well for experimental cases that are in fair agreement with the conditions which were modeled in the numerical simulations. Therefore it is important to recall the assumptions of the numerical work on which this post–treatment method is based on, that add up to the common assumptions listed before;

- the indenter tip geometry is spherical,
- the material is elastic–plastic with isotropic hardening,
- the hardening of the material is modeled by a power law,
- the behavior of the material is rate–independent.

The essence of this method is the use of non–dimensional functions of the indentation issued from simulations, defined in terms of the contact stiffness S, the total work of indentation W_t and the elastic work of indentation W_e. No additional information on the deformed contact geometry is needed to evaluate the elastic modulus of the sample material E_{sample}.

Post–treatment procedure

Step 1
Two parameter sets of a power law expression, similar to (A.2) are fitted to describe the complete loading and the complete unloading periods of the load–displacement curve. The contact stiffness S is evaluated at maximum indentation depth from the expression of the unloading curve fit. The holding period is approximated by a simple linear function.

Step 2
The area under the loading, holding and unloading period of the load–displacement curve is determined by analytical integrals. The total work of indentation W_t and the elastic work of

indentation W_e, correspond to the area under the loading and holding periods and under the unloading period of the load–displacement curve, respectively. The work dissipated by plastic deformation W_p is the difference between the total work of indentation W_t and the reversible elastic work of indentation W_e.

$$W_p = W_t - W_e \tag{A.7}$$

Issues related to the approximation of the numerical fit of the load–displacement curve (particularly in the case of experimental data usually showing a higher dispersion than in the simulations), referred to previously as 'nanoindentation dispersion related to the post–treatment procedure' of course play a role in this step.

Step 3

The reduced elastic modulus of the indenter–sample contact is determined using the following expression:

$$E_{red} = \frac{0.4657\ S^2 \left(\frac{W_e}{W_t}\right) \left(\frac{h_{max}}{R}\right)^{0.62}}{F_{max}} \tag{A.8}$$

with R the nominal radius of the spherical indenter, h_{max} the maximum indentation depth and F_{max} the peak load level of the indentation. Equation (A.8) compacts the trends issued from a numerical model of spherical nanoindentation, considering a wide range of materials. It is emphasized that contrary to the Oliver and Pharr method, for obtaining the reduced elastic modulus of the indentation, the area function of the indenter is not evaluated and the contact depth is not approximated.

Step 4

This step is identical to *Step 5* of the Oliver and Pharr post–treatment method. The elastic modulus of the sample is determined from the reduced elastic modulus making the assumption of an elastic contact between the indenter and the sample.

To sum up, this post–treatment method of nanoindentation depends on the following parameters: W_t, W_e, S, R, h_{max}, F_{max}, and in the final step, common to both methods considered here: ν_{sample}, ν_{ind}, and E_{ind}.

A.2 Benchmark: extrusion of an aluminum cylinder

This section presents the numerical benchmark test of the extrusion of an aluminum cylinder with friction [Laursen 1992; Simo & Laursen 1992], used (together with other benchmark problems) for the validation of the implemented features of finite element code. This problem is particularly challenging from a computational viewpoint, since it involves nonlinearities due to the varying normal and tangential contact conditions, material nonlinearities (elastic–plastic behavior), and geometrical nonlinearities due to the finite deformation of the cylinder.

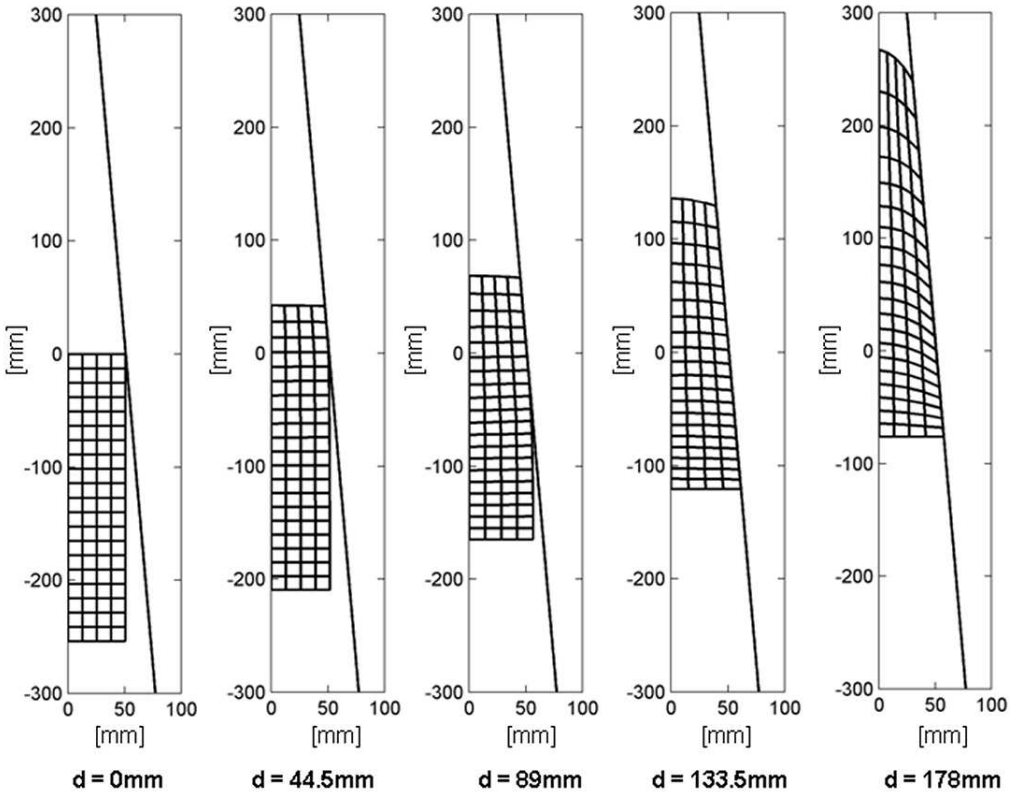

Figure A.5: Snapshots of the deformed mesh at different imposed displacements d, when Coulomb friction is considered on the contact interface (μ = 0.1), as shown in Labilloy [2006]. d = 0mm corresponds to the initial, undeformed configuration. Note the large deformation of the cylinder in the final stages of the extrusion.

The considered problem is the extrusion of an aluminum cylinder of 5.08cm radius and 25.4cm initial length, which is forced into a coaxial, perfectly rigid conical matrix with a 10° cone angle. The imposed displacement at the free end of the deformable cylinder is 17.78cm. The behavior of aluminum is assumed to be elastic–plastic, with linear hardening, and without rate–dependent effects. The von Mises yield criterion is used with the following material parameter set: Young's modulus E = 68.95GPa, Poisson's ratio ν = 0.32, initial yield limit σ_0 = 31MPa, hardening coefficient K = 261MPa and hardening exponent n = 1, in Ludwik's hardening law ($\sigma_v(\kappa) = \sigma_0 + K\ \kappa^n$, where $\sigma_v(\kappa)$ is the current yield stress). A Coulomb friction law, with a

coefficient of friction of μ = 0.1 is considered on the contact interface.
The deformable cylinder is described in a 2D axisymmetric model with 80 4–noded finite elements using the corotational finite deformation formulation, presented in Section 4.1 (with 20 elements in the direction of extraction and 4 elements in the radial direction, as shown in Fig.A.5). There are 24 nodes in the predefined contact interface, declared as contact elements. The contact problem involving friction is solved using the augmented Lagrangian formulation, presented in Section 4.2.
This computation was addressed in Labilloy [2006]. The regularization parameters of the augmented Lagrangian r_n and r_t for the normal and for the tangential contact conditions, respectively were chosen fixed values in the calculation $r_n = 10$ and $r_t = 20$. Note the small magnitude of these parameters with respect to the ones used in the classical penalty method $p_n = 1.55 \times 10^{13}$ and $p_t = 1.55 \times 10^{10}$ to solve the same problem [Laursen 1992].

The size of the imposed displacement increments had to be chosen relatively small for the computation of the contact behavior and for the computation of stresses considering the elastic–plastic material behavior, i.e. in order to guarantee the convergence of the local iteration loop. The average increment size in the computation was $0.1mm$.
In the beginning of the extrusion only one node is in sliding contact, in this case the convergence rate is fast, nearly quadratic (Tab.A.1).

iincr =	60			
iiter =	1	conv =	1.5963	Change
iiter =	2	conv =	3.2451	
iiter =	3	conv =	1.2625	
iiter =	4	conv =	0.17438	
iiter =	5	conv =	0.0049619	
iiter =	6	conv =	7.804e-05	
iiter =	7	conv =	1.6353e-10	

Table A.1: Convergence rate of the computation in the early stage of the extrusion with one node in sliding contact with the matrix. The first column corresponds to the iteration number, the second to the obtained magnitude of the force residuals. ‘Change’ refers to a change in the contact state in the iteration.

A decrease in the rate of convergence potentially appears only when several contact nodes are already in contact. It depends on the number of cycling contact elements between the state of stick and the state of slip (Tab.A.2). Even though these convergence issues could potentially be decreased by the choice of larger regularization parameters $0 < r < 2\ \lambda_{min}(\mathbf{K})$, with $\lambda_{min}(\mathbf{K})$ the smallest eigenvalue of the complete stiffness matrix of the system (proposed in Pietrzak & Curnier [1999]), this was not considered here for the sake of simplicity. An update of the reg-

iincr = 203			
iiter = 1	conv =	5.0608	Change
iiter = 2	conv =	21.011	Change
iiter = 3	conv =	139.72	Change
iiter = 4	conv =	106.42	Change
iiter = 5	conv =	238.96	Change
iiter = 6	conv =	50.568	Change
iiter = 7	conv =	73.804	Change
iiter = 8	conv =	36.246	Change
iiter = 9	conv =	20.042	Change
iiter = 10	conv =	13.981	Change
iiter = 11	conv =	10.76	Change
iiter = 12	conv =	9.3644	Change
iiter = 13	conv =	10.084	Change
iiter = 14	conv =	10.55	Change
iiter = 15	conv =	9.328	Change
iiter = 16	conv =	13.249	Change
iiter = 17	conv =	20.025	Change
iiter = 18	conv =	59.202	Change
iiter = 19	conv =	11.192	Change
iiter = 20	conv =	66.55	Change

Table A.2: The convergence rate of the computation is decreased when oscillation between the state of stick and the state of slip occurs for several contact nodes. The first column corresponds to the iteration number, the second to the obtained magnitude of the force residuals. 'Change' refers to a change in the contact state of one or more contact elements in the iteration.

ularization parameters r_n and r_t during the computation is planned in a future development to overcome the convergence issues related to the oscillating contact state of the contact elements. In this computation a less efficient but simple strategy was chosen; keeping the values of r_n and r_t constant, the maximum number of iterations related to a change of the contact state was limited. If in 20 iterations no stable contact state had been reached, the increment was restarted with a reduced size. Generally an increment converged when a stable contact state had been reached within 5 iterations for the given example.

The obtained deformed shape of the extruded cylinder (Fig.A.5), as well as the trend in the evolution of the reaction forces induced by the forced extraction (Fig.A.6) were found to be in good agreement with [Laursen 1992; Simo & Laursen 1992], where this problem was initially proposed. The quantitative comparison of the obtained extrusion force–displacement curves was not considered, because the computations performed in Laursen [1992]; Simo & Laursen

[1992] use a different (hyperelastic–based) finite deformation formulation (described in detail in Simo [1992]).

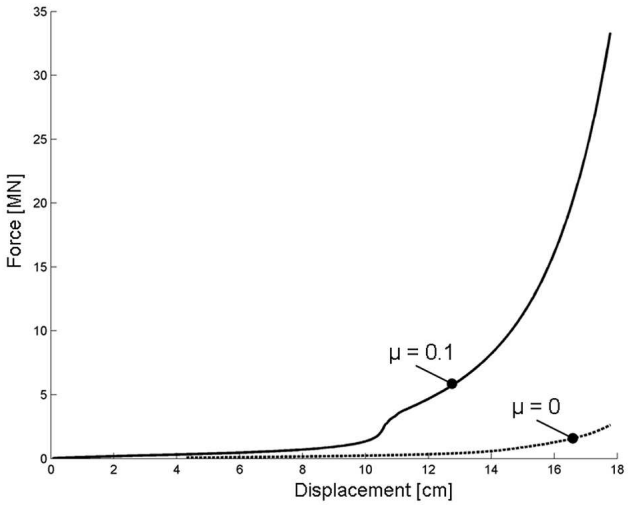

Figure A.6: Extraction force as a function of the displacement of the cylinder for frictional ($\mu = 0.1$), and for frictionless contact ($\mu = 0$). The large difference between the two curves demonstrates the importance of frictional effects in the considered problem.

The important increase in the extraction force level between $10cm$ and $11cm$ of imposed displacement is the result of the contact between the deformable cylinder and the rigid matrix in the complete lateral contact zone. When this contact is realized the deformation of the aluminum cylinder is unconstrained only on the upper surface.